Understanding the formation and evolution of biomass burning organic aerosol using non-target data approaches and mechanism development

Rhianna Louise Evans

Doctor of Philosophy

University of York

Chemistry

February 2025

Abstract

Ambient biomass burning (BB) is the second largest source of organic aerosol (OA) and non-methane organic compounds to the atmosphere which can impact air quality and climate on local, regional and global scales. BB also includes domestic solid fuel combustion, which is a major contributor to particulate matter air pollution in many European cities. Global BB emissions are predicted to rise due to climate change, and growth in the domestic sector is also expected in the coming years. However, a detailed understanding of the chemical composition of emissions from BB and their reactivity in the atmosphere is lacking. This missing understanding is compounded by challenges in the quantification of chemical constituents contributing to OA. A central theme in this thesis is non-target analysis (NTA) of OA chemical composition. First, to overcome challenges facing quantification in NTA, namely the lack of analytical standards and non-universal ionisation in electrospray sources, a semi-quantitative methodology was developed for Ultra-High-Performance Liquid Chromatography coupled to Electrospray Ionisation High Resolution Mass Spectrometry (UHPLC-ESI-HRMS). It was observed that using the UHPLC-ESI-HRMS instrument response (i.e. peak area) could over- or under- estimate a species' abundance within a sample compared to semi-quantification, highlighting the need for quantification of species where no standards are available. Second, a semi-quantitative NTA of OA from wood burning determined compositional changes under different burning conditions and after aging. These results showed the relative aromaticity of the OA decreased upon aging but was dependent on the burning conditions which could have important implications for toxicity. Finally, chamber experiments evaluated the atmospheric photo-oxidation and secondary organic aerosol (SOA) formation of a methoxyphenol compound (guaiacol) emitted during BB. These experiments highlighted the different evolution of guaiacol SOA products in between night and daytime and provides direction for future research.

Contents

List of figures

List of tables

Acknowledgements

In loving memory of my beloved grandad, Dr Sydney Parke, whose footsteps I now follow in 65 years later. Thank you for believing in me, I hope I've made you proud.

Firstly, thanks to my supervisors Dr Andrew Rickard and Professor Jacqui Hamilton. I am very grateful to Andrew for his constant encouragement in anything I wanted to do and enthusiasm for the work in this PhD. I also want to thank Jacqui for all her support, expert analytical knowledge, and helping me navigate the peer-review process in my publications. Secondly, I cannot begin to thank Dan enough for all his support, aerosol and orbi wisdom, and most importantly, all the walks and coffee with Maple. I also thank Alfie for sharing his knowledge of mechanisms and modelling with me. Thank you to my PhD cohort and everyone in WACL for making the last few years so enjoyable, I am extremely grateful for all the friends I have made here. Finally, I have so much love for all the lovely ladies, both past and present, of my row in the office for all the giggles and good times over the years which have got me through.

The work in this thesis would not have been possible without my collaborators at the University of Manchester and EUPHORE. I especially thank Aristeidis at Manchester for agreeing to my participation in these experiments which ended up forming two of my thesis chapters. I also thank the rest of the Manchester chamber team for conducting these experiments. Thank you to all the team at EUPHORE in Valencia for hosting me for an entire month and performing the experiments in an unexpectedly challenging weather period. This experience was a huge highlight of my PhD and I am very grateful for all your hard work to make it happen.

I would absolutely not be here today without the love and support of my family, especially from my mum and dad, as well as, my nana and my wonderful sisters. I feel incredibly lucky to have been raised by a line of strong intelligent women and I am forever grateful for all the sacrifices they made for me to get here. Your support in all my endeavours truly means the world to me. Finally, thank you to my dear Sam for being my biggest supporter and despite being over 5000 miles away never failing to put a smile on my face.

Author's declaration

I declare that this thesis is a presentation of original work and I am the sole author. This work has not previously been presented for an award at this, or any other, University. All sources are acknowledged as References. Some of this work is based on peer-reviewed publications written by myself as the lead author. In the first publication I designed the analytical method, performed the analysis, and wrote the paper. In the second publication, I performed the offline UHPLC-HRMS analysis, contributed to the experiment design, participated in some of the chamber experiments at the University of Manchester and wrote the paper. Collaborators at the University of Manchester conducted the chamber experiments used in each publication and provided online measurements, figures from which were then reproduced by myself. The details of the chapter and corresponding publication are provided below:

- Chapter 2: **Rhianna L. Evans**, Daniel J. Bryant, Aristeidis Voliotis, Dawei Hu, Huihui Wu, Sara Aisyah Syafira, Osayomwanbor E. Oghama, Gordon McFiggans, Jacqueline F. Hamilton, and Andrew R. Rickard, *Analytical Chemistry* **2024** *96* (46), 18349-18358, url: https://doi.org/10.1021/acs.analchem.4c00819

- Chapter 3: **Rhianna L. Evans**, Daniel J. Bryant, Aristeidis Voliotis, Dawei Hu, Huihui Wu, Sara Aisyah Syafira, Osayomwanbor E. Oghama, Gordon McFiggans, Jacqueline F. Hamilton, and Andrew R. Rickard, *Atmospheric Chemistry and Physics*, **2025**, *25* (8), 4367-4389, url: https://acp.copernicus.org/articles/25/4367/2025/

Chapter 1

Introduction

1.1 Global Air Quality

The World Health Organisation estimates 99 % of the global population breathes air containing high levels of air pollution [1], which is defined as the presence or introduction of harmful or poisonous substances into the environment. Air pollution is present in both external and internal environments, such as our homes, and has been attributed to 6.7 million premature deaths each year [1]. Furthermore, the burden of poor air quality is not equally shared with the highest exposures in low- and middle-income countries [2], as well as among women and girls in the indoor environment [1, 3, 4]. It is now widely known that acute and chronic exposure to poor air quality is associated with negative impacts on human health and the environment [5–7]. Furthermore, Lelieveld et al. [5] estimated that at the current state of emissions deaths attributable to exposure to air pollution could double by 2050.

There are thousands of air pollutants in the atmosphere, existing in both the gaseous state and as aerosols, i.e. a solid or liquid particle suspended in the air, where atmospheric aerosols make up a significant fraction of particulate matter (PM) air pollution. Air pollution can be emitted from a wide range of natural and anthropogenic sources. Natural sources include volcanic eruptions, desert dust, wildfires, sea-spray particles and biogenic emissions (i.e. from plants or organisms). Whilst anthropogenic sources largely encompass combustion activity such as from fossil fuels or biomass burning. However, other anthropogenic non-combustion sources of air pollution include industrial solvent use, agriculture and consumer products. Some natural sources

of air pollution are increasingly being exacerbated by anthropogenic activity through climate change feedbacks. For example, increasing numbers of wildfires, from the hotter temperatures and drier land, and enhanced biogenic emissions which have a temperature dependent relationship [8]. Furthermore, anthropogenic evaporative solvent emissions could also likely increase as a function of temperature [9]. Indirect feedbacks with climate change can also occur, such as land use change, which for biogenic emissions can result in different chemical speciation [8].

Certain air pollutants are monitored and regulated by legislation over their quantity in the atmosphere due to their deleterious impacts on health and the environment, and include species such as oxides of nitrogen (NO_x = nitric oxide (NO) + nitrogen dioxide (NO_2)), tropospheric ozone (O_3), sulfur dioxide (SO_2), carbon monoxide (CO) and PM. In the UK, these pollutants are monitored by the Automatic Urban and Rural Network (AURN) consisting of 182 sites nationwide in a multitude of pollution environments. The majority of regulated air pollutants are emitted directly to the atmosphere known as primary air pollutants. However, certain pollutants can be formed in the atmosphere, known as secondary air pollutants, such as the photochemical production of O_3 from NO_x and gaseous hydrocarbons, or volatile organic compounds (VOCs), which is discussed in Section 1.3.2.2. In the case of PM, it can be both a primary and secondary pollutant. For example, secondary organic aerosol (SOA) is an important component of PM and is formed in the atmosphere as discussed in more detail in Section 1.3.2.2 and 1.2.2. In 1992 certain VOCs were incorporated into the UK's air pollution monitoring network, primarily to assess photochemical O_3 production (Section 1.3.2.2). However, over the last 20 years research has shown the importance of VOCs extends far beyond O_3 production, with important contributions to SOA production as well as health implications of the VOCs themselves [10]. The Clean Air Act of 1956 was the first bill to legislate air pollutants in the UK, primarily for black smoke and SO_2 [11]. Updates to the act since then have added further pollutants and set more stringent emission targets. Due to policy intervention there has been a reduction across the UK in many key air pollutants as shown in Figure 1.1. Stricter road transport regulations and improvements in emission control technology have led to significant reductions in NO_x, VOCs and ammonia (NH_3), as well as, transitioning away from coal for power generation which reduced SO_2, PM and NO_x. However, as emissions from

these sectors are reduced, other sources will become more important for future policy efforts [12]. For instance, in the UK domestic solvent use, which includes the use of personal care products and cleaning products, was the highest contributor to total VOC emissions in 2022 [13]. Whereas for PM, the domestic fuel combustion sector is becoming increasingly more important [14].

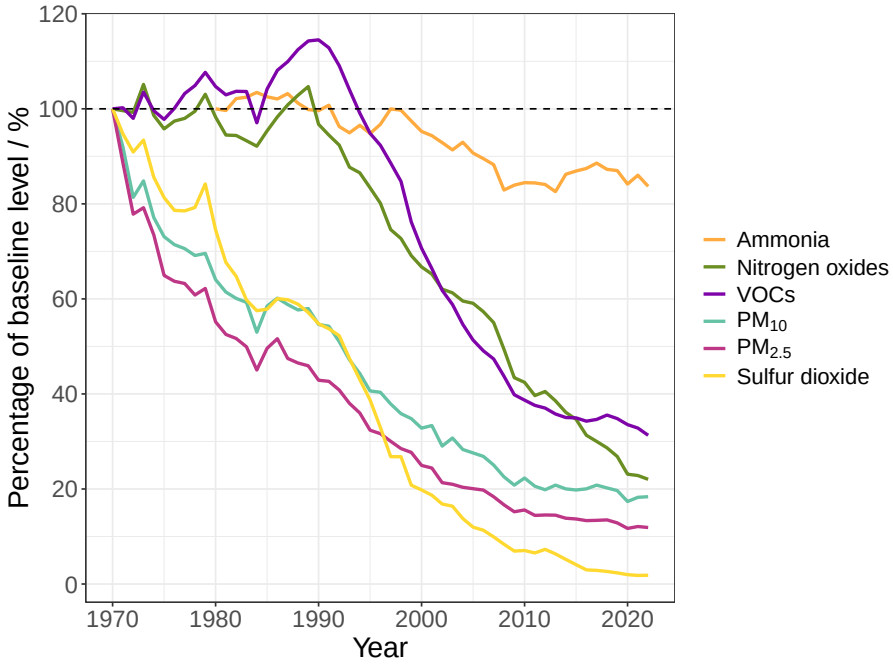

Figure 1.1: *Annual emissions of key air pollutants in the UK from 1970 to 2022 as a percentage of the baseline annual emission, taken as 1970. For ammonia the baseline is from 1980. Data is available at* `https://www.gov.uk/government/statistics/emissions-of-air-pollutants/`

1.2 Particulate Matter Air Pollution

1.2.1 Impact of aerosol on health and climate

PM exists over a range of particle diameters and for regulatory purposes is commonly segregated by aerodynamic diameters of less than 10 μm (PM_{10}) or less than 2.5 μm ($PM_{2.5}$) or less than 1 μm (PM_1). Due to the small size of $PM_{2.5}$ and PM_1, the particles can be inhaled deep into the respiratory system of the human body and ultrafine particles (< 100 nm) can even get into the bloodstream where they are known to cause

diseases such as stroke, heart disease, lung cancer and even diabetes [15–18]. Juginović et al. [6] found a 10 % increase in ambient $PM_{2.5}$ concentrations could increase the number of years of life lost by 16.7 %. The latest estimate of the global disease burden observed in 2021 particulate matter air pollution was the largest contributor to disability adjusted life years (DALYs) with the highest burden across Asia and Africa [7]. DALYs represent the number of years lost due to disability or illness. Furthermore, Apte et al. [19] reported that if the WHO guidelines were abided by for $PM_{2.5}$ (10 μg m^{-3} per annum) life expectancy could increase by 0.6 years, producing an effect similar to eradicating lung and breast cancer. For this reason, $PM_{2.5}$ is one of the most strongly regulated air pollutants with an annual exposure limit of 20 μg m^{-3} in the UK [20]. However, in 2017 McDuffie et al. [15] estimated the global population weighted mean concentration of $PM_{2.5}$ was 41.7 μg m^{-3} which is significantly higher than the WHO guidelines. Furthermore, there are no regulations specifically targeting ultrafine particles yet, but it is hoped that efforts to reduce $PM_{2.5}$ and PM_1 could positively affect ultrafine particle concentrations [21].

There are multiple classes of aerosol which all contribute to the total amount of PM in the atmosphere, and includes inorganic aerosols, such as sea-spray salt, sulfate, nitrate, ammonia, chloride, desert dust and soot, as well as organic aerosol (OA) as discussed in Section 1.2.2 and Figure 1.3. Many inorganic aerosols are emitted directly to the atmosphere as primary aerosols from sources such as volcanic eruptions, desert storms, the ocean, agriculture and combustion processes, meaning they are primary in nature.

An important impact of different aerosol classes is the difference in their radiative forcing effects in the atmosphere, which is defined as the change in net radiative flux due to a perturbation or introduction of an agent. For example, certain aerosols, such as elemental black carbon (BC) or more commonly known as soot, can absorb UV light and re-emit it in the form of infrared radiation at shorter wavelengths producing a warming effect similar to greenhouse gases [22]. Whereas sulfate aerosols can scatter the light leading to an overall cooling effect [23]. Most organic aerosol is considered "white" and scatters visible light [24]. However an additional important class of organic aerosol exists, known as brown carbon (BrC), which contains compounds that can absorb light, and can contribute to climate change in a similar way to BC [24].

Most BrC is from combustion sources such as biomass burning or coal combustion and can be emitted directly or formed photochemically [24]. Aerosols can also impact climate indirectly by affecting cloud lifetime and acting as cloud condensation nuclei. This can affect the formation of clouds and hence the reflectivity of light from clouds [25]. For these reasons, aerosols have the highest uncertainty surrounding their radiative forcing effect (Figure 1.2) [26] and is an important field of active research [27].

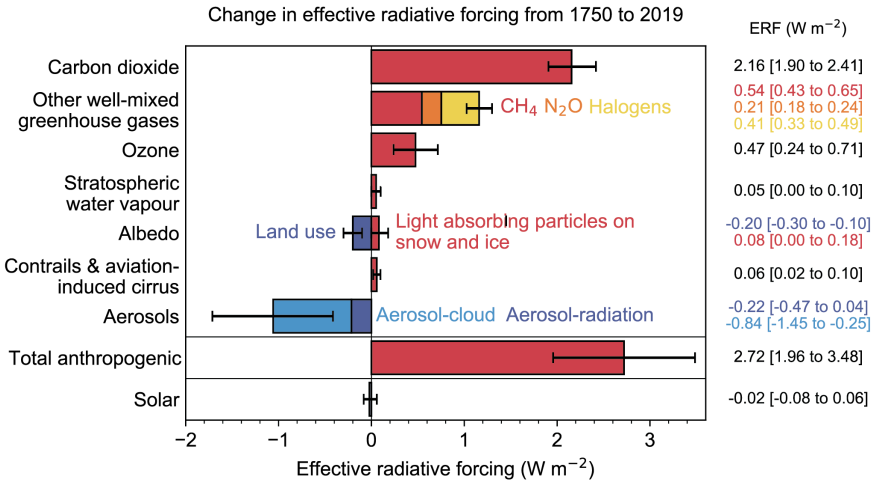

Figure 1.2: *Change in effective radiative forcing from 1750 to 2019 by different forcing agents shown on the left panel. Blue bars represent negative radiative forcing effects and red bars indicate positive radiative forcing effects. Uncertainties in the effect are shown by the error bars. Taken from the IPCC sixth assessment report (2021) [26].*

1.2.2 Sources of atmospheric organic aerosol

As shown in Figure 1.3 the majority of $PM_{2.5}$ globally, and particularly in the Northern Hemisphere, is comprised of OA [28]. OA can be emitted directly to the atmosphere, known as primary organic aerosol (POA), from both natural and anthropogenic sources predominantly via combustion. For example, a major natural combustion source is wildfires, whilst anthropogenic sources include vehicular emissions, industrial processes, shipping emissions, biomass burning and cooking [29–31]. As discussed in Section 1.5, anthropogenic biomass burning includes multiple activities spanning both indoor and outdoor environments such as prescribed burning, crop burning and domestic fuel combustion. However, there are other sources of POA from biological and marine sources, but these are less understood [32]. OA can also be formed in the atmo-

sphere from the atmospheric oxidation of VOCs and is referred to as SOA [31]. This oxidation is described in further detail in Section 1.3.2. Due to the numerous sources of OA, it is a highly chemically complex matrix made up of thousands of different species, which presents a significant analytical challenge in the characterisation of OA as discussed in Section 1.6.

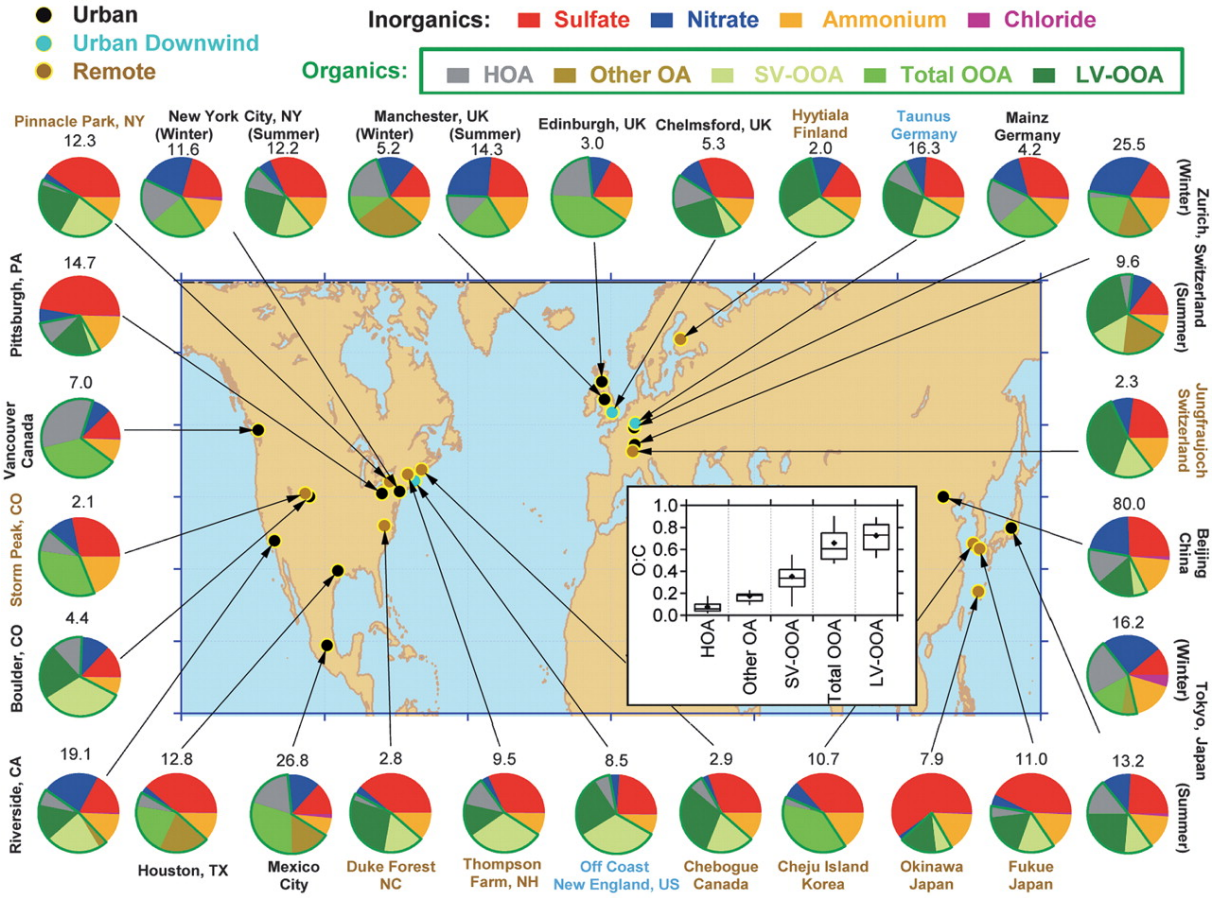

Figure 1.3: *Mass concentrations in μg m^{-3} and mass fractions of non-refractory PM_1 measured by Aerosol Mass Specrometry (AMS) at different locations in the Northern Hemisphere. Inset is the oxygen to carbon ratio for the different classes of organic aerosol (OA): hydrocarbon OA, total oxygenated OA, semi-volatile oxygenated OA and low volatility oxygenated OA. Taken from Jimenez et al., 2009 [28]*

Current estimates of global POA production including both combustion and marine sources are 34-144 Tg yr^{-1} [32], whereas estimates of SOA production are highly uncertain due to the limitations in the understanding of OA production and loss. They can also depend on the method used for calculation (i.e. bottom up and top down). For instance, top down estimates by Goldstein and Galbally [33] were as high as 140-540 Tg yr^{-1} and in a similar approach Hallquist et al. [31] observed a secondary produc-

tion rate of 115 Tg yr^{-1}, whereas bottom up estimates ranged between 13-150 Tg yr^{-1} [32, 34–37]. The largest contributor to the global SOA budget is secondary biogenic organic aerosol emitting approximately 88 Tg of organic carbon per year followed by SOA from biomass burning (Figure 1.4) [31]. Furthermore, Fuzzi et al. [27] show on local scales there is a contribution from both POA and SOA but as the temporal and spatial scales increase SOA becomes more important.

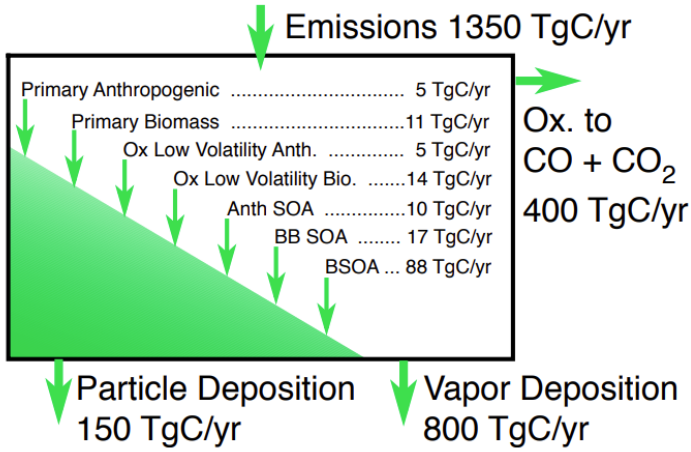

Figure 1.4: *Global fluxes of volatile organic compounds (VOCs) and OA from different sources estimated using a top-down approach. Taken from Hallquist et al., 2009 [31].*

1.3 Atmospheric Chemistry of Air Pollutants

1.3.1 Atmospheric oxidants

Once emitted into the atmosphere VOCs can be oxidised by one of three common atmospheric oxidants: the hydroxyl radical (OH), the nitrate radical (NO_3) or ozone (O_3) [38–40]. Oxidation can also be initiated by photolysis or chlorine radicals. The abundance of OH, O_3 and NO_3 in the atmosphere can be governed by location, local emissions, time of day and season [39]. For example, OH is abundant during the day due to its photochemical production pathways, whereas, NO_3 is dominant during the night when there is no loss by photolysis [41]. As briefly mentioned in the troposphere O_3 is a secondary species which is formed from NO_2 photolysis as shown in Eq 1.1-1.2. However, as NO_2 is produced from the reaction of NO with O_3 (Eq 1.3), this cycle both produces and destroys O_3 in the atmosphere and ultimately can reach a steady state

where there is a net zero production or loss of O_3. However, in the presence of VOCs O_3 formation can be favoured over loss [42] as discussed in Section 1.3.2 and in the atmosphere there is a careful balance between the concentrations of VOCs and NO_x for O_3 production.

$$NO_2 + h\nu \longrightarrow NO + O(^3P) \quad (\lambda \leq 420\ nm) \tag{1.1}$$

$$O(^3P) + O_2 + M \longrightarrow O_3 + M \tag{1.2}$$

$$O_3 + NO \longrightarrow NO_2 + O_2 \tag{1.3}$$

The main source of OH in the atmosphere is from the photolysis of O_3 (Eq 1.4-1.5) [39]. However, other sources include alkene ozonolysis (Section 1.3.2.1) and the photolysis of nitrous acid (HONO) or formaldehyde (HCHO) [40, 43, 44]. The importance of these other production reactions can be more significant in polluted atmospheres [45] or during winter months [44]. HONO photolysis can be particularly significant and is estimated to contribute to 30-48 % of total OH production [39, 43, 46].

$$O_3 + h\nu \longrightarrow O(^1D) + O_2 \quad (\lambda < 320\ nm) \tag{1.4}$$

$$O(^1D) + H_2O \longrightarrow 2\,OH \tag{1.5}$$

NO_3 radicals are rapidly photolysed during the day, with a lifetime of less than 5 seconds [40], and hence are more abundant during the night. In the atmosphere NO_3 is produced from the reaction of NO_2 and O_3 (Eq 1.6). NO_3 can also be rapidly lost through a reaction with NO (Eq 1.7) or via photolysis (Eq 1.8-1.9) or in the presence of NO_2 can form dinitrogenpentoxide (N_2O_5) [40, 41]. In the troposphere the reaction to form N_2O_5 is often in thermal equilibrium with N_2O_5 degradation back to NO_3 (Eq 1.10) [41]. In addition to controlling NO_3 concentrations, N_2O_5 can uptake onto the surface of aerosols where it can hydrolyse to form nitric acid (HNO_3) [47, 48] which in turn impacts on the aerosol acidity. Furthermore, reactive uptake of N_2O_5 is one of the major losses of NO_x in the atmosphere and is therefore important in controlling the oxidative capacity of the atmosphere [41].

$$NO_2 + O_3 \longrightarrow NO_3 + O_2 \tag{1.6}$$

$$NO_3 + NO \longrightarrow 2\,NO_2 \tag{1.7}$$

$$NO_3 + h\nu \longrightarrow NO + O_2 \tag{1.8}$$

$$NO_3 + h\nu \longrightarrow NO_2 + O(^3P) \tag{1.9}$$

$$NO_3 + NO_2 \rightleftharpoons N_2O_5 \tag{1.10}$$

1.3.2 VOC oxidation and photochemical O_3 production

In the case of OH and NO_3 radicals, VOC oxidation can proceed via two pathways; hydrogen abstraction or OH/NO_3 addition to C=C bonds [38]. These pathways yield reactive radical species such as, peroxy radicals (RO_2) and hydroperoxy radicals (HO_2), which undergo further chemistry to yield oxidised products and are key intermediates in the radical cycle which produces O_3 as described in Section 1.3.2.2. O_3 initiates VOC oxidation via a different pathway as described in Section 1.3.2.1.

1.3.2.1 Ozonolysis

O_3 can oxidise unsaturated VOCs by attacking C=C bonds in alkenes producing a primary ozonide which decomposes to form a carbonyl and an excited state zwitterionic compound known as a Criegee Intermediate. The excited Criegee Intermediate can either decompose to form OH and an alkoxyradical, which then proceeds to react in the HO_x cycle described in Section 1.3.2.2, or are quenched to a stabilised Criegee Intermediate (SCI) [38]. The SCI can then undergo bimolecular reactions with species such as H_2O, SO_2 and NO_2 [38, 49] as shown in Figure 1.5. Despite the presence of multiple C=C bonds in benzene rings, many aromatic compounds are resistant to degradation by ozonolysis or when the reaction does occur it proceeds extremely slowly [50]. However, it remains an important oxidant for biogenic VOC oxidation and biogenic SOA formation [51, 52].

1.3.2.2 HO_x cycling

HO_x (HO_2 + OH) cycling describes the downstream production of OH and HO_2 stemming from the initial oxidation of a VOC by an OH radical, or NO_3 radical or ozonol-

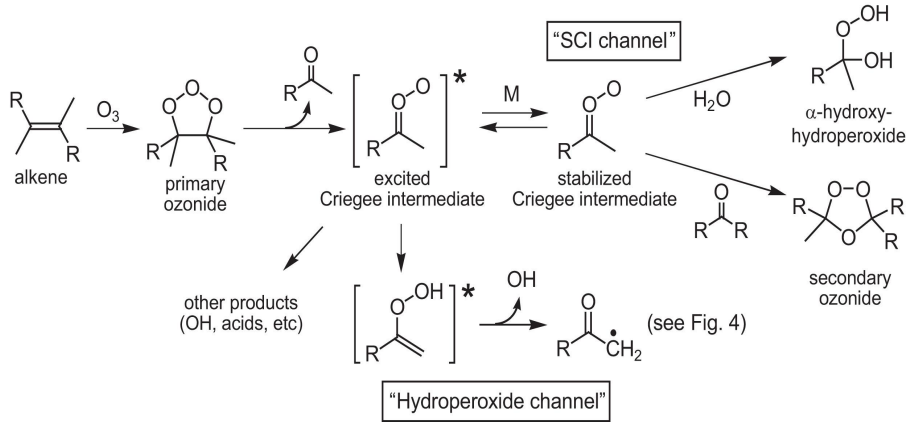

Figure 1.5: *Simplified reaction scheme of ozonolysis of alkenes in the atmosphere. Taken from Kroll and Seinfeld 2008 [38].*

ysis, thereby creating a catalytic cycle, as shown in Figure 1.6. In the catalytic cycle reactive organic radicals can undergo reactions with NO to form other organic products and NO_2 which can then photolyse to form O_3 as in Eq 1.1-1.2. The HO_x cycle is therefore important for controlling oxidant concentrations and the propagation of the NO_x cycle to produce O_3 [40]. However, the cycle is highly non-linear and the ratio of VOC:NO_x is critical for controlling O_3 formation. From Figure 1.6 it can be seen that either increasing or decreasing VOC concentrations could increase or reduce O_3 production respectively. Whereas for NO_x, increased concentrations could increase RO_2 conversions to form NO_2 which then subsequently forms O_3, however, at very high NO_x concentrations the main sink becomes the reactions of NO_2 with OH to form HNO_3. This also ultimately reduces the availability of the OH radicals needed to initiate and propagate the cycle. In the atmosphere there are two main classifications of O_3 production depending on the VOC:NO_x ratio. At high VOC:NO_x ratios the VOC is in abundance and therefore O_3 production is controlled by the availability of NO_x, known as NO_x limited. In this scenario, decreasing NO_x will decrease O_3 production. At low VOC:NO_x ratios, O_3 production is limited by the available VOC (i.e. VOC limited) and NO_x will primarily will be used up in the null O_3 cycle (Eq 1.1-1.3) and in the reaction with OH. Reducing NO_x in this scenario will in fact increase the importance of reactions with RO_2 resulting in more O_3 production [42]. Therefore, policies aimed at reducing O_3 in urban environments must consider this VOC:NO_x balance.

The RO_2 radicals produced by NO_3 or OH initiated oxidation as well as ozonolysis can undergo bimolecular reactions with NO, NO_2, NO_3 or HO_2 and permutation

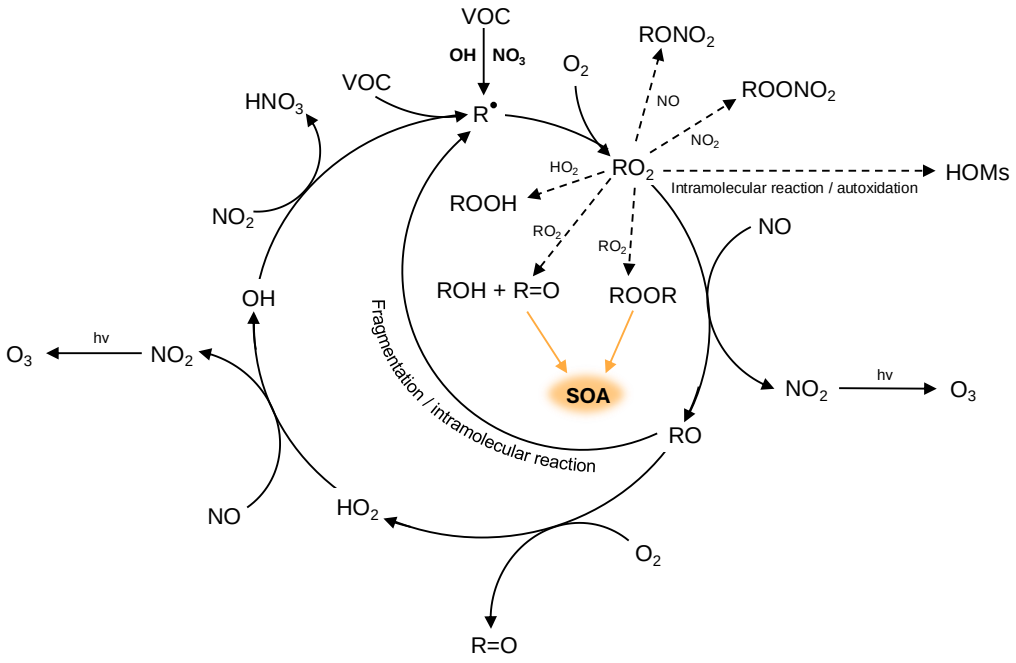

Figure 1.6: *Simplified schematic of the atmospheric VOC degradation by hydroxyl (OH) or nitrate (NO_3) radicals and the propagation of the oxidant recycling to form secondary products such as ozone (O_3) and secondary organic aerosol (SOA).*

reactions with RO_2. The relative rates of these reactions are dependent on the atmospheric conditions and RO_2 structure. Typically in polluted environments the reaction of RO_2 with NO, from anthropogenic emissions, is the dominant loss of RO_2 [38, 53] yielding an alkoxy radical (RO) and NO_2 and is therefore important for O_3 production. Alternatively, the reaction can yield an organonitrate ($RONO_2$) however, the contribution of this reaction depends on the RO_2 structure. Due to NO_3 photolysis during the day the reaction of RO_2 and NO_3 proceeds during the night to produce RO and NO_2. Acyl RO_2 can react with NO_2 to produce peroxyacetyl nitrates (PANs) in a reversible reaction. PANs are considered an important reservoir for NO_x in the atmosphere and in remote environments have important implications for the oxidising capacity of the atmosphere [54]. In low NO_x environments the reactions of RO_2 with HO_2 or RO_2 increases which also inhibits O_3 production from the competition with RO_2-NO reactions [53]. Furthermore, in some urban environments, such as Beijing and Delhi, high concentrations of O_3 can remove NO from the system via Eq. 1.3 increasing the importance of RO_2 reactions with HO_2 and other RO_2 [55]. Reactions with HO_2 typically terminate the radical propagation cycle by predominantly yielding a hydroperoxide

product (ROOH). RO_2 permutation reactions describes the reactions an RO_2 can undergo with other RO_2. These reactions can occur with RO_2 of the same structure or as cross reactions with other RO_2 of different structures. There are a number of reaction products from RO_2 permutation reactions. Typically, the dominant pathway yields a combination of RO radicals which can undergo further reaction in the atmosphere. However, depending on the RO_2 structure the second pathway to produce an alcohol (ROH) and carbonyl (R=O) or third pathway forming peroxide dimers (ROOR) can have larger branching ratios. These ROOR products can be formed via dimerisation of two RO_2 compounds with the same structure or via accretion reactions with two different RO_2 reactants. In the case of cross reactions there are multiple RO, ROOR, alcohol and carbonyl structures which can form resulting in significant complexity. Carbonyl products can be photolysed in the atmosphere which creates radical products and further propagates the HO_x cycling [38]. The RO_2 cross reaction products can contribute to SOA formation as shown in Figure 1.6 due to their lower volatility compared to the parent VOC and large size especially in the case of ROOR. For example, many studies have reported the formation of highly oxygenated molecule (HOM) dimers, largely for biogenic VOCs, from the accretion reactions of RO_2 to ROOR [56–58]. These ROOR compounds have very low volatilities and can nucleate in the atmosphere to form aerosol [59]. Additionally, and as mentioned in Section 1.4.1, RO_2 can undergo intramolecular rearrangements to create sites for further oxidation which rapidly generates HOMs and is an important contribution to SOA formation. For example, in a chamber experiment of isoprene NO_3 oxidation it was estimated that HOMs from autoxidation and accretion reactions to form HOM dimers and trimers could contribute to 3.6 % of the isoprene SOA yield [58].

In the case of RO, O_2 molecules can abstract a hydrogen from the carbon bound to the radical oxygen to produce HO_2 and a carbonyl, both of these products can therefore contribute to further HO_x cycling. Additionally, RO can react with NO_2 and in the case of phenolic RO leads to the formation of nitroaromatic compounds (NACs) which have a -NO_2 functional group on the aromatic ring. NACs are an important class of compounds with harmful impacts to human health and are known chromophores therefore are important contributors to BrC [60]. RO species can also fragment or undergo intramolecular reactions to produce alkyl radicals (R) which rapidly react

with O_2 molecules reforming RO_2 and hence contribute to further HO_x cycling [38].

1.4 Secondary Organic Aerosol (SOA)

1.4.1 Formation pathways of SOA

There are multiple processes by which SOA can form in the atmosphere. The first is gas-particle partitioning whereby once a gas phase species reaches a low enough volatility it can condense into the aerosol phase onto either pre-existing aerosol or nucleate to form new particles, known as new particle formation (NPF). The low volatility gas phase compounds can be formed chemically in the atmosphere as described in Section 1.3.2. The partitioning of gaseous species into the particle phase can be described by equilibrium partitioning theory where the partitioning coefficient, K_p, is described by Equation 1.11 [61, 62]. K_p represents the fraction of a species in the particle phase versus the gas phase. In Equation 1.11 P_i represents the concentration of the semi-volatile species in the particulate phase in ng m^{-3}, TSP is the total absorbing particle mass concentration in μg m^{-3} and G_i is the gas phase concentration in ng m^{-3}. Through a conversion of units the final equation is reached where R is the ideal gas constant, T is the temperature (K), f_{om} is the fraction of the total particle mass that comprises the absorbing phase, MW_{om} is the average molecular weight of the absorbing phase (g mol^{-1}), ζ_i is the activity coefficient of species i in the particle phase and p_i is the vapour pressure of species i. The inverse of K_p, the saturation concentration (C^*), can also describe gas-particle partitioning where the lower the C^* results in greater partitioning [63]. In both theories the partitioning of gas to particles is controlled by the volatility of a species, gas phase concentrations and the available area on which to condense [61, 63].

$$K_{p,i} = \frac{ng/\mu g_{\text{particulate phase}}}{ng/m^3_{\text{gas phase}}} = \frac{P_i/TSP}{G_i} = \frac{760RTf_{om}}{MW_{om}\zeta_i p_i} \times 10^{-6} \tag{1.11}$$

NPF describes the formation of new atmospheric particles and under favourable conditions the following growth to larger particle sizes. Sulfuric acid is one of the most widely reported nucleating species [64–66] with high correlations reported between nucleation rate and sulfuric acid concentration. However, there is still uncertainty in the mechanism of NPF and it is currently an active area of new research. In

addition to sulfuric acid, it has been proposed that other vapours must contribute to nucleation of atmospheric particles in order to fully explain the observed growth rates [67]. Recent research has shown that organic compounds and ammonia can nucleate in the atmosphere [68–72]. For instance, Jiang and Xia [71] report that sulfuric acid, ammonia and organic compounds all contribute to the early growth of new particles, however, the growth of the nucleus is driven by nitric acid and ammonia. Whilst in the Po Valley, oxygenated organics were observed to contribute significantly to the growth stage [73]. Even in the absence of sulfuric acid, NPF was observed in a series of α-pinene ozonolysis experiments at the CERN CLOUD chamber from the highly oxidised oxidation products [74]. These highly oxidised oxidation products are considered to form from a process called autoxidation, in which oxygen is continuously added during VOC oxidation, producing extremely low volatility compounds containing more than 6 oxygen atoms, known as HOMs, which nucleate to form new particles [75]. The production of HOMs from autoxidation of terpenoids and aromatics has been reported to contribute to NPF in multiple studies across rural and urban areas [74, 76–79]. The reaction scheme for autoxidation is shown in Figure 1.7 [80]. For autoxidation to proceed from an RO_2 radical produced by VOC oxidation as in Section 1.3.2.2, the RO_2 must undergo a H atom shift to form a hydrogen peroxide group (-OOH) and an alky radical which reacts with an O_2 molecule to form a second RO_2. This second RO_2 group undergoes another H atom shift to form a second OOH group and an alky radical at the site of the initial OOH group which rapidly decomposes to a carbonyl and an OH molecule. The α-position to the remaining OOH group is reactive to further H abstraction which then propagates the autoxidation [80]. It is also possible to have autoxidation initiated from RO radicals [75].

Alternatively, certain SOA species can undergo reactive uptake onto the aerosol phase by which they react with species in the bulk of the aerosol.This has widely been reported for SOA tracer species formed from the oxidation of isoprene [81, 82], or small dicarbonyl atmospheric degradation products such glyoxal and methylglyoxal [83]. Once in the aqueous phase the dicarbonyls can also oxidise to form organic acids or oligomerise [83].

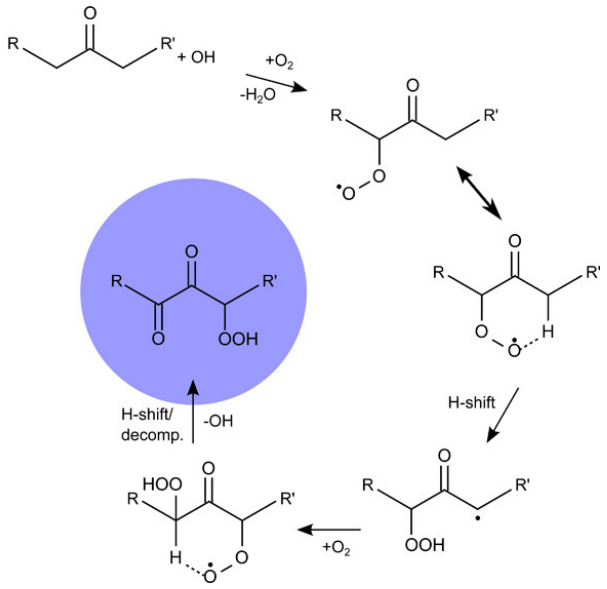

Figure 1.7: *Chemical scheme of autoxidation to form highly oxygenated molecules (HOMs), taken from Crounse et al., 2013 [80].*

1.4.2 Composition of SOA

Despite organic aerosol contributing the most to total $PM_{2.5}$ concentration [28], there is still widespread variation amongst the different components which contribute to the organic aerosol fraction [84] in Figure 1.3. For instance, in many urban environments there are significant contributions from hydrocarbon organic aerosol (HOA) whereas in remote locations or during summertime the fraction from semi-volatile oxygenated organic aerosol (SV-OOA) or low-volatility oxygenated organic aerosol (LV-OOA) increases [28]. HOA is typically emitted by primary combustion sources, such as vehicle exhausts in urban environments, with a diurnal peak during the morning traffic rush hour [85]. Zhang et al. [84] also report cooking as a HOA source. On the other hand, LV-OOA and SV-OOA are associated with SOA. High oxygen-to-carbon ratios (O:C) are observed in LV-OOA consistent with significantly oxidised OA, whereas, SV-OOA has lower O:C and is therefore less atmospherically aged [28]. Since LV-OOA and SV-OOA are secondary in nature their abundance increases during summer months under the more favourable photochemical conditions and the ratio of SV-OOA:LV-OOA can provide an insight into the relative age of emissions [28].

As shown in Figure 1.4 biogenic SOA is a significant source of OA to the atmosphere. The largest contributors to the biogenic SOA burden are terpenoids such

as isoprene (C_5H_8), monoterpenes ($C_{10}H_{16}$), including α-pinene and limonene, and sesquiterpenes ($C_{15}H_{24}$) such as β-caryophyllene. Globally isoprene is the most emitted VOC with an estimated 535 Tg released per year, whereas emissions of monoterpenes are smaller (162 Tg yr^{-1}) [86] yet still significant for SOA production. For example, Zhang et al. [87] observe SOA from monoterpenes accounts for half of the total OA in the Southeastern US. SOA products from isoprene and monoterpenes include species such as organosulfates (OS), organic acids, 2-methyltetrols and nitroxy-organosulfates [31, 88, 89]. OS in particular have warranted much research over the last decades as studies have reported OS can decrease surface tension of aerosols and thereby have implications for aerosol hygroscopicity and the ability to act as cloud condensation nuclei [90]. Furthermore, in urban environments anthropogenic emissions can strongly influence the concentration of OS [88]. Terpenoids are well known to undergo autoxidation which can have important implications for particle formation from HOM formation [75] as discussed in Section 1.4.1. Terpenoids are also emitted by biomass burning, which is the second largest source of SOA to the atmosphere, from the distillation of plant resins at higher temperatures [91]. However, the remaining constituents of biomass burning SOA are primarily formed from the oxidation of aromatics, such as phenolic or furanic species [91, 92], which are released during the breakdown of lignocellulosic biomass during combustion. These species can have high reactivity [91, 93], and some identified SOA products from these compounds include NACs, organonitrates, organoacids and benzoquinones [94–99]. Furthermore, C_{10} dimers have been reported in SOA from the NO_3 oxidation of 3-methylfuran which was largely attributed to RO_2 cross reactions to form ROOR and particle phase accretion reactions [97]. However, the atmospheric chemistry of these oxygenated aromatic VOCs and their potential to form SOA is still largely unknown and understudied [93]. Other anthropogenic SOA, such as that from vehicular emissions or solvent usage, is similarly derived from aromatic species [100–102]. SOA from vehicular emissions can also have substantial contributions from aliphatic hydrocarbons as well as polyaromatic hydrocarbons (PAHs) [102]. However, the contribution of different compound classes to SOA formation between petrol and diesel powered vehicles can vary [102, 103]. Overall, it is clear that the composition of ambient SOA is highly complex due to the presence of numerous SOA sources with different chemical products.

1.5 Biomass Burning

1.5.1 Global importance

Biomass burning is one of the largest sources of OA and trace gases in the atmosphere, emitting approximately 62 Tg yr^{-1}, 77 Tg yr^{-1} and 19 Tg yr^{-1} of VOCs, $PM_{2.5}$ and NO_x respectively to the atmosphere [104]. Satellite imaging of fire activity from the NASA MODIS satellite shows the global extent of biomass burning with extensive wildfires across the United States, South America, Africa and certain parts of Asia (Figure 1.8a). After the monsoon season, the satellite also highlights the agricultural burning of crop fields in South Asia (Figure 1.8b) [105].

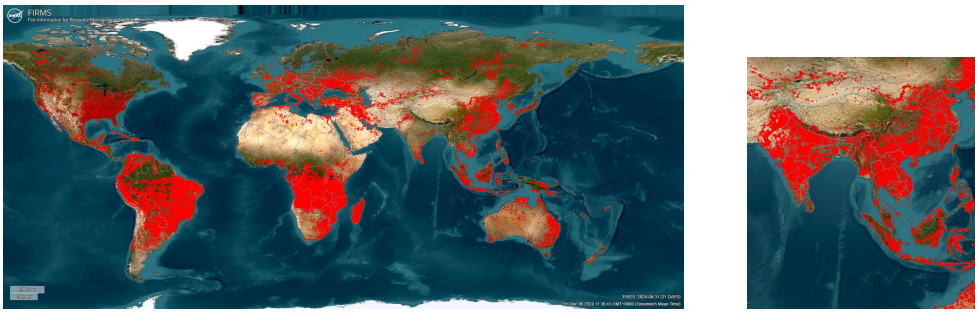

(a) Global fire activity

(b) South Asia fire activity

Figure 1.8: *NASA MODIS Fire Information for Resource Management System (FIRMS) showing active fires during a) August 2024 b) November 2024 (Accessed 06-12-2024)*

VOCs from biomass burning are emitted from the degradation of the lignocellulosic biomass within the fuel during combustion and NO_x emissions from fires typically arise from fuel nitrogen [106]. The majority of VOCs reported from previous controlled burn studies were oxygenated VOCs [107, 108], comprising 61 % of the total biomass burning VOCs (BBVOCs) [108]. However, the atmospheric chemistry of oxygenated aromatic VOCs from biomass burning is relatively understudied and not currently incorporated into chemical models to assess the impact of biomass burning due to the lack of detailed chemical degradation schemes [93]. Oxygenated aromatic BBVOCs, such as catechol ($C_6H_6O_2$), furfurals ($C_5H_4O_2$) and guaiacol ($C_7H_8O_2$), are highly reactive as shown in the top 50 % of measured OH reactivity from biomass smoke in Figure 1.9, and therefore have significant potential to impact on O_3 and SOA

formation.

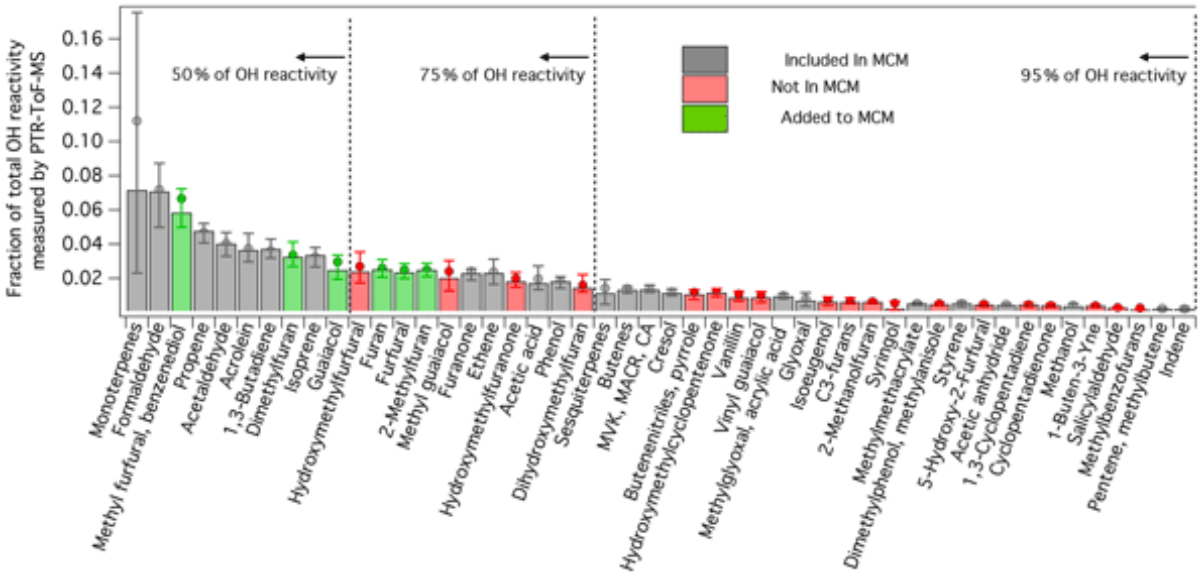

Figure 1.9: *Contribution of individual VOCs to the total OH reactivity measured by Proton Transfer Time of Flight Mass Spectrometry (PTR-ToF-MS) during the 2016 Fire Influence on Regional to Global Environments and Air Quality (FIREX-AQ) Firelab study of wildfire emissions. The colouring of each bar represents the scientific understanding of the compound's atmospheric chemistry. Taken from Coggon et al., 2019 [93].*

For example, studies have reported high contributions of biomass burning to tropospheric O_3 concentrations [109, 110] and Xu et al. [111] estimated that O_3 concentrations can be enhanced by 3 ppb throughout the fire season in the western US. From Figure 1.9, the species not included in the Master Chemical Mechanism (MCM, `https://mcm.york.ac.uk/MCM`), a near-explicit chemical degradation scheme, shown as red bars and those which were recently added shown as green bars are those that significantly contribute to SOA formation in Figure 1.10, such as phenolic compounds [107]. However, of the top 10 oxygenated aromatics reported by Akherati et al. [107] to contribute to SOA formation only 4 are represented in the MCM, therefore, there is a significant gap in the current mechanistic understanding of SOA formation from biomass burning. Furthermore, the simplified mechanism provided for guaiacol in Coggon et al. [93] accounts for a singular product rather than a fully explicit mechanism of all possible oxidation products as would occur in the atmosphere.

In ambient observations of biomass burning plumes over the western US during the Fire Influence on Regional to Global Environments and Air Quality experiment

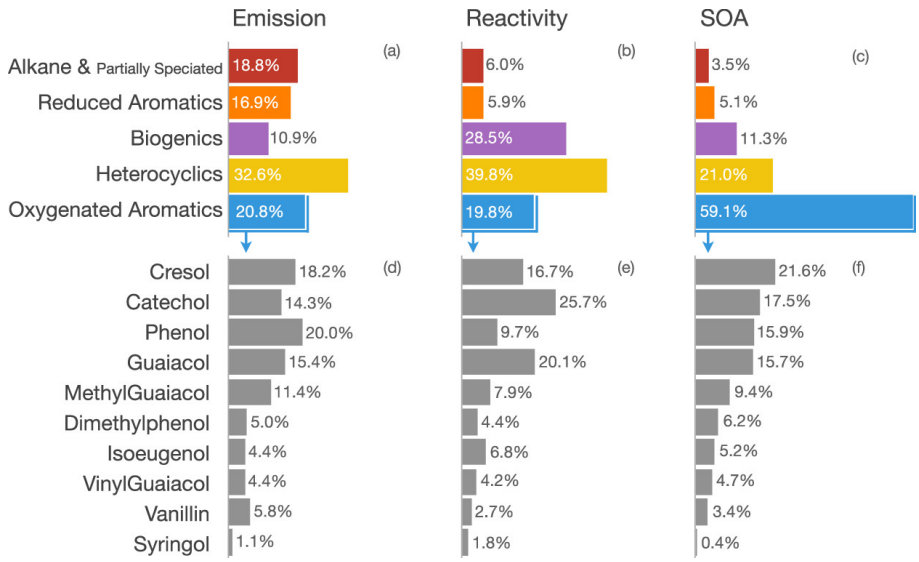

Figure 1.10: *Contribution to the total measured emission, OH reactivity and SOA formation of different compound classes during photo-oxidation experiments of wildfire emissions. The lower panel depicts the top 10 oxygenated aromatics that contribute to SOA production during the experiments. Taken from Akherati et al., 2020.*

(FIREX-AQ), the reported OH concentrations range between 5.3 ± 0.7 $\times 10^6$ molecules cm^{-3} in the daytime [112]. Whereas, in the night-time the estimated concentrations of OH are near zero (-0.5 ± 0.5 $\times 10^6$ molecules cm^{-3}) [112]. Whilst for the same plumes, NO_3 production rates were 0.1-1.5 ppb hr^{-1} [113, 114] which is similar to that reported in urban environments with significant daytime NO_3 chemistry [89]. Due to the thick smoke of biomass burning plumes, it is not unusual for both OH and NO_3 reactivity to be high due to the lower actinic fluxes inside the plume compared to the background resulting in less loss of NO_3 radicals by photolysis [113].

It is estimated that approximately 30 % of the OA emitted by biomass burning is in the form of POA meaning there is a substantial contribution of SOA to biomass burning emissions [115]. Furthermore, Hodzic et al. [34] estimated the global production of SOA from biomass burning was 15.5 Tg yr^{-1}. The most widely used SOA tracers from biomass burning are levoglucosan emitted by cellulose degradation and nitroaromatic compounds formed from the reactions of aromatic VOCs and NO_x which are present in high concentrations within a biomass burning plume [116–119]. Wildfires, agricultural burning, and domestic combustion of solid fuels all fall under the umbrella of biomass burning therefore it represents a wide spread source of air pollution. From Figure 1.11 it can be seen that globally the largest contributors to $PM_{2.5}$ concentrations

are residential combustion and windblown dust. However, across Asia and the United States the contribution of biomass burning activity from residential use and wildfires increases compared to the global average, with increasing usage of solid biofuels across Asia [15]. These findings are in line with the increasing length of the wildfire season in the US [120], the usage of solid fuels by 1 billion people across Asia [121] and the seasonal crop burning in Asia [105]. As seen from Figure 1.11 $PM_{2.5}$ from these sources is linked with heart disease and stroke [15]. Therefore, reducing residential combustion activity from solid fuels is essential for reducing the global disease burden from $PM_{2.5}$.

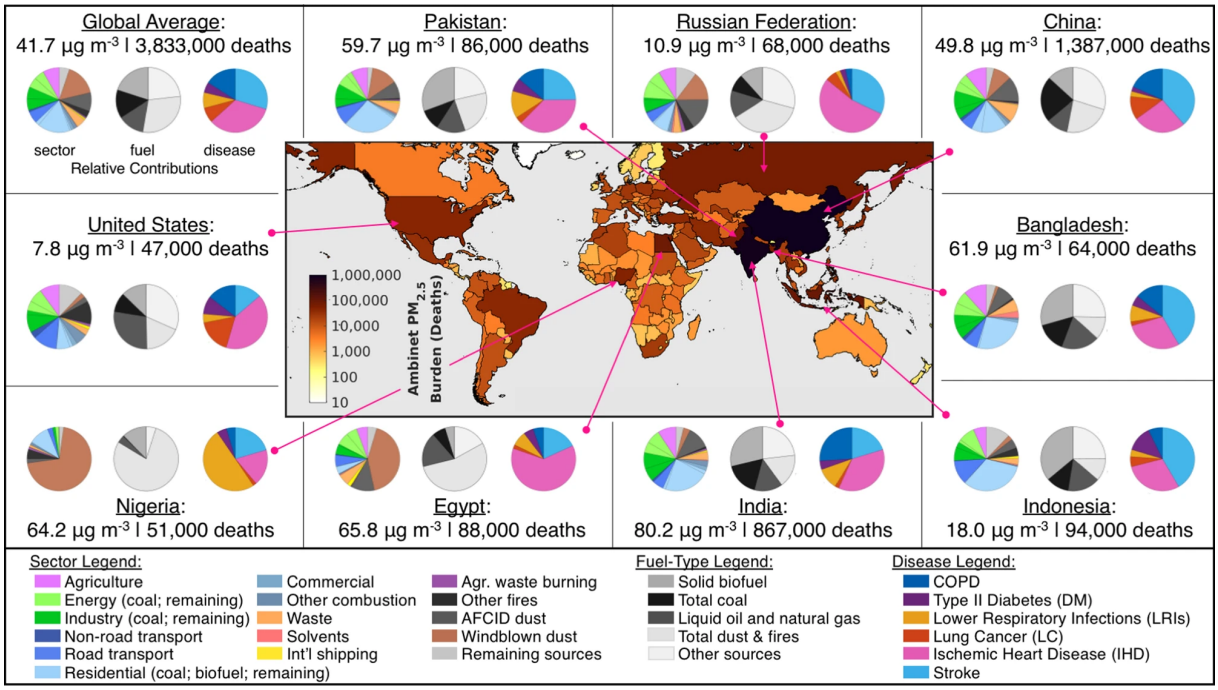

Figure 1.11: *Map showing the global disease burden from particulate matter less than 2.5 µm in diameter ($PM_{2.5}$) in 2017 with the surrounding panel showing the average $PM_{2.5}$ concentrations, mortality rates, source contributions, fuel usage and relative disease contributions to the air pollution related deaths. Taken from McDuffie et al., 2021 [15].*

1.5.2 Domestic wood burning

The work in this thesis predominantly focuses on the composition and atmospheric chemistry of domestic wood burning emissions since it has become in recent years the dominant source of $PM_{2.5}$ in the UK [14]. Compared to the winter of 2007-2008, the contribution of domestic biomass burning to $PM_{2.5}$ concentrations in the West Mid-

lands increased by 7 times during 2021-2022 [122]. The large growth in wood burning in the UK can be attributed to two factors: aesthetic purposes and increasing costs of living. Multiple energy crises in the last few years caused significant rises in the prices of oil and gas for heating [121], therefore, many have sourced cheaper alternative options including the use of wood burning stoves. Furthermore, domestic biomass burning has been promoted as a renewable energy source compared to fossil fuel usage. It is currently estimated that 8 % of the UK population burns wood indoors but of that only 4 % for necessity [14]. Domestic combustion remains a global issue with approximately 2 billion people using solid fuels for heating and cooking [123] which represents a widespread chronic exposure to poor air quality. The World Health Organisation estimated annually solid fuel combustion causes 3.2 million premature deaths [124], however the elimination of domestic biomass burning could prevent 20 % of the global annual deaths caused by $PM_{2.5}$ [15]. Therefore, there is an urgent need to understand the emissions from domestic biomass burning in order to improve future air quality policy and especially given that emissions from wood burning are highly variable. The emission variability can arise from the different phases of a burn cycle, fire aeration, fuel moisture, fuel composition, and the stove appliance used [125–128]. However, certain factors can impact the composition more than others [129]. Factors such as aeration, fuel moisture, fuel type and burn phase also affect ambient wildfires and other biomass burning sources.

1.5.3 Factors impacting biomass burning emissions

The impact of combustion conditions on biomass burning emissions is discussed in more detail in Chapter 3 but in brief flaming fires occur at higher temperatures than smouldering fires which typically occur later in the burn cycle [125]. The composition of particulate emissions from smouldering were previously reported to contain more oxygenated aromatics than from flaming [129] which was similarly observed in the gas phase[127]. Flaming combustion on the other hand, has widely been reported to emit PAHs [127] which are known to have toxic health impacts [130, 131]. Across 18 different fuels collected from 3 regions of the United States, Gilman et al. [126] observed varying contributions of different VOC classes to the total emission. For example, in Southwestern US fuels, from California and Arizona, 41 % of the

VOC mass was comprised of singularly unsaturated oxygenated VOCs such as aldehydes, whereas, in Northern US fuels from Montana this fraction comprised only 23 % with increased contributions of polyunsaturated oxygenated VOCs, which also included phenolic compounds [126]. Andreae [104] and Akagi et al. [132] also report differences in the emission factors of different VOCs in fires from savannahs, grasslands and forests which could be linked with the intrinsic fuel combustion properties [133]. Interestingly, Burling et al. [108] observed that in addition to VOC composition, HONO emission factors could vary between different fuel types which has important implications for OH production and therefore, the oxidative capacity of the plume and subsequent O_3 production. Furthermore, between different classes of biomass burning there can also be variation in emissions, for instance, Zhang et al. [133] observed higher emissions of elemental carbon over organic carbon in wood stoves compared to ambient fires which was attributed to higher combustion temperatures in the stove. To date, many studies have focused on characterising ambient fires under different conditions [91, 92, 126, 127, 134, 135], therefore, more research is needed into understanding biomass burning emissions in the context of a domestic environment.

1.6 Characterisation Techniques for Secondary Organic Aerosol

The chemical characterisation of organic aerosol is important for understanding the sources and chemical mechanisms leading to SOA formation [31]. In addition to understanding the evolution of chemical composition in the atmosphere, resulting from the chemical formation of SOA species as well as evaporative losses. Overall, this means the toxicological properties of the aerosol can change over time. This understanding around potential increases, or indeed decreases, in toxicity with atmospheric aging is a vital component for creating future air quality policy to reduce the detrimental societal impacts from OA [27]. However, the main barrier to understanding the chemical composition of OA is the sheer complexity and quantity of compounds present. For example, Goldstein and Galbally [33] proposed for a C_{10} alkane at least 100 isomers exist, and this number can exceed 1 million once functional groups and heteroatoms are included into the molecule. One of the main analytical instruments that can de-

convolute this complexity is mass spectrometry (MS) [136]. There are two types of MS analysis; online (i.e. high time resolution) and offline (i.e. low time resolution) [31]. Besides MS other analytical techniques capable of analysing SOA composition are Nuclear Magnetic Resonance (NMR) and Fourier Transform Infrared Spectroscopy (FTIR), however, this is primarily for the identification of functional groups rather than molecular identification [136].

1.6.1 Offline Mass Spectrometry

Offline mass spectrometry methods are typically coupled with a chromatography system, such as gas chromatography (GC) and liquid chromatography (LC), which enables the separation of isomeric species and therefore have high chemical resolution. More recently, the separation of enantiomers has also been achieved using LC-MS, enabling source identification of α-pinene SOA [137]. Typically, aerosol is sampled onto a filter and the organic matter is extracted using an organic solvent for analysis (Figure 1.12). However, the main drawback of these techniques is the considerable mass needed resulting in a low time resolution. Furthermore, the choice of solvent can impact the extracted material [138, 139]. Direct thermal desorption of the filter can be used with GC-MS methods for analysis of semi-volatile species and has the advantage that no prior sample preparation is required [138].

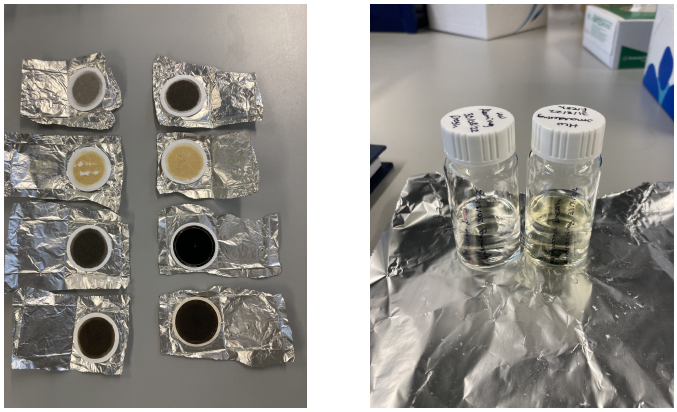

(a) Filter sample from biomass burning

(b) Methanol filter extracts

Figure 1.12: *a) $PM_{2.5}$ filter samples collected from burning of different fuel types: (top) leaves, peat, softwood, hardwood (bottom) b) Differences in filter extracts from wood burning samples under different conditions: flaming (left) and smouldering (right)*

The separation ability of GC can be limited therefore the application of two dimensional GC (GC×GC) to atmospheric samples by Lewis et al. [140] enabled greater resolution from the use of two GC columns in tandem to separate compounds across two intrinsic properties. Most commonly, these are properties such as volatility and polarity. The first use of GC×GC by Lewis et al. [140] used a flame ionisation detector (FID) for identification of gaseous compounds but this technique was later coupled to a Time of Flight MS (ToF-MS) and applied to urban OA enabling the detection of over 10,000 individual compounds from a single sample [138]. Recently, Stewart et al. [141] applied this technique to derive emission factors of particulate phase PAHs from biomass fuels used in domestic burning in Delhi.

Ultra-High-Performance Liquid Chromatography coupled to Electrospray Ionisation High Resolution Mass Spectrometry (UHPLC-ESI-HRMS) has widely been applied to the characterisation of organic aerosol [116, 136, 142–145]. The high mass resolution and tandem mass spectrometry of this technique enables detailed structural and chemical information to be obtained. Furthermore, the ESI source can be operated in two separate modes where ionisation occurs via deprotonation or protonation to produce negatively or positively charged ions respectively [31]. Different functional groups will ionise better in different modes, for instance more acidic compounds will more readily deprotonate in negative mode, leading to selectivity of the chemical space analysed. Therefore, for complete characterisation it is necessary to analyse both compositional spaces. However, in many aerosol studies to date the majority of analysis is conducted in negative mode due to its higher selectivity for species such as organic acids, OS and NACs [116, 117, 142, 144–146]. A common mass detector used in the UHPLC-HRMS system is an Orbitrap MS, shown in Figure 1.13, which has a mass resolution of more than 100,000 [147]. The Orbitrap mass analyser consists of two outer electrodes and a central electrode. A voltage is applied across the outer and central electrode which enables ions to oscillate around the central electrode (Figure 1.14). The ions are separated due to the property that at different mass-to-charge ratios (m/z) ions oscillate at different frequencies, which is then measured by the outer electrodes. A mass spectrum is produced by Fourier Transform of the detected image current signal [147]. Due to the high resolution of an Orbitrap it is possible to directly inject into the MS without prior separation. However, this analysis lacks the capability for isomer

identification and analyte quantification [136].

Figure 1.13: *Ultimate 3000 UHPLC (Thermo Scientific, USA) and Q Exactive Orbitrap MS (Thermo Fisher Scientific, USA) used for OA analysis at the University of York*

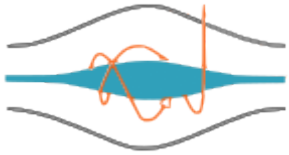

Figure 1.14: *Schematic of the Orbitrap mass detector showing the outer electrodes and the central electrode around which the ions oscillate indicated by the orange trajectory.*

Some of the major challenges associated with offline UHPLC-ESI-HRMS remaining today are ionisation effects and matrix effects. In electrospray ionisation, there is a known phenomenon that ionisation is highly structurally dependent [148, 149]. This ability of a species to ionise is referred to as ionisation efficiency and is discussed in detail in Chapter 2. In summary, this ionisation efficiency effect creates a significant problem in the quantification of compounds for which there are no available authentic standards, as the recorded response on the LC (i.e. peak area) will vary across different compounds at the same concentration [150] as shown in Figure 1.15, where, for example, compound 4 ionises 35.7 times greater than compound 1 (*cis*-pinonic acid). In Figure 1.15 ionisation efficiencies are normalised to *cis*-pinonic acid as it is a commonly observed tracer of SOA and is available to purchase commercially. Secondly, the instrument response of a species in a pure matrix versus in an aerosol sample matrix can vary due to the enhancement or suppression of signal intensity by other analytes in the sample being analysed [151], therefore, leading to erroneous quantification [152]. The exact mechanism causing matrix effects is still unknown. However, it is thought

that matrix effects arise from competition between analytes for the available charge and the impact of co-eluting compounds on droplet evaporation or transport to the droplet surface [153].

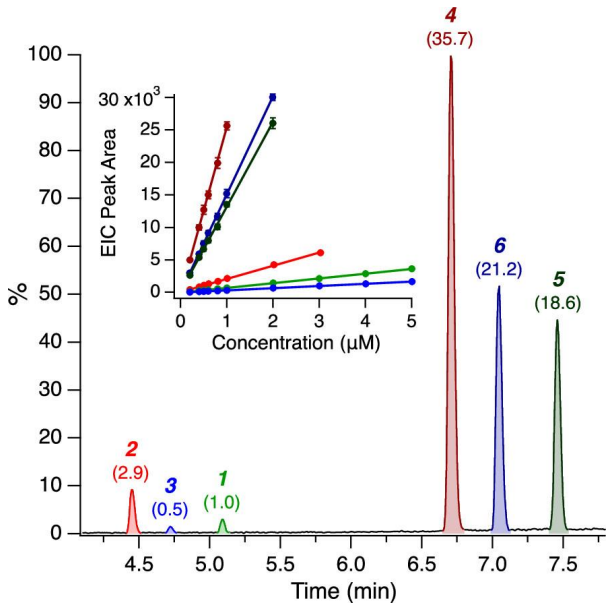

Figure 1.15: *Chromatogram depicting the effect of ionisation efficiency across equimolar aqueous solutions of carboxylic acids (1-3) and dimer esters (4-6) measured by ultra performance liquid chromatography coupled to mass spectrometry with electrospray ionisation. Ionisation efficiencies normalised to cis-pinonic acid (1) are given above the peak. Inset is the calibration curve of each compound from 0.2 to 5 μM. Taken from Kenseth et al., 2020 [150]*

1.6.2 Online Mass Spectrometry

The main advantage of online MS is the high time resolution that is simply impossible to obtain with offline techniques, which involve a two step analysis process and require significantly higher mass loading for analysis. Secondly, the lack of sample collection and preparation prior to analysis can improve in reducing sampling artefacts from storage or extraction procedures [31]. However, the main disadvantage is the lack of chromatographic separation which enables the identification of isomeric species as well as the general use of lower resolution mass spectrometers compared to the Orbitrap for example [147].

The most widely used online MS in the organic aerosol community over the last decades is the Aerosol Mass Spectrometer (AMS) commercialised by Aerodyne Re-

search Inc. in 2002. AMS allows real time measurement of the non-refractory PM components such as sulfate, nitrate, ammonium, chloride and total OA [28, 154]. However, due to the use of electron impact ionisation there is significant fragmentation of the molecular ion preventing complete molecular characterisation compared to offline HRMS and other online MS using soft ionisation techniques [31]. However, distinct fragments can form between molecules of different classes enabling the use of tracer fragments to track chemical composition changes. The most widely used tracer fragments in AMS studies are *m/z* 43, *m/z* 44, *m/z* 57 and *m/z* 60 representing $C_3H_2O^+$ or oxygenated organic aerosol (OOA), increasingly oxidised OOA (CO_2^+), hydrocarbon like OA ($C_4H_9^+$) and biomass burning tracer levoglucosan ($C_4H_2O_2^+$) respectively [69]. The relative ratio of *m/z* 43 and *m/z* 44 fragments changes between SV-OOA and LV-OOA [155] and therefore this ratio can be used to trace atmospheric aging as when the aerosol becomes more oxidised *m/z* 43 decreases and *m/z* 44 increases. The *m/z* fragments can also be interpreted as a fraction of the total OA denoted as f_{43} and f_{44}. The correlation of f_{43} vs f_{44} led to the invention of the triangle plot by Ng et al. [155] who observed all ambient aerosol exists within a defined triangular range with SV-OOA situated in the bottom of the triangle and the convergence to LV-OOA at the top regardless of source [28].

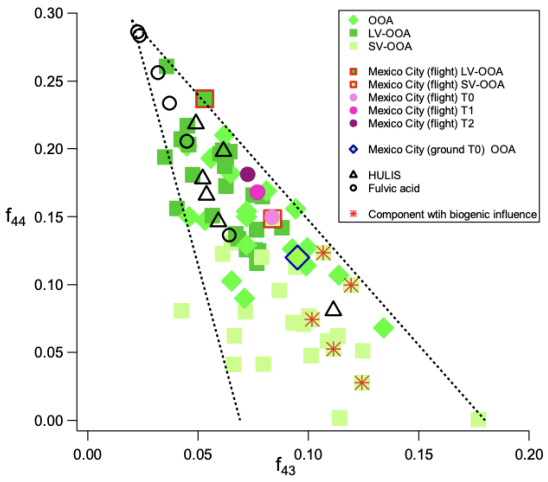

Figure 1.16: *Triangular plot of the fraction of the mass-to-charge ratio (m/z) 43 fragment (f_{43}) and fraction of the m/z 44 fragment (f_{44}) for different sample locations. Dashed triangular lines denote the region where atmospheric oxygenated OA are situated in the f_{43} vs f_{44} space regardless of source or age. Taken from Ng et al., 2010 [155].*

A similar plot was created by Cubison et al. [156] of f_{60} vs f_{44} for understanding the evolution of biomass burning plumes showing the oxidation of levoglucosan along the x-axis and atmospheric aging of the bulk OA on the y-axis, which similar to Ng et al. [155] observed the convergence to high f_{44} and low f_{60} values with aging. Furthermore, AMS can be paired with statistical techniques such as Positive Matrix Factorisation (PMF) which groups characteristic *m/z* fragments into "factors" providing temporal information on the sources contributing to the sampled OA [157]. For instance, Chen et al. [30] applied a rolling PMF approach which observed during winter months in Europe solid fuel combustion is a significant source of OA, constituting on average 21.4 % of the total OA.

The invention of the Filter Inlet for Gases and AEROsols coupled to Chemical Ionisation Mass Spectrometry (FIGAERO-CIMS) [158] and the CHemical Analysis of aeRosol ON-line (CHARON) inlet for Proton Transfer Reaction Time of Flight MS (PTR-ToF-MS) [159] has revolutionised the ability to obtain online detailed chemical composition measurements of OA. Both instruments use soft ionisation techniques enabling less fragmentation of the molecular ion compared to AMS. In the FIGAERO inlet gas and aerosol phases are sequentially analysed. Aerosol is sampled onto a filter whilst the gas phase is analysed in real-time before switching to the aerosol phase which is thermally desorbed from the filter for analysis. The thermal desorption produces a thermogram enabling distinct signal responses from semi-volatile and low-volatility products [158] which can provide information on the aging of SOA products over time as they become increasingly oxidised and hence less volatile [160]. In urban air the FIGAERO technique was reported to explain 24 % of the total OA measured by AMS [161]. Whereas the CHARON inlet operates differently to the FIGAERO. First, a thermal denuder removes gas phase species and then the particles are directed through an aerodynamic lens which enriches the particle phase for analysis and finally the components from the particle phase are volatilised in a thermal desorption unit. The lack of filter collection in the CHARON inlet could therefore reduce potential sampling artifacts compared to other online techniques [159]. Furthermore, the total organics measured by the CHARON PTR-MS was observed to agree within a factor of 2 to that from AMS measurements [162]. This list is not exhaustive and there are other online MS techniques for SOA characterisation, such as, extractive electrospray ionisation

time-of-flight mass spectrometer (EESI-TOF) which uses charged droplets created by the electrospray to extract the soluble aerosol components in real time [163]. Recently, the EESI source has been coupled with an Orbitrap mass detector to enable real time high resolution measurements as well as gain insights into a molecular structures from tandem mass spectrometry [164].

Furthermore, the ionisation of species within a PTR-ToF-MS is considered to be universal as the proton transfer reaction to produce MH^+ ions proceeds at the collision frequency if the proton affinity of the analyte is greater than 10 kcal mol^{-1}. This criteria satisfies many polar and non polar organic compounds found in the atmosphere and means quantification can be achieved from collision theory without the use of an analytical standard [165]. However, both AMS and CIMS similarly to ESI experience ionisation effects [154, 166–168] which are species dependent and often not fully accounted for.

1.6.3 Non-Target Mass Spectrometry Analysis

One of the disadvantages of MS techniques is the small percentage of total OA mass analysed when identifying individual markers. This analysis of known compounds is referred to as targeted analysis and depends on the availability of authentic standards for quantification. In the analysis of organic aerosol there are relatively few commercially available standards and therefore, targeted analyses do not represent the complete composition. For instance, in a targeted analysis of $PM_{2.5}$, Pereira et al. [169] only identified 20 SOA markers with authentic standards which equated to less than 1.1 % of the total mass. Therefore, analysis of the "bulk" OA composition is highly advantageous. A more powerful analysis technique of bulk composition has been developed for use in MS applications which enables molecular formula assignments of all detected analytes. This is known as non-target analysis (NTA) and has been increasingly applied to the UHPLC-HRMS analysis of OA in recent years [139, 169–174], as well as, GC×GC-MS applications [175]. The power of the NTA technique coupled to UHPLC-HRMS is nicely demonstrated by Wang et al. [139] who observed between 1961-28696 features in $PM_{2.5}$ samples from Mainz and Beijing. Of these detected features, 57-78 % were assigned to molecular formulae with a mass tolerance less than 2 ppm error [139]. These studies can provide insight into the sources of aerosol, the impact of aging on

chemical composition and the molecular structure from elemental ratios of hydrogen-to-carbon (H:C) or O:C or nitrogen-to-carbon (N:C), carbon oxidation state and double bond equivalents [116, 176, 177]. These metrics give an indication of how oxygenated or oxidised the compound is, as well as, how many double bonds or aromatic rings or heteroatoms are present in the molecule. Kim et al. [176] also showed that the plot of H:C vs O:C, known as a Van Krevelen diagram, could provide unique fingerprint regions for different chemical classes due to the occupation of different H:C vs O:C space. These types of analysis and application to OA are presented in much greater detail in Chapter 3.

However, the main issue with NTA studies coupled to offline HRMS techniques at present is the use of limited metrics such as number of formulas or peak area to represent a species' relative abundance when there are no authentic standards available for quantification [139, 169–174, 178–180]. As mentioned in Section 1.6.1, ESI has a known ionisation efficiency effect, therefore, using peak area could lead to misinterpretations of source apportionment in these studies. NTA of OA would therefore benefit from approaches which can account for ionisation efficiency leading to improved quantification, for example, predictive ionisation efficiency models or surrogate standard quantification [181–185]. This is currently an active and growing field of research across many environmental matrices which is discussed in greater depth for OA applications in Chapter 2.

1.7 Thesis Outline

Overall this thesis aims to improve our understanding of biomass burning organic aerosol (BBOA) and the atmospheric chemical mechanisms that lead to its formation. Using UHPLC-ESI-HRMS, investigations into the chemical characterisation of BBOA from a range of different conditions were taken using novel non-target methodologies which deliver improvements in the quantification of unknown species. By improving our understanding of the chemical composition of BBOA it is possible to infer the impact of biomass burning emissions on human health by linking the composition with toxicity estimates and on climate by understanding species contributing to BrC. In addition, understanding the chemical mechanisms of BBVOCs enables more reliable estimates of SOA and O_3 formation potentials from biomass burning in air quality modelling, therefore, enabling an understanding of the impact on local, regional and global scales. From this research, improvements can be made to air quality policy such as that surrounding the use of solid fuel combustion in urban areas and improved insights into the growing global detrimental impact of increased biomass burning can be gained.

Chapter 2 presents the development of a semi-quantitative strategy for use in non-target compositional analysis of complex OA samples. Quantification is achieved from multiple close eluting and chemically similar surrogate standards within short retention time windows of the unknown analyte. Overall, the new method performs well when compared to other quantification strategies in non-target analysis such as predictive ionisation efficiency models and highlights the inadequacy of not accounting for ionisation efficiency (i.e. peak area).

Chapter 3 presents the application of the semi-quantitative non-target methodology developed in Chapter 2 to wood burning organic aerosol from a series of controlled burn experiments performed at the Manchester Aerosol Chamber in 2022. The campaign aimed to understand compositional differences between flaming and smouldering burn phases and the impact of atmospheric aging. This work highlights the importance of the burn phase on the total aromatic contribution to the organic aerosol and thereby the implications for toxicity.

Chapter 4 presents the development of a near-explicit chemical mechanism of an

important understudied BBVOC, guaiacol, for inclusion into the MCM. The mechanism is validated against results from a series of atmospheric simulation chamber experiments conducted at the EUropean PHOtoREactor in May 2023. The proposed mechanism is able to well reproduce the observable chemistry. The analysis of several particulate phase guaiacol oxidation products is also presented to understand the potential difference between night- and daytime emission sources. This work highlights the difference between night and day emissions of guaiacol on the composition of SOA formed in relation to toxicity and atmospheric chemistry.

Chapter 5 provides a summary of the findings and conclusions from Chapters 2 to 4 and a discussion of future research topics to further improve the analysis of BBOA and the gaps that remain in our understanding of the atmospheric chemistry from biomass burning.

Chapter 2

Development of a semi-quantitative non-target approach for compositional analysis of complex OA

2.1 Introduction

The ability to probe molecular composition has been revolutionised by liquid chromatography coupled to electrospray ionisation (ESI) high resolution mass spectrometry (LC-HRMS). LC-HRMS coupled with non-target analysis (NTA) methods allows the detection of thousands of compounds present within complex sample matrices compared to a relatively small number of compounds (< 100) in targeted analyses. For instance, in a targeted analysis of ambient particular matter, Pereira et al. [169] only identified 20 compounds which equated to less than 1.1% of the total mass, highlighting the significant advantages of using NTA. NTA approaches using LC-HRMS have previously been applied to detect emerging contaminants and hazardous substances in a range of complex samples such as environmental matrices and the food and drink industry [169, 186–188]. However, quantification of unknown compounds remains challenging as traditional methods of calibration with authentic standards are not possible due to the lack of commercial availability and the sheer numbers of detected compounds.

For this reason many prior NTA studies of complex samples use metrics such as peak area and number of molecular formulas to convey the relative abundance of

different compounds [169, 172, 178–180, 186, 189]. However, the variability in the relationship between instrument signal and compound concentration means this approach does not lead to accurate quantification [149]. This phenomenon is a result of ionisation efficiency, which is a measure of the ability of a species to ionise within the ESI source. Ionisation efficiency is highly structural specific and can vary by multiple orders of magnitude between different compounds including structural isomers [148, 149]. Additionally, the choice of ESI source, mobile phase, pH and the percentage of organic modifier content across a gradient elution programme could further affect ionisation efficiency [190–193]. However, Kruve [190] observed that generally ionisation efficiency values were well correlated between methanol and acetonitrile mobile phases.

Recent efforts to quantify unidentified compounds have utilised machine learning to build predictive models of ionisation efficiencies using physicochemical properties of analytes such as pKa, polarity and the mobile phase composition [148, 190, 194, 195]. Alternatively, a second class of models predict relative ionisation efficiencies (RIE), i.e. how well a species ionises relative to a reference compound [181, 182, 185, 196]. Despite differences in the reference compound, the predictive RIE models developed by Mayhew et al. [182] and Bryant et al. [185] and Liigand et al. [181] perform similarly with R^2 and root-mean-square error (RMSE) ranging from 0.62-0.66 and 0.35-0.59 respectively. Furthermore, the model developed by Liigand et al. [181] was constructed using data from a range of chromatographic conditions however little effect was observed on the model prediction accuracy. Application of the Liigand et al. [181] model to quantify myotoxins and pesticides in cereals yielded a quantification error of 5.4 which is defined as the ratio between predicted concentration and the true concentration certified via an authentic standard. However, the main drawback of these models is the need to know the structure for quantification. In a NTA workflow the number of structurally assigned compounds is usually low compared to the total number of detected compounds [169], which can be further impacted by the instrumental workflow and data quality across multiple samples. For instance, the use of data dependent fragmentation mass spectrometry (ddMS^2) will fragment the top most abundant ions per scan. A more recent approach used fragmentation spectra (MS^2) to obtain molecular descriptors for the prediction of the ionisation efficiency,

allowing non-structurally identified compounds to be quantified with an average prediction error, the ratio of predicted:true concentration, of 4 [197]. However, in data-dependent analysis used in 60% of NTA studies for environmental matrices [198], not all compounds will reach the threshold for subsequent fragmentation. Therefore, if relying on MS^2 spectra for quantification there can be a loss of compositional information. For example, Wang et al. [146] observed in a typical non-target workflow using data-dependent acquisition that only 39% of detected compounds have MS^2 spectra meaning the majority of data was discarded from compositional analysis. Using data-independent acquisition (DIA) can provide improved MS^2 spectral coverage [199] and recent advances in DIA strategies such as sequential window acquisition of all theoretical fragment ion spectra mass spectrometry (SWATH-MS) provide high quality, quantitation accuracy and reproducibility [200]. However, the data processing to deconvolute the DIA spectral output can be more challenging and time consuming [199].

Complete characterisation of molecular composition requires all compounds with and without MS^2 spectra to be quantified. The analysis presented here uses a quantification methodology known as semi-quantification where multiple proxy standards are used for quantification via surrogate calibration curves. In many semi-quantification studies to date, typically a singular structurally similar proxy standard is used [171, 201–209]. However, the selection of an appropriate surrogate is essential to reduce quantification errors [210]. Reported semi-quantification errors, defined as the ratio of predicted:true concentration, can be as high as 10 [170, 171, 184, 201]. The study of organosulfates in organic aerosol (OA) which are commonly used as tracers for secondary organic aerosol (SOA), has widely applied semi-quantification methods [202–205, 207–209, 211]. For example, Li et al. [202] suggested using camphorsulfonic acid as a surrogate standard for nitroxy organosulfates due to its similar structure. For C_2-C_3 organosulfates multiple studies use glycolic acid sulfate as a proxy [203–205]. However, this incorrectly assumes that all compounds of the same chemical class, in this case organosulfates, ionise equally to that of a singular quantification marker. In reality, ionisation in an ESI source is structurally specific, can increase with retention time [212] and be affected by gradient elution due to changes in mobile phase [211]. Therefore, improved semi-quantification methods adopt closely eluting surrogate standards to the target compound [183, 184, 206–208, 213] with reported prediction errors of

1.74 - 3.20 compared to quantification with authentic standards. However, the majority of semi-quantification studies using structurally similar surrogate standards were only applied to quantify a small subset of compounds (< 10) and were quantified using a singular marker [183, 201–203, 205]. In this Chapter, a new semi-quantification method is presented using 110 authentic standards and a series of 25 different retention time windows to derive functional group specific scaling factors and uncertainty estimates from multiple proxy standards with a range of ionisation efficiencies in each window. The new methodology was then applied within a NTA workflow for the compositonal analysis of chamber generated biomass burning organic aerosol (BBOA) from wood burning, containing up to 2357 detected organic compounds in a single extract.

2.2 Methodology

2.2.1 Sample collection

The samples were taken from a series of wood burning experiments conducted at the Manchester Aerosol Chamber (MAC). The design and characterisation of the MAC has previously been described in detail in Shao et al. [214]. In brief, the wood burning experiments aimed to investigate the impact of the burn phase, i.e. flaming and smouldering conditions, on the physical and chemical characteristics of the emitted aerosol. Particulate matter was sampled onto filters either at the flue of the wood burner for 5 minutes at 2 L/min or after an aging period (≈ 6 hours) in dark or light conditions inside the MAC at a flow rate of 3 m^3/min for 4 minutes. Under dark conditions no further oxidants were added to the chamber therefore it does not reproduce the chemistry of a nitrate radical (NO_3) or ozone (O_3) oxidation observed in the atmosphere at night. Instead, changes in the aerosol composition are likely driven by evaporation and in-particle chemistry. We define these 3 sample types per burn phase as fresh flue, dark aged and light aged (photo-oxidation). The fresh samples and photo-oxidation experiments are used in Chapter 3 where the procedure is explained in greater detail.

Quartz filters (Whatman QMA, 47mm) were individually wrapped in foil and pre-baked at 500 °C for 5 hours prior to use. After collection, the filters were wrapped in the pre-baked foil then stored in the freezer at the University of Manchester before being transported at -20 °C to the University of York for offline ultra-high-performance

liquid chromatography coupled to high resolution mass spectrometry (UHPLC-HRMS) analysis.

2.2.2 Non-Target Ultra-High-Performance Liquid Chromatography High Resolution Mass Spectrometry (UHPLC-HRMS)

2.2.2.1 Filter extraction

The 47 mm quartz filters collected from the chamber experiments in Section 2.2.1 were cut into 1 cm^2 pieces, placed in a 20 mL glass vial and 10 mL of methanol (LC-MS Optima Grade) was added. However for fresh samples taken from the stove flue, half a 47 mm filter was used due to their higher mass concentration. The resulting solution was sonicated for 45 minutes, using ice packs to lower the temperature of the water bath. The methanol extract was transferred to a second 20 mL glass vial using a 0.22 μm syringe filter (Milipore) then dried using a Genevac vacuum solvent evaporator. The sample was reconstituted in 200 μL 90:10 H_2O (LC-MS Optima Grade): MeOH (LC-MS Optima Grade) for UHPLC-HRMS analysis.

2.2.2.2 Authentic standard preparation

110 authentic standards were chosen for the construction of the semi-quantitative approach. The functionality of the standards reflect those which are expected to ionise favourably in negative mode electrospray ionisation (ESI). Authentic standard solutions, using compounds in Table 2.1, were prepared in mixtures of 50:50 MeOH:H_2O with no overlapping of retention time between standards across the concentration range: 5, 2.5, 1, 0.5, 0.25, 0.125 and 0.0625 ppm.

Table 2.1: *Retention time windows and 110 standards used in the construction of the semi-quantification methodology. An asterisk (*) denotes identification in wood burning OA samples*

Retention time window / min	Chemical class	Standards in window	Window key
0-1	CHO	pyruvic acid, malonic acid, maleic acid, succinic acid*, malic acid, L(+) tartaric acid, aconitic acid, citric acid and shikimic acid	a
1-2	CHO	crotonic acid, acetoxyacetic acid, methylmalonic acid, citraconic acid*, itaconic acid, levulinic acid*, glutaric acid*, methylsuccinic acid, 1,2,4-butane-carboxylic acid and 3,4-dihydroxybenzoic acid*	b
2-3	CHO	valeric acid, 2-hydroxy-3-methylbutyric acid, adipic acid*, 1,3-butadiene-1,4-carboxylic acid 2,5-dihydroxybenzoic acid and 3,4-dihydroxy-phenylacetic acid	c
3-4	CHO	butyric acid, furoic acid, 4-hydroxybenzoic acid 2,6-dihydroxybenzoic acid*, 4-hydroxyphenyl-acetic acid and DL-mandelic acid	d
4-5	CHO	3,3-dimethylglutaric acid*, 3-methyladipic acid*, pimelic acid, 4-hydroxybenzaldehyde*, 3-hydroxy-benzoic acid, 4-methyl-catechol*, 3-hydroxyphenyl-acetic acid, vanillic acid and homovanillic acid	e
5-6	CHO	3,3-dimethylacrylic acid, DL-alpha-hydroxycaproic acid, 1,4-cyclohexanedicarboxylic acid, vanillin* 3-(4-hydroxyphenyl)propionic acid*, 2,6-dimethoxy-benzoic acid, 3,5-dimethoxy-4-hydroxybenzoic acid*	f
6-7	CHO	isophthalic acid, phenoxyacetic acid, hydroxy-cinnamic acid* and p-coumaric acid	g
7-8	CHO	4-hydroxy-3-methoxycinnamic acid, homoveratric acid, 2,4,5-trimethoxybenzoic acid, 3,5-dinmethoxy-4-hydroxycinnamic acid, sorbic acid, benzoic acid, suberic acid*, phenylacetic acid, 2-hydroxy-3-methoxy-benzoic acid and 3,4-dimethoxybenzoic acid	h
8-9	CHO	ketopinic acid, pinonic acid, 5-methoxysalicylic acid and 3,4,5-trimethoxybenzoic acid*	i

9-10	CHO	camphoric acid and 4-methoxybenzoic acid	j
10-11	CHO	2-benzylsuccinic acid, 2,3-napthalenedicarboxylic acid, o-toluic acid and azelaic acid*	k
11-12	CHO	4,4-bis(4-hydroxyphenyl)valeric acid, m-toluic acid p-toluic acid, 3,5-dimethoxybenzoic acid and trans-cinnamic acid	l
12-13	CHO	2-methoxycinnamic acid and 3-methoxycinnamic acid	m
13-14	CHO	4-phenylbutyric acid*, sebacic acid*, 1-napthlacetic acid and 2-benzoylbenzoic acid	n
14-16	CHO	3-hydroxy-2-napthoic acid, isoborneolacetic acid 3,4-dimethylbenzoic acid	o
16-18	CHO	4-tert-butylbenzoic acid	p
18+	CHO	dodecanoic acid, cholic acid and nonanoic acid	other
0-3	CHON	2-nitrobenzoic acid	a
3-6	CHON	2-nitroresorcinol and 4-nitrocatechol*	b
6-9	CHON	2,4-dinitrophenol*, 2-nitrophenol, 3-nitrophenol and 4-nitroguaiacol*	c
9-11	CHON	2-methyl-4-nitrophenol*, 4-methyl-3-nitrophenol, 2-methyl-5-nitrophenol, 2-methyl-3-nitrophenol and 3-methyl-4-nitrophenol and 4-methoxy-2-nitrophenol	d
11-12.71	CHON	2,6-dimethyl-4-nitrophenol*	e
12.71-14.9	CHON	2-methyl-6-nitrophenol, 4-methyl-2-nitrophenol and 5-methyl-2-nitrophenol	f
14.9-18	CHON	4-nitro-1-naphthol*	g
18+	CHON	2-nitro-1-naphthol	other
-	CHOS	camphorsulfonic acid	-

2.2.2.3 UHPLC-HRMS analysis

Filter sample extracts and authentic standard solutions were analysed using an Ultimate 3000 UHPLC (Thermo Scientific, USA) coupled to a Q Exactive Orbitrap MS (Thermo Fisher Scientific, USA) with heated electrospray ionisation (HESI) in negative mode. Compound separation was achieved using a reversed phase C_{18} 2.6 μm × 2.1 mm × 10 mm Accucore column held at 40 °C. The mobile phase consisted of 0.1 % (v/v %) formic acid (Acros Organics) in water (A, LC-MS Optima Grade) and methanol (B, LC-MS Optima Grade). A gradient elution was used, starting at 90 %

(A) with a 1 minute post injection hold, decreasing to 10 % (A) at 26 minutes before returning to the starting conditions at 28 minutes and a further 2 minute hold to allow for the re-equilibration of the column. The flow rate was set to 0.3 mL min^{-1}. Prior to analysis samples were stored in an autosampler tray at 4 °C. The injection volume was set to 4 μL, however injection volumes up to 10 μL were used for lower concentration samples. The HESI was operated under the following conditions: a spray voltage of 4 kV, a capillary and auxiliary gas temperature of 320 °C, a sheath gas flow rate of 45 (arb.) and an auxiliary gas flow rate of 10 (arb.) Spectra were acquired in negative and positive mode using data dependent tandem mass spectrometry (ddMS^2). The scan range was set to a mass-to-charge ratio (m/z) of 85 to 750, with a mass resolution of 140,000. Tandem mass spectrometry was performed using a higher collision dissociation with a stepped normalised collision energy of 10, 20 and 45. In each scan the 10 most abundant species were selected for MS^2 fragmentation.

The wood burning samples were analysed once by UHPLC-HRMS along with solvent blanks and chamber blanks, taken from a clean chamber. The UHPLC-HRMS methodology is based on a well-characterised method developed by Bryant et al. [88] and Pereira et al. [169] for the exploratory compositional analysis of OA. These chromatographic conditions enable the separation of a wide range of polar and non-polar compounds [136] and the more acidic mobile phase can improve chromatographic retention and resolution, as well as increase sensitivity [215–217].

2.2.2.4 Non-Target Analysis (NTA) workflow

Spectra were acquired using XCalibur 4.3 (Thermo Scientific, USA) and analysed using an untargeted workflow developed in MZmine 2.53 and MZmine 3.9.0 software [218, 219]. Detailed NTA workflows are given in Tables 2.2 and 2.3.

Table 2.2: *Workflow and module parameters for the non-target feature detection in MZmine 2.53*

Mass Detection	Retention time = 0 - 20 min
	MS Level = 1
	Polarity = -
	Spectrum type = profile
	Mass detector = Exact Mass
	Noise level = 50000
FTMS Shoulder Peaks Filter	Mass resolution = 140,000
	Peak model function = Lorentzian
Mass Detection	Retention time = 0 - 20 min
	MS Level = 2
	Polarity = -
	Spectrum type = profile
	Mass detector = Exact Mass
	Noise level = 0
ADAP Chromatogram Builder	Min group size in # of scans = 5
	Group intensity threshold = 50000
	Min highest intensity = 60000
	m/z tolerance = 0.001 m/z or 3 ppm
Smoothing	Filter width = 7
Chromatogram Deconvolution	Algorithm = local minimum search
	Chromatographic threshold = 80 %
	Search minimum in RT = 0.3 min
	Minimum relative height = 30 %
	Minimum absolute height = 50000
	Min ratio of peak top/edge = 1.2
	Peak duration = 0 - 2 min
	m/z centre calculation = median
	m/z range for MS2 scan pairing = 0 Da
	RT range for MS2 scan pairing = 0.05 min
Join Aligner	*m/z* tolerance = 0.001 *m/z* or 3 ppm
	Weight for *m/z* = 3
	RT tolerance = 0.1 min
	Weight for RT = 1
Isotopic Peaks Grouper	*m/z* tolerance = 0.001 *m/z* or 3 ppm
	RT tolerance = 0.01 min
	Maximum charge = 1
	Representative isotope = most intense
Duplicate Peak Filter	Filter mode = new average
	m/z tolerance = 0.0008 *m/z* or 1.5 ppm
	RT tolerance = 0.01 min
Formula Prediction	Charge = 1
	Ionisation type = [M-H]-
	m/z tolerance = 0.001 *m/z* or 3 ppm
	Max best formulas per peak = 5
	Elements = $C_{1\text{-}40}H_{0\text{-}100}O_{1\text{-}10}N_{0\text{-}4}S_{0\text{-}2}Cl_{0\text{-}2}$
	Element count heuristics Y
	RDBE restrictions Y

Table 2.3: *Workflow and module parameters for the spectral library search in MZmine 3.9.0*

Mass Detection	Retention time = 0 - 26 min
	MS Level = 1
	Polarity = -
	Spectrum type = profile
	Mass detector = Exact Mass
	Noise level = 50000
Mass Detection	Retention time = 0 - 26 min
	MS Level = 2
	Polarity = -
	Spectrum type = profile
	Mass detector = Exact Mass
	Noise level = 0
ADAP Chromatogram Builder	RT = 0 - 26min
	MS level = 1
	Polarity = -
	Spectrum type = profile
	Min group size in # of scans = 5
	Min intensity for consecutive scans = 10000
	Min highest intensity = 50000
	m/z tolerance = 0.0008 *m/z* or 2 ppm
Minimum Search Feature Resolver	Algorithm = local minimum search
	Chromatographic threshold = 90 %
	Minimum search range in RT = 0.3 min
	Minimum absolute height = 50000
	Min ratio of peak top/edge = 1.5
	Peak duration = 0 - 2 min
	Minimum scans = 5
	MS/MS scan pairing = TRUE
	MS1 to MS2 precursor tolerance = 0.01 *m/z* or 10 ppm
Isotopic Peaks Grouper	Chemical elements = C,H,O,N,S,Cl
	m/z tolerance = 0.0005 *m/z* or 10 ppm
	Maximum charge = 1
	Search in scans = single most intense
Join Aligner	*m/z* tolerance = 0.0008 *m/z* or 2 ppm
	Weight for *m/z* = 3
	RT tolerance = 0.1 min
	Weight for RT = 1
Spectral Library Search	Scans for matching = MS level $\geq$ 2 (Merged)
	Precursor *m/z* tolerance = 0.001 *m/z* or 5 ppm
	Spectral *m/z* tolerance = 0.0015 *m/z* or 10 ppm
	Minimum matched signals = 4
	Similarity = weighted cosine similarity
	Minimum cos similarity = 0.7
	Handle unmatched signals = keep all and match to 0
	RT tolerance = 0.25 min

MZmine 2.53 software assigned molecular formulae to detected features and MZmine 3.9.0 software enabled identification of species via an in-house built spectral library of authentic standards. The workflows were then merged for the remainder of the analysis. Post processing of the MZmine output was achieved by *(i)* choosing the best formula predicted by MZmine 2.53, *(ii)* performing a blank subtraction and *(iii)* removing duplicated data. Formula predictions were allocated providing the following criteria was met: $0.5 < H/C < 3.0$, $0.05 < O/C < 2.0$, $N/C < 1.0$, $S/C < 0.5$ and $Cl/C < 0.2$. The formula with the lowest mass tolerance in ppm was then selected as the "best" formula. The accuracy of the formula prediction is essential for the successful application of the semi-quantification methodology. In a previous study the algorithm for formula prediction in the MZmine 2 framework was tested across 48 chemicals observing that 79 % of compounds were predicted correctly as the highest ranking candidate (i.e. lowest difference in ppm) [220]. In this study, 12066 features were identified in total across all chemical functionality in the wood burning extracts with the highest ranking candidate accepted as the "best" formula for 97.6 % of features. Furthermore, the possibility a CHO species could be mistakenly predicted as a CHON compound was minimal given the odd mass of odd nitrogen species and the isotope fitting applied in the MZmine workflow. However, in the 443 cases where a CHO species had a CHON compound as the second ranking candidate which occurred exclusively for $C_xH_yO_5$ compounds, the second candidate was a $C_xH_yN_4O$ compound. This is a highly unlikely combination of heteroatoms to be observed in OA and therefore formula misidentifications were considered to be minimal in this work. Blank subtraction involved three steps: (1) common species detected in the sample and filter blank or chamber blank were removed if the sample-to-filter-blank signal was < 10 or sample-to-chamber-blank signal ratio was < 10 to ensure removal of all false positive peaks; (2) a list of the 20 most abundant surfactants and chlorinated organonitrate compounds in the chamber background, not removed in the first step due to large signals, were also removed from the sample owing to poor chromatography; (3) only species with a signal-to-noise ratio > 3 were accepted. In the final step *(iii)* species which also ionised in positive mode were only retained in the negative mode analysis if better ionisation (i.e. larger peak area) was achieved. This step, although not crucial for this work as the semi-quantification method was developed in negative mode, enables

positive and negative mode to be merged in future analysis where ideally NTA covers both compositional spaces. This workflow was applied to the wood burning aerosol extracts in order to evaluate its performance compared to traditional peak area methods frequently used in OA analysis. In total 389 - 2357 features for semi-quantification were detected by the NTA across the different samples, where variation in the feature detection is largely due to variability in filter mass concentration.

2.2.3 Determination of matrix effects and recovery

Whilst the standard solutions used to construct the methodology were analysed in pure solvent, matrix effects can arise when in the wood burning sample matrix [151, 152] leading to enhancement or suppression of peak signal. This can result in over- or under-estimations of species concentration. 27 species were structurally identified to Schymanski Level 1 [221] in the wood burning samples shown in Table 2.1 and therefore the matrix effect was evaluated for these compounds. Using quality control recommendations by Schulze et al. [222], a pooled sample of wood burning samples was taken to represent an "average" sample matrix effect. Of each sample, depending on availability a 25-75 μL aliquot was taken and combined into a pooled sample (450 μL in total). Due to the low sample availability the matrix effect was determined from a 4 point internal standard calibration. 10 μL aliquots of 2.5, 2.0, 1.5 and 1.0 ppm standard solutions of the 27 analytical standards in 90:10 H_2O:MeOH were spiked into four 90 μL aliquots of the pooled sample, giving a 1 in 10 dilution to produce the final calibration concentrations of 250, 200, 150 and 100 parts per billion (ppb) as well as a blank pooled sample. The same volume of stock solution was then spiked into 90μL of 90:10 H_2O:MeOH to produce pure standard solutions at the same concentrations for comparison. Calibration curves of the pure standard solutions and the internal standard solutions were constructed. Of the 27 identified compounds only those with a linear standard addition calibration curve ($R^2 \geq 0.8$) (Table 2.4) were evaluated for matrix effects to reduce the impact of anomalous compounds with poor linearity. These calibrations were more highly perturbed by the matrix and were predominantly compounds which eluted early (< 2 minutes) as seen previously [223] or had lower ionisation efficiencies ($\times 10^6$-10^7). In the external calibrations the R^2 was greater than 0.98 for 26 of the 27 identified compounds and therefore the deterioration in linearity

can be attributed to the matrix.

The matrix effect is expressed as the ratio of the internal standard to external standard calibration gradient for each compound. The peak area of the internal standards was determined by subtracting the pooled sample peak area from the spiked pool sample peak area. The gradient matrix effect was then determined as the ratio of the internal standard to external standard calibration gradient for each compound (Table 2.4). To further understand the impact on species concentration standard addition calibration curves were constructed from the spiked pooled samples without removing the pooled sample peak area and then extrapolating the line to y = 0 to determine the pooled sample concentration. This concentration was the compared to that determined from solving the external calibration regression line at the pooled sample peak area. The concentration matrix effect reported in Table 2.4 is expressed as the ratio of the externally calibrated concentration to the standard addition determined concentration.

Recovery of 27 analytical standards which were identified in the wood burning samples were determined from spiking 50 μL of a 100 ppm standard solution for each standard onto a blank filter to achieve an on column concentration of 5 ppm or 5 μg mL^{-1}. The spiking procedure was repeated 3 times on 3 separate filters. Each spiked filter and a blank non-spiked filter were extracted according to the methodology described in Section 2.2.2.1. A pure 1 mL stock solution of 5 ppm of each analyte in 90:10 H_2O:MeOH was made up and analysed by UHPLC-HRMS at the same time as the spiked filters to determine the analyte recovery shown in Table 2.4, calculated as the percentage of the filter peak area at 5 ppm compared to the 5 ppm pure standard solution.

Peak detection for the matrix effect and recovery compounds was computed using an accurate mass and retention time library in TraceFinder 4.1 (Thermo Scientific, USA) with a retention time window of 30 seconds and a minimum signal-to-noise ratio of 3. For species not detected by the TraceFinder library, the peak area was manually integrated in the acquisition software XCalibur 4.3 (Thermo Scientific, USA). For levulinic acid the repeatability of the recovery samples was poor therefore a single sample was taken resulting in the lack of a standard deviation value in Table 2.4.

Table 2.4: *Calculated matrix effects and percentage analyte recovery from the filter extraction associated with the semi-quantification methodology and the relative standard deviation (RSD) associated with the extraction recovery for the identified species in the wood burning extracts*

Compound	Extraction recovery / %	RSD / %	Gradient matrix effect	Concentration matrix effect
2,6-dihydroxybenzoic acid	104.4 ± 2.9	2.7	-	-
2,6-dimethyl-4-nitrophenol	75.8 ± 3.2	4.2	-	-
2-4-dinitrophenol	80.7 ± 11.1	13.8	-	-
2-methyl-4-nitrophenol	92.5 ± 12.3	13.3	0.759	0.557
3,4,5-trimethoxybenzoic acid	94.0 ± 4.2	4.4	-	
3,4-dihydroxybenzoic acid	91.4 ± 3.1	3.4	0.943	0.927
3,5-dimethoxy-4-hydroxybenzoic acid	80.5 ± 2.5	3.0	0.850	0.994
3-(4-hydroxyphenyl)propionic acid	85.3 ± 10.2	11.9	-	-
3-hydroxy-2-napthoic acid	82.5 ± 1.5	1.8	0.762	0.145
3-methyladipic acid	76.2 ± 2.3	3.1	0.914	1.658
4-hydroxybenzaldehyde	80.9 ± 0.5	0.7	0.644	1.254
4-methyl-catechol	62.5 ± 10.2	16.3	0.708	0.770
4-nitro-1-napthol	61.6 ± 4.3	7.0	-	-
4-nitrocatechol	96.5 ± 8.4	8.7	0.449	0.559
4-nitroguaiacol	74.6 ± 3.2	4.3	-	-
4-phenylbutyric acid	82.8 ± 7.1	8.5	-	-
adipic acid	94.6 ± 1.8	1.9	0.145	0.116
azelaic acid	90.9 ± 5.2	5.8	0.754	0.732
citraconic acid	97.5 ± 11.2	11.5	2.260	1.870
glutaric acid	110.5 ± 14.6	13.2	1.410	0.960
hydroxycinnamic acid	86.4 ± 3.9	4.5	0.785	0.837
levulinic acid	146.8	-	0.957	1.485
methylsuccinic acid	97.7 ± 6.7	6.8	-	-
sebacic acid	95.2 ± 2.3	2.4	0.905	1.271
suberic acid	100.8 ± 4.0	4.0	0.660	0.743
succinic acid	92.5 ± 4.8	5.2	-	-
vanillin	54.4 ± 6.7	12.3	0.781	0.861

2.3 Results and discussion

2.3.1 Evaluation of matrix effects and recovery

Average matrix effects were determined from the 17 internal calibrations with $R^2 \geq 0.8$. On average, the gradient matrix effect was relatively low (0.864 ± 0.442) and showed the external standard gradient was higher, by ≈ 15 % than the internal calibration gradient. However, this difference in ionisation efficiency is likely accounted for within the uncertainty of the semi-quantification method by adopting upper and lower quartile gradients per retention time window. The ratios of the externally calibrated concentrations to the standard addition calibration were also calculated with a mean average of 0.925 ± 0.475, indicating that the use of an external calibration can underpredict concentration in this case. Using the classification adopted for quality control and method validation for pesticide analysis as there is yet a universal quality assurance and control framework to exist for OA [222], the calculated matrix effects are within the accepted range of ± 20 % suppression or enhancement [224–227] and comparable to a previous OA study [228]. Nonetheless, in a non-target analysis where the majority of compounds are unknown it is impossible to quantify an exact matrix effect for each compound and using a surrogate internal standard cannot fully compensate for the analytical variation [229]. Furthermore, the extraction recovery of an analyte from OA collected on a filter can be challenging to exactly replicate in a laboratory as this involves the recovery from a matrix adsorbed onto a second matrix. Instead, the recovery of the 27 identified compounds was approximated from spiking standards at known concentration onto a blank filter resulting in an average recovery of 88.5 ± 3.9 % (Table 2.4). The relative standard deviation of the individual recoveries in Table 2.4 were less than 20 % and therefore were considered satisfactory [230].

2.3.2 Development of the semi-quantitative approach

To overcome differences in ionisation efficiencies, calibration is required using authentic standards. However, in a complex sample containing thousands of unknown species the lack of commercially available authentic standards means accounting for ionisation efficiency is practically impossible. Instead, a semi-quantification approach

can be used in which calibration gradients from proxy standards are applied to unknown species. Calibration gradients for oxygenated (CHO), organonitrate (CHON) and organosulfate (CHOS) species were obtained across a 7 point calibration curve for each analytical standard. Concentrations were analysed in triplicate, the linear fit was not forced through 0 and *y-axis* intercepts were ignored as in Bryant et al. [185]. 110 standards were used in total; 90 predominantly organoacids and alcohols, for the CHO class, 19 nitroaromatic standards for the CHON compounds and the use of camphorsulfonic acid for CHOS species. Due to the operation of the ESI source in negative mode, the chosen standards were expected to ionise favourably under these conditions. The standards and their corresponding gradients are presented in Evans et al. [231].

The acquired chromatogram from the UHPLC-HRMS method was divided into retention time windows assigning each authentic standard to a retention time window, as shown in Table 2.1. For CHO the number of standards allowed retention time windows of 1 minute from 0 - 14 minutes and windows of 2 minutes from 16 - 20 minutes resulting in 17 retention time windows. For CHON retention time windows range between 2-3 minutes due to the lower number of available standards resulting in 8 retention time windows. A scaling factor was obtained for each retention time group by calculating the median calibration gradient across the authentic standards within each retention time group. To allow for estimates of uncertainty, the lower quartile, upper quartile, minimum and maximum calibration gradients were also computed per retention time window as shown in Table 2.5 and Figure 2.1. Figure 2.1 shows that the magnitude of the interquartile range used to calculate the uncertainty in quantification is generally neither a function of the retention time or the number of standards used.

Table 2.5: *Median, lower quartile, upper quartile, minimum and maximum gradients per retention time window used in the semi-quantification method*

Chemical class	RT window key	Median	Lower quartile	Upper quartile	Maximum	Minimum
CHO	a	2.73E+07	3.90E+06	3.43E+07	5.36E+07	1.50E+06
CHO	b	7.11E+07	1.58E+07	9.40E+07	1.14E+08	2.52E+05
CHO	c	5.99E+07	1.22E+07	1.09E+08	1.45E+08	5.53E+06
CHO	d	3.82E+07	9.41E+05	1.07E+08	4.39E+08	6.51E+04
CHO	e	1.07E+08	2.17E+07	1.92E+08	7.17E+08	6.11E+06
CHO	f	3.69E+07	3.79E+06	4.99E+07	2.24E+08	2.10E+04
CHO	g	1.47E+08	7.95E+07	1.93E+08	2.03E+08	6.51E+05
CHO	h	8.98E+06	2.75E+06	1.24E+08	3.89E+08	1.22E+05
CHO	i	3.90E+07	1.12E+07	1.48E+08	4.02E+08	2.14E+06
CHO	j	1.14E+08	5.88E+07	1.69E+08	2.23E+08	3.90E+06
CHO	k	2.32E+08	1.22E+08	3.64E+08	5.34E+08	1.71E+07
CHO	l	6.28E+06	4.91E+06	5.29E+07	1.01E+08	4.05E+06
CHO	m	1.52E+07	7.92E+06	2.24E+07	2.97E+07	6.65E+05
CHO	n	1.82E+08	2.50E+06	3.75E+08	4.13E+08	2.34E+06
CHO	o	6.30E+08	3.17E+08	6.55E+08	6.80E+08	3.49E+06
CHO	p	8.42E+06	-	-	-	-
CHO	other	1.11E+07	1.08E+07	2.32E+08	4.53E+08	1.04E+07
CHON	a	1.78E+07	-	-	-	-
CHON	b	4.37E+08	2.29E+08	6.45E+08	8.53E+08	2.05E+07
CHON	c	6.59E+08	3.11E+08	9.49E+08	1.08E+09	1.47E+07
CHON	d	9.82E+08	4.59E+08	1.13E+09	2.08E+09	3.37E+06
CHON	e	3.12E+09	-	-	-	-
CHON	f	1.00E+07	9.52E+06	1.02E+07	1.04E+07	9.02E+06
CHON	g	3.14E+09	-	-	-	-
CHON	other	2.34E+07	-	-	-	-

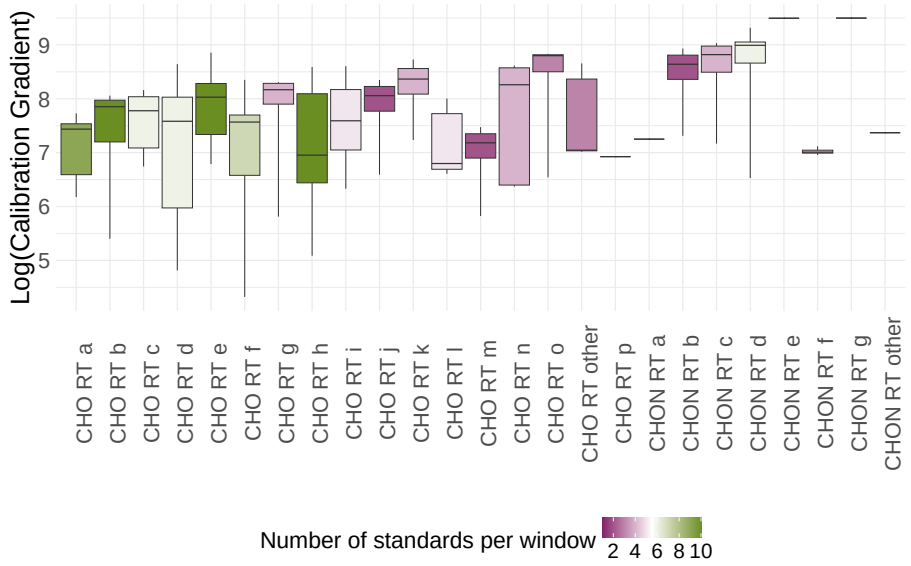

Figure 2.1: *Median, maximum, minimum and interquartile range of calibration gradients used in the semi-quantification method per retention time window group coloured by the number of standards in each window. Single lines represent groups with a singular standard.*

For those compounds identified by the spectral library to Schymanski Level 1 [221], scaling is achieved using the authentic standard calibration gradient. For non-identified compounds, the chromatogram is split into the retention time windows described above and scaled with the corresponding averaged retention time window calibration gradient to enable the semi-quantification of all species detected by the NTA. The overview of this strategy is presented in Figure 2.2.

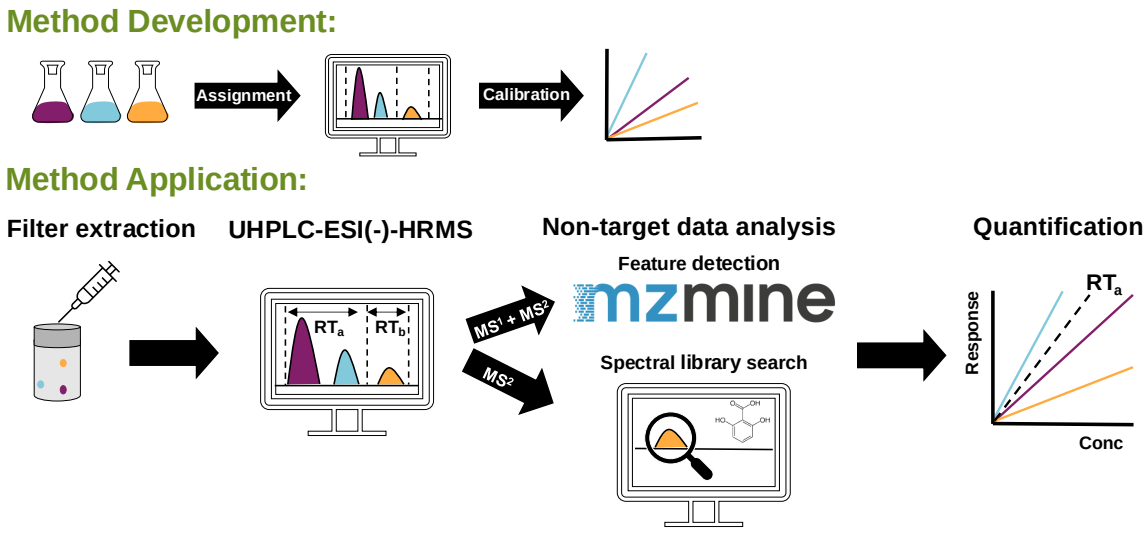

Figure 2.2: *Summary of the semi-quantification methodology construction and application in a non-target workflow*

2.3.3 Validation of the semi-quantification method

The semi-quantification method was applied to a series of BBOA extracts from the controlled burn experiments described in Section 2.2.1. In order to determine the performance of the semi-quantification method, the semi-quantified concentrations of structurally identified compounds were compared to quantification using authentic standards. Quantification errors were determined from the ratio of a species concentration estimated via the semi-quantification method to the concentration determined with an authentic standard (Eq. 2.1). The error is represented as n times the concentration determined using an authentic standard in μg m^{-3}. This notation has been adopted by previous NTA quantification methods and allows the comparison of different methodologies on the same scale. An overall quantification error for the method is taken as the median of the individual species error. The concentrations used in Eq. 2.1 were not subject to logarithmic transformations and ratios greater than and less than 1 were included in this calculation. Of the 27 structurally identified species detected in the wood burning samples, 70% of the concentrations determined by the semi-quantification method were within a factor of 2 of the authentic standard derived concentration (i.e. errors between 0.5-2 times). These compounds are shown in grey in Figure 2.3, suggesting the majority of compound concentrations are accurately estimated by the semi-quantification method. The compounds outside of this error range are shown in colour in Figure 2.3. It is important to note that due to the use of the median gradient for each retention time window some of the identified compounds may be scaled with their own authentic standard gradient, more likely for the CHON species due to the smaller number of surrogate standards, and therefore sit on the 1:1 line in Figure 2.3. However, the sensitivity of the error to this factor was found to be negligible.

$$Error_{prediction} = \frac{[concentration]_{semi-quantification}}{[concentration]_{authentic}} \tag{2.1}$$

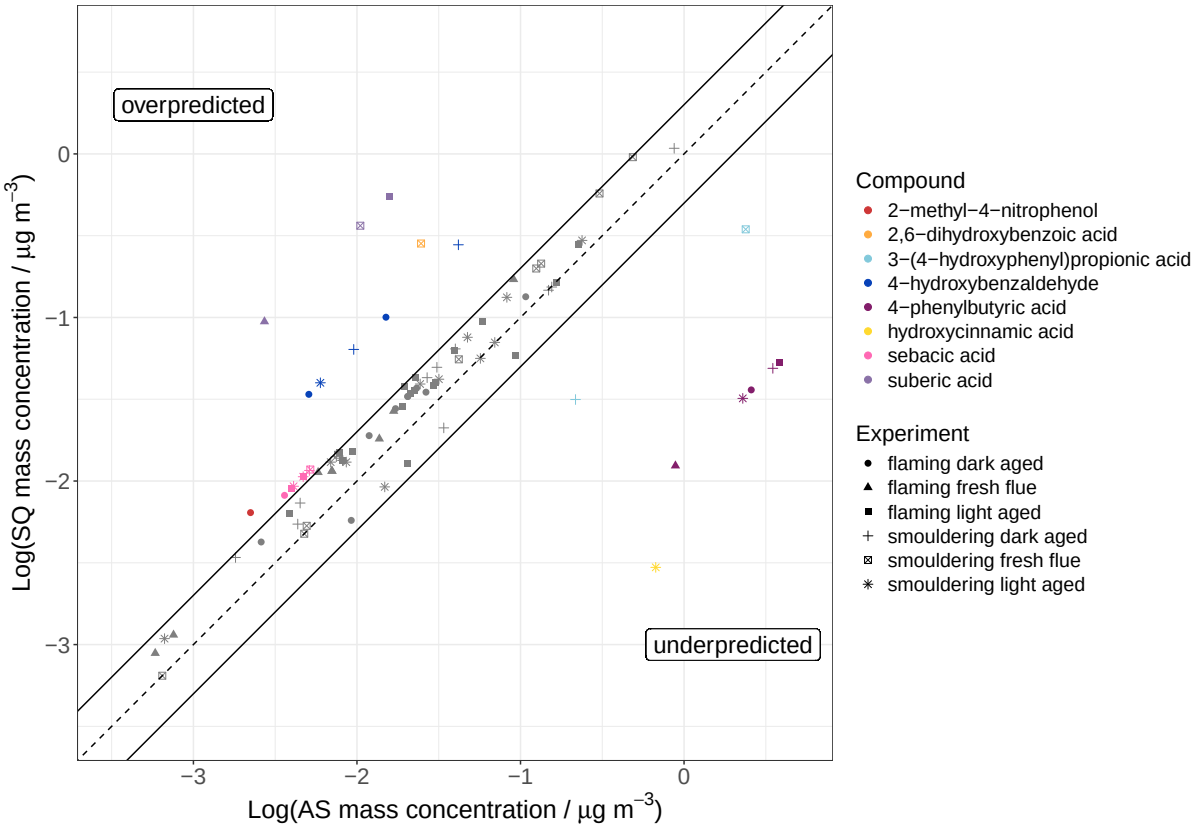

Figure 2.3: *Comparison of the estimated concentrations from the semi-quantification (SQ) method with authentic standard (AS) quantification for the 27 identified compounds present in the BBOA samples with different conditions shown by the marker type. 1:1 line is presented as a dashed line and factor of 2 lines are indicated by the solid lines. Compounds outside of the factor of 2 error range are presented in colour.*

McCord et al. [201] similarly demonstrated low prediction bias (< 48%) for the quantification of emerging perfluoroethercarboxylic acids (PFECAs) in drinking water using 4 different surrogate PFECAs standards which eluted within a 4 minute retention time window of the unknown PFECAs. However, the method validation for the semi-quantification was only applied to a single known compound therefore, McCord et al. [201] estimated prediction errors up to ten-fold (i.e 10 ×) for the unknown emerging PFECAs. Prediction errors of 1.74 times and 3.2 times compared to quantification by authentic standards were observed by Pieke et al. [183] and Kruve et al. [184] respectively for quantification of unknown compounds in food and ground wa-

ter analysis using closely eluting markers, typically ± 2 min. Comparatively, the semi-quantification method developed in this work had a median prediction error of 1.52 and mean prediction error of 3.14 times across 27 structurally identified compounds showing improved prediction accuracy when using more than a single proxy standard for quantification. Removal of the two CHON species on the 1:1 line in Figure 2.3 from the error calculation resulted in an overall median prediction error of 1.60 indicating little effect on the metrics used to validate the methodology. The prediction error is lower for CHON species (1.32) compared to CHO compounds (1.52). This is in contrast to the quantification error observed in the predictive ionisation efficiency model developed by Sepman et al. [197] with larger prediction errors in CHON quantification ranging up to a factor of 10. However, the model was developed for positive mode ESI therefore the analysed compounds likely possess different functionality to the CHON species presented in this work.

For the species predicted outside of the factor of 2 error range, the uncertainty in concentration, calculated using the interquartile range of calibration gradients in each retention time window, was compared to quantification by authentic standard (Figure 2.4) . This showed improvements in 3 outlying species; sebacic acid, 4-phenylbutyric acid and 3-(4-hydroxyphenyl)propionic acid.

The remaining outliers typically have gradients at the extremities of their corresponding retention time window. The outliers were not correlated with retention time and therefore were assumed to be little affected by the increasing organic modifier content of the mobile phase. Furthermore, outliers were present at multiple retention times throughout the chromatography runtime indicating species polarity is also not a determining factor. Instead, they could be the result of other structural properties affecting ionisation efficiency, including pKa and molecular weight of a species[148, 191]. This influences the interactions of the analytes with the solvent droplet and the ease of deprotonation in negative mode ESI. In Figure 2.3 overprediction resulted from scaling with a lower gradient compared to the authentic slope whereas underprediction occurred from scaling using larger gradients than the authentic slope. pKa, which governs the ability to deprotonate, may affect the overprediction of 2,6-dihydroxybenzoic acid concentrations. For instance, 2,6-dihydroxybenzoic acid possessed the highest ionisation efficiency of the compounds within its reten-

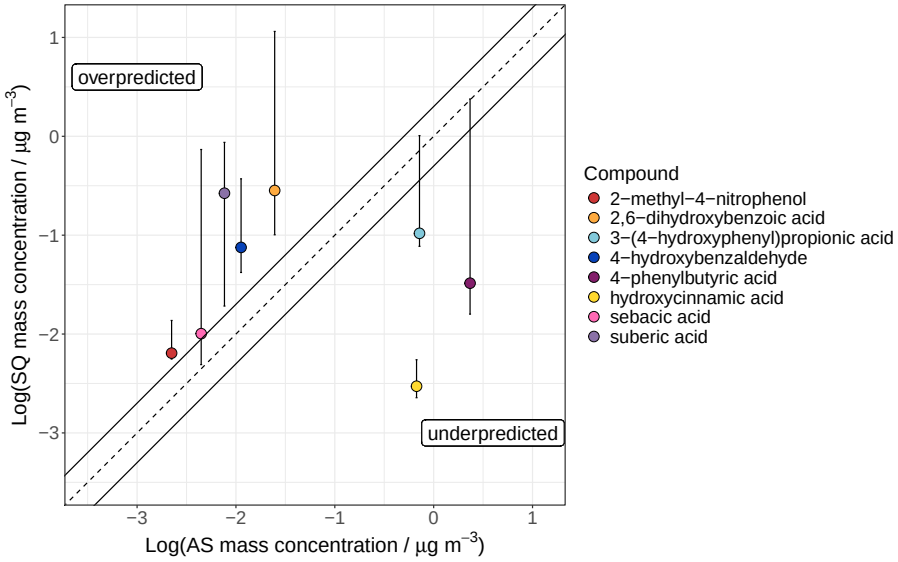

Figure 2.4: *Comparison of the average estimated concentrations from the semi-quantification (SQ) method and authentic standard (AS) quantification for the 8 outlying compounds in the BBOA samples from Figure 2.3 and the uncertainty in the concentration estimation derived from the upper and lower quartile scaling factors. 1:1 line is presented as a dashed line and factor of 2 lines are indicated by the solid lines.*

tion time window whilst simultaneously having the lowest pKa, predicted by ChemDraw 21.0.0 software, which suggests greater deprotonation ability compared to other species within the same window. On the other hand, multiple ionisation sites as in suberic acid, a dicarboxylic acid, could increase ionisation efficiency compared to the monocarboxylic acids within the same retention time window. In addition to pKa and the number of deprotonation sites, stabilisation of the deprotonated ion further affects ionisation efficiency. For instance, despite ionisation at a higher pKa alcohol group, the deprotonated 4-hydroxybenzaldehyde ion could exhibit charge stabilisation effects thereby increasing its ionisation efficiency compared to the other compounds within the same window. However, further work is needed to investigate these effects and if they can be accounted for.

Due to the nature of NTA the chemical functionality present within a sample can be difficult to predict therefore a wide range of standards of different chain length, aromaticity and functionality were used in this study (Table 2.1). As such retention time groups can have large variations in calibration gradients owing to the molecular

properties previously discussed. For instance, the retention time group which overpredicted 2,6-dihydroxybenzoic acid concentrations, had the maximum observed difference of 4 orders of magnitude between the maximum (2,6-dihydroxybenzoic acid) and minimum (butyric acid) gradient in the window. Removing the butyric acid gradient from this group decreased the difference in gradients to 3 orders of magnitude and the overprediction of 2,6-dihydroxybenzoic acid was reduced from 11 times to 6 times compared to quantification by authentic standard. Therefore, prior chemical knowledge of the sample could improve quantification through the selection of targeted standards which better reflect the sample composition. However, due to the lack of commercially available authentic standards this approach is not always possible.

2.3.4 Comparison to predictive ionisation efficiency models for quantification

In a number of previous studies ionisation efficiency has been predicted from machine learning models, based on either physicochemical properties, structural descriptors or chemical fingerprints [181, 182, 185, 195–197, 232]. Bryant et al. [185] used chemical structural fingerprints obtained from the ChemDes platform [233] to predict RIEs of 89 CHO and CHON compounds using *cis*-pinonic acid as the reference compound for the quantification of biogenic SOA markers. However, this method required prior knowledge of the structure in order to predict the RIE and therefore is not applicable to unknown compounds. More recently, molecular descriptors from MS^2 have been used to predict ionisation efficiency which could yield further improvements in quantification for structurally unidentified compounds [197]. However, for species without MS^2 quantification remains a challenge. RIE predictions were taken from Bryant et al. [185] and applied to the wood burning samples to determine the concentration of 18 structurally identified compounds that were quantifiable by both methods. Figure 2.5 shows the comparison of the concentration predicted by the semi-quantification approach developed here with the RIE predictions from Bryant et al. [185] for estimating concentrations of structurally identified compounds within the wood burning extracts. Comparison to other existing predictive ionisation efficiency models is difficult due to the use of different LC methodologies which could induce additional ionisation effects from the solvent system as well as, the use of different reference

compounds for calculating RIE [181, 182, 185]. However, future work should aim to include inter-laboratory comparisons when applying the same methodology to ensure the performance is consistent as recently demonstrated by Malm et al. [234] across 37 laboratories. Of the 18 common compounds quantified by both methods, a third were semi-quantified to within a factor of 2 compared to quantification with the Bryant et al. [185] RIE predictions including sebacic acid, azelaic acid, 3-methyl adipic acid, adipic acid, glutaric acid and succinic acid. A further 6 organoacid species could be semi-quantified to within a factor of 2 of the RIE method by applying the semi-quantification method's uncertainty range, calculated from the interquartile range of concentration. Overall, this indicated good agreement between the methods for the quantification of CHO compounds but greater discrepancy for the quantification of CHON which were further away from the factor of 2 prediction errors lines in Figure 2.5.

Compared to quantification by authentic standards, the predicted RIEs from Bryant et al. [185] tended to overpredict species concentration compared to using the semi-quantification methodology (Figure 2.6) as a result of underpredicting the RIE. The compounds in grey in Figure 2.6 represent a low prediction error (i.e. less than a factor of 2) in both methods compared to quantification with authentic standards and were mostly compounds with good agreement between the methods (Figure 2.5). Given that the majority of the compound concentrations estimated by the semi-quantification method in Figure 2.6 were more closely situated to within a factor of 2 of the concentration determined using authentic standards, demonstrated improved prediction errors compared to the RIE methodology. However, significant exceptions exist for suberic acid and 4-phenylbutyric acid with prediction errors compared to quantification by an authentic standard of 34.72 and 0.01 (or 100 times lower) respectively using semi-quantification compared to 2.52 and 0.80 (or 1.25 times lower) respectively using RIE predictions. Overall, the CHO compounds had a median prediction error of 1.52 and 2.05 for the semi-quantification and RIE predictive model approaches respectively, showing similar performance between the methods for estimating concentration compared to using authentic standards. The estimation of nitroaromatic compound concentrations was less certain using the RIE approach with median prediction errors of 14.94 times compared to quantification by authentic standard, how-

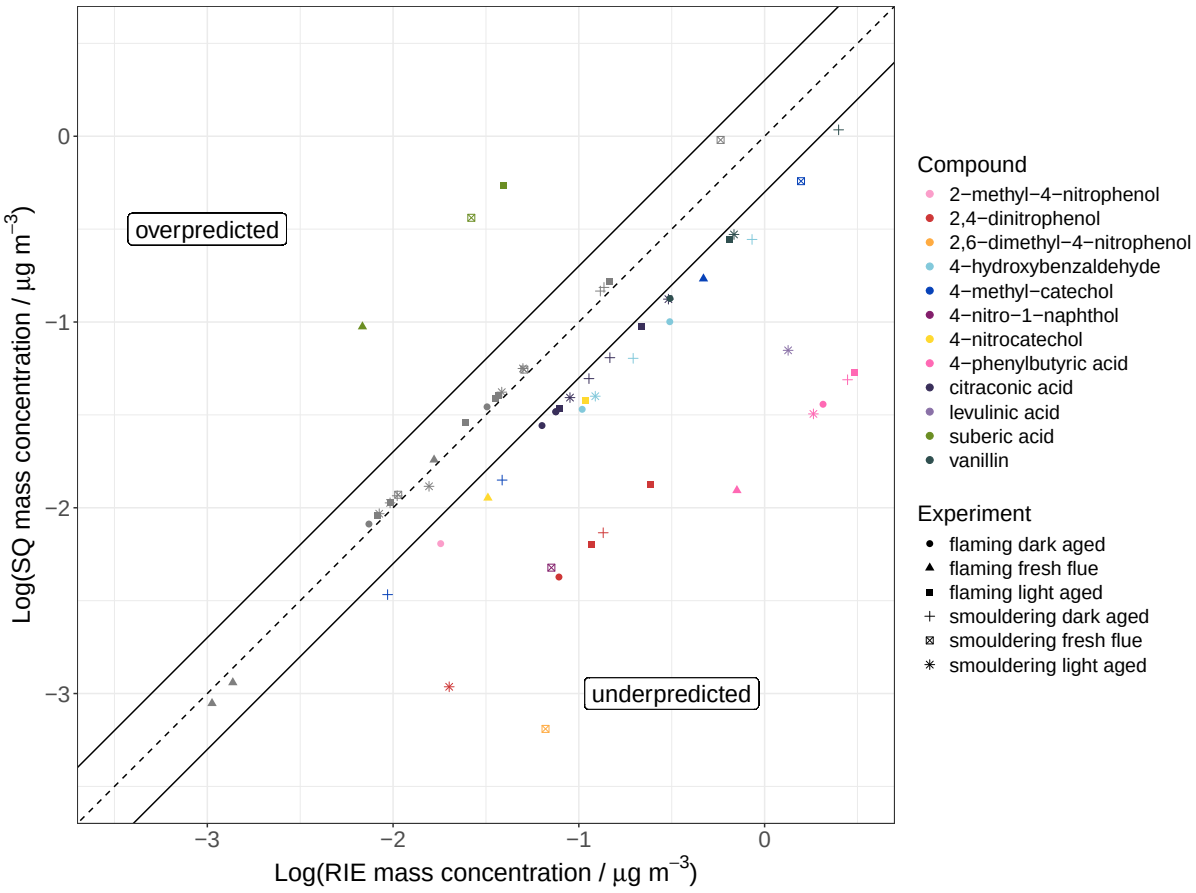

Figure 2.5: *Comparison of the estimated concentrations from the semi-quantification (SQ) method with the Bryant et al. [185] RIE model quantification for the 18 common identified compounds across both methods with different conditions shown by the marker type. 1:1 line is presented as a dashed line and factor of 2 lines are indicated by the solid lines. Compounds outside of the factor of 2 error range are presented in colour.*

ever, the RIE model developed by Bryant et al. [185] under represents nitroaromatic compounds in the training data leading to an underprediction of their RIE. However, the semi-quantification method used a similar number of nitroaromatic compounds to create the retention time windows and had a lower prediction error of 1.63 times for the same compounds compared to quantification by authentic standard. Furthermore, in the inter-laboratory study by Malm et al. [234] they observed semi-quantification using singular close eluting standards performed worse compared to RIE model approaches. Therefore, the semi-quantification approach developed here using multiple close eluting standards shows that choosing suitable retention time windows even

with a relatively small number of standards can be a more effective method to improve quantification, yielding similar or more accurate concentrations than predictive ionisation efficiency model approaches.

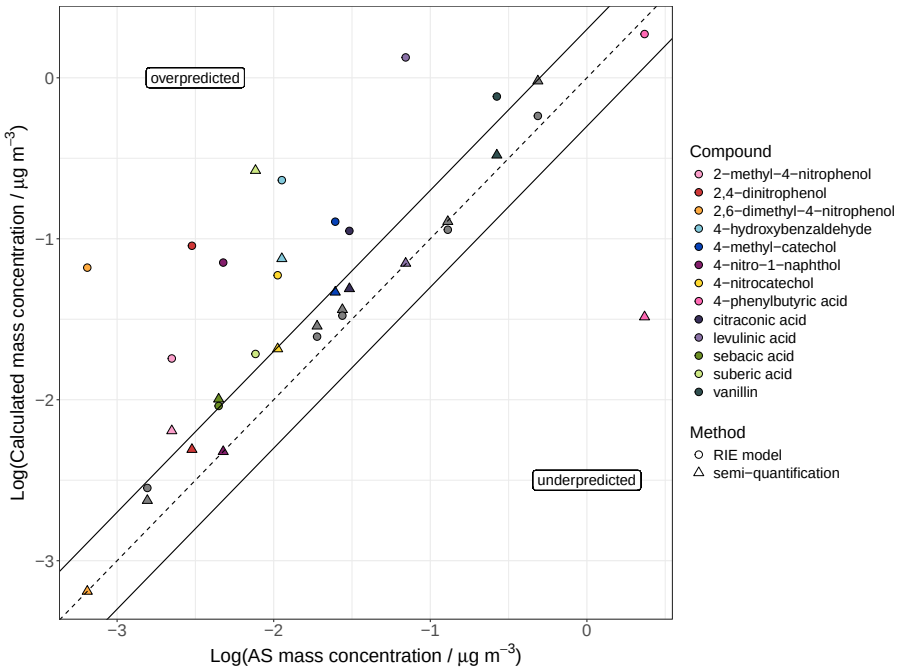

Figure 2.6: *Comparison of the semi-quantification (triangle markers) and RIE predictive model (circle markers) methodologies with authentic standard (AS) quantification (x-axis) for the 18 identified compounds, shown as average concentrations across all wood burning experiments, in the BBOA samples. 1:1 line is presented as a dashed line and factor of 2 lines are indicated by the solid lines. Compounds within a factor of 2 to the authentic standard concentration in both methods are shown as grey markers. Compounds which remain are greater than a factor of 2 from the AS concentration are presented in colour.*

2.3.5 Application of semi-quantification methodology to complex OA

The semi-quantitative non-target methodology was designed for use in highly chemically complex samples such as BBOA due to the sheer number and functionality of compounds present. The standards used in the methodology construction reflect what would be observed in a BBOA sample analysed in negative mode ESI. However, the general methodology framework of using multiple retention time windows with numerous chemically relevant standards is applicable to other chemically complex en-

vironmental and biological matrices and future research is encouraged in these fields. The chemical composition of BBOA is highly dependent on fuel type, burning conditions and atmospheric aging, as discussed in Chapter 3, resulting in a large variation and degree of chemical complexity [129, 135, 235]. Application of the semi-quantification method enabled distinct differences in the bulk composition to be observed between different burn phases and aging processes. In this example, the relative ratio of CHO:CHON contributions to the total OA mass were evaluated (Figure 2.7). In Figure 2.7 relative abundance was derived from the quantification of each compound using the median, lower quartile, upper quartile, maximum and minimum calibration gradient for their corresponding retention time window. The uncertainty of the method for estimating relative abundance was then derived from the interquartile range of abundance shown in Figure 2.7.

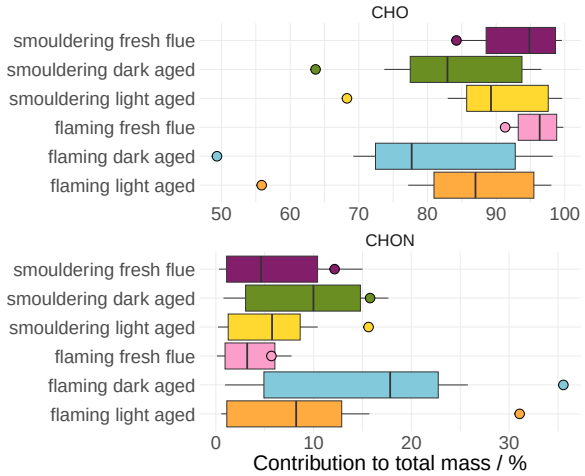

Figure 2.7: *Percentage contribution of CHO and CHON compounds to the total mass concentration in wood burning OA, coloured by different experimental conditions. The boxplot represents the relative abundance determined from quantification using the median, lower quartile, upper quartile, minimum and maximum calibration gradients for each compound in each retention time window. The circular points show the relative abundance derived when using peak area.*

Across the BBOA samples the average uncertainty in relative abundance, determined from the interquartile range in Figure 2.7, was on average 12.8 % and 10.2 % for CHO and CHON species respectively. Depending on the metric used to estimate abundance in NTA the overall compositional contributions can vary leading to differences in source apportionment. For instance, as shown in Figure 2.7, on average CHO compounds contribute 88.1 ± 7.1 % to the total mass using the semi-quantification

method or 68.8 ± 16.2 % of the total peak area. Therefore, using peak area to determine abundance underestimated the contribution of CHO species to the total BBOA mass by 19 ± 10 %. The compounds in the CHON group contribute 8.2 ± 5.2 % or 19.3 ± 11.5 % using semi-quantification and peak area respectively, resulting in an over-prediction of 11 ± 8% on average. Furthermore, the difference between the methods for estimating abundance can reach up to 31 % depending on the sample (Table 2.6) which has important implications for source apportionment studies using peak area.

Furthermore, CHON species from biomass burning have been largely assigned as nitroaromatic compounds and are widely used as tracers for biomass burning in ambient aerosol due to their conceived high abundance when using peak area metrics [172, 179] and important contribution to atmospheric brown carbon formation [60, 172, 236]. However, this study determined the average relative abundance of CHON to be 8.2 % which is lower than that estimated if using peak area suggesting peak area can significantly over estimate the contribution of CHON to BBOA. Instead, the semi-quantification method found a significant contribution of CHO (> 85 %) to BBOA, indicating CHO species could be important tracers of biomass burning. Furthermore, these differences in the estimation of relative abundance of each compound when using semi-quantificaton or peak area can be propagated into metrics commonly used to characterise OA composition and atmospheric oxidation in non-target studies such as the average molecular formula and oxygen:carbon ratios as shown in Table 2.6.

Table 2.6: *Comparison of the semi-quantification method and peak area to determine average weighted non-target OA metrics including: oxygen:carbon ratio (O:C), hydrogen:carbon ratio (H:C), molecular formula and relative abundance*

		Semi-quantification				Peak area			
Sample type	**Category**	**O:C**	**H:C**	**Formula**	**Relative abundance / %**	**O:C**	**H:C**	**Formula**	**Relative abundance / %**
Flaming fresh flue	CHO	0.28	1.05	$C_{12.8}H_{13.0}O_{3.3}$	96.4	0.33	1.09	$C_{11.4}H_{11.9}O_{3.3}$	91.3
Flaming dark aged	CHO	0.38	1.33	$C_{10.4}H_{13.8}O_{3.5}$	77.8	0.47	1.34	$C_{8.5}H_{11.1}O_{3.5}$	49.3
Flaming light aged	CHO	0.42	1.39	$C_{10.1}H_{14.6}O_{3.8}$	87.0	0.47	1.31	$C_{8.7}H_{11.6}O_{3.9}$	55.9
Smouldering fresh flue	CHO	0.35	1.04	$C_{10.6}H_{10.4}O_{3.3}$	94.9	0.40	1.09	$C_{9.6}H_{10.0}O_{3.5}$	84.2
Smouldering dark aged	CHO	0.45	1.45	$C_{9.4}H_{13.0}O_{3.6}$	83.0	0.50	1.44	$C_{8.4}H_{11.5}O_{3.7}$	63.7
Smouldering light aged	CHO	0.49	1.63	$C_{9.4}H_{15.4}O_{3.9}$	89.3	0.53	1.53	$C_{8.1}H_{12.3}O_{3.8}$	71.9
Flaming fresh flue	CHON	0.54	1.74	$C_{13.5}H_{23.1}O_{5.2}N_{1.6}$	3.2	0.47	1.44	$C_{11.5}H_{17.6}O_{4.6}N_{1.2}$	5.7
Flaming dark aged	CHON	0.32	1.43	$C_{14.6}H_{23.2}O_{4.2}N_{1.4}$	17.7	0.42	1.36	$C_{10.9}H_{16.6}O_{4.0}N_{1.3}$	35.6

Flaming light aged	CHON	0.41	1.25	$C_{11.2}H_{14.5}O_{4.3}N_{1.5}$	8.2	0.47	1.03	$C_{8.7}H_{9.5}O_{3.7}N_{1.3}$	32.1
Smouldering fresh flue	CHON	0.42	1.18	$C_{10.4}H_{12.3}O_{3.7}N_{1.3}$	4.6	0.47	1.05	$C_{8.8}H_{9.4}O_{3.8}N_{1.1}$	12.1
Smouldering dark aged	CHON	0.35	1.35	$C_{13.7}H_{18.6}O_{3.8}N_{2.1}$	9.9	0.39	1.30	$C_{11.3}H_{15.6}O_{3.8}N_{1.5}$	15.8
Smouldering light aged	CHON	0.46	1.39	$C_{11.1}H_{15.9}O_{4.7}N_{1.7}$	5.7	0.51	1.24	$C_{9.1}H_{12.0}O_{4.1}N_{1.4}$	15.6

2.4 Conclusions

A semi-quantification method to estimate concentrations of unidentified compounds was developed for NTA of complex OA analysed by UHPLC-HRMS. The method was created as an open-source workflow and the framework, as calibration gradients are instrument specific, can be applicable to other chemically complex matrices. The methodology used 25 retention time windows and a total of 110 authentic standards to derive unique scaling factors from multiple authentic standards for each defined window. The total quantification of chemical space is improved by quantifying both MS^1 and MS^2 features whereas existing predictive ionisation efficiency models require a known structure or access to MS^2 chemical fingerprints. The method was validated against 27 structurally identified species within a range of BBOA filter extracts with an overall average prediction error, defined as the ratio of concentration determined with the semi-quantification method to using an authentic standard, of 1.52. This improved upon previous semi-quantification methods using singular closely eluting quantification markers which yield errors up to one order of magnitude. Compared to a predictive ionisation efficiency model, the semi-quantification method demonstrated improved performance for the quantification of nitroaromatic species despite using a similar number authentic standards. Comparison of the semi-quantification method to peak area in a NTA workflow of complex OA highlighted the inadequacy of peak area weighted metrics. Differences in the relative abundance of different compound classes reached up to 31% between the two methods, representing a significant potential to misinterpret source apportionment contributions when using peak area. Future work is needed to fully comprehend matrix effects in highly complex samples. It would be beneficial to do a matrix analysis of all 110 standards used in the methodology to determine the impact of the sample matrix on the external calibration gradient and also apply the method to positive mode ionisation for complete quantification. An important feature of the methodology for use in the wider analytical chemistry community is the ability for independent usage or combined usage with existing predictive ionisation efficiency models to create a robust NTA quantitative workflow of all (MS^1 and MS^2) detected features for application in complex samples. Overall, the newly developed methodology highlights the need to standardise non-target quantification

metrics, especially for OA applications.

Chapter 3

Impact of combustion conditions and atmospheric aging on the composition of BBOA

3.1 Introduction

Biomass burning (BB) encompasses a range of combustion processes such as wildfires, agricultural burning, and domestic combustion of solid fuels or referred to herein, domestic BB. Biomass burning is one of the largest sources of organic aerosol (OA) and trace gases to the atmosphere, emitting approximately 62 Tg yr^{-1}, 77 Tg yr^{-1} and 19 Tg yr^{-1} of volatile organic compounds (VOCs), particulate matter less than 2.5 μm in diameter ($PM_{2.5}$) and nitrogen oxides (NO_x) respectively to the atmosphere [104]. Biomass burning VOCs (BBVOCs) can oxidise in the atmosphere leading to the production of secondary organic aerosol (SOA) which is a major component of $PM_{2.5}$. Approximately 2 billion people globally use solid fuels for heating and cooking [123] and annually solid fuel combustion causes 3.2 million premature deaths [124]. Especially in the UK, wood burning is a growing issue, with approximately 8 % of the population burning wood indoors but of that only 4 % for necessity [14] and in London solid fuel emissions comprised approximately 7-9 % of total $PM_{2.5}$ during 2022 [237]. Furthermore, Allan et al. [238] observed in London emissions from solid fuels comprised approximately 26 % of the total primary OA (POA) during cold weather conditions. Therefore, there is a need to understand the emissions from stoves in order to improve

future air quality policy given that emissions from wood burning are highly dependent on combustion conditions, the fuel burnt, and the stove appliance used [239].

A full burn cycle consists of multiple stages *i)* ignition, *ii)* flaming combustion and *iii)* smouldering combustion [125]. During flaming the lignocellulosic biomass is partially or completely burned and char is produced, typically occurring at high temperatures. Whereas smouldering occurs during the latter stages of the burn cycle at lower temperatures, starting once all the combustible volatile fuel is consumed and the oxidation of char begins [125]. Due to these unique conditions a characteristic mixture of VOC emissions arises at each stage from temperature dependent pyrolysis mechanisms at varying abundances [125, 141, 240, 241]. For instance, Czech et al. [240] observed the greatest emissions from the ignition phase followed by ember (smouldering) and stable burn (flaming) phases. Previously the change in emissions between burn phase was identified using positive matrix factorisation (PMF) which separated BBVOC emissions into two factors; low and high temperature combustion. Low temperature combustion contained more oxygenated aromatics and furanic compounds in agreement with particle phases enriched in oxygenated organic compounds from smouldering combustion [127, 129]. In contrast, BBVOCs from high temperature combustion consisted of polyaromatic hydrocarbons (PAHs), terpenes and aliphatic unsaturated hydrocarbons [127, 135].

Ultra-high-performance liquid chromatography coupled to electrospray ionisation high-resolution mass spectrometry (UHPLC-ESI-HRMS) is a valuable technique for studying the composition of OA enabling the detection of thousands of compounds and separation of isomeric species. Various tracer species from biomass burning OA (BBOA) have been previously identified using UHPLC-HRMS [116, 142, 143, 179, 242–247], but most commonly consisted of levoglucosan and nitroaromatic compounds (NACs) [116–119, 142, 242, 248]. Biomass burning plumes are ideal conditions for NAC formation due to high emissions of NO_x and aromatic VOCs from lignin degradation which is primarily comprised of 3 aromatic alcohol units; coumaryl, sinapyl and coniferyl alcohol [249]. In particular NACs such as nitrophenols are widely adopted as tracers due to strong correlations with levoglucosan [117, 250, 251] and depending on the fuel type emission factors range between 1.4 - 31 mg kg^{-1} [116, 117, 242, 243]. These compounds also have important climatic impacts by contributing to brown car-

bon (BrC) hence their extensive study in the wider literature [60, 172, 252–254]. However, by selecting a small number of compounds to analyse, limited compositional information can be obtained by targeted approaches, for instance, Pereira et al. [169] estimated only 1.1 % of the mass of an ambient OA filter could be quantified via a targeted approach using 60 authentic standards.

Non-target analysis (NTA) can overcome these limitations by enabling chemical information, such as molecular formula, of all detected analytes within a complex mass spectral output to be rapidly obtained. For example, NTA enabled the identification of 190 NACs in $PM_{2.5}$ from Beijing, with a third attributed to biomass burning [173]. Furthermore, species associated with lignin pyrolysis such as vanillin, coniferaldehyde and benzoic acid and sugars including levoglucosan, sucrose and fructose from cellulose degradation were previously identified in BBOA via NTA approaches [189, 246, 255]. However, due to the lack of commercially available authentic standards many previous NTA studies used limited metrics such as number of molecular formulas or peak area to estimate relative abundance [eg., 169, 172, 178–180, 186, 189]. The lack of standardised metrics to estimate abundance can lead to differences in inferred composition. Using peak area, Wang et al. [172] and Brege et al. [179] observed a large quantity of organonitrogen compounds (CHON) in OA during periods influenced by biomass burning, which were attributed to NACs. In contrast, using the number of formulas showed a greater contribution of oxygenated organic compounds (CHO) in BBOA [178, 180, 189]. For example, at the Pico Mountain Observatory in the North Atlantic, analysis of $PM_{2.5}$ samples showed CHO compounds accounted for 70 % of the molecular assignments in air masses influenced by wildfires [178] and Smith et al. [189] observed CHO compounds represented 80-90 % of all detected mass spectral features in BBOA.

Whilst the number of formulas can provide some information on sample complexity it is not quantitative for concentration and although peak area is often considered as quantitative neither of these approaches accounts for differences in ionisation efficiency (IE) between different species. As mentioned in Chapter 2 IE is a measure of the ability of a species to ionise within an ESI source and is highly structural specific. The quantification of unidentified compounds is challenging and previous approaches shown in Chapter 2 have relied on predicting ionisation efficiency from known struc-

tures or chemical fingerprints limiting the analysis to compounds with MS^2 spectra. This is an issue in the widely used data-dependent acquisition (DDA) MS^2 mode where only a certain number of species are selected for fragmentation in each scan and inevitably some compositional information is lost by only considering these species. For example, in the NTA workflow of winter $PM_{2.5}$ from Beijing Wang et al. [146] observed only 39 % of detected compounds had MS^2 spectra using DDA. Alternatively for quantification of all detected analytes semi-quantification approaches, as in Chapter 2, can be adopted which historically used a singular structurally similar surrogate standard to quantify unknowns [183, 184, 203, 205, 213]. However, as shown in Chapter 2 using multiple surrogate standards eluting within a short retention time can yield lower quantification errors than previous semi-quantification methods.

The work presented in this chapter outlines the quantified results, using the Chapter 2 methodology, from the chamber experiments conducted at the Manchester Aerosol Chamber (MAC) to investigate the effect of combustion conditions and aging on the chemical composition of BBOA. Overall this work, at the time of writing, is the first molecular level semi-quantitative NTA of domestic BBOA. The findings presented in this Chapter indicate oxygenated aromatics as important contributors to POA and a significant source of reactivity upon aging with burn dependent oxidation and loss. These differences in composition and oxidation were concluded to have important implications for toxicity, air quality and climate.

3.2 Methodology

3.2.1 Controlled burn chamber experiments

3.2.1.1 Experimental design

Controlled burn chamber experiments were conducted over two campaigns during April 2022 and September 2022 at the Manchester Aerosol Chamber (MAC) located at the University of Manchester, UK. The experiments aimed to investigate the aerosol composition under different burning conditions (April) and fuel types (September). $PM_{2.5}$ filter samples were taken for detailed offline composition analysis and a large suite of online instrumentation measured aerosol composition, aerosol physical prop-

erties and trace gases, including carbon monoxide (CO), carbon dioxide (CO_2), ozone (O_3) and NO_x. The MAC has previously been described in detail elsewhere [214]. However, breifly the MAC consists of an enclosed and suspended 18 m^3 fluorinated ethylene Teflon bag supported by 3 rectangular aluminium frames, where the outer frames move freely allowing the bag to expand or contract when filling or emptying the chamber. The chamber was illuminated using two 6 kw xenon arc lamps with quartz fibre glass filters and 4 rows of halogen lamps (64 bulbs) to simulate atmospheric solar wavelengths, which enables the photolysis of NO_2 to produce O_3. O_3 is then subsequently photolysed in the presence of water molecules to produce hydroxyl radicals (OH) [214, 256, 257]. Heterogeneous wall chemistry will also produce nitrous acid (HONO), which is photolysed to yield OH and NO. The OH concentration inside the MAC has been previously calculated as ca. $1{\times}10^6$ molecules cm^{-3} [256, 258] at similar NO_x concentrations to these experiments. Purified dry air was supplied to the chamber by passing laboratory air through a 3-phase blower and 3 filters comprising *i)* purafil/charcoal mixture, *ii)* charcoal and *iii)* HEPA. The chamber had automated fill/flush cycles before and after experiments, detailed in Shao et al. [214], to reduce the chamber background signal and was cleaned overnight with high concentrations of O_3 ($\approx$ 1 ppm) to oxidise any residual species. A harsher cleaning programme was performed once a week by illuminating the chamber for 4-5 hours under high O_3 concentrations ($\approx$ 1 ppm). During the controlled burn campaigns multiple background experiments were conducted whereby a clean chamber, i.e. no added smoke from the stove, was irradiated with light for 6 hours. After this time, a filter sample was collected of the chamber air via the flush line at approximately 3 m^3 min^{-1} for 4 minutes.

For the controlled burn experiments, hardwood (Beech), which typically provides more heat and burn for longer than softwood, was burnt in a Ecodesign stove (Esse Model 175 F) to represent a typical domestic fuel in the UK. The emissions from the burn were sampled during flaming or smouldering phases. However, given the nature of a burn which will be composed of both flaming and smouldering processes it is difficult to separate distinct phases therefore the burns are referred to herein as "flaming dominated" and "smouldering dominated". The catalytic filter within the stove, which would enable the "particulate reburn" technology to reduce particulate emissions beyond that of the UK Ecodesign requirements, was removed to replicate more

conventional stoves in the UK market. A filter of the POA was taken from the flue of the wood burner at 2 L min^{-1} for 5 minutes for offline chemical composition analysis. The wood smoke from the flue derived from either smouldering or flaming dominated phases (2 L min^{-1}) was then diluted with a flow of compressed air (2 L min^{-1}) before injection into the chamber using an eDiluter (eDiluter Pro, Dekati, Finland). The smouldering dominated phase was controlled by allowing the wood to be consumed by flames and subsequently closing the stove ventilation to reduce the presence of oxygen in the stove. Injection into the chamber started when there was a lack of visible flames. No additional reactants were injected into the chamber. The injection of the smoke proceeded until the total particle mass concentration measured in the chamber was twice the target concentration at half the chamber volume. Then the final addition of scrubbed particle free air into the bag achieved the target concentration of around 200 μg m^{-3} at full chamber volume. Due to the relatively low particle concentration of 200 μg m^{-3} inside the chamber the fresh aerosol was sampled directly from the flue of the wood burner to yield sufficient mass for offline chemical composition analysis rather than from the chamber itself. Following injection, 40-60 minutes of background data was collected to allow instrumentation with long cycle times to obtain several cycles of data. After this period the chamber was irradiated to produce OH radicals for photo-oxidation. The relative humidity throughout the experiment was controlled between 50-60 % and the temperature inside the chamber was kept around 25 °C. The smoke was aged for approximately 6 hours before sampling the chamber via the flush line for 4 minutes to collect the aged aerosol onto a pre-baked Quartz filter for offline chemical composition analysis. The exact flow rate of the vacuum line for collection was not directly measured however the MAC can be entirely flushed from full in approximately 6 minutes therefore the flow rate is approximated as 3 m^3 min^{-1} [214]. After collection the filters were wrapped in the pre-baked foil, transported on ice to the University of York and finally stored at -20 °C before UHPLC-HRMS analysis.

Each aging experiment was repeated once resulting in two sample types per burn phase, fresh and light aged, with one filter for the fresh emissions and two filters for the aged experiments. However, one smouldering aging repeat was observed to contain significant flaming character such that neither phase dominated the emissions as the burn could be described by both high CO_2 concentrations associated with flam-

ing leading to a high modified combustion efficiency (MCE) of 0.95 and high ratios of organic carbon:black carbon (OC:BC) associated with smouldering. The experiments, their sample ID referred to in this chapter, initial concentrations of gas and particle phase species before aging and MCE are presented in Table 3.1.

Table 3.1: *List of the OA samples used in this study and the initial conditions at the start of the aging period, The asterisk (*) denotes OC refers to the total organic content measured by AMS*

Date of experiment	Conditions	Sample ID	Aging time / hrs	PM / μg m^{-3}	OA / μg m^{-3}	NO_x / ppb	OC:BC*	MCE
21/04/2022	Flaming light aged	FL_AGED_1	5:50	243.6	7.7	100.8	0.32	0.96
26/04/2022	Smouldering light aged	SM_AGED	6:05	213.6	102.5	11.21	406.3	0.78
28/04/2022	Flaming light aged	FL_AGED_2	6:05	153.4	5.4	41.4	0.21	0.93
30/08/2022	Flaming fresh flue	FL_FRESH	-	-	-	-	-	-
31/08/2022	Smouldering fresh flue	SM_FRESH	-	-	-	-	-	-
20/04/2024	Intermediate light aged	IM_AGED	6:07	169.8	75.4	42.1	21.94	0.95

For the flaming and smouldering dominated burns described in the remainder of the Chapter the MCE values are in the normal range for each burn phase. Note that fresh aerosol samples were taken from the September campaign as the April campaign only sampled aerosol from the chamber. A preliminary analysis of aging experiments of the same Beech wood combustion in the September campaign showed the same overarching trends in composition that are concluded in this Chapter for the April aging experiments. The September experiments weren't used in the remainder of this analysis due to a lack of supporting CO_2 measurements inside the chamber. Therefore, despite fresh sampling occurring on a different day to the aging experiments the burns across the campaigns were determined to be repeatable and the conclusions drawn remain valid. Due to the fresh sampling at the flue there is likely some evaporative

losses once inside the chamber and future work should aim to sample both fresh and aged emissions from the chamber to account for this. Atmospheric aging is therefore defined in this Chapter as all oxidation, dilution and evaporation processes as would occur in the ambient after a smoke plume is emitted.

3.2.1.2 Online aerosol measurements

The experiments used a variety of online instrumentation to monitor the evolving aerosol and gaseous composition throughout the photo-oxidation of the wood burning smoke inside the MAC. Non-refractory PM_1 (particulate matter less than 1 μm in diameter) composition was measured via a high-resolution-time-of-flight aerosol mass spectrometer (HR-ToF-AMS) enabling real-time measurements of ammonium (NH_4^+), nitrate (NO_3^-), chloride (Cl^-), sulfate (SO_4^{2-}) and the organic fraction. The extent of oxidation could be monitored using the fraction of the *m/z* 44 fragment (CO_2^+) compared to the total organic fraction (f_{44}) with higher f_{44} levels associated with more oxygenated organic aerosol. Whilst the signal at *m/z* 60 ($C_4H_2O_2^+$) has been associated as a fragment from biomass burning tracers such as levoglucosan and other structurally similar sugars [156]. Therefore, the degradation of the wood smoke throughout photo-oxidation was also monitored using the fraction of *m/z* 60 to the total organic fraction (f_{60}). Detailed composition measurements of organic gas and particulate phase species were obtained from a Filter Inlet for Gases and AEROsols coupled to an Iodide Chemical Ionisation Mass Spectrometer (FIGAERO-I-CIMS). However, for the April campaign the FIGAERO-I-CIMS was operated in an offline mode for filter analysis at a later date due to technical issues during the campaign and the data processing of this is ongoing at the time of writing. Additionally, particle concentrations were measured using a Scanning Mobility Particle Sizer (SMPS) across a size range of 10-700 nm and measurements of black carbon (BC) mass and coating thickness were obtained from a Single Particle Soot Photometer (SP2).

3.2.1.3 Non-Target Ultra-High-Performance Liquid Chromatography High Resolution Mass Spectrometry

As in Chapter 2 the filters were extracted based on the method used in Bryant et al. [144]. The 47 mm quartz filters were cut into 1 cm^2 pieces, placed in a 20 mL glass

vial and 10 mL of methanol (LC-MS Optima Grade) was added. For fresh aerosol samples half a 47mm filter was used due to the higher aerosol mass loading. The resulting 10 mL solution was sonicated for 45 minutes, using ice packs to lower the temperature of the water bath. The methanol extract was transferred to a second 20 mL glass vial using a 0.22 μm syringe filter (Milipore) then dried using a Genevac vacuum solvent evaporator. The sample was reconstituted in 200 μL 90:10 H_2O (LC-MS Optima Grade): MeOH (LC-MS Optima Grade) for UHPLC-HRMS analysis.

The offline filters were characterised at the University of York using an Ultimate 3000 UHPLC (Thermo Scientific, USA) coupled to a Q Exactive Orbitrap MS (Thermo Fisher Scientific, USA) with heated electrospray ionisation (HESI) enabling high resolution and detailed chemical information to be obtained. Compound separation was achieved using a reversed phase C_{18} 2.6 μm × 2.1 mm × 10 mm Accucore column held at 40 °C. The mobile phase consisted of 0.1 % (v/v %) formic acid (Acros Organics) in water (A, LC-MS Optima Grade) and methanol (B, LC-MS Optima Grade). A gradient elution was used, starting at 90 % (A) with a 1 minute post injection hold, decreasing to 10 % (A) at 26 minutes before returning to the starting conditions at 28 minutes. A final 2 minute hold at 10 % (A) allowed the column to re-equilibrate. The flow rate was set to 0.3 mL $min^{-1}$and prior to analysis samples were stored in an autosampler tray at 4 °C. The injection volume was set to 4 μL, however injection volumes up to 10 μL were used for lower concentration samples. The HESI was operated under the following conditions: a spray voltage of 4 kV, a capillary and auxiliary gas temperature of 320 °C, a sheath gas flow rate of 45 (arb.) and an auxiliary gas flow rate of 10 (arb.) Spectra were acquired in negative and positive mode using data dependent aquisition (ddMS^2). However, this Chapter considers only negative mode analysis due to the creation of the semi-quantification method in negative mode. The scan range was set to a mass-to-charge ratio (m/z) of 85 to 750, with a mass resolution of 140,000. Tandem mass spectrometry was performed using a higher collision dissociation with a stepped normalised collision energy of 10, 20 and 45. In each scan the 10 most abundant species were selected for MS^2 fragmentation. The wood burning samples were analysed once with solvent blanks and chamber blanks analysed at the start of the sequence for blank subtraction in post-processing. Spectra were acquired from XCalibur 4.3 (Thermo Scientific, USA) and analysed using the semi-quantitative non-target

workflow developed in Chapter 2.

3.3 Results

3.3.1 Insights into the oxidation of organic aerosol from online measurements

Emissions from domestic BB under different burning conditions, i.e. flaming dominated or smouldering dominated phases, were photo-oxidised inside the MAC to observe the impact of atmospheric aging on the chemical composition of domestic BBOA. The particulate emissions from flaming dominated or smouldering dominated burn phases indicated that flaming is primarily formed of BC whereas smouldering is largely comprised of OC (Table 3.1) which could impact the particle morphology [259] and thereby the aging of OA. The photo-oxidation of domestic BBOA was monitored in real time with an AMS to gain insight into the evolving organic fraction of non refractory PM_1 alongside instrumentation to measure the concentrations of trace gases such as nitrogen oxides (NO_x = NO + NO_2). Generally due to particle wall loss in the MAC [214] the OA concentration for both flaming and smouldering experiments decreased over time, therefore, alternative metrics were used to trace oxidative processes. Figure 3.1a shows the relationship between f_{44}, representing oxidised components, and f_{60}, indicative of the levoglucosan-like species typically used as tracers of BB, over the course of the experiment and generally exhibits a negative trend of f_{60} with increasing f_{44}. This trend therefore indicates the components of the fresh BB emissions are undergoing various aging processes, due to the reduction in f_{60}, including chemical oxidation to form more oxidised species as indicated by the increase in f_{44}. Furthermore, for flaming the ratio of the organic fraction in the AMS to BC denoted here as OC:BC increased upon aging indicating the formation of SOA, whereas, for smouldering OC:BC decreased suggesting an overall loss of OA upon aging and different aging processes to that of flaming burn phases [260]. The negative correlation with f_{60} shown in Figure 3.1a varies between the emissions from flaming and smouldering dominated experiments further indicating the composition and atmospheric aging of OA is impacted by the burning conditions. This was similarly observed in a study investigating

solid fuel emissions in London which associated two factors derived by PMF with two distinct f_{44} and f_{60} spaces arising from differences in burning phase or fuel type [261]. The increase in f_{44} ranges between 0.065 - 0.08 depending on the burn phase which is similar to the increase in f_{44} observed by Brege et al. [179] (+0.055) between fresh and aged ambient BBOA. For the flaming dominated emissions the reduction in f_{60} is considerably less (-0.0006-0.0013) than the smouldering dominated phase (-0.025). This could be a result of reduced levoglucosan emissions during the flaming phase [262, 263]. The observed range of f_{44} and f_{60} values in Figure 3.1a are in agreement with previous BBOA studies [156, 264, 265] which are typically situated within the triangular bounds of f_{44} (0.05-0.25) vs f_{60} (0.01-0.04) observed by Cubison et al. [156]. Overall these results indicate the oxidation of POA from fresh domestic BB emissions to form oxidised POA (oPOA) and SOA as these components are indistinguishable with respect to f_{44} and f_{60} [266]. Multiple aging processes such as the evaporation of semi-volatile species, condensation of oxidised vapours and the photochemical formation of SOA could contribute to the increased f_{44} in the aged OA.

The concentration of NO_x was greater from the flaming dominated emissions compared to the smouldering dominated phase as shown in Figure 3.1b which is as expected and in agreement with previous flaming phase observations [104, 125, 126, 267]. The ratio of NO:NO_2 was used to infer the photochemical conversion of NO to NO_2 (Figure 3.1c) indicative of the oxidation of VOCs, which results in the production of secondary species such as O_3 and SOA. NO:NO_2 ratios were initially higher under the flaming dominated conditions compared to smouldering dominated emissions which is consistent with NO as the end product of nitrogen oxidation at higher temperatures [268] and flaming as a more efficient burn phase. In the smouldering phase, NO_2 emission can account for up to 40 % of the total NO_x [268] resulting in a lower NO:NO_2 ratio which is in agreement with the observed NO_2 contribution (36 %) to the total initial NO_x during the smouldering dominated phase in this study. After aging the NO:NO_2 ratios in both burn phases converge to a steady state (≈ 0.2) in Figure 3.1c as NO is photochemically converted to NO_2, through the reaction with peroxy radicals formed from BBVOC oxidation. Ambient BB plumes report NO:NO_2 ratios up to 3-5 [269, 270] which are greater than those presented in Table 3.1 suggesting an increased proportion of NO_2 in this work. This was observed in a previous chamber study and

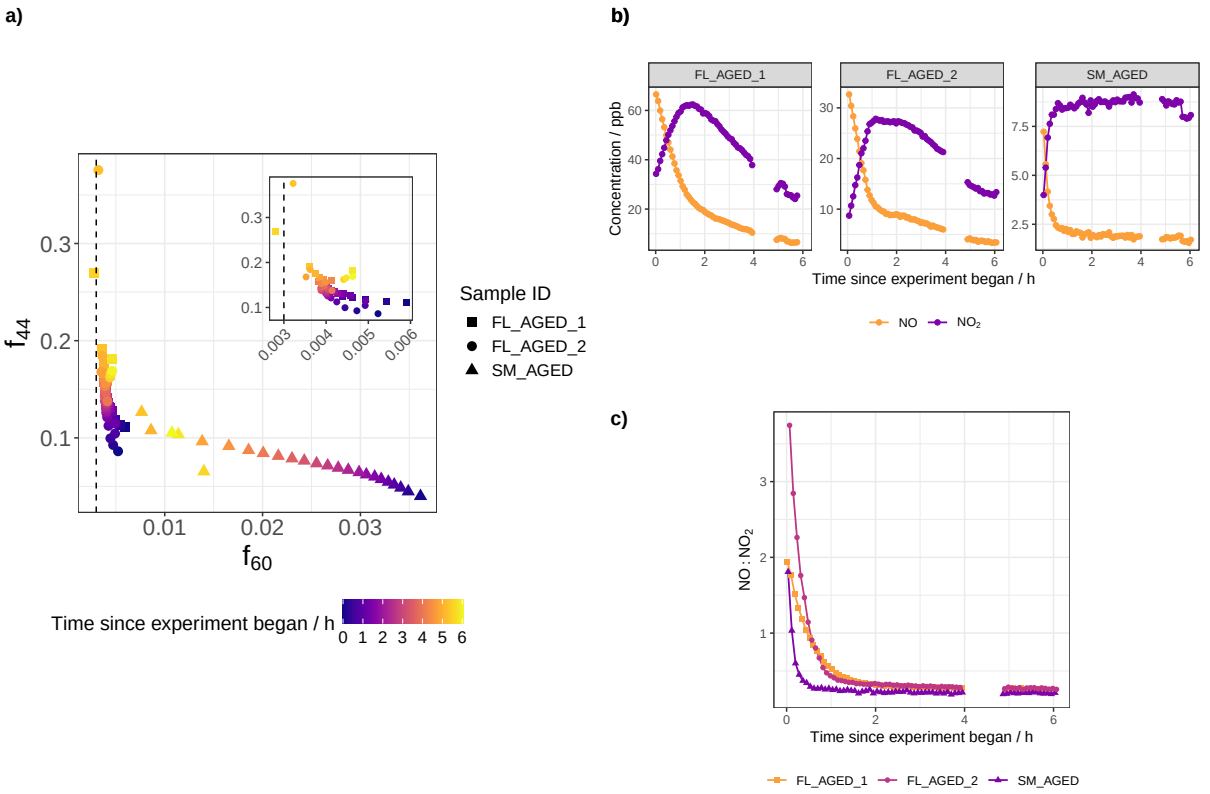

Figure 3.1: *a) Timeseries of f_{44} vs f_{60} for flaming dominated and smouldering dominated burn phases, averaged to 15 minute intervals. The inset plot displays the zoomed in flaming data. The vertical dashed line at $f_{60} \approx 0.3$ % represents non biomass burning influenced OA b) NO_x timeseries averaged to 5 minute intervals, data gaps indicate interference due to filter sampling. c) NO:NO_2 timeseries during aging experiments averaged to 5 minute intervals.*

attributed to the presence of O_3 within a dark chamber [271]. However, due to interference from conjugated VOCs the concentrations of O_3 inside the chamber cannot be accurately quantified from the absorption measurement technique used at the MAC.

3.3.2 Non-target analysis of organic aerosol derived from different burn phases

The NTA methodology described in Chapter 2 enables large quantities of chemical information to be obtained and quantified for all detected compounds, including those with unknown structural identities. The OA was predominantly comprised of CHO compounds, on average contributing 90 % to the total detected mass across the studied experiments in this Chapter with a general increase in the contribution of CHON species to the total mass after aging. The NTA molecular formula assignments were

used to investigate the composition of domestic BBOA derived from domestic BB emissions via carbon number, oxygen number, double bond equivalents (DBE) (Eq. 3.1) and aromaticity index (AI) distributions [272] (Eq. 3.2 -3.4). Using the AI, aromatic species are determined as having an AI value greater than 0.5 otherwise they are considered non-aromatic (aliphatics), furthermore, monoaromatics are classified in the range of 0.5-0.67 and polyaromatics ≥ 0.67. The DBE metric provides an insight into the number of unsaturated bonds or functionalities within a compound which coupled to the carbon number or oxygen can provide information on the structure of a species.

$$DBE = 1 + C - \frac{H}{2} + \frac{N}{2} \tag{3.1}$$

$$DBE_{\mathrm{AI}} = 1 + C - \frac{O}{2} - S - \frac{H}{2} - \frac{N}{2} \tag{3.2}$$

$$C_{\mathrm{AI}} = C - \frac{O}{2} - S - N \tag{3.3}$$

$$AI = \frac{DBE_{\mathrm{AI}}}{C_{\mathrm{AI}}} \tag{3.4}$$

3.3.2.1 Chemical composition of organic aerosol derived from flaming dominated emissions

In POA from flaming emissions, CHO compounds have two main regions of high abundance between C_8-C_{11} and between C_{13}-C_{17} as shown in Figure 3.2a. In the first region the DBE ranges between 4-7 (Figure 3.2a) which is indicative of aromatic species which typically possess a DBE of 4 or more. The presence of DBE values greater than 4 coupled with $>C_6$ suggests these CHO species could be functionalised monoaromatics or small oxygenated polyaromatic species, for instance, napthalene-like species (C_{10}) which comprise two fused aromatic rings. Using the aromaticity index [272] (Eq.3.2-3.4) to classify species as non-aromatic, monoaromatic or polyaromatic, 51 % and 6 % of the detected CHO mass was monoaromatic and polyaromatic respectively. Between C_8-C_{11} the AI suggests approximately 42 % of the mass in this region as monoaromatic in nature (Figure 3.3a). This coupled with $> C_6$ strongly indicates the presence of functionalised monoaromatics in the first region, such as, phenoxyacetic acid ($C_8H_8O_3$) and phenyl acetic acid ($C_8H_8O_2$) which were identified using authentic standards. In the second region of high abundance between C_{13}-C_{17} the DBE has a larger range of 6-12 (Figure 3.2a). From Figure 3.2 and Figure 3.3a, the second region at C_{13}-C_{17} contains

DBE values which are generally double that of the first region and the AI suggests that the mass in this region is predominantly monoaromatic in nature (65 %). This suggests these compounds contain two aromatic rings linked via short sections of C-H and C=O bonds reflecting the structure of the biomass polymer lignin. Figure 3.3a also shows a small contribution of polyaromatic compounds in the C_{13}-C_{17} region, with a relative contribution of 10 % on average. This is in accordance with observations of PAH emissions in previous studies from flaming combustion [127, 135, 273], however, it is clear for this study monoaromatics are of greater quantity in fresh emissions. In a NTA of ambient BBOA, Brege et al. [179] observed a peak in relative abundance of CHO species at C_{15} - C_{16} which was attributed to terpene SOA products. However, in Figure 3.2 there is no evidence of sesquiterpene ($C_{15}H_{24}$) derived SOA products which would have relatively low DBE values. Liang et al. [274] previously observed chamber studies often underrepresent BB terpene sources due to the lack of distillation from nearby heated and unburnt vegetation. Given that domestic BBOA is the combustion of non-living material, terpene derived SOA products could be more important in ambient BBOA from wildfires or crop burning in the presence of live vegetation.

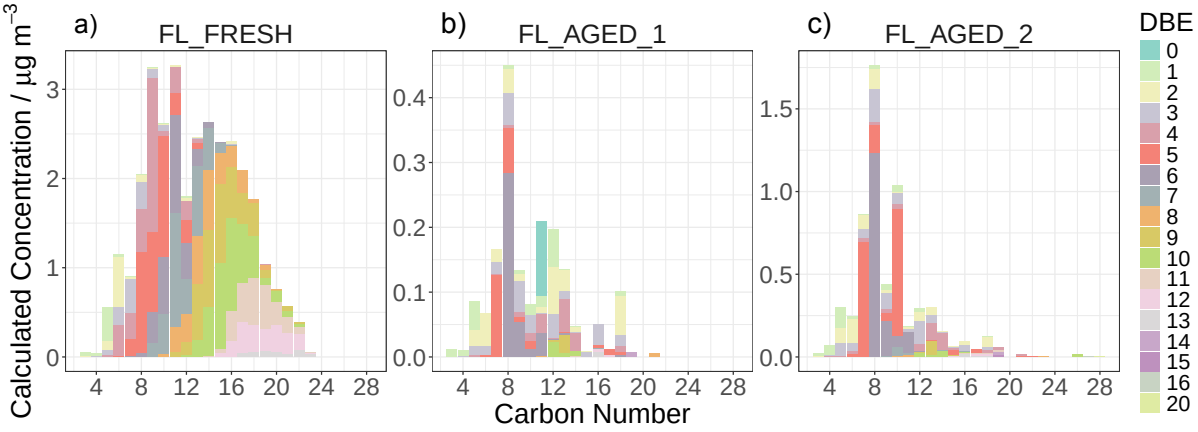

Figure 3.2: *Carbon number vs concentration distribution coloured by the DBE of CHO compounds present in the POA from fresh emissions from flaming dominated burning conditions and after aging (POA+oPOA+SOA). The different filter sample IDs from the flaming dominated combustion experiments are given in each panel*

After photo-oxidation inside the chamber, the CHO carbon distribution is shifted to lower carbon number species (C_7-C_{10}) indicating the fragmentation of the larger

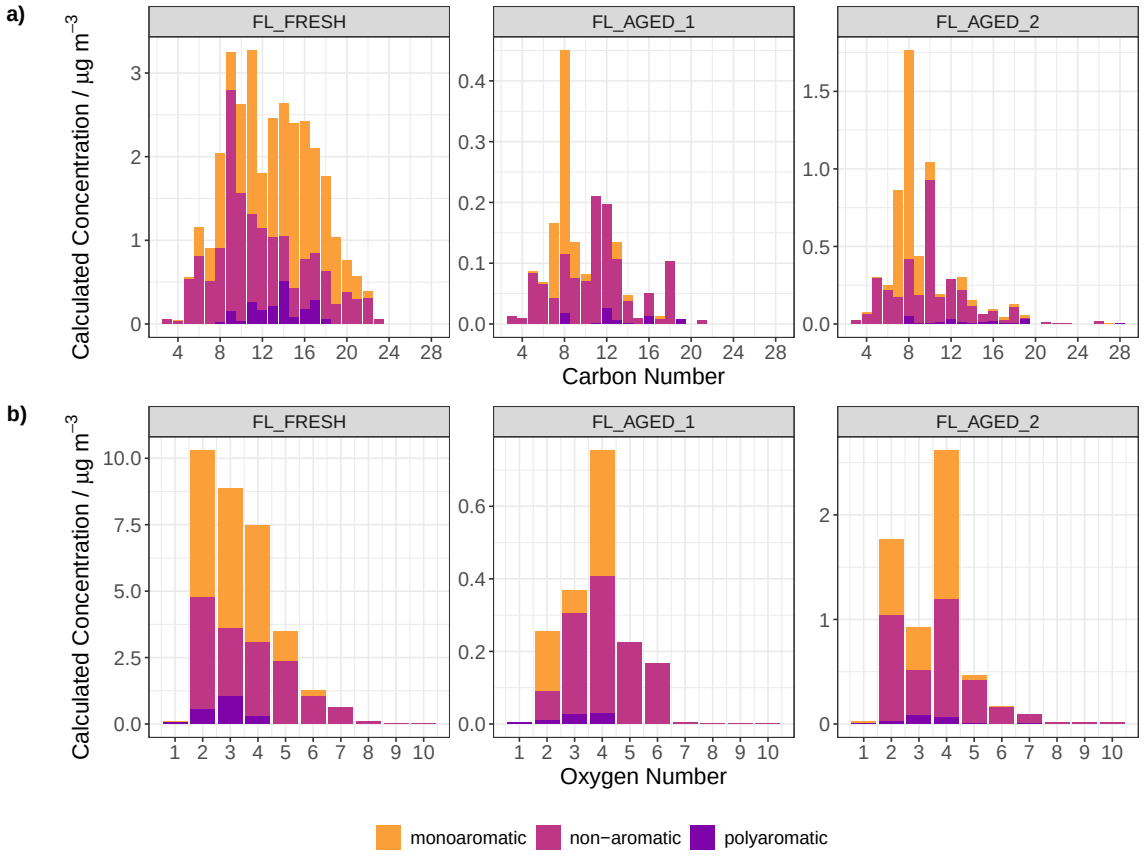

Figure 3.3: *a) Carbon number vs concentration distribution coloured by the AI estimations of CHO compounds in the POA of fresh emissions from flaming dominated burn phase and after aging (POA+oPOA+SOA). Different experiments are given in each panel. b) Oxygen number vs concentration distribution with the same design aesthetics as Figure 3.3a*

species with aging (Figure 3.2b-c). At the same time the main peak in the oxygen distribution increases from $C_xH_yO_2$ to $C_xH_yO_4$ indicating more oxidised CHO compounds in the aged aerosol (Figure 3.3b). Li et al. [235] suggested the higher NO_x concentrations from flaming emissions could promote fragmentation pathways through the reactions of peroxy radicals (RO_2 + HO_2) with NO. However, other processes such as photolysis and heterogeneous photo-oxidation may also result in the production of small molecules. The aged C_7-C_{10} CHO compounds possess DBEs in the range of 2-6 indicating some formation of non-aromatic compounds. However, using the AI, after atmospheric aging the CHO composition of the OA from flaming dominated emissions still contained a large degree of aromatic character (41 %). The largest peak in the aged distributions in Figure 3.2b-c at C_8 has a DBE value of 6 and is predominantly monoaromatic in nature (Figure 3.3a). The mass of this peak is dominated by $C_8H_6O_4$

which can be attributed to phthalic acid from previous observations [275, 276] and $C_8H_8O_3$ was confirmed as vanillin using an authentic standard.

For the CHON species, POA from flaming emissions has a main peak in the carbon number distribution at C_6 (Figure 3.4) and approximately 74 % of the detected CHON mass in fresh OA has an O:N ratio ≥ 3 suggesting the presence of a nitro (-NO_2) group. Using a modified AI calculation derived for this work to account for the presence of the two N-O bonds within a -NO_2 group (Eq. 3.5-3.7), 42 % of the detected CHON mass is aromatic in nature.

$$DBE_{\mathrm{AI}} = 1 + C - \frac{O-2}{2} - S - \frac{H}{2} - \frac{N-1}{2} \tag{3.5}$$

$$C_{\mathrm{AI}} = C - \frac{O-2}{2} - S - (N-1) \tag{3.6}$$

$$AI = \frac{DBE_{\mathrm{AI}}}{C_{\mathrm{AI}}} \tag{3.7}$$

As shown in Figure 3.4 the aromatic mass is predominantly comprised of C_6 monoaromatic compounds which coupled with the large proportion of nitro containing compounds is highly indicative of nitro-monoaromatic species. For instance, 3-nitrophenol ($C_6H_5NO_3$) and 4-nitrocatechol ($C_6H_5NO_4$) were detected in the fresh OA and have been commonly observed as tracers of BB in previous studies [116, 117, 119, 142, 242, 248]. After photo-oxidation the ratio of relative abundance between CHO:CHON decreases from 41.5 to 8.7-9.2 indicating an increased contribution of CHON compounds to the aged OA composition. In the aged OA, the abundance of larger compounds (i.e. > C_{10}) increases, in particular polyaromatic C_{12}-C_{14} species, such as $C_{12}H_9NO_4$ which accounts for 10 % of the total CHON aromatic mass (Figure 3.4). Zhang et al. [133] previously observed $C_{12}H_9NO_4$ in ambient OA from the Los Angeles basin which had significant contributions from anthropogenic emissions and wood burning sources, however it was attributed to a nitro-monoaromatic compound. Whereas, in this work we assign $C_{12}H_9NO_4$ as a derivative of napthalene using the modified AI in Eq 3.5-3.7. Furthermore, the percentage mass of CHON with an O:N ratio ≥ 3 remained largely unchanged (≈ 70 %) after aging indicating CHON in aged OA are also predominantly NACs. Overall, these metrics and observation indicate flaming aged OA CHON composition contains a similar contribution of NACs to the POA. This could result from a combination of unreacted species, loss of oxidation products to the gas phase and the

condensation of new secondary products to the particle phase.

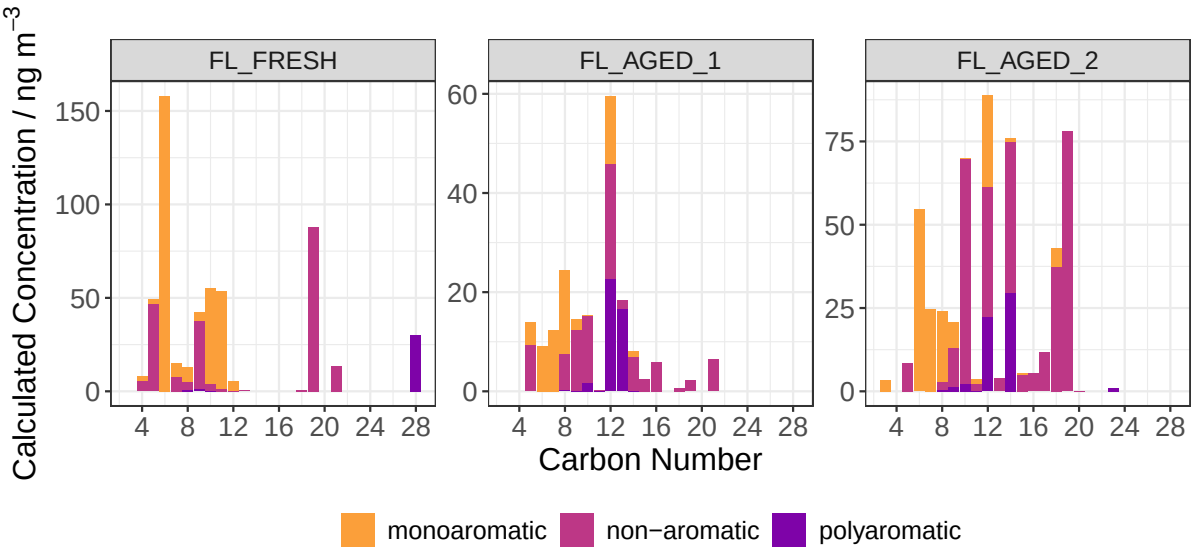

Figure 3.4: *Carbon number vs concentration distribution coloured by the AI estimations of CHON compounds in the POA of fresh emissions from flaming dominated burn phase and after aging (POA+oPOA+SOA). Different experiments are given in each panel.*

3.3.2.2 Chemical composition of organic aerosol derived from smouldering dominated emissions

The measured carbon distribution of POA from a fresh smouldering dominated burn shows a peak between C_8-C_{11} (Figure 3.5a) which largely has DBEs in the range of 4-8 and the AI estimated the majority of the mass in this carbon number region as aromatic (54.4 %). The largest peak in the distribution shown in Figure 3.5a is from C_{10} compounds with a DBE of 6 predominantly consisting of $C_{10}H_{10}O_3$ which was previously attributed to coniferylaldehyde in BBOA [60, 246]. Furthermore, Figure 3.6a shows the majority of the CHO compounds are aromatic with a 50 % and 16 % contribution from monoaromatic and polyaromatic species respectively. This indicates the C_8-C_{11} species are predominantly functionalised monoaromatic compounds as similarly observed for flaming. However, in this region there is also a greater concentration of polyaromatic compounds compared to flaming OA (see Figure 3.3), such as $C_{11}H_8O_2$ and $C_{11}H_8O_3$ which are naphthoic acid derivatives previously observed in primary and secondary wood combustion products [277]. From Figure 3.6a the smouldering

dominant POA shows an increased concentration of smaller C_{11}-C_{12} oxygenated PAHs (o-PAHs) compared to flaming dominant POA which has the largest contribution from C_{14} o-PAHs. A previous study observed the formation of PAHs and o-PAHs was dependent on the temperature and oxygen availability observing at higher temperatures in the absence of oxygen larger PAHs can form whilst smaller PAHs arise at lower temperatures [278]. Therefore, the relative PAH concentration and PAH composition will be dependent on the burn phase. Furthermore, the observed increased contribution of o-PAHs in the smouldering dominated burn is in agreement to findings by Orasche et al. [279]. In addition to functionalised monoaromatic compounds contributing to the C_8-C_{11} peak, such as, phenylacetic acid ($C_8H_8O_2$) and 3-(4-hydroxyphenyl)propionic acid ($C_9H_{10}O_3$), a previous study found smouldering had higher emissions of methoxyphenols [280] which possess > C_7 and is consistent with the observed range of carbon numbers and DBE values in Figure 3.5a.

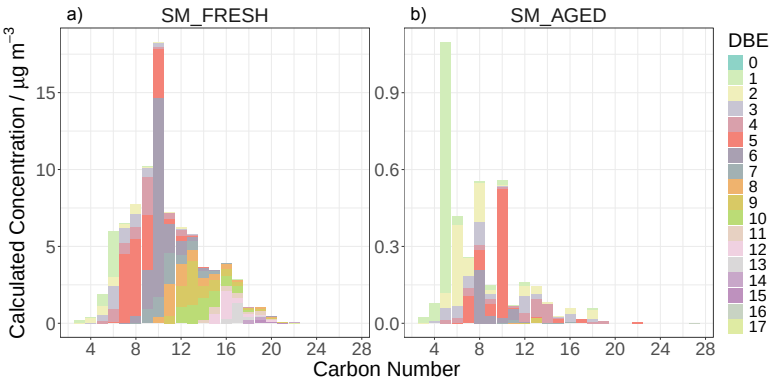

Figure 3.5: *Carbon number vs concentration distribution coloured by the DBE of CHO compounds present in the POA from fresh emissions from smouldering dominated burning conditions and after aging (POA+oPOA+SOA). The different filter sample IDs from the smouldering dominated combustion experiments are given in each panel*

After photo-oxidation, the main region in the carbon number distribution reduces to C_5-C_8 (Figure 3.5b) with a second prominent peak at C_{10}. The DBE range also decreases to 1-6 after aging. The AI values indicate a large reduction in aromaticity after atmospheric aging as the percentage contribution of aromatic CHO to the detected mass decreases from 66 % to 13 %, which is also evident in the AI carbon number distribution (Figure 3.6a). Brege et al. [179] observed a comparable shift to lower DBEs (1-5) in ambient BBOA after aging and Fang et al. [281] showed SOA from

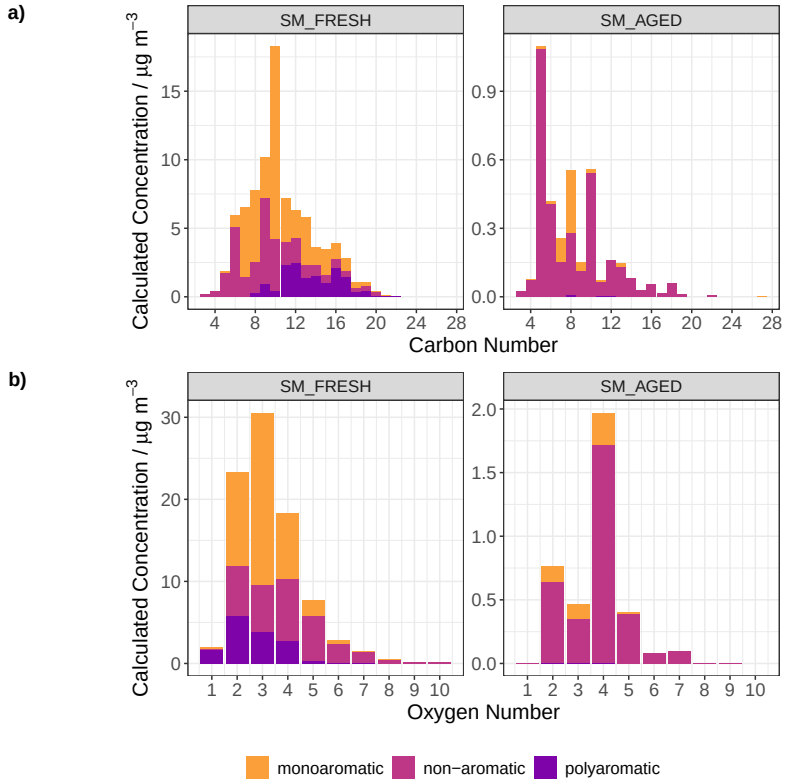

Figure 3.6: *a) Carbon number vs concentration distribution coloured by the AI estimations of CHO compounds in the POA of fresh emissions from smouldering dominated burn phase and after aging (POA+oPOA+SOA). Different experiments are given in each panel. b) Oxygen number vs concentration distribution with the same design aesthetics as Figure 3.6a*

oxidised smouldering POA had significant contributions from oxygenated aliphatic species. From the oxygen number distribution shown in Figure 3.6b the main peak increases from $C_xH_yO_3$ to $C_xH_yO_4$ indicating the presence of more oxidised species in aged OA. Overall this suggests OH functionalisation products contribute to the aged OA as well as the significant fragmentation of aromatic ring containing species from the POA. In Figure 3.5b, the peaks between C_4-C_6 with DBEs of 1-2 are largely comprised of small but highly oxidised species such as $C_4H_8O_4$, $C_5H_{10}O_4$, $C_5H_8O_{3\text{-}5}$ and $C_6H_{10}O_{4\text{-}5}$. Kalogridis et al. [260] observed higher emission factors of succinic and glutaric acids in smouldering compared to flaming therefore, these species could be derivatives of succinic acid (C_4) or glutaric acid (C_5) [260, 282, 283]. This could also explain the lack of low DBE C_4 and C_5 compounds in the carbon number distribution derived from flaming dominated OA shown in Figure 3.2. $C_5H_{10}O_4$ was also previously attributed to deoxyribose in BBOA [246], however this is likely not detected by the

negative mode UHPLC-HRMS. The remaining aromatic mass after photo-oxidation in smouldering dominated OA is predominantly formed of C_7-C_8 monoaromatic species (Figure 3.6a), such as, vanillin in addition to $C_8H_6O_4$ and $C_7H_6O_2$ which were previously attributed to phthalic acid and benzoic acid respectively [275]. Phthalic acid and benzoic acid were also identified as oxidation products of napthalene [275] which is in agreement with the observed reduction in polyaromatic C_{10}-C_{11} species in Figure 3.6. Similar to flaming, polyaromatic species contributions were significantly reduced after aging in agreement with previous studies, which observed the emission factors of o-PAHs to decrease by 20 % between fresh and aged BBOA [284] and the degradation of particle bound PAHs after aging smoke particles [285]. Considering the damaging health impacts of oxygenated PAHs, the reduction of their contribution with aging could lead to important implications for the OA toxicity.

For CHON species, the fresh OA distribution shows high concentrations at C_9 for non-aromatic compounds and C_6 for monoaromatic species (Figure 3.7) which is similar to the peak in C_6-C_{10} CHON species observed in ambient fresh BBOA [179]. These peaks predominantly consist of species such as $C_9H_{11}NO_4$ and $C_6H_5NO_5$ which were previously observed in ambient cloud water samples influenced by agricultural BB [286] and in fresh BBOA from controlled burn experiments [253]. In addition, 72 % of the CHON mass had a O:N $\geq$ 3 suggesting the presence of -NO_2 functionality. This is therefore in accordance with Lin et al. [236] who attributed $C_6H_5NO_5$ in BrC originating from a major BB event to nitrobenzenetriol. After photo-oxidation inside the chamber the ratio of relative abundance between CHO:CHON decreases from 29.2 to 10.9 indicating a greater contribution of CHON species to the overall OA composition. Similar to flaming, the OA distribution in Figure 3.7 shows an increase in larger CHON species (i.e. $> C_{10}$) after aging, however the concentrations are significantly lower. Monoaromatic compounds in the aged OA, are predominantly comprised of C_5, C_6 and C_{12} species such as $C_5H_5NO_4$, $C_6H_5NO_3$, $C_6H_4N_2O_5$ and $C_{12}H_{12}N_2O_4$ (Figure 3.7). $C_6H_5NO_3$ and $C_6H_4N_2O_5$ were identified as 3-nitrophenol and 2,4-dinitrophenol respectively using authentic standards and $C_5H_5NO_4$ was previously observed in BrC from a major BB event [236] but the structure could not be elucidated. However, a monoaromatic C_5 species is indicative of furanic origins as previous observations indicate furans are important for SOA production in smouldering fires [135]. In the aged

OA, the relative contribution of aromatic compounds to the CHON mass decreased from 45 % to 31 % and the proportion of compounds with O:N ≥ 3 reduced to 47 % which overall indicates a reduction in the contribution of NACs to the OA composition after atmospheric aging.

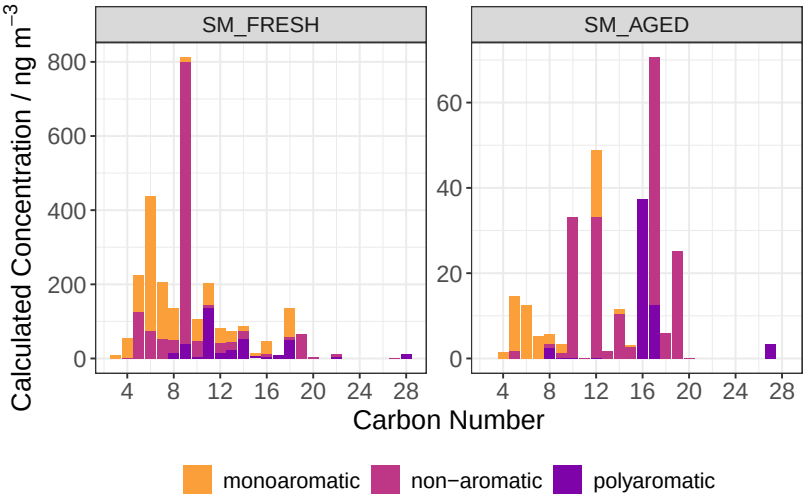

Figure 3.7: *Carbon number vs concentration distribution coloured by the AI estimations of CHON compounds in the POA of fresh emissions from the smouldering dominated burn phase and after aging (POA+oPOA+SOA). Different experiments are given in each panel.*

3.3.3 Impact of the burn phase on the oxidation and aged chemical composition of organic aerosol

As discussed in Section 3.3.2.1 and 3.3.2.2 the burning conditions influence the POA composition and POA mass with subsequent atmospheric aging producing unique burn-phase specific distributions which could enable the development of tracer species to identify flaming and smouldering sources in the ambient. Overall there is a comparable contribution of aromatic species (> 50 %) to the POA composition under both conditions which is in accordance with Akherati et al. [107] and Gilman et al. [126] who observed oxygenated aromatics had the greatest SOA formation potentials and contributed to nearly 60 % of the SOA mass from BB. However, after aging, the change in the contribution of aromatic compounds to the OA composition differed with a significant reduction observed for smouldering dominated compared to flaming dominated burns. In particular, smouldering dominated emissions showed a greater reduction in polyaromatic contributions to the OA mass after aging (-16.2 %) compared to

the flaming dominated phase (-2.6 %). This difference in compositional change indicates aging of OA from smouldering emissions could result in more oxidised products compared to flaming.

In order to compare the effect of atmospheric aging processes on the OA composition from domestic BBOA, O:C ratios of aromatic and non-aromatic compounds were examined via their probability density distributions to visualise the differences in the population of observable O:C values which provide insight into the level of oxidation. The distribution shown in Figure 3.8 is constructed using a kernel density estimation which fits a smooth distribution across a series of band widths to a histogram of the observed O:C values in the domestic BBOA samples. The *y axis* represents density meaning the probability of the OA having a certain O:C value can be computed by integrating the area under the curve. In this analysis the peaks in the O:C distributions of fresh and aged OA are examined to observe differences in the composition and hence provide insight into the magnitude of OA oxidation under different burning conditions. Generally, the peak of the O:C distributions in Figure 3.8 of aromatic compounds for flaming dominated and smouldering dominated experiments show a greater change between fresh and aged aerosol compared to non-aromatic species. This demonstrates that oxidation of aromatic compounds is significant for the observed compositional change as inferred from Section 3.3.2.1 and 3.3.2.2 and therefore non-aromatic compounds will be disregarded for the remaining analysis.

The smouldering dominated POA shows a broader distribution, i.e. spanning a wide range of O:C values, in Figure 3.8 indicating the presence of more oxygenated compounds than from the flaming dominated burns, as also seen in the oxygen number distributions (Figure 3.3b and Figure 3.6b). After aging, the distributions shift to higher O:C values consistent with the observed increased oxygen content and fragmentation of the carbon backbone indicative of the oxidation of OA [28]. For aromatic CHO compounds the increase in O:C after aging is greater in the smouldering dominated burn compared to the flaming dominated burns. In smouldering dominated OA the main peak in the O:C ratio for aromatic CHO compounds increased from 0.25 to 0.50 with a smaller peak at 0.80. Upon aging in the flaming dominated burn the main peak of the O:C ratio increased from 0.22 to 0.29 with a smaller peak at 0.50. Furthermore, the area under the distribution represents probability and at the O:C value of

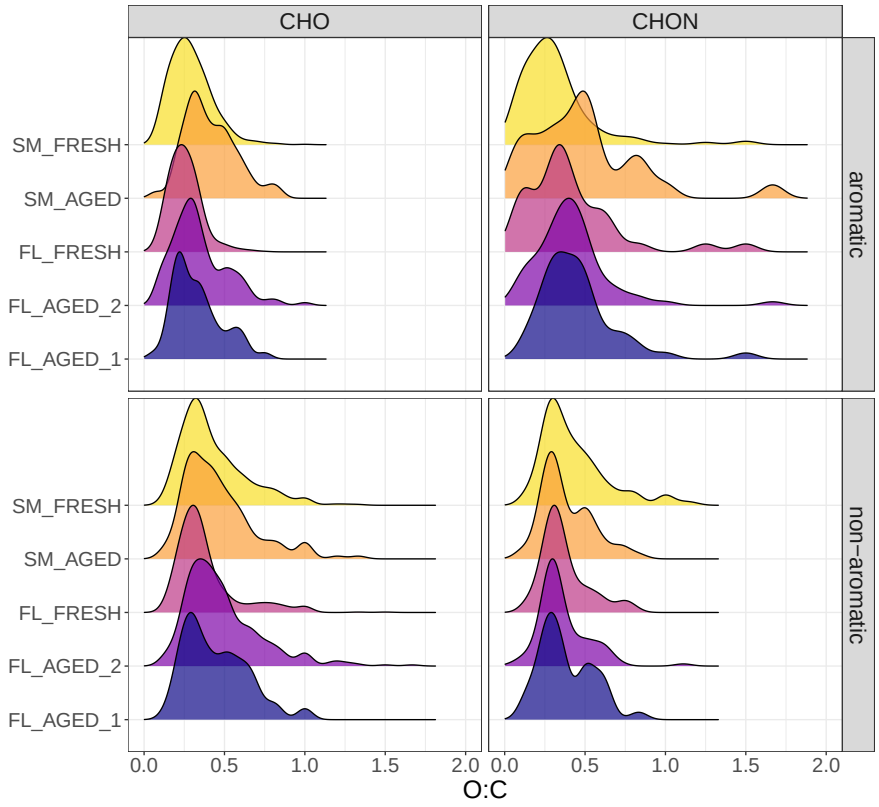

Figure 3.8: *Probability density distribution for each experiment (y-axis label) of observed O:C ratios present within the detected CHO and CHON compounds shown in the left and right panels respectively and separated into aromatic (top panel) and non aromatic compounds (bottom panel) using the AI estimations.*

0.50, the area was greater for smouldering dominated than flaming dominated phases suggesting a larger number of oxidised species. Additionally the presence of high O:C values (≈ 0.80) from the smouldering dominated phase derived OA which are absent in the flaming dominated burn distribution similarly indicates a greater proportion of increasingly oxidised compounds. This is in agreement with Li et al. [235] who observed greater oxidation of smouldering emissions compared to flaming.

For aromatic CHON species, there is a significant difference in the POA probability density distributions with a broader distribution in the smouldering dominated phase compared to 3 resolved peaks for the flaming dominated phase. The smouldering dominated POA distribution peaks at an O:C value of 0.25 whereas the flaming dominated POA distribution contains 3 distinct peaks at O:C ratios of 0.15, 0.34 and

0.60 with the greatest density at 0.34. However, the lower value of the O:C ratio peak in smouldering dominated POA compared to flaming dominated POA could be due to the greater contribution of polyaromatic species (Figure 3.6) which typically possess relatively low O:C values. Similarly, after aging the O:C distributions in Figure 3.8 show different trends for flaming dominated and smouldering dominated experiments. In smouldering dominated aged OA there is a clear increase in O:C from 0.25 to 0.47 which is in agreement with previous observations of the change in O:C (0.09-0.30) from smouldering fires [287–289]. Whereas for flaming, the distributions of aromatic CHON compounds are relatively similar between fresh and aged OA and the increase in O:C from the main peak is relatively low (0.07). $C_6H_5NO_3$ (nitrophenol), $C_7H_7NO_4$ (nitroguaiacol) and $C_{10}H_7NO_3$ (nitro-1-napthol) were identified in both POA and aged OA from the flaming dominated phase with an increase in concentration after aging, indicating the formation of similar CHON compounds to POA during photo-oxidation.

Van Krevelen diagrams of the O:C vs H:C space can also provide insight into the differences in composition and atmospheric aging between smouldering and flaming derived OA (Figure 3.9) due to the characteristic occupation of certain species at unique ratios and trend lines which can indicate the types of reactions occurring [176]. For instance, POA derived from fresh smouldering dominated emissions has a greater range of O:C values across a similar range of H:C ratios as fresh flaming dominated emissions in Figure 3.9 suggesting increasingly oxygenated OA. In addition, Figure 3.9 shows POA from fresh smouldering dominated emissions has a greater quantity of polyaromatic CHO and CHON compounds as previously observed in the carbon number distributions (Figure 3.6 and Figure 3.7). After aging, there is a significant reduction in aromatic species for the smouldering dominated phase and to a lesser extent in the flaming dominated phase (Figure 3.9). In the aged OA from smouldering dominated emissions the reduction in polyaromatic compounds is significantly greater compared to flaming dominated derived OA, with almost complete loss of the polyaromatic CHO species in Figure 3.9. Whereas for flaming dominated OA, the number of aromatic CHON species in the Van Krevelen space increased after aging, notably for polyaromatic CHON species. This trend can also be seen for the flaming experiments in the carbon number distribution shown in Figure 3.4 with increased C_{12}-C_{14} polyaromatic CHON species in aged OA and a simultaneous decrease of C_{12}-C_{14} polyaro-

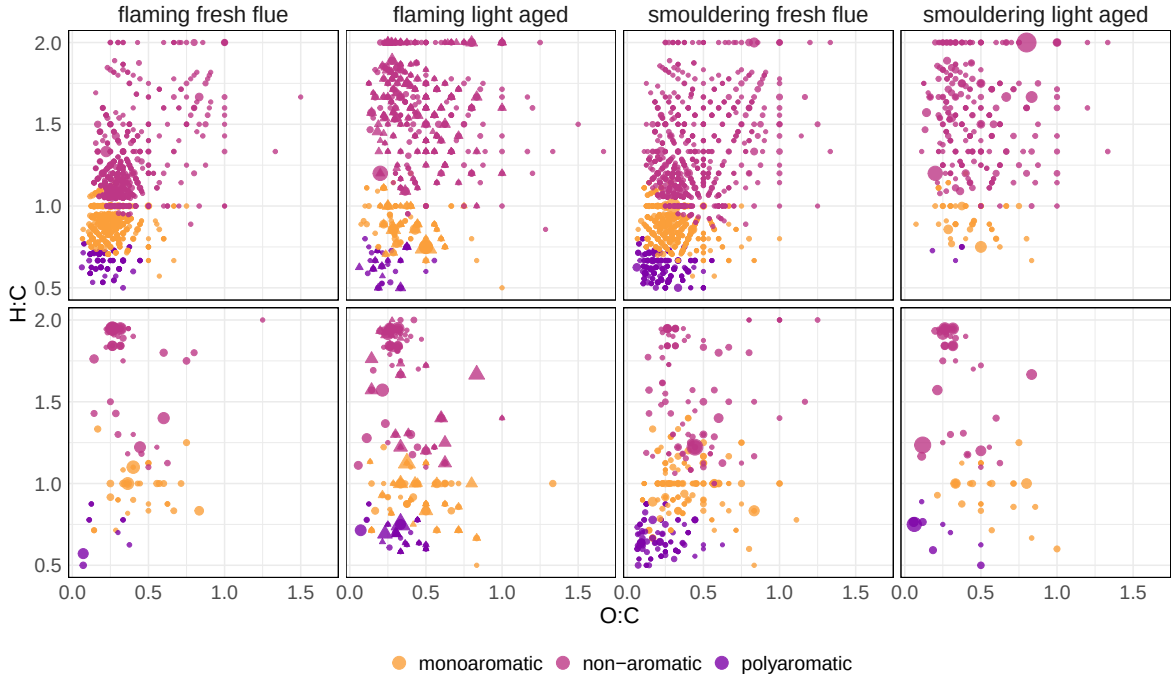

Figure 3.9: *Van Krevelen plot of H:C vs O:C of the detected CHO and CHON compounds with each panel depicting the experiment type and the point colour representing the aromaticity as determined by the AI. The size of the marker represents concentration. In the flaming light aged panel the point shape represents the two repeats: FL_AGED_1 (circles) and FL_AGED_2 (triangles).*

matic species in the CHO carbon distribution (Figure 3.3a). Therefore, this suggests the formation of NACs from the oxidation of aromatic CHO compounds during the flaming dominated phase. The same trend of polyaromatic loss in smouldering versus CHON polyaromatic production in flaming was also observed in the Van Krevelen of species detected in positive mode ESI indicating the conclusions drawn for the composition detected by negative mode are representative of the whole sample (Figure 3.10). The production of NACs could be greater from the flaming dominated burn since NO_x emissions from flaming are typically higher than smouldering (Table 3.1 and Figure 3.1) thus leading to the formation of ring retained nitroaromatic species.

The observed O:C ratios of the aromatic compounds in aged OA shown in Figure 3.9 are in agreement with those for SOA derived from aromatic oxidation (eg. toluene, m-xylene and napthalene) with reported values ranging between 0.57-0.75 [207, 290–292] and the observed range for phenolic SOA oxidation products (0.3-1.0) [293]. Furthermore, the observable H:C vs O:C space in Figure 3.9 is within the range reported for lignin-like compounds (1-1.5 vs 0.2-0.6) [294] as expected for BBOA. Overall, these

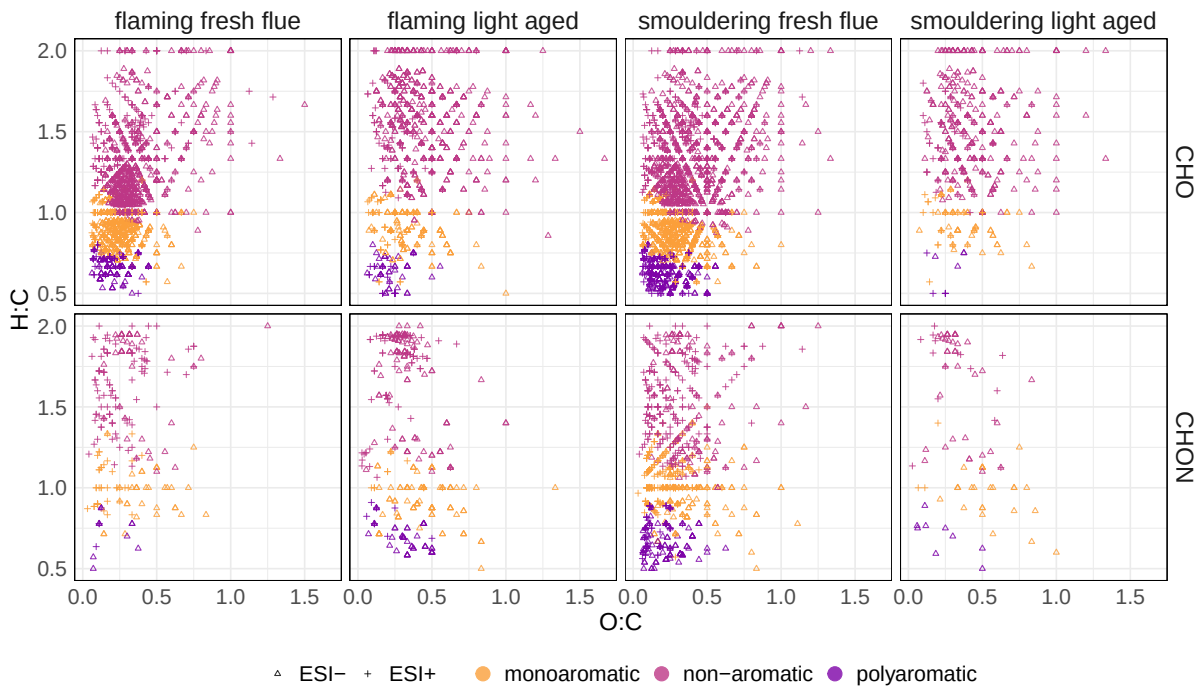

Figure 3.10: *Van Krevelen plot of H:C vs O:C of the detected CHO and CHON compounds with each panel depicting the experiment type, the point colour representing the aromaticity as determined by the AI and point shape showing the detected compounds in negative and positive mode ESI.*

results show SOA from aromatic compounds via ring-opening and ring retained nitroaromatic formation routes contribute substantially to the aged OA composition and their volatile products may have important implications for subsequent atmospheric chemistry and O_3 formation [295] and hence are the topic of Chapter 4.

The notable variation of the aromatic contribution to aged OA compositions and significant differences in the concentration of polyaromatic species between burn phase could lead to important implications for toxicity. Kim et al. [285] previously investigated the toxicity of wood smoke particles and observed that after aging the mutagenicity was lower compared to fresh particles when considering PAHs. Furthermore, on an equal particle mass basis aged flaming smoke particles had a higher potential toxicity value with respect to PAHs than aged smouldering smoke particles [285]. This could potentially be the result of an increased fraction of nitro-PAH compounds from flaming (Figure 3.9), some of which are known to exceed the toxicity of their parent

PAH. Therefore, the OA composition under different burning conditions can be an important factor affecting the toxicity but often the greater observed emission factors from smouldering [296, 297] prevail in the determination of the toxicity for policy based interventions.

The volatility of the domestic BBOA was estimated using the Li et al. [298] 2-dimensional volatility basis set (2D-VBS) parameterisation to determine differences in aging processes which could explain the observed differences in composition. The 2D-VBS estimation error was shown to increase for lower saturation mass coefficients therefore some caution must be taken when considering low volatility products [298]. Compounds were classed as volatile organic compounds (VOC) when $C_0 > 3 \times 10^6$ μg m^{-3}, intermediate volatile organic compounds (IVOC) when $300 < C_0 < 3 \times 10^6$ μg m^{-3}, semi-volatile organic compounds (SVOC) when $0.3 < C_0 < 300$ μg m^{-3}, low volatile organic compounds (LVOC) when $3 \times 10^{-4} < C_0 < 0.3$ μg m^{-3} and extremely low volatile organic compounds (ELVOC) when $C_0 < 3 \times 10^{-4}$ μg m^{-3}. Figure 3.11 shows the Van Krevelen distribution coloured by the OA volatility which indicates after aging there is a slight increase in volatility likely from the formation of smaller compounds as shown in Sect. 3.3.2.1 and 3.3.2.2.

For the smouldering dominated burn aging resulted in the almost complete loss of low volatile organic compounds (LVOC) and semi-volatile organic compounds (SVOC) from the aged OA. OA from the flaming dominated phase in the region of H:C < 1 and O:C < 0.5 conversely showed a notable increase in the SVOC CHON compounds and a simultaneous reduction of SVOC CHO compounds, suggesting the formation of NACs after aging as observed in Figure 3.9. This difference in processing between the burning conditions is in accordance with Kalogridis et al. [260] who similarly observed changes in OC from flaming to be driven by the production or partitioning of organic compounds to the particle phase whereas for smouldering, evaporation of semi-volatile species was considered an important sink of OC.

3.3.4 Impact of non-ideal burn conditions

In reality due to maloperation of domestic stoves or in ambient biomass burning events, flaming and smouldering combustion can occur simultaneously resulting in a complex mixture of emissions. Therefore, it is of interest to characterise these emissions.

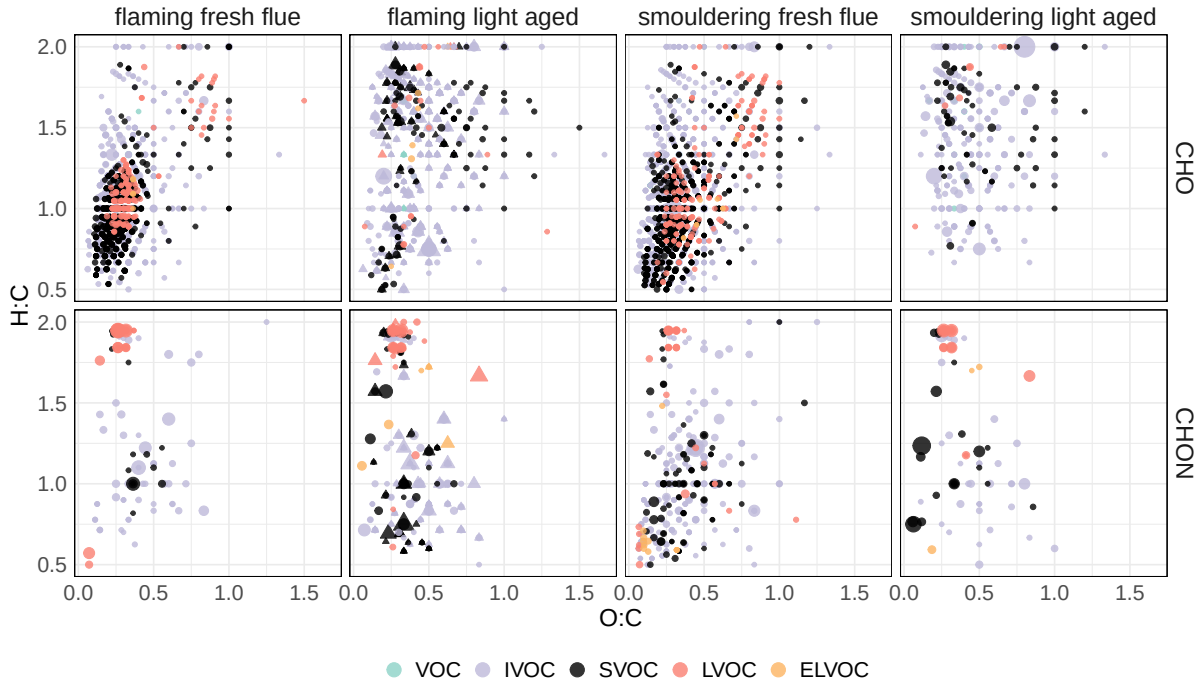

Figure 3.11: *Van Krevelen diagrams of H:C and O:C ratios for CHO (top row) and CHON (bottom row) compounds in the OA derived from flaming dominated and smouldering dominated burn phases. The size of the marker represents concentration. In the flaming light aged panel the point shape represents the two repeats: FL_AGED_1 (circles) and FL_AGED_2 (triangles).*

Firstly, the carbon number and DBE distribution of the aged aerosol from the intermediate burn in Figure 3.12a shows a similar distribution to smouldering (Figure 3.5) with a peak between C_5-C_8 and DBE 1-6. This indicates the aerosol phase is dominated by smouldering due to the higher OC emissions from this burn phase. Secondly, as shown in Table 3.1 the intermediary burn has higher NO_x and CO_2 emissions due to a similar MCE to the flaming burns than classical smouldering, which is attributed to the partial flaming combustion conditions. These enhanced gaseous emissions could create a different oxidative environment compared to entirely smouldering conditions. From AMS measurements of f_{44} and f_{60} the intermediate burn had a greater loss of f_{60} (-0.033) relative to smouldering (-0.0254) and the increase in f_{44} (+0.085) was similar to flaming (+0.083-0.085). Overall, this indicates the enhanced gaseous emissions of flaming could induce further oxidation. For instance in Figure 3.12b, the polyaromatic CHON compounds at low O/C (< 0.25) and H/C (< 1) present in the flaming and smouldering samples are absent in the intermediate aged aerosol indicating the

further oxidation of nitro-PAHs. However, there is no fresh emission of this burn for comparison therefore it is difficult to wholly understand how aging has affected the composition. Furthermore, the intermediary burn represents a single sample and further work is required to more accurately replicate the effects of burn phase mixtures on emissions of PM and trace gases to draw conclusions.

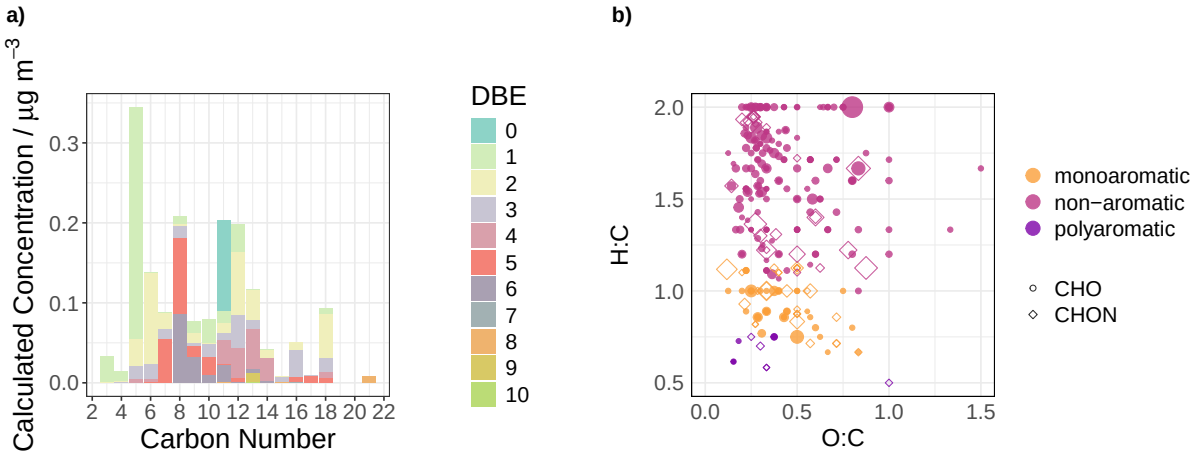

Figure 3.12: *a) Carbon number vs concentration distribution coloured by the DBE of the CHO compounds present in the intermediary burn after aging (POA+oPOA+SOA) b) Van Krevelen diagram of H:C vs O:C for the detected CHO and CHON compounds, given by the point shape, in the intermediary burn and coloured by the AI index estimations of aromaticity. The size of the marker represents concentration.*

3.4 Conclusions

The chemical composition of domestic biomass burning organic aerosol from a series of controlled burn chamber experiments, was investigated using the newly developed semi-quantitative NTA methodology in Chapter 2 and is the first study to account for ionisation effects in an NTA of BBOA using retention window scaling [231]. The NTA approach enabled the detection of up to 2357 features in a single sample which is simply impossible from a targeted approach with a limited number of standards. Significant compositional differences between the OA derived from emission under different burn phases (i.e. flaming dominated and smouldering dominated phases) and after aging were observed. However, the experimental methodology used here could be im-

proved by sampling directly from the chamber at the start of the experiment but this remains challenging for offline approaches due to the higher sample volume required and the low particle mass used in this study. Overall, the composition of domestic BBOA was dominated by CHO compounds. On average CHO compounds constituted 90 % of the total detected mass with a smaller contribution ($\leq$ 10 %) of CHON species, which suggests the wide usage of nitroaromatic compounds as tracers of biomass burning may not be ideal as these compounds typically have high ionisation efficiencies and therefore appear more abundant when using peak area metrics. In agreement with other studies, the estimated concentrations of the detected compounds were markedly higher in OA from smouldering dominated emissions compared to flaming dominated emissions, as a result of the larger OA emission factors associated with smouldering. This indicates the burn phase in a domestic environment is a critical factor for controlling indoor air pollutant concentrations along with air filtration and the stove model [299]. Considering the OA chemical composition from fresh emissions, flaming dominated POA had a large contribution of CHO compounds between C_8-C_{11} and C_{13}-C_{17} which were predominantly comprised of functionalised monoaromatic compounds. Smouldering dominated POA emissions had a higher concentration of lower molecular weight CHO species, predominantly in the region of C_8-C_{11} with a peak at C_{10}, which were also attributed to functionalised monoaromatic compounds. Furthermore, smouldering dominated POA also had a greater percentage contribution from o-PAHs of 16 % over the same carbon range compared to the flaming dominated POA (6 %) which has important implications for the toxicity of POA. For CHON species, the observed POA composition contained comparable concentrations of C_6 monoaromatic species between the burn phases that were largely assigned as NACs such as widely used BB tracers, nitrophenols and nitrocatechols. However, after aging, the OA composition between the burning conditions significantly diverged particularly in the relation to the contribution of aromatic CHO and CHON compounds to the aged OA composition which was attributed to burn specific aging processes. For OA from the smouldering dominated phase, aging decreased the relative contribution of aromatics with almost complete reduction of both polyaromatic CHO and CHON species resulting in the formation of ring-opened products. In comparison, for the flaming dominated burns, the reduction in the contribution of aromatic compounds to the de-

tected OA mass after aging was less than in smouldering and Van Krevelen analysis indicated the number of polyaromatic CHON species notably increased, suggesting the formation of NACs from aromatic CHO species. These differences in the aromatic contribution to the OA composition between the burn phases have important implications for toxicity, particularly in relation to polyaromatic species which are known carcinogenic species. The formation of ring retained NACs from the flaming dominated burns highlight important implications for both toxicity and BrC formation. In contrast, higher volatility ring-opened products were an important contribution to OA from aged smouldering dominated emissions. These products could volatilise from the particulate phase and impact on atmospheric chemistry and O_3 formation, invariably leading to the creation of compounds of unknown toxicities. At present, toxicology endpoints used for policy-making decisions on mitigating impacts for human health are typically based on mass. In reality, this is a more complex picture with multiple factors affecting the toxicity of domestic BBOA such as the emission factor of a compound, the OA composition as studied here, the total mass of fuel burnt and ultimately the length of time exposed to the emission.

Chapter 4

Development of a chemical mechanism for the photo-oxidation of guaiacol and understanding the contribution to biomass burning SOA formation

4.1 Introduction

Biomass burning is the second largest global source of non-methane organic compounds, (500 Tg yr^{-1}) to the atmosphere after biogenic emissions (1000 Tg yr^{-1}) [300] and the dominant source of primary organic aerosol (POA) and black carbon (BC) [22]. Emissions of biomass burning VOCs (BBVOCs) can undergo photo-oxidation in the atmosphere to produce gaseous and particle phase species such as, secondary organic aerosol (SOA) and tropospheric ozone (O_3) in the presence of nitrogen oxides (NO_x = nitric oxide (NO) + nitrogen dioxide (NO_2)). These emissions and their products can then impact on climate by affecting the radiation budget, plant productivity through stomatal uptake of O_3, and human health [19, 301, 302]. For instance, Apte et al. [19] reported that in 2016 exposure to $PM_{2.5}$ air pollution reduced life expectancy by 1 year across the globe and in South Asia alone up to 1.56 years. This region also experiences frequent burning events such as agricultural crop burning, wildfires and residential combustion [303–305]. However, despite the importance of biomass burning for atmospheric composition and the resulting impacts, the atmospheric chemistry

of biomass burning emissions remains poorly understood.

During the day, the hydroxyl radical (OH) is considered the dominant oxidant of BBVOCs where in-plume OH concentrations can be up to an order of magnitude greater than the background air [306]. Whereas in a nighttime ambient wildfire plume Decker et al. [114] observed 53% of BBVOCs were oxidised by the nitrate radical (NO_3) whilst 43% were oxidised by ozonolysis. Within a biomass burning plume monoterpenes and oxygenated aromatics (i.e. furans and phenols) are the main source of reactivity [93, 114, 126] and have been reported as the dominant SOA precursors in biomass burning [307]. Furthermore, Chapter 3 shows the significant contribution of oxygenated aromatic POA and SOA products to the chemical composition of wood burning organic aerosol. However, the detailed atmospheric chemistry of oxygenated aromatics is relatively understudied [134]. Therefore, theoretical and laboratory studies have been performed on single precursor systems and biomass smoke to elucidate their oxidation products and propose a reaction scheme with OH or NO_3 in order to understand the formation of SOA from these precursors [93, 98, 308–313]. However, the majority of these schemes have not been translated into a detailed semi-explicit mechanism for implementation into chemical models. To date, only Coggon et al. [93], Müller et al. [308], and Jiang et al. [311] have developed chemical mechanisms with OH for furanic species for inclusion into chemical models. For phenolic species, they were either omitted or a basic mechanism with OH or NO_3 was supplied [93, 114].

An important class of oxygenated aromatics from biomass burning emissions are methoxyphenols which form from the degradation of lignin within plant cell walls during combustion [314–316]. Depending on the intrinsic structure of lignin within the plant cell wall across different plant species, the relative emissions of different methoxyphenols can vary [317]. For example, softwoods are primarily formed of the guaiacyl unit (2-methoxyphenol), whilst hardwoods contain equal amounts of guaiacyl and syringyl units (2,6-dimethoxyphenol) [314]. This can result in a significant emission of guaiacol from biomass burning with reported emission factors as high as 172-276 mg per kg of fuel burnt [318]. Critically, guaiacol has a high OH reactivity (k = 7.53 × 10^{-11} cm^3 $molecule^{-1}$ s^{-1} at 294K) [319] and SOA yield (0.28-0.87) [94, 309, 320]. Coggon et al. [93] previously proposed a basic mechanism for guaiacol which accounted only for the formation of nitroguaiacol. In reality, there will be a much larger

number of oxidation products which can contribute to SOA and O_3 formation.

Typically, there are two major pathways for the reaction of aromatic VOCs with OH; OH addition to the ring and H abstraction which can occur in differing proportions depending on the VOC structure [295]. Previous studies investigating the reaction of guaiacol with OH have largely performed theoretical calculations to understand the energetically favourable routes in each pathway or reported a basic scheme based on product observations [309, 321–324]. However, neither approach translated these results to an explicit chemical mechanism scheme for use in atmospheric chemical modelling studies. From the H abstraction pathway, Lauraguais et al. [94] reported that nitroguaiacols were the dominant products under high NO_x conditions with gas phase yields of 16 % and the high potential of these compounds to partition to the aerosol phase where they are known contributors to brown carbon (BrC) [60, 172, 252–254]. In computational studies of guaiacol OH oxidation [321–324] and in experiments performed by Yee et al. [309] under low NO_x conditions, OH addition products such as methoxybenzoquinone, methoxybenzene-1,4-diols, unsaturated dicarbonyls and epoxides were observed. In computational studies intermediates deriving from the H abstraction of the methoxy group [321] and OH addition on the ring at the ortho and ipso position to the methoxygroup [323, 324] were considered the most energetically favourable pathways yielding nitroguaiacols under high NO_x conditions [94, 323, 324]. Furthermore, An et al. [323] suggest H abstraction reaction pathways were dominant (≈60 %) over OH addition reactions (≈40 %). This may have implications for the SOA toxicity from the significant formation of ring-retained products from this pathway, which are considered to be more toxic than ring-opened products due to higher reported oxidative potentials [96]. A more unusual reaction pathway including the loss of the methoxy group to form catechol was observed experimentally by Yee et al. [309], which could have impacts on O_3 and SOA formation with reported catechol SOA yields over 100 % [325]. However, catechol has been observed as a 1% impurity of guaiacol in a commercial standard and in a previous theoretical study the enthalpy change for this reaction was endothermic; therefore, more studies are needed to understand and confirm the formation of this product [326].

This chapter proposes a new mechanism for the photo-oxidation of guaiacol using the latest Master Chemical Mechanism v3.3.1 (MCM, `https://mcm.york.ac.uk/MCM`)

development protocol. The MCM is a widely used near-explicit chemical mechanism describing the detailed gas phase atmospheric degradation of 142 non-methane VOCs and methane containing in its current iteration 17,224 reactions. Subsets of the MCM can then be implemented into atmospheric chemical processing box models used in policy development. The guaiacol mechanism performance was evaluated on chamber experiments performed at the EUropean PHOtoREactor (EUPHORE) during May 2023 and shortcomings in the proposed mechanism are identified and discussed. Furthermore, as the emission period of biomass burning sources can span across days and nights in the atmosphere the chemical composition of guaiacol SOA products was evaluated between nighttime and daytime initiated chemistry. Overall, the findings from this Chapter highlight the importance of gas phase dihydroxyarene products from OH addition on the degradation of guaiacol and propogation of RO_2 cycles under daytime conditions.

4.2 Methodology

4.2.1 Chamber experiments

4.2.1.1 Chamber description

Chamber experiments were performed at EUPHORE, in Valencia, Spain, for 4 weeks during May 2023. The EUPHORE facility was described in detail by Bloss et al. [295, 327] but in summary, it has two 200 m^3 Teflon domed outdoor chambers to perform experiments in (Figure 4.1). Each chamber has a large internal fan for mixing and is situated on the rooftop with a retractable housing so that the chamber can be irradiated by sunlight or left in the dark. The housing can also be partially be retracted in windy conditions to protect the chamber against the wind whilst also allowing full irradiation of the chamber base. Multiple different atmospheric oxidants can be used in the chamber such as OH, O_3 and NO_3. A pen-ray lamp with a flow of 99.9 % purity oxygen at 2 bar pressure is used to generate O_3 and NO is added to the chamber from a 5000 ppm gas cylinder at 3 bar pressure. NO_2 is chemically produced inside the chamber from the reaction of NO and O_3. EUPHORE is a highly instrumented facility capable of measuring both gaseous and particle phase species. The instrumentation deployed

in this campaign to measure oxidation products and particle growth is presented in Table 4.1. O_3 was measured by Fourier Transform Infrared Spectroscopy (FTIR) due to interference from conjugated VOCs on the 254 nm UV absorption EcoTech Instrument. Mass spectra from Iodide Chemical Ionisation Mass Spectrometry (I-CIMS) were analysed in Tofware v3.2.5 in Igor Pro 8. All data throughout the remainder of the Chapter is represented as Coordinated Universal Time (UTC).

Figure 4.1: *200 m^3 Teflon chamber at the EUropean PHOtoREactor (EUPHORE) facility in Valencia, Spain*

Table 4.1: *Instrumentation at the EUPHORE facility available during the campaign, the species measured and instrument parameters*

Instrument	**Species Measured During Campaign**	**Measurement Technique and Parameters**
Teledyne T500U	NO_2	Cavity Attenuated Phase Shift (CAPS)
Teledyne T200UP	NO	Chemiluminescence: NO + O_3 = NO_2 NO_2 luminescence measured
AEROLASER 4021	HCHO	Florescence Hantzsch reaction of HCHO+pentadione+NH_4
Long Path Absorption Photometer (LOPAP)	HONO	Wet chemistry sampling with photometric detection
Scanning Mobility Particle Sizer (SMPS)	PM	Size range: 10-1000 nm
Fourier Transform Infrared Spectroscopy (FTIR)	O_3, NO_2, HONO, SF_6,HCHO, guaiacol, glyoxal and HNO_3	Wavenumber range: 723.2-1240 cm^{-1}
Agilent Technologies 5975T LTM-GC/MSD (GC-MS)	glyoxal and methylglyoxal	Derivatised for carbonyls
Aerodyne Filter Inlet for Gases and AEROsols Iodide Chemical Ionisation Mass Spectrometry (FIGAERO-I-CIMS)	Oxidation products	Polonium ionisation source I^- and IH_2O^- reagent ions produce M+I^- species
IONICON Proton Transfer Time of Flight Mass Spectrometry (PTR-ToF-MS)	Oxidation products	Heated line H_3O^+ reagent ion produces M+H^+ species

As air is taken out of the chamber for analysis there is a replacement flow, meaning over time the chamber contents will be diluted but given the large volume of the chamber this effect is minimised. Nonetheless it is important to measure this dilution of the chamber therefore, 6 mL of sulfur hexafluoride (SF_6) is added to the chamber at the beginning of each experiment as a tracer for the chamber dilution. SF_6 was measured by FTIR at $\approx$ 950 cm^{-1} and can be used as a tracer due to its inert reactivity and strong absorption of infrared light. For these experiments a combination of open and closed chambers were used to simulate "pure" daytime, "pure" nighttime and transitions between night and day or vice versa. The campaign investigated 4 different BBVOCs: guaiacol, catechol, furfural and 2-methylfuran. However, this chapter exclusively focuses on the guaiacol oxidation experiments shown in Table 4.2.

Table 4.2: *List of guaiacol experiments performed at EUPHORE in May 2023 used in the analysis of this Chapter*

Date	**Experiment Type**	**ID**	Roof Position	**Duration**
15-05-2023	Gas Phase Mechanistic Study	GPM	Open	5:03
29-05-2023	Day-to-Night	DTN	Open to Closed	6:16
30-05-2023	Night-to-Day	NTD	Closed to Open	6:17

4.2.1.2 Experiment protocol

For the gas phase mechanism experiment (GPM) approximately 500 ppb of guaiacol ($\geq$ 99 %, Sigma Aldrich) and 100 ppb of NO_x (50 ppb NO + 50 ppb NO_2) was added to the chamber resulting in a moderate VOC:NO_x ratio of $\approx$ 5:1 (Table 4.3). The experiments were performed under dry conditions and these initial conditions in Table 4.3 are similar to those used in previous campaigns at EUPHORE to understand the photo-oxidation of aromatics [295, 328] and the reported ratios from VOC:NO_x FIREX-AQ campaigns [93]. However, the VOC concentration used is significantly higher than that previously reported in the FIREX-AQ campaign during controlled burn experiments which observed concentrations of guaiacol around 40 ppb and calculated the emission ratio relative to CO to be 1.3 ppb/ppm CO [91]. These higher VOC concentrations were used here in order to clearly observe oxidation products used in the validation of the guaiacol mechanism, such as glyoxal determined from FTIR. How-

ever, for future experimental design the I-CIMS measurements may be more suited to lower concentrations in order to prevent saturating the reagent ions. Seinfeld [42] reported that VOC:NO_x less than 8:1 is indicative of a VOC limited O_3 production regime which is typically observed from fresh emissions [329, 330]. The conditions here can thereby be considered to represent a fresh biomass burning plume but at higher concentrations for mechanism evaluation purposes. GPM experiments were performed with the roof open, unseeded to allow homogeneous nucleation yields to be calculated and OH was generated through the photolysis of nitrous acid (HONO) (Table 4.3) based on precampaign simulations. The experiment was conducted with the roof open for 5 hours however for modelling purposes (Section 4.2.3) the first 90 minutes are taken due to further additions of HONO and guaiacol later in the experiment. Furthermore, large reductions in the I-CIMS reagent ion, from the high VOC loading, were observed meaning the data at the later stages of the experiment could be more uncertain. Furthermore, as seen from the SMPS number concentration (Figure 4.2) the majority of the particle growth occurs during this time despite further additions of guaiacol and HONO after 11:17 (UTC) and 10:01 (UTC). At the end of the roof open period a filter was sampled at a flow rate of 11.5 L/min for 1 hour for offline analysis with Ultra-High-Performance Liquid Chromatography coupled to High Resolution Mass Spectrometry (Section 4.2.2).

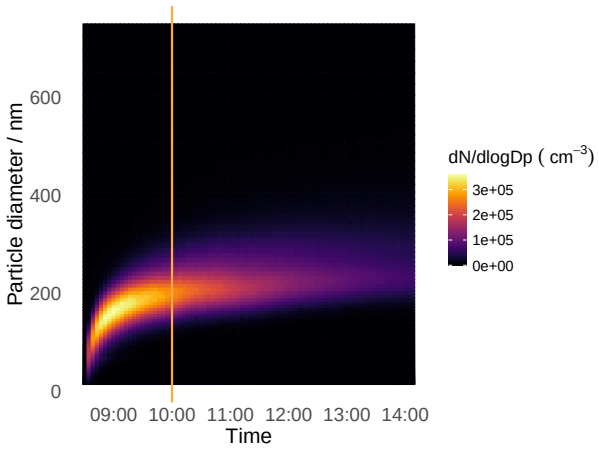

Figure 4.2: *SMPS particle number concentrations for the guaiacol GPM experiment conducted on 15-05-2023. The orange line represents the end of the box model period.*

For the night-to-day (NTD) and day-to-night (DTN) transitions, acidified ammonium sulfate seed was initially added using an atomiser (TSI, Model 3076) at a con-

centration of 50 μg m^{-3}, ≈ 200 ppb of guaiacol (≥ 99 %, Sigma Aldrich) was injected and the chamber was humidified at a relative humidity (RH) of 50 % throughout the experiment. The amount of NO_x and O_3 initially added depended on whether night or daytime conditions were being simulated, resulting in different VOC:NO_x ratios. For NTD experiments the roof was initially closed and approximately 200 ppb and 150 ppb of NO_2 and O_3 were added, respectively, for the production of NO_3 radicals (Table 4.3). After 4 hours the roof was then opened to observe the transition of night to day. For DTN experiments the chamber was initially irradiated with the roof open in the presence of 50 ppb of NO_x. After 4 hours the roof was closed and NO_3 radicals were generated from the addition of further NO_2 (20 ppb) and O_3 (100 ppb). Whilst the guaiacol precursor is not anticipated to react very quickly with O_3, it is possible that in the dark oxidation products of guaicol may react with O_3 due to the method used for NO_3 generation. Therefore, the nighttime chemistry may include both NO_3 oxidation and ozonolysis as generally occurs in the real atmosphere. In order to separate NO_3 chemistry future experiments may instead use N_2O_5 as the radical source. At the end of the roof open or roof closed period a filter was sampled at a flow rate of 12.5-13.1 L/min for 1 hour for offline analysis with Ultra-High-Performance Liquid Chromatography couple to High Resolution Mass Spectrometry (Section 4.2.2).

Table 4.3: *Initial experimental concentrations used in the guaiacol GPM, DTN and NTD experiments analysed in this Chapter*

ID	Guaiacol / ppb	O_3 / ppb	NO_2 / ppb	NO / ppb	HONO / ppb	VOC:NO_x
GPM	441	17	63	36	41	4.45
DTN	210	11	39	8	5.1	4.47
NTD	244	86	174	6	2.2	1.36

4.2.2 Ultra-High-Performance Liquid Chromatography coupled to High Resolution Mass Spectrometry

The offline filters were stored at EUPHORE until the end of the campaign before being transported on ice to the United Kingdom and characterised at the University of York using an Ultimate 3000 UHPLC (Thermo Scientific, USA) coupled to a Q Exactive Orbitrap MS (Thermo Fisher Scientific, USA) with heated electrospray ionisation (HESI).

As in Chapter 2 the filters were extracted based on the method used in Bryant et al. [144]. The 47 mm quartz filters were cut into 1 cm^2 pieces, placed in a 20 mL glass vial and 8 mL of methanol (LC-MS Optima Grade) was added. The resulting 8 mL solution was sonicated for 45 minutes, using ice packs to lower the temperature of the water bath. The methanol extract was transferred to a second 20 mL glass vial using a 0.22 μm syringe filter (Milipore) then 2 mL of methanol was used to wash through the syringe filter yielding a 10 mL extract. The 10 mL extract was subsequently dried using a Genevac vacuum solvent evaporator. The sample was reconstituted in 200-300 μL 90:10 H_2O (LC-MS Optima Grade): MeOH (LC-MS Optima Grade) for UHPLC-HRMS analysis.

Compound separation was achieved using a reversed phase C_{18} 2.6 μm × 2.1 mm × 10 mm Accucore column held at 40 °C. The mobile phase consisted of 0.1 % (v/v %) formic acid (Acros Organics) in water (A, LC-MS Optima Grade) and methanol (B, LC-MS Optima Grade). A gradient elution was used, starting at 90 % (A) with a 1 minute post injection hold, decreasing to 10 % (A) at 26 minutes before returning to the starting conditions at 28 minutes. A final 2 minute hold at 10 % (A) allowed the column to re-equilibrate. The flow rate was set to 0.3 mL $min^{-1}$and prior to analysis samples were stored in an autosampler tray at 4 °C. The injection volume was set to 4 μL. The HESI was operated under the following conditions: a spray voltage of 4 kV, a capillary and auxiliary gas temperature of 320 °C, a sheath gas flow rate of 45 (arb.) and an auxiliary gas flow rate of 10 (arb.) Spectra were acquired in negative and positive mode using $ddMS^2$. The scan range was set to a mass-to-charge ratio (m/z) of 85 to 750, with a mass resolution of 140,000. Tandem mass spectrometry was performed using a higher collision dissociation with a stepped normalised collision energy of 10, 20 and 45. In each scan the 10 most abundant species were selected for MS^2 fragmentation. The samples were analysed once with solvent blanks every 10 samples. Spectra were acquired from XCalibur 4.3 (Thermo Scientific, USA). However, there was significant contamination between different experiments from the filter collection line, therefore it is challenging to compare concentrations between experiments. This was especially observed for 4-nitroguaiacol.

4.2.3 Box modelling approach

Chamber box models of the guaiacol chamber experiments were run using the AtChem2 box model [331] coupled to the University of York's supercomputer, Viking2. AtChem2 is an open source zero-dimensional box model which can be used for experimental chamber studies as well as longer simulations associated with field campaigns. More information on the construction of AtChem2 can be found in Sommariva et al. [331]. The models were constrained to RH, temperature and the measured photolysis rate of NO_2 (J_{NO2}). The remaining photolysis rates were calculated by the MCM protocol based on the latitude and longitude coordinates of the EUPHORE chamber (39.551,-0.462) provided to AtChem2 [332]. However, to account for variation in photolysis rate due to cloud cover the calculated rates are scaled by a parameter referred to as JFAC. JFAC is calculated based on the ratio of the measured J_{NO2} compared to the MCM calculated J_{NO2}. However, it is important to note that the different wavelengths of light can be blocked to different extents therefore applying a generic JFAC term assuming equal changes in photolysis rate may lead to over or underestimations of photolysis rates. HONO as the OH source for the experiment was also constrained, using FTIR measurements, so OH could be accurately simulated, though there are no measurements to verify this. HONO constraints can also allow a good representation of NO_x in the chamber. For the mechanism development, the models were initially constrained to the constraints mentioned above and observational data of NO_x, O_3, formaldehyde (HCHO) and guaiacol to control the observable radical production. These constraints were either applied all together or individually, i.e. only constraining NO_x. However, it was concluded that not constraining to the additional experimental data resulted in an improved fit of the model to the experimental observations for species such as NO_x and O_3. Furthermore, by not constraining it was possible to observe where chemistry was missing or overpredicted which aided efforts to adjust the mechanism to fit the experimental data.

An auxiliary mechanism of the chemistry that can occur on the chamber walls from photolysis and wall deposition [333] was also inputted using the parameters described in Bloss et al. [295], Zádor et al. [334], previous University of York campaigns at the EUPHORE chamber and previous EUPHORE reference experiments available on the Eurochamp website. These reactions are detailed in Table 4.4.

Table 4.4: *Auxiliary mechanism added to the EUPHORE box modelling to account for wall chemistry in the chamber.*

Rate coefficient	Reaction
(JFAC × 1.62×10^7) + ((1-JFAC) × 1.40×10^7) molecules cm^{-3} s^{-1}	HCOOH production
$(3.1 \times 10^{17}) \times J_{NO2} \times e^{(-5686/T)} \times 3$ molecules cm^{-3} s^{-1}	HCHO production
$(7.3 \times 10^{21} \times J_{NO2} \times e^{(-8945/T)})$ + $(J_{NO2} \times (5.8 \times 10^8) \times (RH^{0.36}))$ molecules cm^{-3} s^{-1}	HONO production
JFAC × 3.86×10^6 molecules cm^{-3} s^{-1}	O_3 production
0.7×10^{-5} s^{-1}	NO_2 = HONO
1.6×10^{-5} s^{-1}	NO_2 = $wHNO_3$
J_{HNO3} s_{-1}	$wHNO_3$ = OH + NO_2
J_{NO2}× 2.46×10^9 molecules cm^{-3} s^{-1}	NO_2 production
(JFAC × 5.98×10^6) + ((1-JFAC) × 1.85×10^6) × 1.7 molecules cm^{-3} s^{-1}	NO production
JFAC × 6.4×10^{-5} s^{-1}	O_3 wall loss

4.2.4 Master Chemical Mechanism protocol

A fully explicit chemical mechanism can be impractical to use given the large number of reactions and products formed; therefore some simplifications are applied within the MCM development protocol making the MCM near-explicit [332, 335, 336]. These simplifications are the non-inclusion of low probability channels (i.e. < 5 %) which are then redistributed amongst other channels, parameterisation of RO_2 reactions with other RO_2 radicals and the simplification of oxidation product degradation schemes. For example, taking the addition of OH to aromatic rings, there are multiple possible addition points depending on the substituents present resulting in the formation of numerous RO_2 isomers. The permutations of such a large number of isomeric RO_2 species in self or cross RO_2 reactions therefore requires simplification to reduce the overall number of species in the MCM. Generally the MCM uses kinetic data that have been extensively reviewed eg. Atkinson and Arey [50], Atkinson and Carter [337], and Atkinson et al. [338], or, if available, more recent laboratory observations. However,

where neither recommendation nor experimental data exists, the rates are approximated. Most commonly, this is from Structure Activity Relationships (SARs) which apply a generic rate calculation that is modified depending on the functional groups present or the rate coefficient of a close analogue can be applied. This approach enables rate coefficients beyond the primary VOC degradation, i.e. for degradation products where it is more unlikely to have experimental data, to be approximated and hence the creation of a detailed chemical mechanism.

4.2.5 Development of a chemical mechanism

4.2.5.1 Structure Activity Relationships (SARs)

The mechanism development protocol was taken from the MCM as described in Section 4.2.4 and using the updated SAR protocols developed by Jenkin et al. [53, 339]. The rate coefficient for reaction with OH (k_{OH}) is derived by a summation approach using calculated partial rate coefficients for H-abstraction and OH addition to each potential site of attack. This approach also enables the attack distribution to be calculated for the evaluation of branching ratios on the first generation products. These branching ratios and overall rate coefficient are therefore used as the starting point for the mechanism development. The calculations from the initial SAR are presented in Eq 4.1 which shows the partial rate coefficients ($\times 10^{-12}$ cm^3 molecule^{-1} s^{-1}) and the summation to k_{OH}. The calculated k_{OH} of 6.99×10^{-11} cm^3 molecule^{-1} s^{-1} agrees well with experimental observations (7.53×10^{-11} cm^3 molecule $^{-1}$ s^{-1})[319].

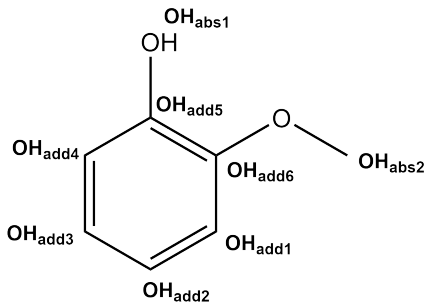

Figure 4.3: *Schematic of the structure activity relationship used to calculate k_{OH} for guaiacol.*

$$
\begin{aligned}
OH_{add1} &= k_{arom} \times F(o,m) \times R(o)_{OR} \times R(m)_{OH} = 17.136 \\
OH_{add2} &= k_{arom} \times F(m,p) \times R(m)_{OR} \times R(p)_{OH} = 4.313 \\
OH_{add3} &= k_t arom \times F(p,m) \times R(p)_{OR} \times R(m)_{OH} = 17.136 \\
OH_{add4} &= k_{arom} \times F(o,m) \times R(m)_{OR} \times R(o)_{OH} = 4.313 \\
OH_{add5} &= k_{ipso} \times F(o) \times R(o)_{OR} \times R(ipso)_{OH} = 16.679 \\
OH_{add6} &= k_{ipso} \times F(o) \times R(ipso)_{OR} \times R(o)_{OH} = 4.198 \\
OH_{abs1} &= k_{OHabs} = 2.6 \\
OH_{abs2} &= k_{OMeabs} \times F(-Ph) = 3.51 \\
k_{OH} &= \sum OH_{add1} + OH_{add2} + OH_{add3} + OH_{add4} \\
&\quad + OH_{add5} + OH_{add6} + OH_{abs1} + OH_{abs1} \\
&= 69.885 \times 10^{-12} cm^3 molecule^{-1} s^{-1}
\end{aligned}
\tag{4.1}
$$

By taking the ratio of the partial rate coefficients to k_{OH}, the initial branching ratios of OH addition and OH abstraction can be calculated. From the initial SAR the OH abstraction pathways are minor ($\leq$ 5 %) which would normally be ignored by the MCM protocol. For the H-abstraction of the OMe (OH_{abs2}) the branching ratio is $\approx$ 5 %, therefore this pathway, in agreement with the protocol, is disregarded; however, nitroguaiacol is a known reaction product from the H-abstraction of the OH group [94]. For this pathway a literature yield of nitroguaiacol (16 %) is used for the branching ratio assuming the resulting radical exclusively reacts with NO_2 to produce nitroguaiacol [94]. This is a similar approach to other phenolic compounds already in the MCM. However, this assumption ignores other possible products which may form via H-abstraction, such as, quinones [340]. The other first generation reaction products were derived following the aromatic degradation scheme in Jenkin et al. [339] and as shown in Figure 4.4 to produce a dihydroxyarene from the $k_{abs\text{-}O2}$ pathway, or an epoxide and a bicyclic peroxy radical from the $k_{add\text{-}O2}$ pathway. Because OH can add to the ring at multiple sites there are many isomers that can form; therefore, to calculate the branching ratios of the aforementioned first generation products, the site with the highest partial rate coefficient was chosen. As the ortho and para addition yield the same partial rate coefficient, the branching ratios for the ortho position were calculated (Figure 4.4). However, para addition of OH would yield similar results ($\pm$ 10 %).

Partial rate coefficients are calculated for the abstraction and addition of O_2 following the protocol of the Jenkin et al. [339] SAR. Branching ratios for the first generation products were then calculated as the ratio of $k_{abs\ O2}$ or $k_{add\ O2}$ to k_{TOT} (Equation 4.2).

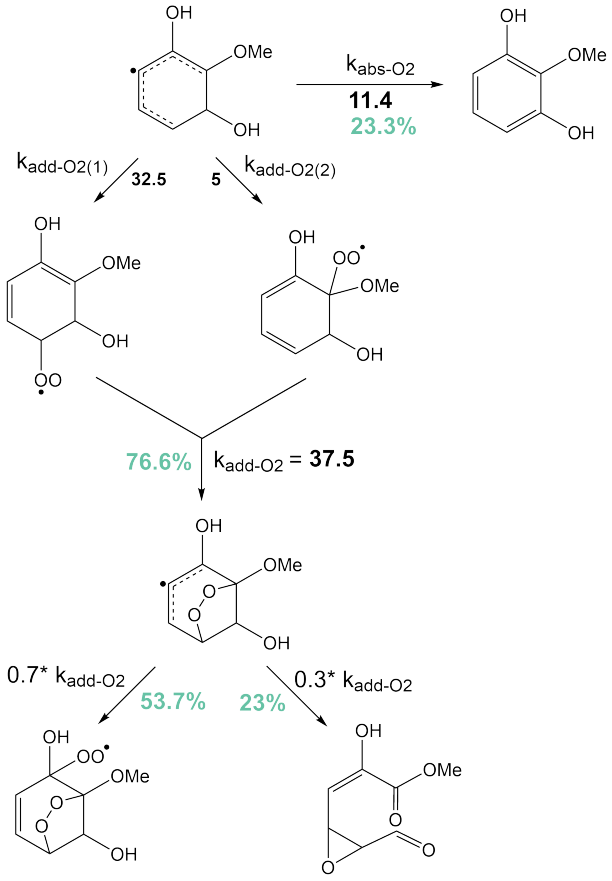

Figure 4.4: *Degradation of the resulting hydroxyarene radical formed from OH addition at the ortho position for the calculation of 1st generation branching ratios. The numbers in bold black font represent the partial rate coefficients (× 10^{-12} cm^3 molecule^{-1} s^{-1}) for the abstraction pathway ($k_{abs\text{-}O2}$) or O_2 addition pathway to form a bicyclic radical ($k_{add\text{-}O2}$). The percentages in blue represent the branching ratio of each pathway as a percentage of the total rate coefficient ($k_{abs\text{-}O2}$ + $k_{add\text{-}O2}$).*

$$
\begin{aligned}
k_{absO2} &= 11.4 \\
k_{addO2} &= 5 \times \frac{F_4}{\sqrt{2}} \times \frac{F_5}{\sqrt{2}} = 32.5 \\
k_{addO2} &= 5 \times \frac{F_1}{\sqrt{2}} \times \frac{F_2}{\sqrt{2}} = 5 \\
k_{TOT} &= \sum k_{absO2} + k_{addO2} = 48.9
\end{aligned}
\tag{4.2}
$$

However, the Jenkin et al. [339] SAR does not account for the formation of catechol which has been reported as an oxidation product from OH chemistry [309, 326].

Kroflič et al. [326] suggest the catechol formation route involves OH addition in the ipso position to the OMe group and the subsequent addition of water where methanol is lost as a by product. However, the addition of water to the ring will be competing with the addition of O_2 which is likely to be the dominant reaction producing the bicyclic peroxy radical. Furthermore, GPM experiments were performed under dry conditions (RH < 1%) so the concentration of catechol formed from oxidation could be quite low relative to the amount which is present as an impurity of guaiacol. From the SAR shown in Eq 4.1 the branching ratio for catechol formation is calculated from the contribution of the methoxy ipso OH addition partial rate coefficient (OH_{add6}) to the total rate (k_{OH}). This yielded a branching ratio of 6 % for the catechol formation route. Using the ratios in Figure 4.4 the remaining branching ratios are recalculated after subtracting the 6 % of catechol and 16 % of nitroguaicol formation.

To determine the reactions of RO_2 species produced from the initial OH addition reaction the Jenkin et al. [53] SAR was used. RO_2 can undergo several bimolecular reactions with species such as NO, NO_2, HO_2 and NO_3, as well RO_2-RO_2 cross and self reactions including intramolecular rearrangements followed by autoxidation. The rates of these reactions ultimately depend on the ambient conditions and the RO_2 structure. The rates of RO_2 with species such NO, NO_2, HO_2 and NO_3 are already built in to the MCM from previous SARs. However, where updated branching ratios are provided for these reactions, which typically depend on the RO_2 structure (i.e. primary, secondary, tertiary), then these new values are applied. For RO_2 cross and self reactions to form carbonyls, alcohols, peroxides and alkoxy radicals the equations to determine the rate coefficient and branching ratios in the updated Jenkin et al. [53] are implemented. Future work and SARs should aim to incorporate a parameterisation for potential intramolecular RO_2 chemistry.

Finally, a rate for the reaction of guaiacol with NO_3 was calculated from the fully explicit GECKO-A generator [341]; however, it is several orders of magnitude lower than the reaction with OH and was deemed inconsequential in the observed chemistry from the guaiacol GPM experiment. An experimental literature rate coefficient for this NO_3 reaction (3.2×10^{-12} cm^3 $molecule^{-1}$ s^{-1} at 298 K) [313] was higher than the GECKO-A calculation but remains one order of magnitude lower than the OH rate coefficient. However, the addition of NO_3 chemistry in future work would be of value

for the NTD and DTN experiments. Applying these equations [53, 339], the MCM protocol rules [332, 335, 336], and using the existing MCM aromatic mechanisms as a guide, the mechanism shown in Figure 4.5 was produced.

As can be observed from the mechanism in Figure 4.5, most species are not already included in the MCM. Therefore, further SARs for guaiacol oxidation products were carried out to determine reaction rates with OH in subsequent degradation. For example, a subset of OH chemistry was added for the first generation OH addition product (i.e a dihydroxyarene), referred to as OMCATECHOL in Figure 4.5. This added chemistry is shown in Figure 4.6 and indicates further SARs are required for the degradation of OMCATECHOL oxidation products. An additional k_{OH} rate coefficient calculated in the same way as shown in Eq. 4.1 was also supplied for the degradation of the second generation OH addition product, OMBENZ135OH.

In total the mechanism proposed for guaiacol in this work contains 414 reactions and 134 species. In comparison, the atmospheric degradation scheme for isoprene in the MCM contains is significantly more complex with 1974 reactions and 610 species. However, compared to the MCM mechanism for benzene degradation, the guaiacol mechanism has a similar number of reactions (454) and species (157). It is important to note, however, there are further reactions of guaiacol with NO_3 to be incorporated. The guaiacol mechanism used in the AtChem2 box modelling of the EUPHORE experiments described in Section 4.2.3 is provided in Appendix A.

4.2.5.2 Methods for mechanism evaluation

The newly developed mechanism, presented in Figure 4.5 and Figure 4.6, was evaluated by comparing the experimental data from the EUPHORE guaiacol photo-oxidation GPM experiment to the modelled concentrations from chamber box models (Section 4.2.3). Time profiles of key inorganics, oxidation markers and guaiacol decay were used for comparison. This included species such as NO, NO_2, O_3, HCHO, nitric acid (HNO_3), and glyoxal (GLYOX). Furthermore, oxidation products shown in Figures 4.5 and 4.6 were compared to I-CIMS and PTR-MS measurements. However, as there are no calibrations for these compounds only the shapes of the time profiles between modelled and measured data are compared to confirm the rates of production and loss of each product are occurring at the correct timings in the experiment.

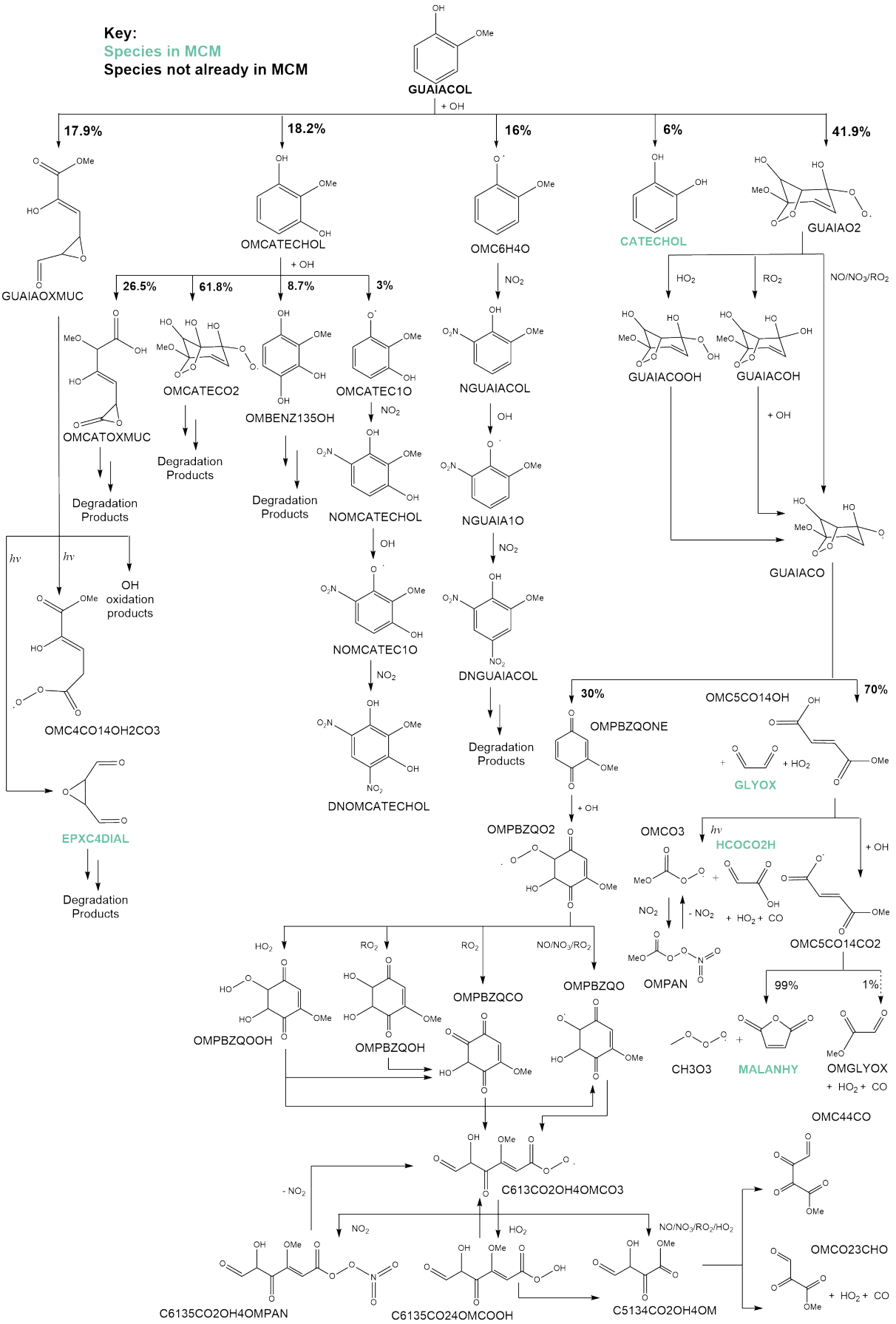

Figure 4.5: *Guaiacol OH degration scheme produced by the protocol in Section 4.2.5.1 until the 4th generation*

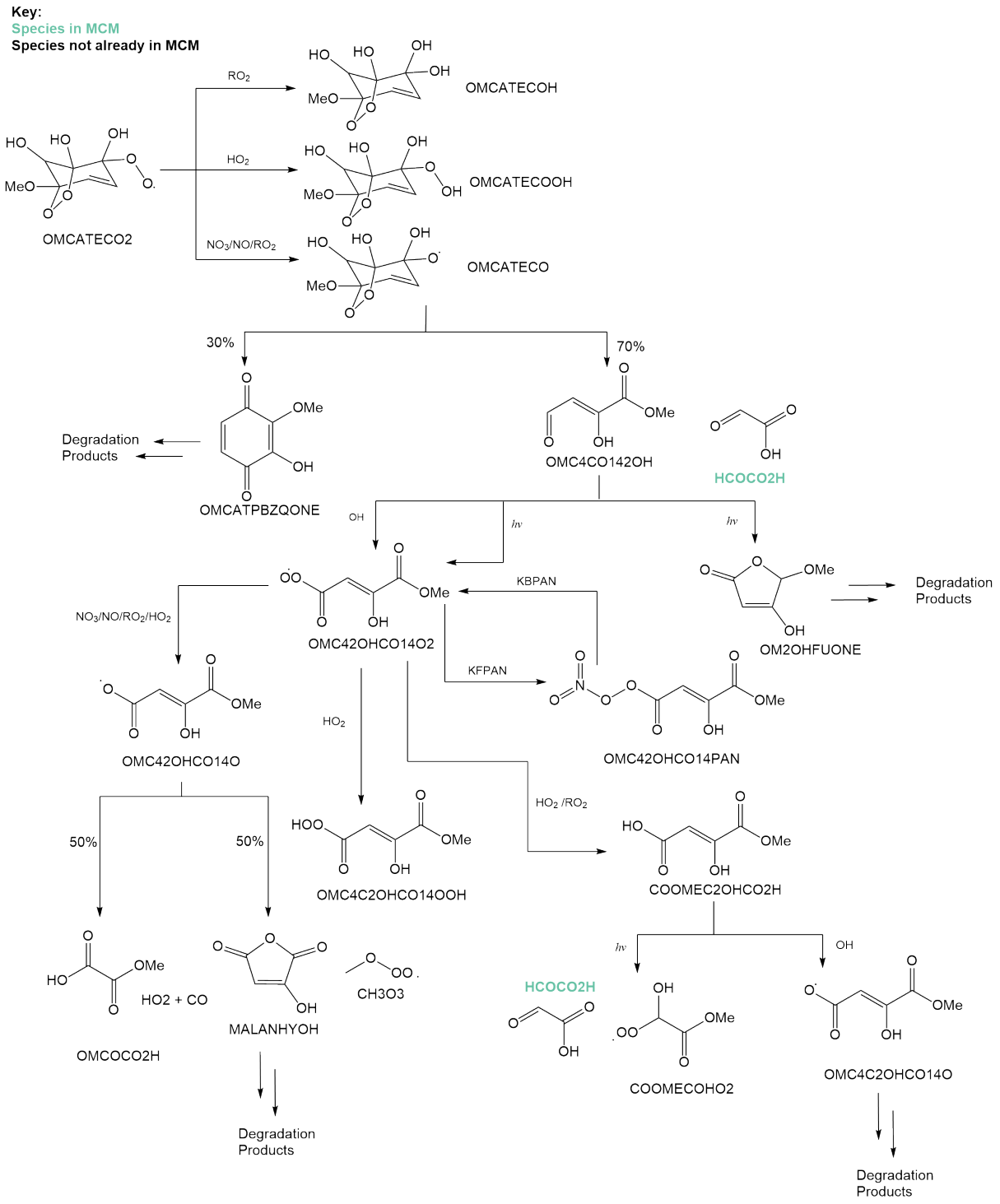

Figure 4.6: *Additional OMCATECHOL OH degration scheme produced following the protocol in Section 4.2.5.1 for guaiacol*

4.3 Results

4.3.1 Evaluation of the guaiacol mechanism

Using the initial chemistry presented in Figure 4.5 the modelled concentration of guaiacol shown in orange in Figure 4.7 is overpredicted by over 100 ppb compared to the FTIR measurement. However, after the inclusion of the OMCATECHOL chemistry the modelled guaiacol concentration (blue trace) is improved compared to the measurement in Figure 4.7. The guaiacol overprediction remains, but is reduced to 64 ppb. This indicates the propogation of the OMCATECHOL RO_2 is an important degradation pathway within the mechanism for increasing reactivity of the initial precursor.

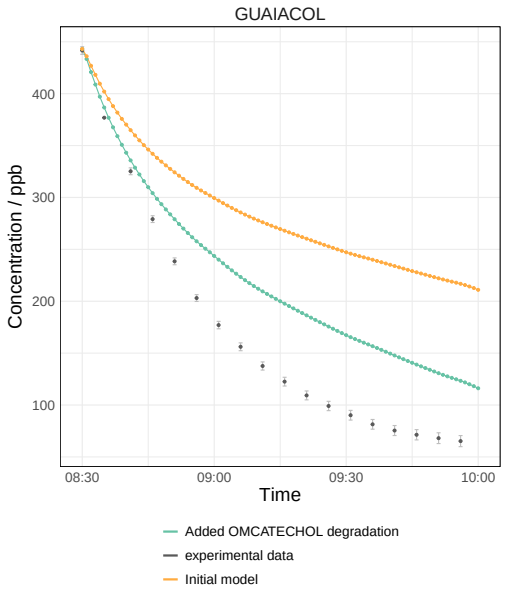

Figure 4.7: *Comparison of the observed guaiacol concentration (black) with the modelled concentrations using the initial guaiacol mechanism (orange) and after adding the OMCATECHOL chemistry in Figure 4.6 (blue). Error bars indicate the error on the measurement.*

An analysis of the top OH production reactions was undertaken in the model before and after adding the OMCATECHOL degradation scheme shown in Figure 4.6 and observed that the addition of this chemistry increased the overall OH production rate from HO_2 chemistry. From Figure 4.8, this is primarily the reaction of HO_2 with NO but towards the end of the experiment it can be seen to also react with O_3 to form OH. This indicates the OMCATECHOL RO_2 further propagates the HO_x cycle to produce more OH in the system hence depleting the initial guaiacol precursor at a faster rate

than in the initial scheme. However, further work is required to close the gap between modelled and measured concentrations. Using the literature k_{OH} rate coefficient which is faster than the SAR calculation in Eq 4.1, the guaiacol decay is slightly improved, but still underestimates the guaiacol loss compared to the measurement by 44 ppb. This overall indicates there is some missing reactivity as already mentioned in the construction of the mechanism and as shown in Figures 4.5 and 4.6.

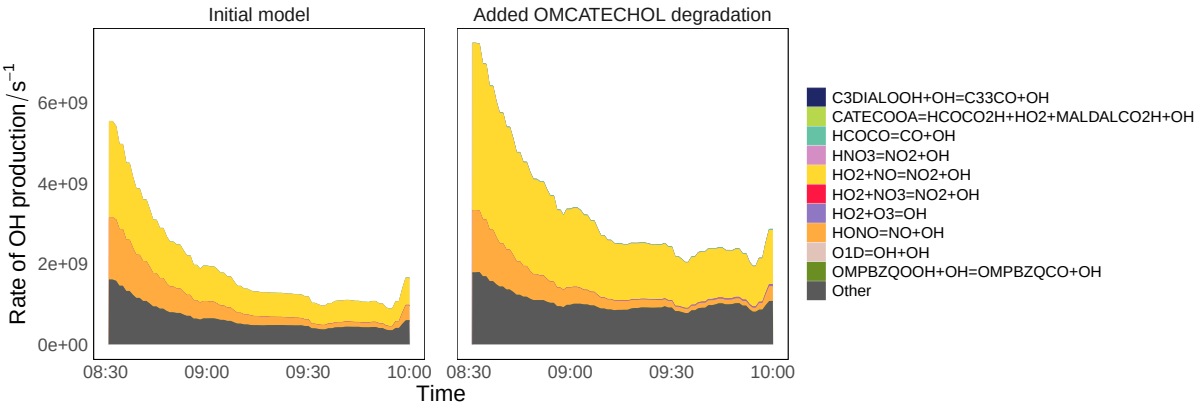

Figure 4.8: *Top 10 reactions contributing to OH production within the model in the initial model with the initial guaiacol chemistry (orange data in Figure 4.7) and after inclusion of OMCATECHOL degradation mechanism (blue data in Figure 4.7)*

From Figure 4.7 it is evident that the OMCATECHOL chemistry is important for guaiacol degradation. However, using the branching ratios from the SAR calculated in Section 4.2.5.1 there is still further improvement required due to a significant over-prediction of glyoxal concentrations (the blue model in Figure 4.9) of approximately 50 ppb. Bloss et al. [327] report in MCM v3.1 the 1,2-hydroxyarene is the dominant product compared to the nitro-product and quinone yielding pathways for phenolic compounds. As shown in Figure 4.5 the only known source of glyoxal is via the guaiacol RO_2 (GUAIAO2) pathway. However, other possible glyoxal sources may exist in the degradation of later generational compounds. In order to constrain the mechanism to the observed glyoxal concentrations the branching ratios between the GUAIAO2 pathway and the OMCATECHOL formation pathway were adjusted. Figure 4.9 shows the effect of increasing the OMCATECHOL formation pathway by decreasing the branching ratio of GUAIAO2. There is a relatively minimal impact on the guaiacol decay or formation of HCHO, HNO_3 and O_3. However, the fit of the modelled NO_2 decay with

the experimental data improves, especially in the latter stages of the model, as the OMCATECHOL pathway increases and as the GUAIAO2 pathway decreases with optimal fitting at a 30 % increase or decrease respectively (red model in Figure 4.9). In real terms this means the branching ratios in Figure 4.5 are now 17.9 % (GUAIAOXMUC), 48.2 % (OMCATECHOL), 16 % (OMC6H4O), 6 % (CATECHOL) and 11.9 % (GUAIAO2). As anticipated, the largest impact of changing the branching ratios is on the prediction of glyoxal, changing by almost 10 ppb at each 10 % increase, with an improved fit as the OMCATECHOL branching ratio increases. Yet, at the 30 % increased branching ratio there is still an overprediction of the modelled glyoxal (≈ 10 ppb).

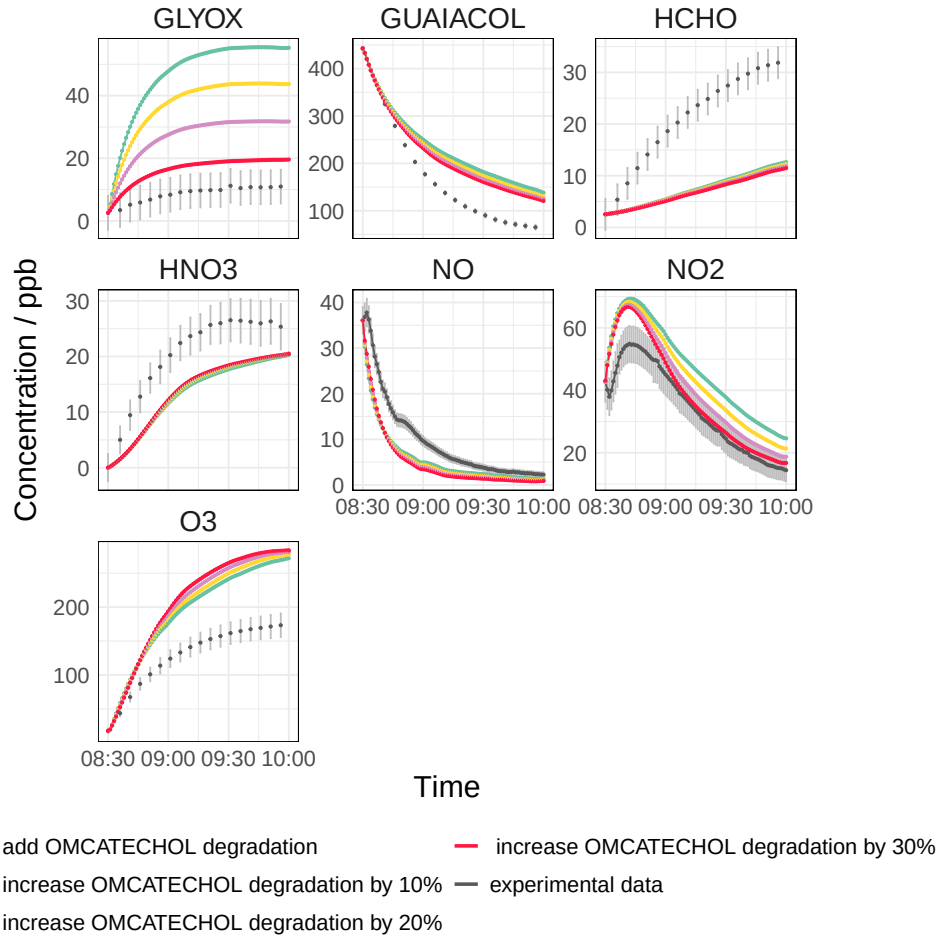

Figure 4.9: *Comparison of the observed concentrations of glyoxal (GLYOX), guaiacol (GUAIACOL), formaldehyde (HCHO), nitric acid (HNO3), NO, NO_2 and O_3 (grey) with increasing proportions of the OMCATECHOL branch contributing to the mechanism and reducing contribution of the RO_2 pathway (GUAIAO2). Error bars indicate the error on the measurement.*

Furthermore, in the red model shown in Figure 4.9 it is clear there is still missing

OH reactivity from the guaiacol decay, with a difference of ≈ 58 ppb between modelled and measured guaiacol concentration, and at the same time an overprediction of O_3 (≈ 110 ppb). In Figure 4.9 the initial formation of NO_2 is also too fast indicating the rate of NO-NO_2 conversion via reactions with RO_2 is too quick and other OH production pathways such as RO_2 isomerisation [327] and autoxidation may be required to increase reactivity whilst reducing NO-NO_2 conversion. Existing aromatic degradation schemes in the MCM have similar known deficiencies [295]. These are an overprediction of O_3 from missing OH reactivity and underprediction of OH concentration, as well as, underprediction of NO oxidation rate i.e. NO reactions with peroxy radicals (RO_2). The missing reactivity and O_3 overestimation shown here for guaiacol are on a similar magnitude to those in Bloss et al. [295] for toluene, p-xylene and 1,3,5-trimethylbenzene.

From the mechanism in Figure 4.5 the only known production of glyoxal occurs at the degradation of the guaiacol alkoxy radical (GUAIACO) to form either a quinone product (OMPBZQONE) or an unsaturated dicarbonyl product (OMC5CO14OH). The branching ratios presented in Figure 4.5 for this reaction are taken from the observed relative branching ratios for toluene in Bloss et al. [295]. Using the 30 % increased OM-CATECHOL model (red model in Figure 4.9) the ratio of OMPBZQONE:OMC5CO14OH was adjusted from the original 30:70 ratio shown by the red model to 70:30 as shown in Figure 4.10.

Increasing the ratio to favor the formation of OMPBZQONE reduces the production of glyoxal with an optimal fit at 70:30 in the green model. There is no effect of this ratio on the prediction of the other inorganic species, therefore, this model is considered the final optimised mechanism. There is still an underprediction of the guaiacol decay and overprediction of O_3 which has been linked with missing OH reactivity; therefore, more SARs and experimental studies are needed to evaluate second-generation products or confirm the reaction rate of guaiacol with OH as there is only one experimental study in the literature [319].

A study of the rates of production and loss of RO_2 was carried out to understand the dominant reactions propagating the chemistry. Figure 4.11 shows the top 9 reactions as a percentage of the total instantaneous RO_2 production (Figure 4.11a) or loss Figure 4.11b). Reactions outside the top 9 are shown as a lumped sum "other" in

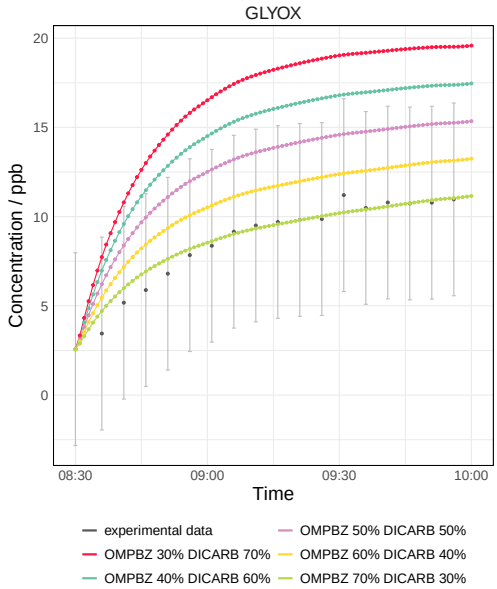

Figure 4.10: *Comparison of the observed concentrations of glyoxal from FTIR (grey) with increasing proportions of the quinone product (OMPBZ) to the dicarbonyl product (OMC5CO14OH or DICARB) from the GUAIAO2 degradation pathway.*

Figure 4.11. In both cases the RO_2 formed from OMCATECHOL degradation are the greatest contributors after the initial formation of OMCATECHOL via the GUAIACOL + OH reaction. This indicates that OMCATECHOL degradation is important for radical propagation in the system and therefore agrees with the improved guaiacol decay through inclusion of this chemistry (Figure 4.7).

Interestingly, despite the formation of CATECHOL as a relatively small branch (6 %) the reaction of nitrocatechol is important for the generation of nitrogenated RO_2 (Figure 4.11a) which has implications for SOA formation given the high SOA yield of catechol and low volatility of nitrocatechol [325]. Furthermore, Chapter 3 shows nitrocatechol contributes to the SOA formation from wood burning which indicates guaiacol as a potentially important SOA precursor in the Chapter 3 experiments. Quinones are known toxic species [96] and the contribution of quinone derived species to RO_2 production in Figure 4.11a such as OMPBZQO2 may have significant implications for toxicity with the formation of increasingly oxidised quinone type species. Furthermore, in both RO_2 production and loss (Figure 4.11) peroxyacetylnitrate species (PANs) are important and may be of significance for ambient biomass burning plumes, where injection of plumes into the free troposphere at higher altitudes and colder temperatures could allow PANs to be transported over large distances [110]. The trans-

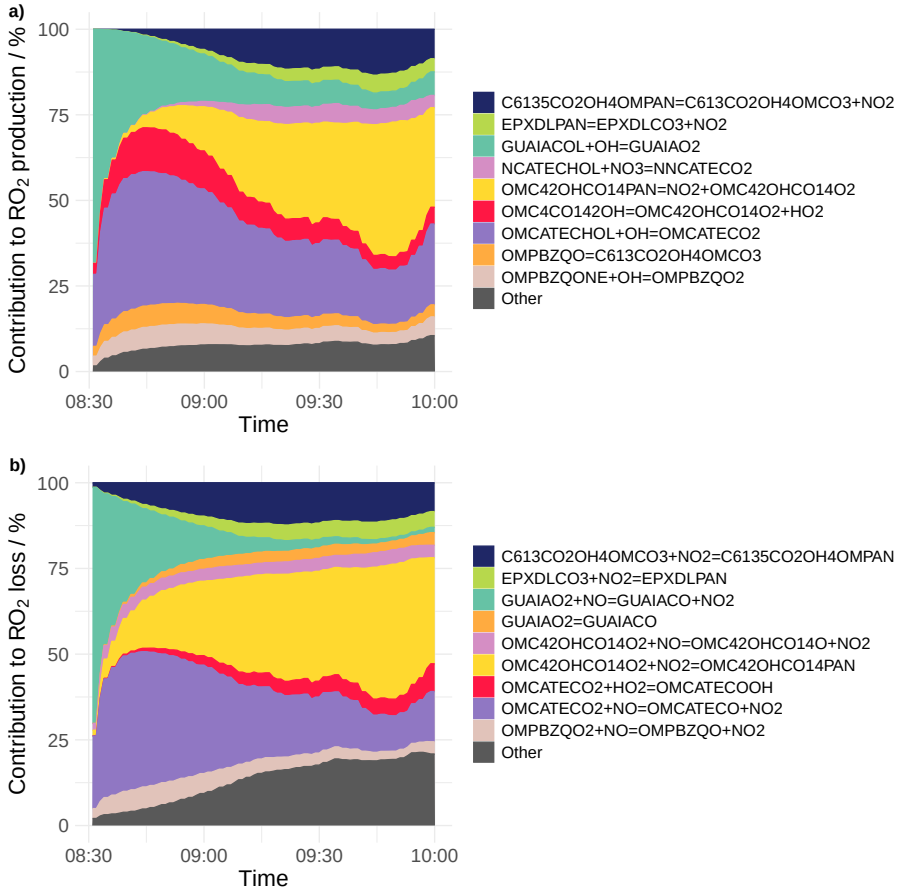

Figure 4.11: *a) Top reactions contributing to RO_2 production in the modelled GPM experiment as a proportion of the total rate of RO_2 production. b) Top reactions contributing to RO_2 loss in the modelled GPM experiment as a proportion of the total rate of RO_2 loss.*

portation of PANs from biomass burning is a large reservoir of NO_x that may impact on the tropospheric O_3 production in the remote atmosphere where the O_3 budget is driven by NO_x rather than VOCs [342]. Tropospheric O_3 has important implications for climate and air quality as it is a greenhouse gas [343, 344] and photolysis of O_3 is a major source of OH radicals [39] thereby influencing the oxidising capacity of the atmosphere and the loss of other important greenhouse gases.

Typically, the dominant loss of RO_2 is through reactions with NO [53] as seen in the early stages of Figure 4.11b, however, as NO is used up (Figure 4.9) the contribution of "other" RO_2 loss routes increased which were largely RO_2/RO_2 cross and self reactions. The dominant products of these "other" RO_2/RO_2 reactions in Figure 4.11b are alkoxy radicals which typically form carbonyl products in subsequent reactions [345]. These "other" reactions may also be important for later stage SOA formation from guaiacol

oxidation from the production of large low volatility peroxide dimers [346]. These "other" RO_2/RO_2 reactions therefore may become important as the biomass burning plume ages and the NO_x concentrations decreases, with Takegawa et al. [347] reporting in an ambient plume a short NO_x lifetime of 0.1-0.3 days.

4.3.2 Identification of oxidation products

I-CIMS and PTR-MS were used to measure the realtime formation of guaiacol oxidation products from the mechanism presented in Figure 4.5. There are no standards for the I-CIMS or PTR-MS data, therefore the species response is measured in normalised counts per second (ncps). ncps for I-CIMS was calculated by dividing the counts per second of the oxidation product by the sum of the reagent ions (I^- and H_2IO^-) at the same timestamp. It is important to consider that the I-CIMS and PTR-MS may be more sensitive to different chemical spaces and therefore care must be taken when analysing the measured signals of guaiacol oxidation products. An intercomparison of the I-CIMS and PTR-MS was taken to evaluate the trends observed by each instrument for any common detected oxidation products (Figure 4.12). For 4 of the 6 common compounds between the two measurements, both instruments largely report the same trend in their formation and evolution in Figure 4.12 but PTR-MS measurements of catechol do indicate the presence of a potential impurity [326] which is present in all guaiacol experiments presented throughout this Chapter. Furthermore, it is possible to see a small increase in the catechol I-CIMS signal before the roof is opened after the initial addition of guaiacol to the chamber but this signal is 3 orders of magnitude lower than during the oxidation experiment and therefore not clearly visible in Figure 4.12. Further work is needed to quantify the production of catechol from guaiacol or the magnitude of the potential impurity observed in these experiments.

There are also significant exceptions for GUAIAOXMUC and OMPBZQONE. For GUAIAOXMUC there are two other known products in the guaiacol mechanism at the same mass. GUAIAOXMUC, OMPBZQOH and OMBENZ1345OH all have *m/z 172* and the same molecular formula of $C_7H_8O_5$. The modelled concentrations of these compounds are presented in Figure 4.13 which shows the increase in each product at different times in the experiment, with GUAIAOXMUC as a first generation, and OMPBZQOH and OMBENZ1345OH as third generation products. However, there is

little formation (< 1 ppb) of OMPBZQOH. Compared to the modelled timeseries in Figure 4.13 the PTR-MS signal shown in Figure 4.12 resembles more closely that of the OMBENZ1345OH product whereas the I-CIMS data agrees more closely with that of the GUAIAOXMUC epoxide. The sum of the profiles show the main contributor to the total concentration at this *m/z* is GUAIAOXMUC. This example shows the advantage of having chromatographic separation prior to mass spectral measurement, which would improve the mechanism evaluation of these compounds.

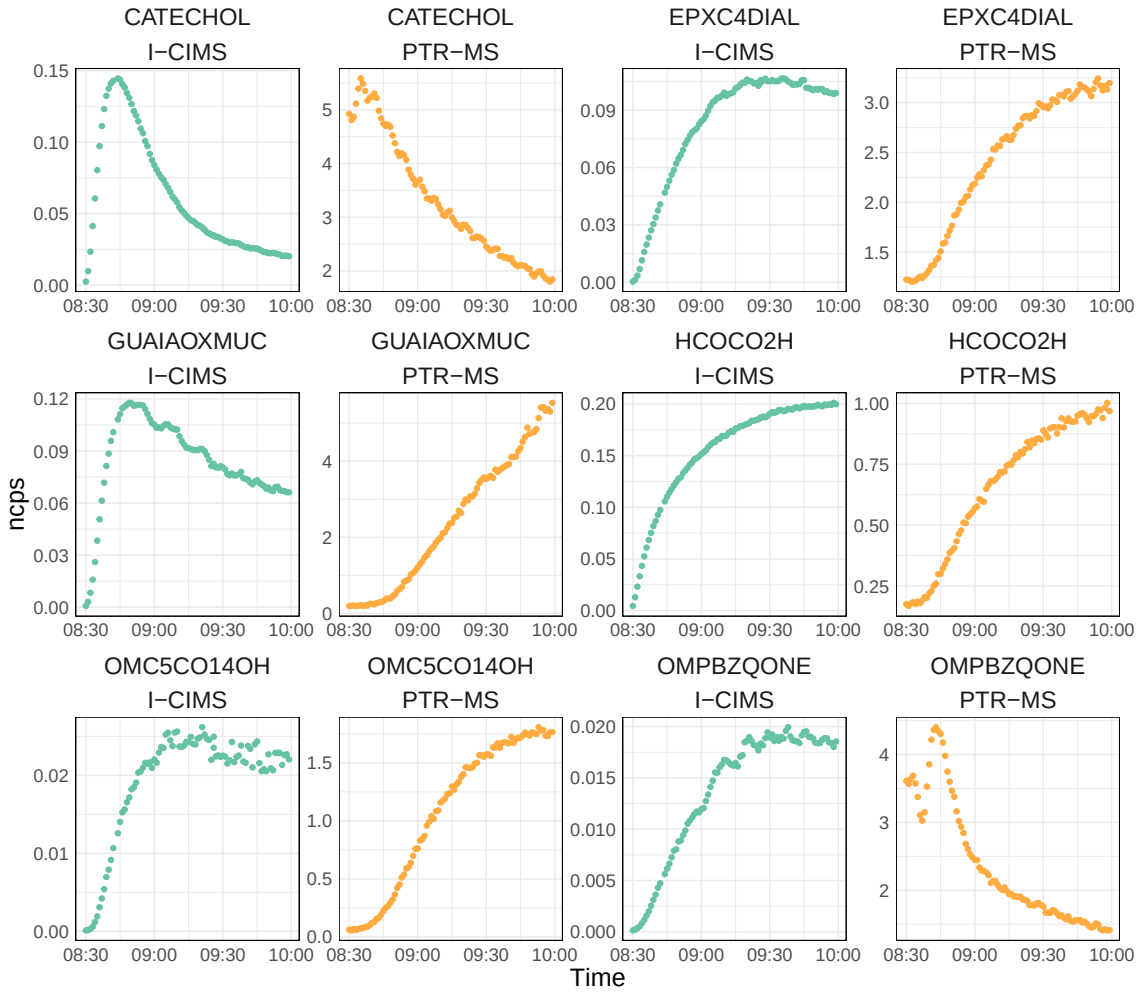

Figure 4.12: *Intercomparison of the guaiacol oxidation products measured by I-CIMS and PTR-MS for the model duration period of the gas phase mechanism experiment on 15-05-2023.*

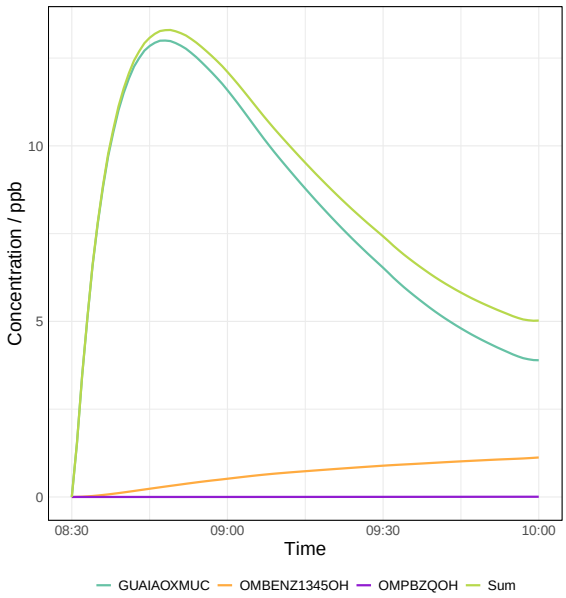

Figure 4.13: *Modelled concentrations of the evolution of m/z 172 oxidation products for the gas phase mechanism experiment on 15-05-2023*

Figures 4.14 and 4.16 show the timeseries of first and second generation oxidation products identified during the photo-oxidation GPM experiment with the modelled data shown in grey and the mass spectral data in colour for each compound. As there are no available standards for quantification the profile is compared between the modelled MCM concentrations in parts per billion (ppb) on the left axis and the species response measured by I-CIMS or PTR-MS in normalised counts per second (ncps) on the right axis. Note that the products from the bicyclic peroxy radical route, such as GUAIACOH and GUAIACOOH, were considered to be second generation after consulting the modelled timeseries data and are hence not presented in Figure 4.14.

Generally the measured profiles of the first generation products show good agreement with the modelled concentration profiles in Figure 4.14. However, there are some deviations between the modelled and measured profiles.

Firstly, it can be seen that the rate of production of NGUAIACOL is faster than observed. NGUAIACOL is a lower volatility compound and is likely to be in the aerosol phase as a previous study observed nitroguaiacol as the dominant particle phase product [94]. NGUAIACOL in the form of 4-nitroguaiacol could be identified using an authentic standard in UHPLC-HRMS analysis (Figure 4.15) indicating the deviation in Figure 4.14 could be due to gas-to-particle partitioning. Secondly, after the first 30 minutes there is a deviation in the comparision between modelled GUAIAOXMUC

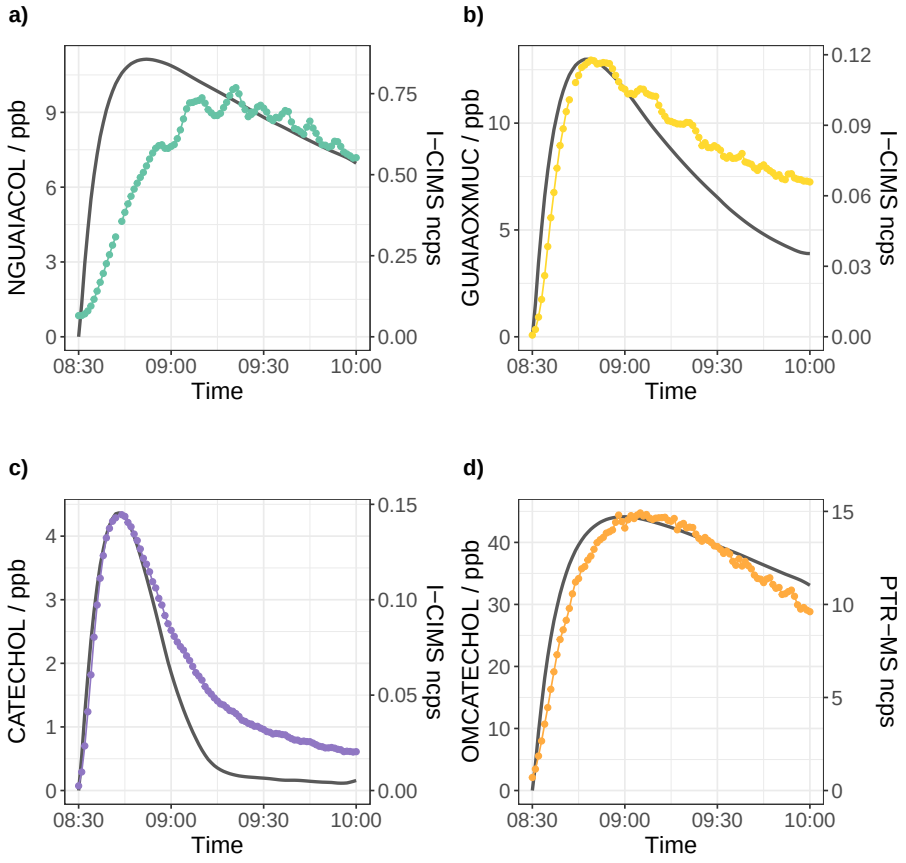

Figure 4.14: *Comparison of the modelled concentrations (grey) of 1st generation oxidation products from Figure 4.5 to the detected I-CIMS signal in normalised counts per second (ncps) shown in colour for each species.*

concentrations and the I-CIMS signal for the detected $C_7H_8O_5I^-$ ion. As already mentioned and shown in Figure 4.13 there are other oxidation products forming at the same *m/z* that may also contribute to the I-CIMS signal resulting in some deviations in the agreement. For instance, at 09:00 UTC when the deviation starts to occur in Figure 4.14 the OMBENZ1345OH product begins to increase (Figure 4.13) which could contribute to the slower decay in the I-CIMS signal. However, the sum of all modelled at *m/z* 172 products produces a similar profile (Figure 4.13) and indicates there are other missing oxidation products. Catechol was unfortunately unable to be quantified by either mass spectrometry measurements or FTIR, however, the modelled profile shows it is significant source of reactivity rapidly decaying 15 minutes (08:45 UTC) into the experiment. In the case of FTIR the catechol concentration was thought to be too low for quantification.

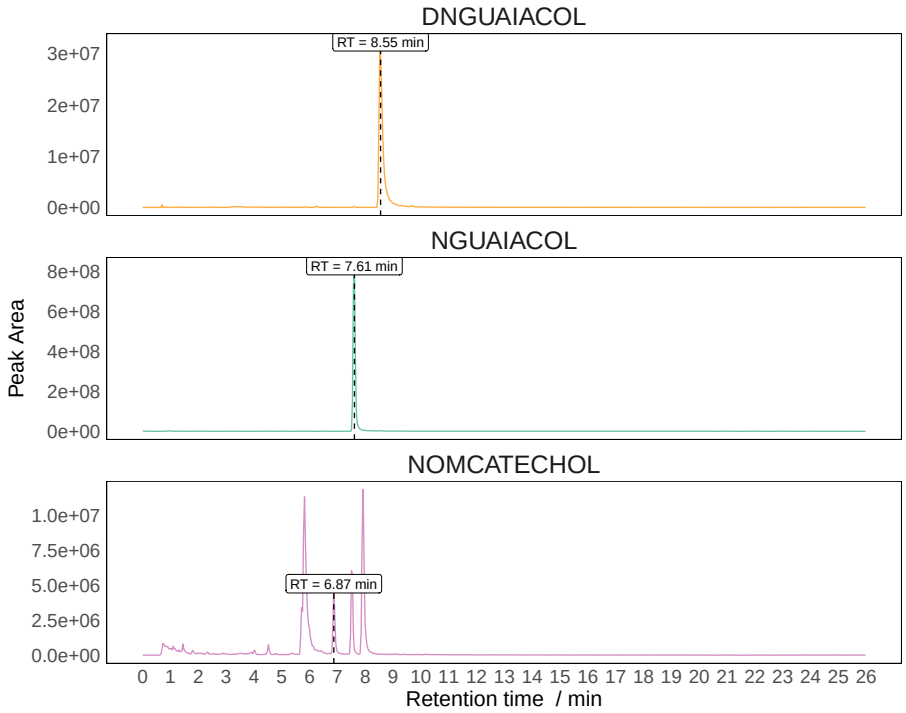

Figure 4.15: *Chromatograms of the guaiacol nitroaromatic oxidation products in the aerosol phase detected by the UHPLC-HRMS analysis*

Similarly the I-CIMS measurement of second generation products also show good agreement with the modelled concentration profiles (Figure 4.16). However, deviations between the model and measurement occur again for nitrocompounds such as DNGUAIACOL and NOMCATECHOL. Although for NCATECHOL the modelled and measured I-CIMS profiles are in agreement. Note that the measured ncps for the GUAIACOH product is noisy towards the end of the modelled period due to a peak fitting drift but overall has a similar trend to the model. The I-CIMS measurement timeseries in Figure 4.16 for HCOCO2H shows a faster production than would be expected for a third generation product of guaiacol. However, it is an early decomposition product from the OMCATECHOL RO_2 (OMCATECO2) in Figure 4.6 and the improved fit in this profile after addition of the OMCATECHOL degradation adds further support to the inclusion of the OMCATECHOL chemistry into the mechanism as an important source of reactivity.

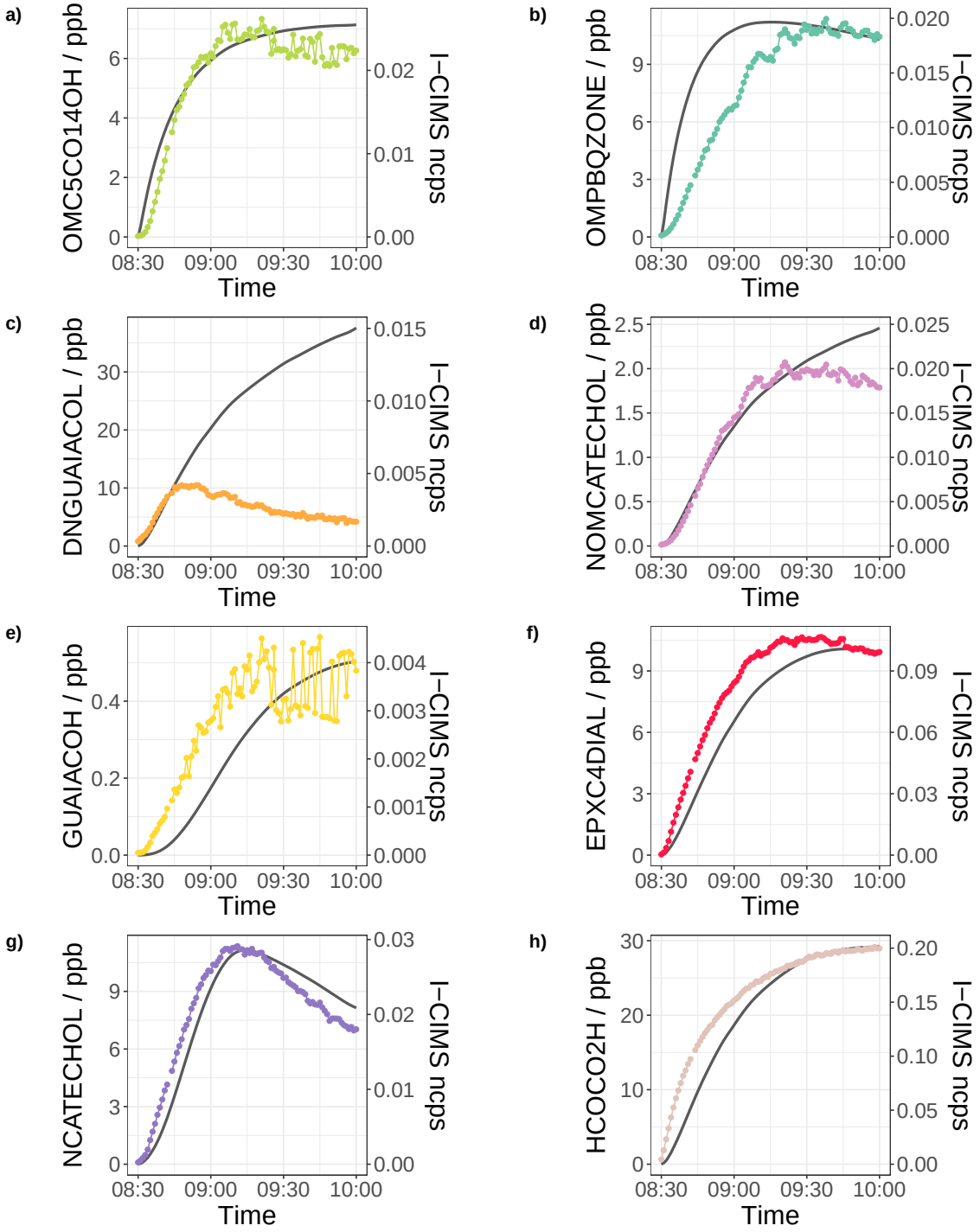

Figure 4.16: *Comparison of the modelled concentrations (grey) of 2nd generation oxidation products from Figure 4.5 to the detected I-CIMS signal in normalised counts per second (ncps) shown in colour for each species.*

At 08:45 UTC the NCATECHOL profile shows a significant increase as catechol simultaneously decays in Figure 4.14. For DNGUAIACOL which contains two nitro groups the deviation occurs within 15 minutes and after 1 hour for NOMCATECHOL

which contains only one nitro group. The nitro group functionality again indicates these compounds as likely candidates for SOA formation and as observed in Chapter 3 C_6-C_8 nitroaromatics were the main contributors to the aromatic organonitrogen (CHON) mass in aged OA from wood burning. DNGUAIACOL and NOMCATECHOL were observed in UHPLC-HRMS analysis (Figure 4.15) and suggest nitroaromatic compounds are important in the early stages of SOA formation in this guaiacol + OH system. Similar to NGUAIACOL the model is not accounting for gas-to-particle partitioning which could result in the observed profile difference.

4.3.3 Guaiacol SOA yield

It is clear that guaiacol can rapidly produce SOA from the particle number concentration timeseries shown in Figure 4.2 and the presence of certain nitroaromatic oxidation products in offline UHPLC-HRMS analysis (Figure 4.15). The guaiacol SOA yield (Y) was calculated according to Equation 4.3 using the mass of SOA formed from SPMS in μg m^{-3} (ΔSOA) and the amount of guaiacol reacted in μg m^{-3} (ΔVOC). In this experiment the SOA yield is described as the homogeneous nucleation yield and was calculated to be 0.15 which is less than previously reported at similar concentrations of guaiacol (0.54-0.65) [94, 320]. However, Lauraguais et al. [94] conduct the experiments under dry conditions, Liu et al. [320] used an oxidation flow reactor and the NO_x concentrations were different which may be important in the formation of SOA for phenolic compounds [320]. Over a wider range of guaiacol concentrations and in seeded or unseeded experiments previous studies have reported yields of 0.003-0.87 [94, 309, 320]. Therefore, it is evident that further experiments are required over a greater range of conditions than that studied here to accurately determine the SOA yield.

$$Y = \frac{\Delta SOA}{\Delta VOC} \tag{4.3}$$

4.3.4 Evolution of guaiacol products between night and day

At present, many studies experimentally evaluate biomass burning chemistry in the presence of one oxidant, and there are few studies analysing the transitions in SOA composition between day and night. Understanding this transition is important for

the oxidation of real word emissions in the atmosphere over the course of 24 hours. Furthermore, in the case of biomass burning events such as wildfires the active emission period can exist over numerous days and certain plumes have been described as optically thick, meaning there is a significant contribution of dark aging processes during the plume transport despite "daytime" emission [113]. As well as domestic combustion occurring predominantly at night [238]. Therefore, the day-to-night (DTN) and night-to-day (NTD) experiments described in Section 4.2.1.2 and Table 4.3 aimed to understand the changes in chemical regime and resulting differences in the SOA composition formed between these two transitions. The SOA composition was monitored online by FIGAERO-I-CIMS and offline by UHPLC-HRMS. Figure 4.17 shows the timeseries of the guaiacol precursor, NO_x and O_3 for each experiment where the vertical line represents the change between day or night chemistry.

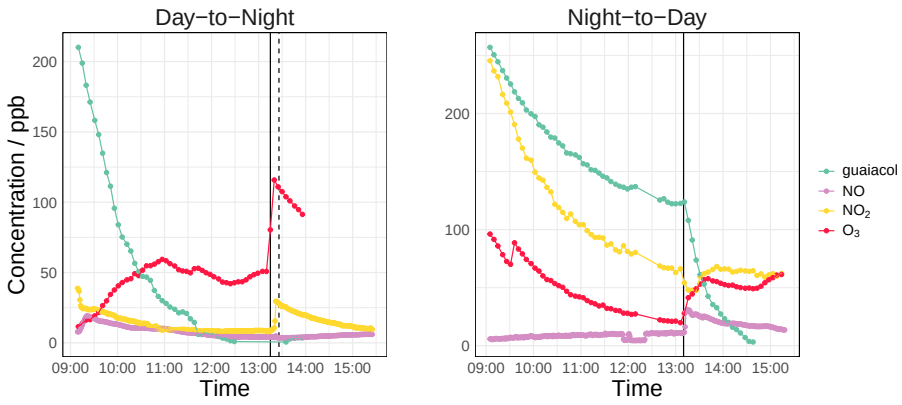

Figure 4.17: *Timeseries of guaiacol, NO_x and O_3 during the DTN and NTD experiments conducted on 29-05-2023 and 30-05-2023. The vertical black solid line indicates when the roof was either closed (DTN) or opened (NTD) and the dashed line in the DTN shows the end of the NO_2 and O_3 injections to the chamber to produce NO_3.*

During the night there is decay of guaiacol from reactions with NO_3, as evident by the decay of NO_2 and O_3 in Figure 4.17 and subsequent increase in the N_2O_5 ion signal observed by I-CIMS indicating the production of NO_3 radicals. However, as previously mentioned it is possible that there may also be ozonolysis reactions due to the high concentrations of O_3 inside the chamber and further experiments should be designed to investigate ozonolysis of guaiacol oxidation products. Whilst in the day there is production of both NO_2 and O_3 indicating photochemical oxidation by the OH radical. From Figure 4.17 in the DTN experiment guaiacol is used up at the

end of the day period whereas in the NTD experiment 123 ppb of guaiacol remains unreacted at the end of the dark period. Due to high humidity in the night portion of the DTN experiment, the FTIR data could not be collected during the entire two hour dark period. Furthermore, the O_3 profile shown in the day portion of the NTD experiment peaks shortly after roof opening before increasing again in the final half hour when the guaiacol precursor is used up. The reasoning for this trend remains unclear and would benefit from further repeats.

4.3.4.1 Trends in SOA mass concentration

Distinct differences in the formation of aerosol was observed using SMPS which showed significant and sustained particle growth in the day compared to the night in Figure 4.18.

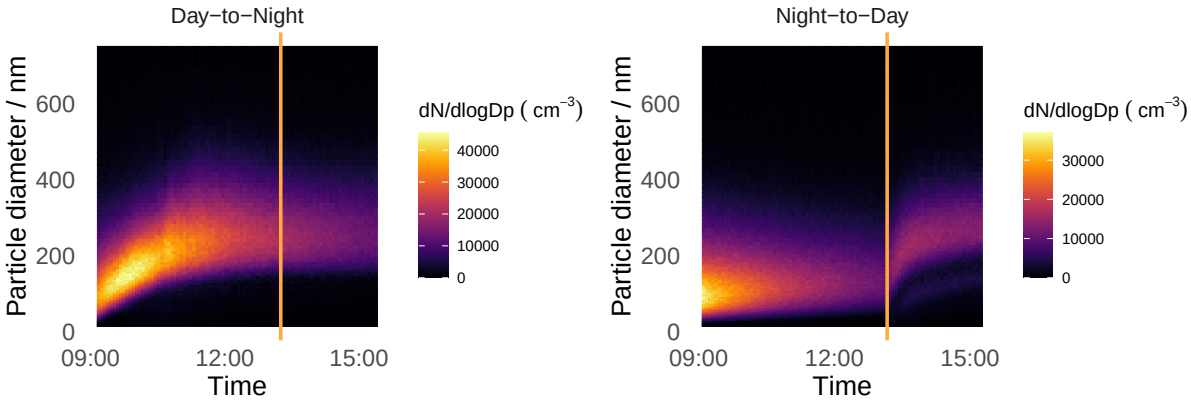

Figure 4.18: *SMPS particle number concentrations for the DTN and NTD experiments conducted on 29-05-2023 and 30-05-2023. The orange vertical line represents when the chamber roof is either closed (DTN) or opened (NTD).*

This was true for the daytime period of both the DTN and NTD experiment. It can also be seen that when guaiacol was injected in the dark there is some growth of particles but to a lesser extent than when the injection began during the day. After the night period in the chamber and upon transition to the daytime conditions the particle mass concentration in the chamber increased by 153 %. Additionally, the transition from

day to night shows an overall loss of particles equating to a 32 % decrease in particle mass concentration. This trend in PM concentration was observed previously with elevated mass concentrations in the day compared to the night [348] and higher numbers of nucleation particles in the day [349]. However, the rapid increase of particles from night to day could also be due to the difference in the initial guaiacol precursor left.

In the DTN experiment, water was continuously added during the day to maintain a relative humidity (RH) of ≈ 50 %, however, upon closing the roof there is a drop in temperature from 306 K to 300 K and a subsequent increase in humidity to 80 % over the course of the nighttime period. Figure 4.19 shows the correlation between the aerosol mass concentration measured by SMPS and RH. During the day there is negligible influence of RH on the aerosol mass concentration with a widespread of data points across the mass concentration range (Figure 4.19). However, in the nighttime period, there is a strong inverse relationship in Figure 4.19 indicating the potential loss of particles from wet deposition. In a previous study of the OH oxidation of m-xylene, an aromatic analogous to guaiacol, a lower SOA yield in humid conditions was also observed [350].

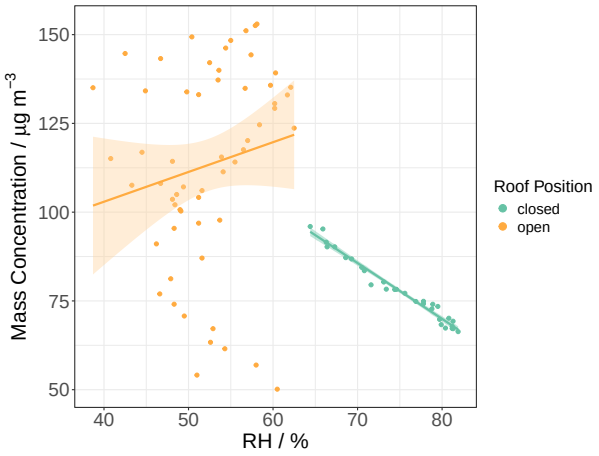

Figure 4.19: *Correlation between SMPS particle mass concentrations in µg m^{-3} and the percentage relative humidity (RH) for the DTN experiment as a function of the roof closed (blue) or opened (orange)*

4.3.4.2 Differences in overall SOA composition

The FIGAERO-I-CIMS was used to monitor the particle composition in real-time over the NTD and DTN experiments. The measurement occurs over a 1 hour cycle in which particle phase species are sampled for 15 minutes onto a filter whilst the gas phase species are simultaneously monitored. After these 15 minutes, the particle products from the filter are gradually thermally desorbed over 45 minutes. Figure 4.20 shows the mass spectra from the end of each phase of the NTD and DTN experiment, where peaks shown in colour represent compounds with identified molecular formulae. These are predominantly compounds from the guaiacol mechanism (Figure 4.5) but some additional compounds were identified as part of the peak fitting algorithm in the I-CIMS data processing or from previous literature. However, only 5 products that were identified from previous literature [95, 309, 351, 352] were not part of the original mechanism in Figure 4.5. In total, the mechanism products contribute to 49.2-78.7 % of the total product signal, whereas including all identified compounds results in a contribution of 50.4-85.3 %. Therefore, the majority of products shown in Figure 4.20 are from the guaiacol mechanism and improving the NO_3 chemistry in the mechanism would increase the proportion of identified compounds in the nighttime spectra which had the lowest contribution (49.2 %). In both experiments the mass spectra show the ion counts are higher in the daytime compared to the nighttime, which is in agreement with the greater particle mass observed during the day in Figure 4.18.

From the full mass spectrum it can be seen that the highest intensity peaks are from CHON compounds shown in orange across both NTD (Figure 4.20a) and DTN (Figure 4.20b) experiments as well as HNO_3 shown in purple. The dominant CHON signals belong to nitrocatechol at *m/z* 281.9269 and nitroguaiacol at *m/z* 295.9425. It is clear that during the day nitrocatechol is the most prominent SOA product, for example, from night to day the nitrocatechol signal increases by more than one order of magnitude. In a previous study the gas phase nitrocatechol yield from guaiacol was 0.6 %, and was determined to be a minor reaction pathway under high NO_x conditions [94]. However, this work shows the yield of nitrocatechol could be much higher especially in the particle phase. Therefore, future work should aim to quantify the production of catechol from guaiacol to constrain the branching ratio for this pathway. Nitrocatechol can also be observed in the mass spectra of the NTD experiment in the night

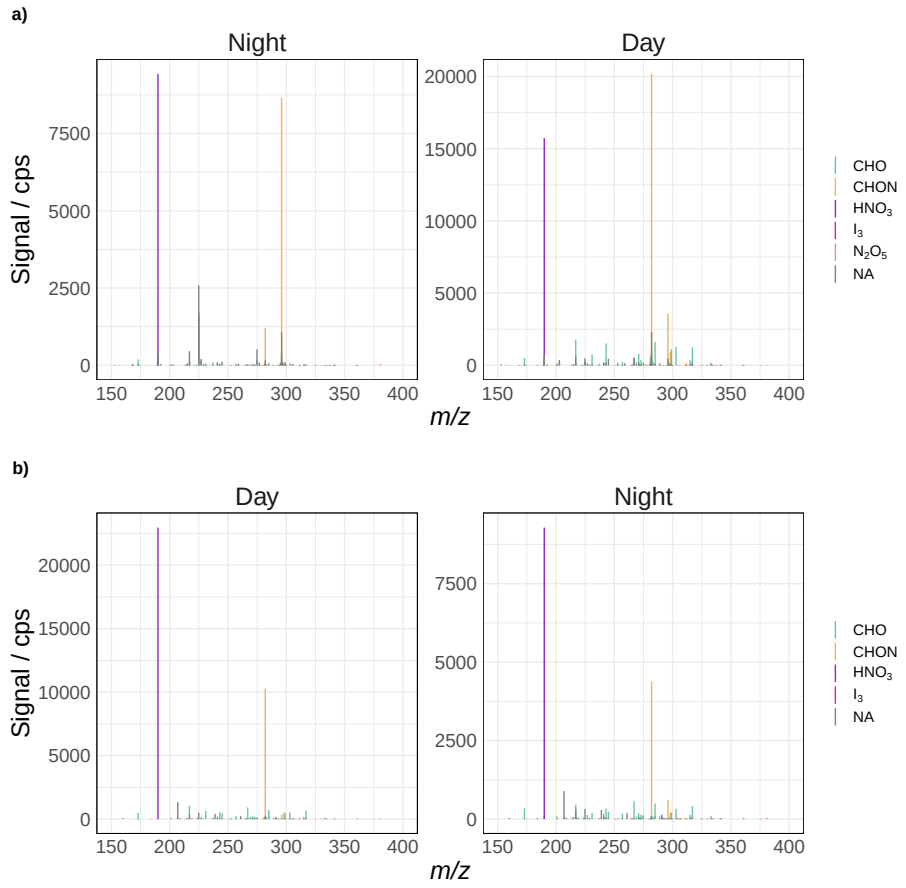

Figure 4.20: *Average FIGAERO-I-CIMS mass spectrum at the end of the night or day period coloured by the chemical composition of the identified compounds in the a) NTD experiment b) DTN experiment*

period, though this could be due to the presence of catechol as a natural impurity of commercial guaiacol standards [326]. Furthermore, as expected, when the experiment is started in the night nitroguiacol is more abundant than nitrocatechol but not when the experiment started in the day. At the time of roof closure in the DTN experiment, the guaiacol precursor is fully depleted which may result in the lower intensity of the nitroguaiacol peak in the night portion of the DTN experiment compared to the NTD experiment. Although in a direct comparison of counts the nitroguaiacol peak still increased by a factor of 2 from day to night.

Figure 4.21 shows the mass spectra for the DTN and NTD experiments zoomed in to capture the lower intensity peaks and with nitroguaiacol and nitrocatechol removed. It can be seen that from night to day there is significant change in the composition with a decrease in the main unidentified peak at *m/z* 225 and an increase in the number of

identified compounds which are primarily oxygenated organics (CHO). On the other hand, from day to night there is an overall decrease in signal intensity but less change in the overall distribution of peaks, especially for CHO compounds. Overall, these spectra show that CHO compounds have important daytime formation routes. For CHON there is some small changes in the dominant peaks. The CHON peaks in Figure 4.21 predominantly include other nitroaromatic compounds such as $C_6H_5NO_5$ and PANs. Particulate N_2O_5 was also identified in the NTD experiment but at very low counts therefore is not visible in the spectra shown in Figures 4.20 and 4.21.

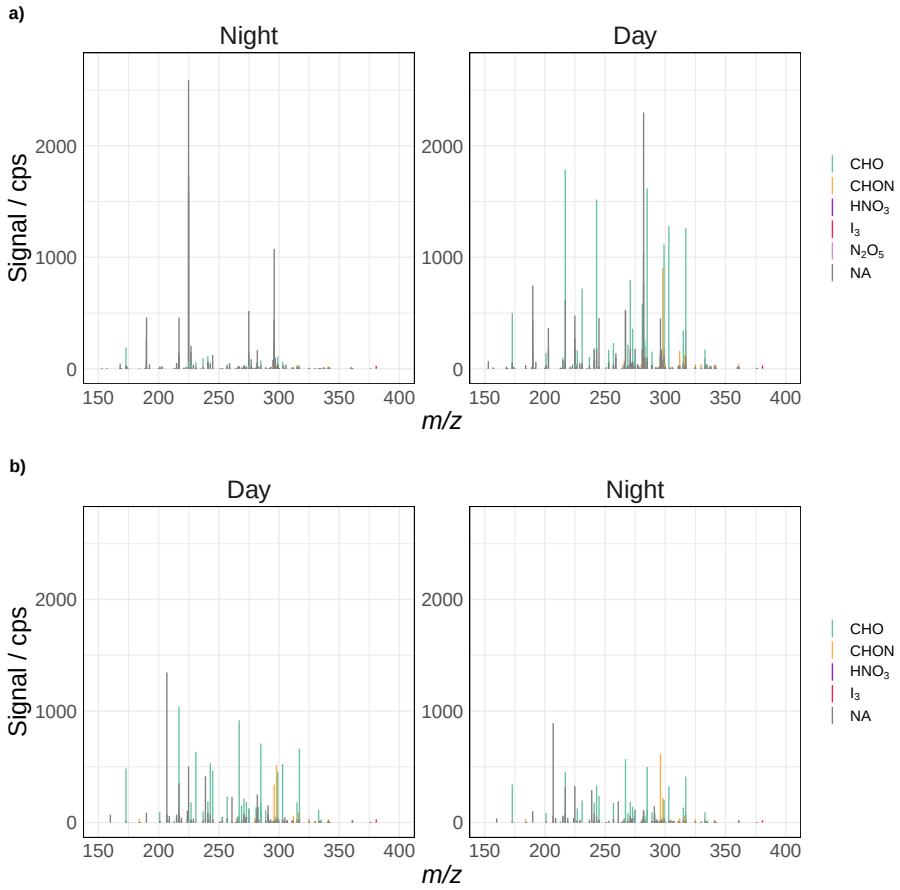

Figure 4.21: *Average FIGAERO-I-CIMS mass spectrum at the end of the night or day period zoomed in to the lower intensity ions and coloured by the chemical composition of the identified compounds in the a) NTD experiment b) DTN experiment*

4.3.4.3 Trends in SOA products

SOA products predicted using the guaiacol mechanism (Figure 4.5) were monitored in detail by FIGAERO-I-CIMS. Many of the guaiacol mechanism SOA products showed

enhancements during the day compared to the night due to their formation from OH and from Figure 4.21 these are predominantly CHO compounds. However, some of the proposed oxidation products in Figure 4.5 will also have a nighttime formation route via the NO_3 radical. Nitroaromatics have been previously identified as dominant products from methoxyphenolic NO_3 oxidation [310, 313] and were the prominent signals in Figure 4.20. Therefore, the guaiacol nitroaromatic products compounds were selected as ideal candidates to study between night and day (Figure 4.22) and as Section 4.3.2 shows these products already have an affinity to be present in the aerosol phase (Figure 4.15).

Figure 4.22 shows the particle ramp data in pink across the entire desorption and the average gas phase normalised counts per seconds per 15 minute sample period in orange for the nitroaromatic compounds in the guaiacol mechanism between NTD and DTN experiments. Note that increases and decreases in the particle abundance is evaluated against both the baseline trend of the ramp data and the height of each ramp.

In the night period of the NTD experiment there is a rapid increase in both gaseous and particulate phase NGUAIACOL which subsequently decays in the day as a result of photolysis [353]. Furthermore, in the DTN experiment NGUAIACOL shows an initial increase and then starts to decrease in the final hour of the daytime. After the nighttime transition there is a slight enhancement in the gas and particle phase NGUAIACOL signal. Overall, compared to the NTD experiment the evolution of NGUAIACOL from day to night is different and the abundance of NGUAIACOL is significantly less in the DTN experiment. This difference is consistent with a previous study which observed the NO_3 oxidation of wildfire emissions led to a larger enhancement in CHON compounds in the resulting aerosol compared to daytime oxidation [354] which showed the loss of chromophoric species, such as nitroaromatics, on longer timescales [354, 355]. However, Figure 4.20 does show significant daytime production of nitrocatechol in the early stages of oxidation.

In the NTD experiment, the particulate phase signal of DNGUAIACOL shows some increase in the night, however, it is less compared to the day. This could be the result of a slower rate of reaction of NGUAIACOL with NO_3 compared to OH and a faster reaction of NO_3 with the guaiacol precursor than other nitrocompounds as observed for

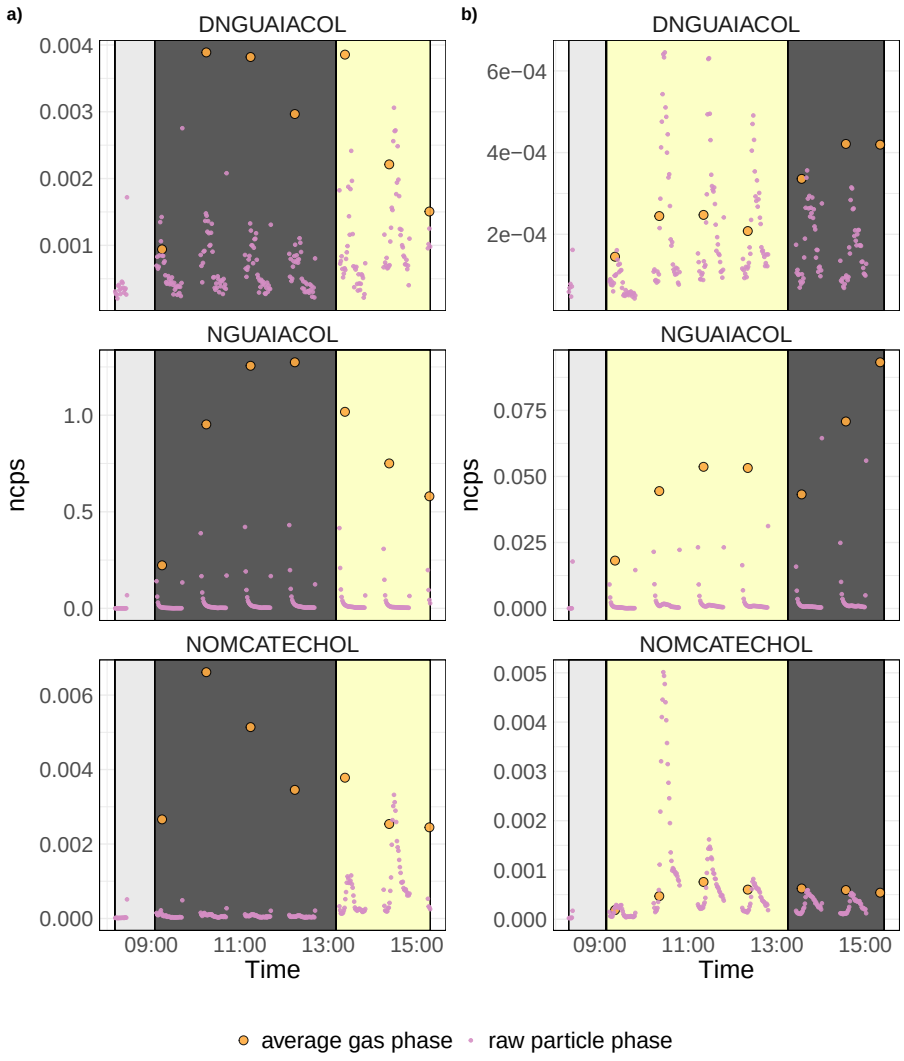

Figure 4.22: *FIGAERO-I-CIMS ncps timeseries for nitroaromatic oxidation products in the guaiacol mechanism. Average gas phase ncps per 15 minute gaseous sampling period are shown as orange markers. Particulate ncps are shown across the full 45 minute desorption ramp averaged to 1 minute intervals in pink markers. Pale yellow backgrounds indicate the daytime period and grey background indicate the nighttime period. a) NTD b) DTN. Note the particle phase DNGUAIACOL signal is multiplied by 10 in panel a) for visibility.*

other phenolics present in the MCM. In the NTD experiment once the roof is opened the DNGUAIACOL gas phase signal decreases as the particulate phase signal increases which could suggest condensation onto pre-existing aerosol as well as new formation from NGUAIACOL which shows a decrease in the day. However, these trends are complex and require further study to form a conclusion. Whereas for the DTN experiment, although the particulate phase DNGUAIACOL decreases in the night consistent with

the overall loss of aerosol (Figure 4.18) there is an increase in the gas phase concentration which could be the nitration of pre-existing gas phase NGUAIACOL from daytime oxidation.

As expected, NOMCATECHOL shows significant enhancement in the particulate phase during the day in both NTD and DTN experiments due to the formation via the OH addition of guaiacol to OMCATECHOL and subsequent nitration to form NOMCATECHOL. There is some gas-phase formation of the NOMCATECHOL ($C_7H_7NO_5I^-$) ion in the nighttime, however, the reasoning for this remains unclear. A possibility is the presence of an interfering species at the same mass, however, it is clear further investigation is needed.

The same trends in the particle phase abundance can also be observed in the thermogram data from the FIGAERO-I-CIMS, however, the thermogram from nitroguaiacol is not included due to a potential interference upon switching from the gas phase. From the thermograms in Figure 4.23 it can be clearly seen that NOMCATECHOL rapidly forms in the particle phase in the second hour of the daytime in the DTN experiment and subsequently decays which is likely due to further oxidation [355]. Furthermore, the peak temperature in the thermogram for each compound in both NTD and DTN experiments is similar over the course of the experiment which could indicate the formation of similar isomers [356] as observed by the presence of peaks at the same retention time in UHPLC-HRMS analysis (Table 4.5).

Whilst ionisation effects can exist for I-CIMS [166–168] similar to those mentioned in Chapters 2 and 3 for ESI mass spectrometry the ratio of the counts are compared between the NTD and DTN to observe enhancements of the day- or night-time period on the subsequent chemistry. For NGUAIACOL, the ncps during the NTD experiment are significantly higher than that of the DTN experiment, indicating that the emission of guaiacol during the night will yield NGUAIACOL as the dominant product in the night and at higher concentrations than if the emissions began during the day. Whereas for NOMCATECHOL and DNGUAIACOL the DTN experiment shows enhanced ncps in both the day and night periods compared to the NTD experiment. This suggests the prior daytime period enhances the nighttime particulate phase concentration of these compounds compared to their nocturnal formation. As shown in Figure 4.18 there is less particle growth in the night compared to the day as well as potentially slower

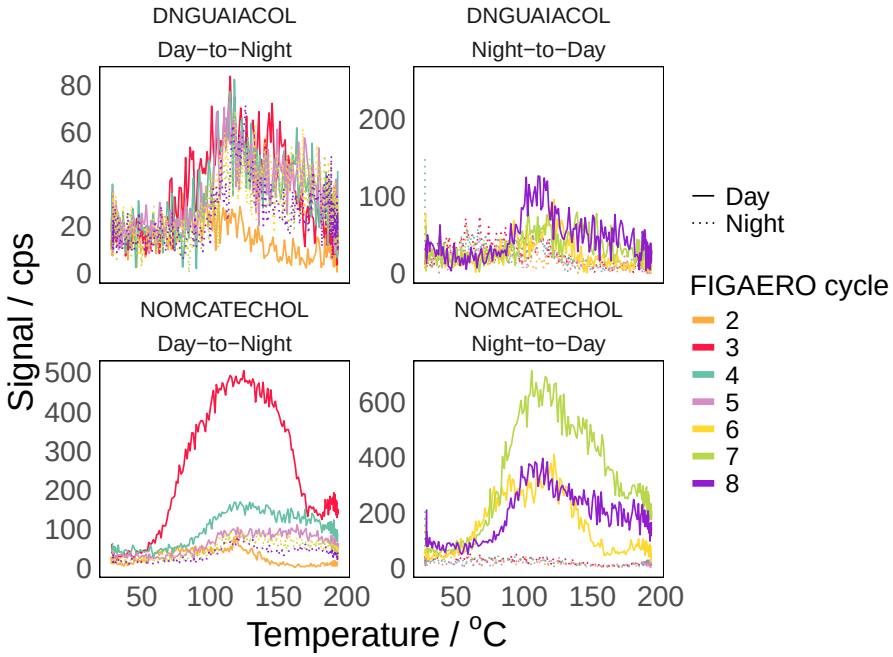

Figure 4.23: *Measured ion thermograms for DNGUAIACOL and NOMCATECHOL across the day-to-night and night-to-day experiments. The cycle numbers represent the time of the experiment where 2-5 are the first 4 hours and 6-8 are the final 2 hours of the experiment. The linetype shows whether the chamber is irradiated or in the dark for day and night respectively.*

reactions of the precursors with NO_3 compared to OH.

The trend of the nitroaromatics abundance in Figure 4.22 was also investigated using the relative peak areas in the UHPLC-HRMS analysis (Table 4.5) where the ratio represents the peak area after roof change:peak area before roof change. The same trends in the relative increase or decrease after transition shown in Figure 4.22 can be seen in the relative ratio of the UHPLC-HRMS peak area in Table 4.5. Furthermore, in the case of DNGUAIACOL it can be seen the nighttime peak area is greater in the DTN experiment than the NTD experiment, in agreement with the I-CIMS. For NOMCATECHOL, a peak at 6.90 min is only observable in the daytime spectra which is in line with NOMCATECHOL as an OH addition derived product. These differences in observed aerosol composition depending on the start time of the emission have important implications for toxicity. For instance, in a residential setting the major use of combustion stoves will be during the night [238] allowing a build up of large concentrations of nitroguaiacol which is considered to be a toxic pollutant. The following morning, there can then be the conversion of nitroguaiacol to dinitroguaiacol and other photolysis or

photo-oxidation products of unknown toxicities.

Table 4.5: *Nitroaromatic compounds from the DTN and NTD experiments detected by UHPLC-HRMS analysis and their corresponding retention time (RT), peak area in the night and day periods and relative changes in signal intensity after transition.*

Compound	RT	Experiment	Day Peak Area	Night Peak Area	Ratio
nitroguaiacol	7.62	DTN	2.06×10^9	3.64×10^9	1.76
dinitroguaiacol	8.55	DTN	3.97×10^8	2.62×10^8	0.66
NOMCATECHOL	6.88	DTN	6.11×10^5	-	-
nitroguaiacol	7.60	NTD	8.59×10^9	1.93×10^{10}	0.45
dinitroguaiacol	8.55	NTD	5.71×10^8	1.83×10^8	3.12
NOMCATECHOL	6.90	NTD	1.26×10^7	-	-

In the atmosphere PANs are a large reservoir of NO_x and are important for controlling the oxidative capacity of the atmosphere. As shown in Figure 4.11 the production and loss of PANs in the gas phase is an important factor in controlling the radical budget of the guaiacol oxidation system. Furthermore, PANs were also tentatively identified in the aerosol in Figure 4.20 in both day and night periods. Therefore, to further investigate the transformation of particulate CHON species, PANs were also selected for study in detail by FIGAERO-I-CIMS shown in Figures 4.24 and 4.25. From Figures 4.24 and 4.25 the particulate formation of PANs occurs predominantly in the day time. For EPXDLPAN and HCOCOHPAN there could be some nighttime particle formation in the NTD experiment but it is more unclear due to presence of background peaks.

The production of PANs relies on the presence of RO_2 and NO_2 and therefore the availability of NO_2 in each system may result in the different observed formation rates of PANs. For example, there are multiple known competing loss routes of NO_2 during the night such as the formation of NO_3 radicals as seen in the decrease of NO_2 and O_3 in Figure 4.17, HNO_3 or HONO production (Figure 4.26) and the formation of nitroaromatic compounds discussed in Figure 4.22. It was observed in Figure 4.26 that during the night of the NTD experiment up to approximately 12 ppb of HONO is formed compared to a maximum of 8 ppb during the day of the DTN experiment. A previous study observed the formation of HONO at night in Beijing was primarily via heterogeneous chemistry on wet surfaces [357]. After the transition, it can be seen

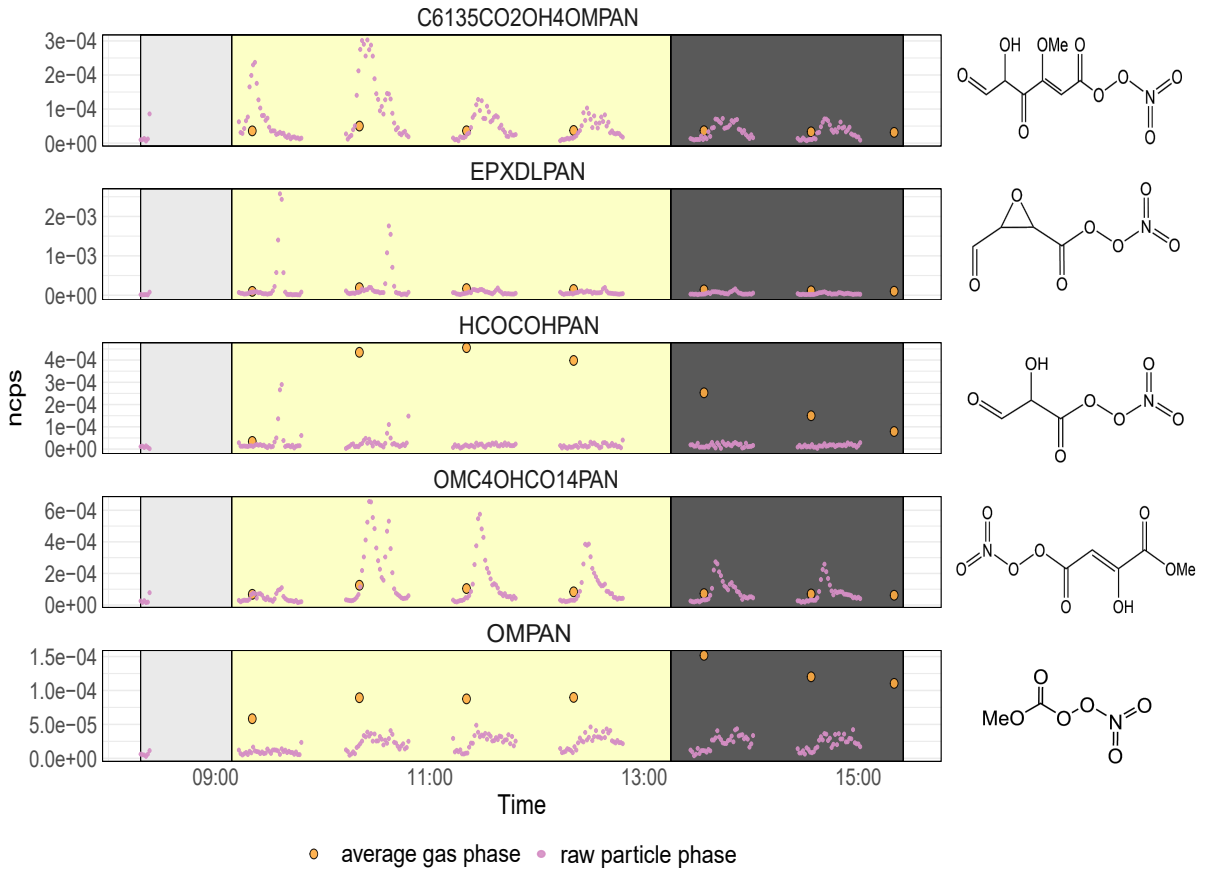

Figure 4.24: *FIGAERO-I-CIMS ncps timeseries for peroxyacetyl nitrates (PANs) products in the guaiacol mechanism during the DTN experiment. Average gas phase ncps per 15 minute gaseous sampling period are shown as orange markers. Particulate ncps are shown across the full 45 minute desorption ramp averaged to 1 minute intervals in pink markers. Pale yellow backgrounds indicate the daytime period, dark grey backgrounds indicate the nighttime period and light grey backgrounds show the pre experiment data. The structures of each PAN compound are shown to the right of each panel.*

the nighttime HONO reservoir decreases, likely due to HONO photolysis to form OH. This is in agreement with previous observations where the dominant production of OH after sunrise was the photolysis of HONO [45].

In Figure 4.25 there is also evidence of some gas phase production of PANs during the night, especially for OMPAN, however, the abundance is generally lower than when the emission begins during the day (Figure 4.24). Interestingly, in the NTD experiment (Figure 4.25) the gas phase of the daytime ncps of nearly all PAN species, except for C6135CO2OH4OMPAN, reach a higher intensity than if the emissions begin during the day (Figure 4.24). To investigate plausible explanations for this phenomenon the

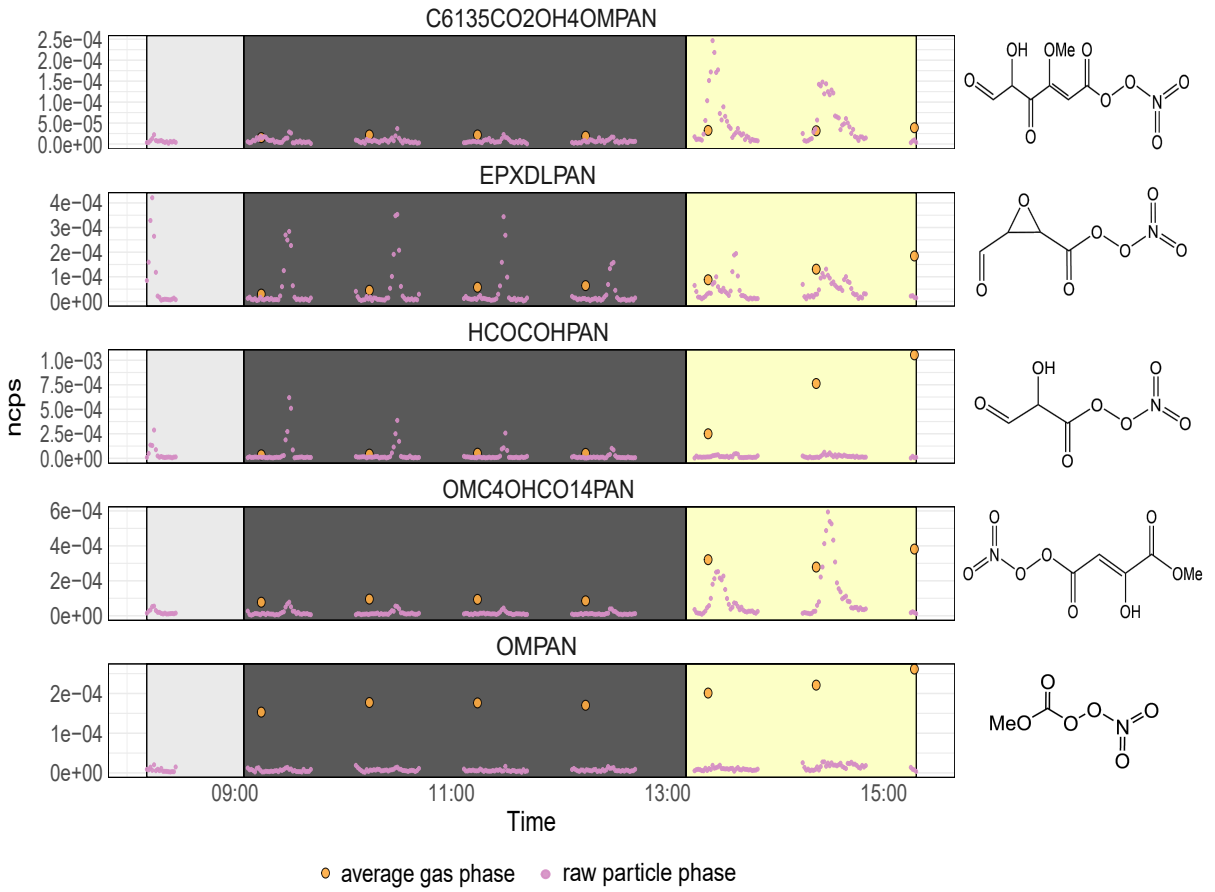

Figure 4.25: *FIGAERO-I-CIMS ncps timeseries for peroxyacetyl nitrates (PANs) oxidation products in the guaiacol mechanism during the NTD experiment. Average gas phase ncps per 15 minute gaseous sampling period are shown as orange markers. Particulate ncps are shown across the full 45 minute desorption ramp averaged to 1 minute intervals in pink markers. Pale yellow backgrounds indicate the daytime period, dark grey backgrounds indicate the nighttime period and light grey backgrounds show the pre experiment data. The structures of each PAN compound are shown to the right of each panel.*

NO:NO_2 ratio was evaluated. As shown in Figure 4.27 between the NTD transition and the start of the daytime period of the DTN experiment NO:NO_2 is comparable ($\approx$ 0.2), however, the NO_2 concentration is 15 ppb higher. Therefore, this rapid increase in PANs after the nighttime period could be due to the photolysis of NO_3 and HONO during the day to produce NO_2 and OH radicals. The newly formed OH radicals can then propagate the VOC-HO_x cycle to produce RO_2 which in the presence of NO_2 yields PAN products. This difference in the production of PANs was observed in a previous case study of a wildfire after sunset which observed the main NO_x reservoir pre-sunset was the formation of PANs whereas after sunset the NO_x is used up in

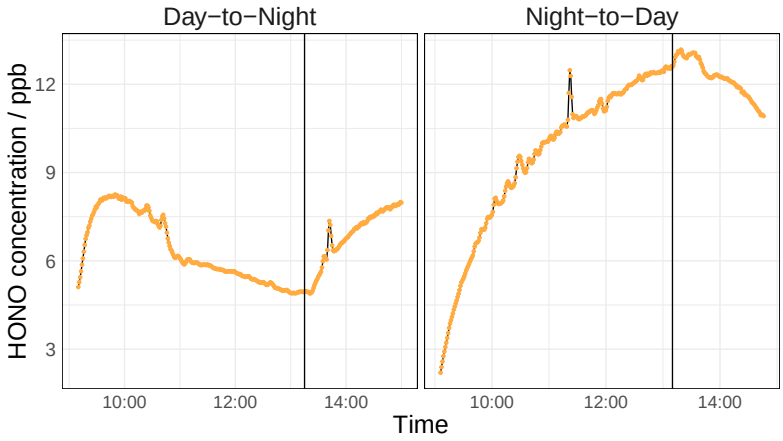

Figure 4.26: *HONO concentration timeseries, measured by the LOPAP, for the DTN and NTD experiments conducted on 29-05-2023 and 30-05-2023. Solid vertical black line indicate when the roof is closed (DTN) or opened (NTD)*

the formation of nitrophenolic compounds [113]. In the case of wildfire plumes, this indicates nighttime burning can have large impacts on oxidant budgets especially if able to be transported to remote atmospheres. However, future investigations into the NO_3 chemistry of guaiacol should be undertaken to fully elucidate the nighttime formation of guaiacol derived PANs.

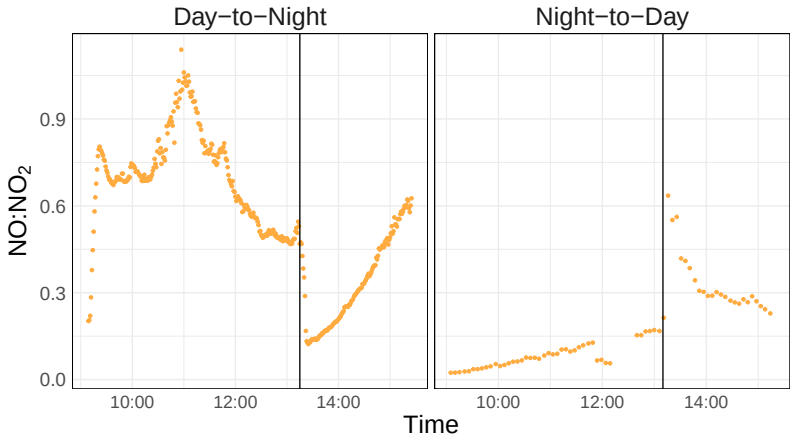

Figure 4.27: *Ratio of NO:NO_2 concentrations timeseries for the DTN and NTD experiments conducted on 29-05-2023 and 30-05-2023. Solid vertical black line indicate when the roof is closed (DTN) or opened (NTD)*

The thermograms from the FIGAERO-I-CIMS analysis were also examined for the PAN products in Figure 4.28, except for OMPAN which had a considerably noisy profile. In Figures 4.24 and 4.25 it is possible to observe in the particle phase counts the

shape of the desorption curve changes between night and day. In Figure 4.28 compounds such as EPXDLPAN and OMC4OHCO14PAN show different peaks in the desorption in the day and night periods. For OMC4OHCO14PAN in the second hour of the DTN experiment there is a peak at ≈ 175 °C which then decays over the course of the experiment. However, when the emission begins in the night this peak doesn't occur in the daytime period. Similarly, EPXDLPAN shows a peak at ≈ 175 °C at the start of both DTN and NTD experiments which decays over time. Whereas, the day period of the NTD experiment has a main peak at 100 °C. It is possible that the shift of the peak to lower temperatures could be from the presence of a desorption product [356]. Furthermore, certain products such as OMC4OHCO14PAN and C6135CO2OH4OMPAN show a higher intensity desorption peak in the daytime period of the NTD experiment compared to the DTN experiment, similar to that observed for the gas phase as explained above. However, further work is needed to examine these profiles in greater detail to draw conclusions on the shape of the peak and trend in volatility.

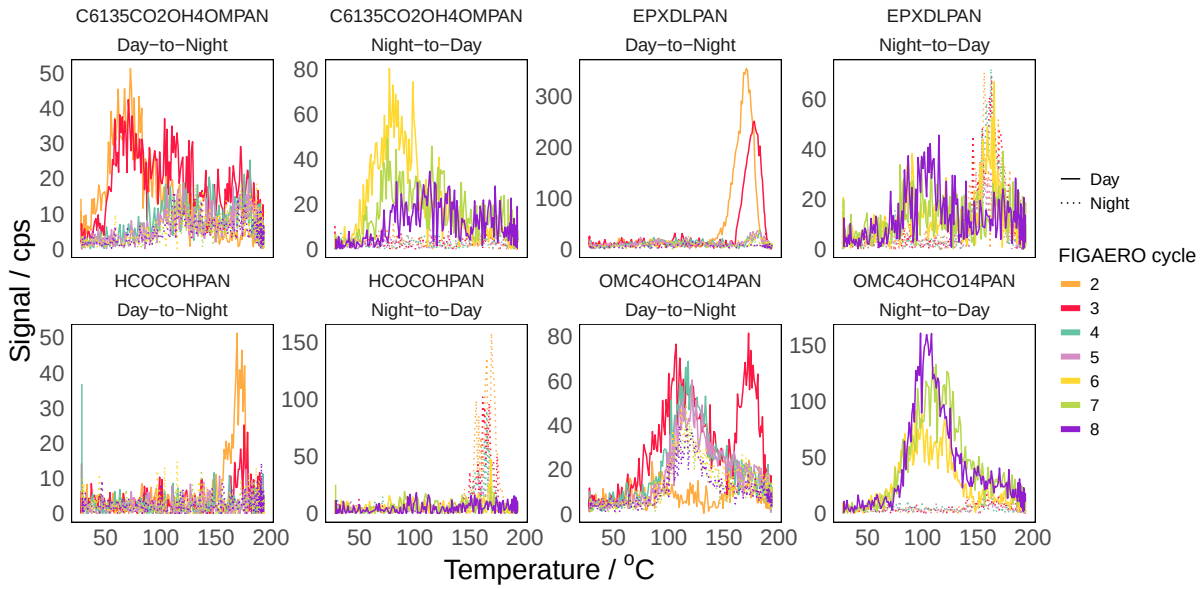

Figure 4.28: *Measured ion thermograms for particulate phase PAN compounds across the day-to-night and night-to-day experiments. The cycle numbers represent the time of the experiment where 2-5 are the first 4 hours and 6-8 are the final 2 hours of the experiment. The linetype shows whether the chamber is irradiated or in the dark for day and night respectively.*

4.3.4.4 Atmospheric implications

There has been studies showing the relative differences between the toxicities of ring opening products and ring retained species formed from aromatic precursors, where it was observed that ring retained nitroaromatics and quinones were considered more harmful towards human health [96]. A targeted analysis was undertaken wherein the species proposed in the guaiacol mechanism detected by FIGAERO-I-CIMS were split into species which retained the original aromatic ring from the guaiacol precursor and those which broke down the aromatic ring based on the proposed structures in Figure 4.5 and Figure 4.6. Certain products at the same *m/z* were comprised of both ring opened and ring retained species and are therefore labelled as "open+close isomers" in Figure 4.29. Catechol and the oxidation products of catechol, such as nitrocatechol, were originally removed from the analysis to reflect the "guaiacol-only" products from Figure 4.5 and due to the likely presence of a catechol impurity at the start of the experiments which wasn't able to be quantified. Figure 4.29 shows relative contribution of ring opened and ring closed products to the total ncps signal of the particle ramp data at each timestep and the average gas phase contribution per 15 minute sampling interval. There is a significant contrast between the proportion of ring opened and ring closed products in the NTD and DTN experiments and the changes upon transition. For the NTD experiment during the night over 75 % of the particle phase and over 90 % of the gas phase signal is dominated by ring closed products, likely to be nitroguaiacol. In the particulate phase the proportion of ring closed products continues to increase over the night until the roof is opened where after there is a rising contribution of ring opened products from photo-oxidation. The gas phase however remains dominated by the nitroguaiacol signal into the daytime. In the DTN experiment there is less change in the relative contributions of ring opened and ring closed products between the day and night periods. Overall the DTN particulate phase is largely comprised of ring opened guaiacol products throughout the day and night.

However, inclusion of nitrocatechol to the analysis does increase the contribution of the ring closed compounds to the total signal in the DTN experiment to a maximum of 75 % near the start of the experiment indicating it as an important daytime product in the initial SOA formation with increases in ring opened species thereafter, but further investigations are needed with quantifiable measurements. Nonetheless the same

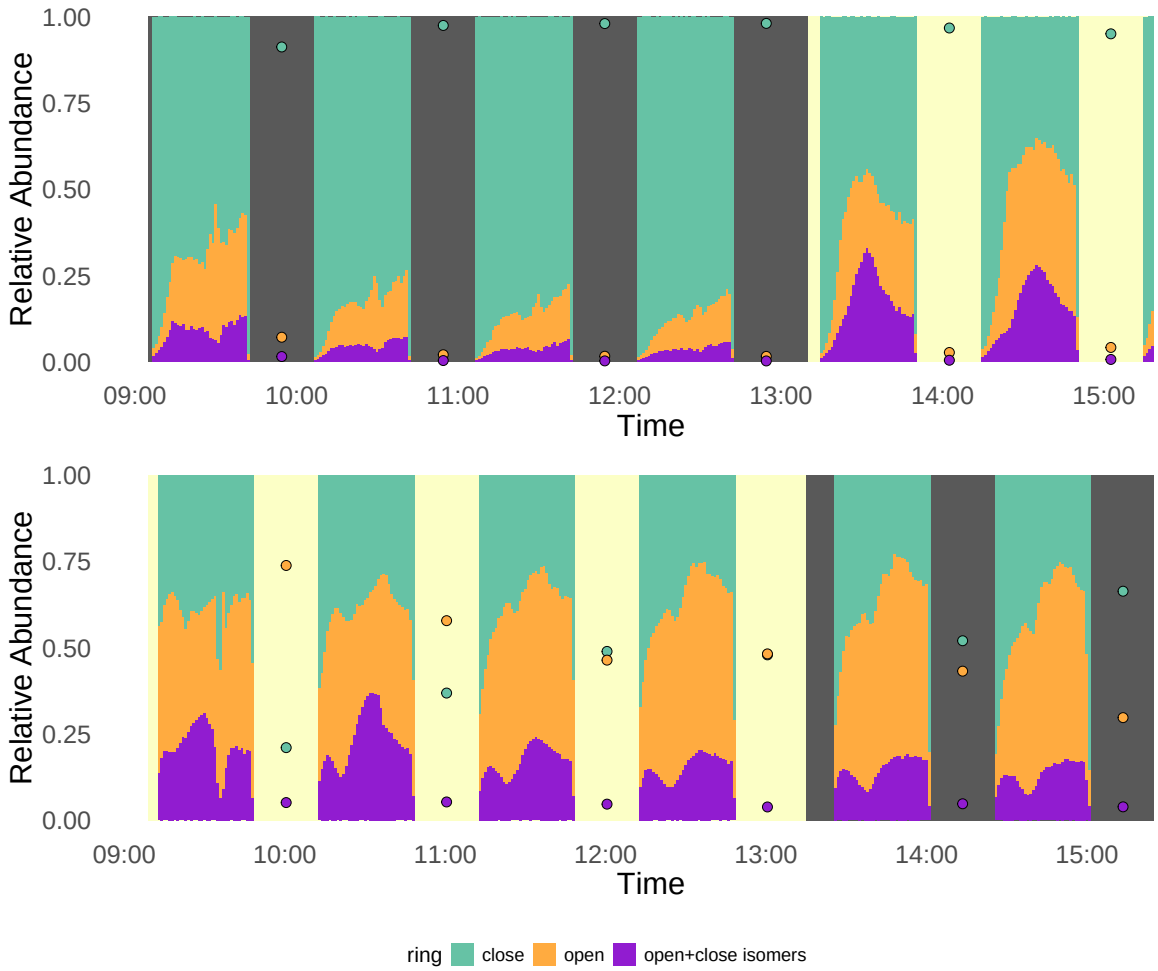

Figure 4.29: *Percentage contribution to the detected ncps signal from FIGAERO-I-CIMS of ring opened and ring closed guaiacol SOA products for NTD (top panel) and DTN (bottom panel). Species with molecular formulas of ring retained and ring opened compounds are referred to as "ring open + close isomers". Data is shown across the full particle ramp (bars) and as an average for each gas phase sampling period (circular point). Grey backgrounds represent the night period and pale yellow backgrounds show the daytime periods*

overall trend of less compositional change upon nighttime transition is still observed. In the relative gas phase contributions during the DTN experiment a shift is observed with increasing amounts of ring closed species until the contributions are equal to that of ring opened compounds during the day. Following the roof closure the ring retained compounds become the dominant gas phase contributors. These separate regimes indicate particulate emissions starting in the night have the potential on an equal mass basis to be more toxic with the greater accumulation of ring closed compounds over the nighttime aging period [96] than those when the emissions begin in the day and

are aged for the same equivalent number of hours. Furthermore, the ring closed products may also contribute more to BrC formation, from nitroaromatics for example, and have important implications for climate [253].

However, from the total ion count profile for each particle desorption (Figure 4.30) it is clear that the daytime in each experiment exhibits a greater abundance of products from the higher number of counts, which is consistent with the observed particle number timeseries (Figure 4.18). Therefore, whilst the composition is an important factor in determining the toxicity as discussed in Chapter 3, the concentration must also be taken into consideration to draw conclusions about the relative toxicity. Overall, these results highlight an important case study of how emissions age between night and day which warrants further study.

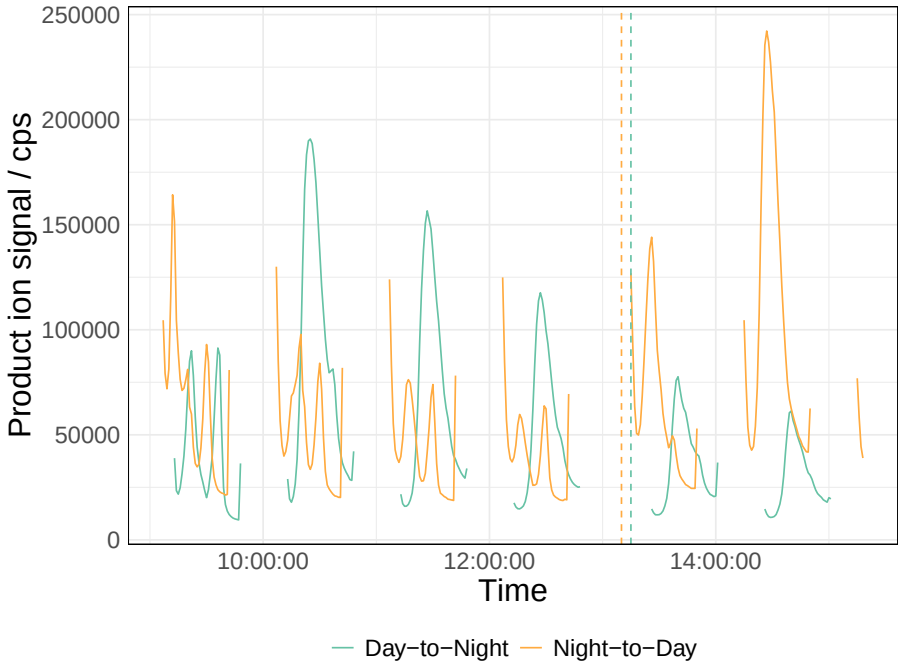

Figure 4.30: *Total ion count averaged per minute in each thermal desorption cycle of the FIGAERO-I-CIMS measurement, coloured by the experiment type. Dashed lines indicate the transition from day-to-night (blue) or night-to-day (orange).*

4.4 Conclusions

A new photo-oxidation mechanism for inclusion into the Master Chemical Mechanism was proposed for guaiacol, a methoxyphenol emitted by biomass burning, for which

the current understanding of its reactivity is limited. The mechanism was evaluated and optimised against smog chamber experiments at EUPHORE during May 2023 and model simulations well reproduced the observable chemistry through comparison with the temporal evolution of organic oxidation products. Deviations between modelled concentrations and measured timeseries arose in certain oxidation products containing nitro functionality (-NO_2) due to the partitioning of these compounds to the particle phase. However, the current mechanism still underpredicted the guaiacol loss and overpredicted the O_3 production which is a common feature of oxidative chamber experiments of aromatic systems with missing OH reactivity. Therefore, further work is required to close this gap by adding further subsets of chemistry for later generational guaiacol oxidation products or by performing chamber studies with the guaiacol products as the initial precursors. In addition, more experimental rate coefficients are needed as only one measurement exists for the reaction of guaiacol with OH. SOA formation from guaiacol oxidation was investigated between night-to-day and day-to-night conditions which showed different particle growth rates and relative quantities of oxidation products depending on the start time of the guaiacol emission. For instance, increased contributions of nitroguaiacol were observed from a nighttime emission as well as a greater change in the proportion of ring opened compounds contributing to the particle phase composition upon transition from night-to-day than from day-to-night. Nitrocatechol was also identified as a key SOA product and further work is needed to constrain the photochemical production of catechol from guaiacol oxidation. Furthermore, it was observed that the nighttime formation of NO_3 and HONO could enhance the formation of PANs during the following day compared to when the start of the emission (i.e. guaiacol injection) occurred in the daytime. Ultimately, these results highlight differences in the composition, and therefore potential toxicity, of the resulting aerosol between night- and day- time biomass burning emissions and the important implications for global oxidant concentrations from the relative production of PANs. Furthermore, the addition of seed in the SOA experiments could add more complexities to the observed chemistry such as the uptake of NO_3 to the aerosol in the form of N_2O_5 during the night. Therefore, more repeats of the SOA and GPM experiments are required under different VOC:NO_x ratios, in the presence or absence of seed and for longer oxidation times to observe the chemistry over

multiple hours. Lastly, to better replicate the chemistry of an optically thick wildfire plume, experiments involving the transition between dark-light-dark periods could be performed to simulate the majority dark oxidation with intermittent photo-oxidation.

Chapter 5

Conclusions

5.1 Summary

Organic aerosol (OA) is a significant component of particulate matter with a diameter less than 2 μm ($PM_{2.5}$) which has detrimental impacts on todays society through the adverse health effects and climatic influence it can cause. Therefore, an improved understanding of the chemical composition of OA as well as the formation of secondary organic aerosol (SOA) could yield significant benefit for improving air quality. However, there are certain barriers affecting this understanding, such as the quantification of OA and the mechanism of SOA formation from certain volatile organic compounds (VOCs), which remain poorly understood. The work in this thesis pertains to the second largest global source of OA, biomass burning, for which the atmospheric chemistry and SOA formation pathways are largely unknown and understudied. One of the central themes of this work is the chemical characterisation of SOA from biomass burning sources in order to gain a better understanding of the potential health effects from exposure to such sources and improve future policy.

The lack of commercially available standards for use in OA analysis means quantification of species without standards is challenging. This has led to either studies only targeting a selected number of compounds or using limited metrics such as instrument response in the form of peak area or number of molecular formulas as a measure of concentration in previous compositional OA analysis. Both approaches have drawbacks such as the small number of compounds analysed relative to total OA composition or the lack of accounting for ionisation efficiency. More recently, there

have been a number of developments in the quantification of unknown compounds detected by non-target analysis. However, many fail to address quantification of species lacking fragmentation mass spectra (MS^2) in typical non-target workflows or the wide spread in ionisation efficiency of closely eluting surrogate standards. Chapter 2 illustrates the development of a new quantification strategy for use in non-target analysis of OA using Ultra-High-Performance Liquid Chromatography coupled to High Resolution Mass Spectrometry (UHPLC-HRMS) using negative mode electrospray ionisation (ESI) wherein retention time window and functional group specific calibration factors are applied to the quantification of unknowns. More specifically, unknown compounds are quantified using the corresponding retention time window scaling factor calculated from averaging the calibration factors of multiple standards eluting within the same retention time window as the unknown. This approach enabled more reliable quantification compared to previous approaches adopting a singular close eluting standard for quantification [183, 184]. The newly developed approach reported a quantification error, defined as the ratio of the semi-quantified concentration to that from an authentic standard, of 1.52 which improved on previous single standard studies. Compared to machine learning approaches predicting relative ionisation efficiencies (RIE), which require MS^2 to do this, the semi-quantification performed similarly or surpassed the model quantification error [185]. This improvement compared to the model was largely for nitroaromatic compounds for which there are fewer observations resulting in difficulty predicting RIE and indicates even with a relatively small number of standards it is possible to semi-quantify to reasonable accuracy. Another barrier in OA analysis using UHPLC-HRMS are matrix effects which occur in complex matrices, such as SOA, containing many co-eluting species. For a non-target analysis it can be even more challenging to address this issue as it is unknown how much the quantification of a species may be affected in the sample matrix without a standard and means the matrix effect cannot be accurately determined for unknown compounds. The matrix effect was evaluated for the known compounds in the biomass burning organic aerosol (BBOA) samples analysed by the semi-quantification method and observed to be within an accepted range of ± 20 %. However, it is impossible to say with certainty whether this magnitude of signal suppression or enhancement would be the same for unknown compounds and is a significant drawback of the current approach. The main

advancement of this approach, however, is in the comparison with peak area for determining the relative contributions of different chemical groups to total OA, where using peak area would lead to an underestimate of oxygenated organic compounds (CHO) compounds and overestimate of organonitrogen (CHON) compounds in BBOA in negative mode ESI. Generally, CHON compounds in BBOA are assigned as nitroaromatic compounds which have been widely used as tracers whereas this work shows that these compounds may contribute less to the SOA composition than previously thought and future work should adopt tracers with greater compositional contribution. This work observed these tracers should be CHO compounds, contributing on average to more than 85 % of the total mass detected in negative mode ESI, and are likely organic acids.

Chapter 3 leads on from the methodology developed in Chapter 2 to observe bulk compositional differences between flaming and smouldering burn phases in a domestic wood burning context. As well as the change after aging and the implications these changes may have on OA toxicity, subsequent atmospheric chemistry and climate. At present, wood burning is a significant area for policy improvement in the UK to reduce both detrimental impacts on the local air quality and on health from regular exposure to such sources. In recent years shifts in consumer trends has meant indoor wood burning is more commonplace in domestic homes, but unfortunately the vast majority of users have alternative sources of heating and burn wood inside their homes out of personal choice. It is currently estimated of the 8% of the UK population which burn wood indoors that only 4% is for necessity [14], and the number of users is likely to grow especially amongst the most affluent in society. Similar movements are occurring across Europe. However, in some of the poorest regions of the world there is a lack of access to clean fuels, and 2.1 billion people are forced to use solid fuel combustion for cooking and heating [123]. Therefore, there is an urgent need to evaluate the chemical composition of domestic combustion emissions, which over the course of a lifetime represents a chronic exposure. The results from this work show that fresh emissions in both burn phases are largely comprised of oxygenated aromatic compounds which can be harmful towards health and in particular smouldering combustion emits significantly higher concentrations of all oxygenated organics. At present, most policy surrounding $PM_{2.5}$ is based on mass concentration and therefore smouldering emissions

are likely considered more adverse to health in this respect. Interestingly, after aging, flaming emissions could become more toxic due to the formation of nitroaromatics and nitro-PAHs which are generally more harmful than the parent polyaromatic hydrocarbon (PAH). Whereas, smouldering emissions show substantial loss of aromaticity and indeed nitroaromatics potentially altering the relative toxicity compared to flaming on an equal mass basis. The differences upon aging also led to the identification of certain products which could be used as tracers for each burn phase in ambient air. For example, aged smouldering OA observed the presence of low mass C_4-C_5 compounds which were lacking in flaming mass spectra. Whereas, $C_{12}H_9NO_4$ was identified as a nitro-PAH and was unique to the aged flaming emissions. For future policy, it is apparent from this work that both mass concentration and composition must be taken into account when considering the adverse health effects of wood burning emissions. As well as, for how long a person may be exposed to the emissions from each burn phase. Furthermore, The International Energy Agency has set a goal of delivering clean fuels for all by 2030 which would require significantly greater efforts in sub-Saharan Africa where access is most lacking [123]. However, until access to clean fuels is granted for all guidance on the optimal procedure for solid fuel combustion that delivers both low particle mass concentrations, as well as, lower primary emissions or indeed secondary formation of toxic products must be considered.

To further investigate the role that oxygenated aromatics play in SOA formation from biomass burning, the chemistry of an understudied methoxyphenol, guaiacol, was evaluated in smog chamber experiments at the EUropean PHOtoREactor (EUPHORE). Guaiacol was chosen as it has both a high OH reactivity and SOA yield and it is not currently represented in the Master Chemical Mechanism (MCM, `https://mcm.york.ac.uk/MCM/`). Reported emissions of guaiacol from biomass burning are currently estimated as 172-276 mg per kg of fuel [318] which represents a significant source of SOA, especially when considering the millions of hectares of land and thus fuel burnt in wildfires across the globe. Furthermore, it is likely that the oxidation products from guaiacol could have contributed to the SOA characterised in Chapter 3. O_3 is also an important secondary product from biomass burning with adverse impacts on health and crop productivity. In this work it was observed that the guaiacol SOA yield was 15 % and per 1 ppb of guaiacol reacted in daytime conditions in VOC:NO_x

ratios similar to wildfires, 0.41 ppb of ozone (O_3) was produced. Therefore, an improved understanding of the gas and particle products from guaiacol oxidation could improve air quality models that predict the detrimental local, regional and global effects of wildfires. The main findings of Chapter 4 showed that the proposed guaiacol OH oxidation mechanism developed from structure activity relationships (SARs) well reproduced the observable chemistry. However, there was some missing OH reactivity resulting in an overprediction of the O_3 production which is a well known phenomenon for aromatic VOC oxidation with missing chemistry [295]. Deviations between modelled concentrations and measured timeseries for low volatility oxidation products such as nitroaromatic compounds were also observed and attributed to missing aerosol partitioning. This gas-to-particle partitioning of low volatility products was not possible to incorporate into the current MCM framework, however, with other atmospheric chemistry modelling tools it may be possible. One such option is the indoor air quality model INCHEM-Py [358] which could be adapted to represent the EUPHORE chamber. Therefore, further work is required to improve the SARs for methoxyphenols and add further chemistry or gas-to-particle partitioning for later generational products. This work also highlighted the importance of conducting experiments beyond that of single oxidant chamber studies for improving the understanding of transitions between night and day chemical regimes. The results indicated that guaiacol emissions that first undergo nighttime oxidation rapidly accumulates ring closed nitroguaiacol particle products which then subsequently forms ring open products during the day, whereas from day to night there was less change in the overall proportions of ring closed and ring opened products. Although this is just one case study it highlights a potential difference in the toxicity of the resulting aerosol which warrants further investigations as this understanding could be vastly important for wildfires which begin after sunset or in the context of domestic wood burning for heating which predominantly occurs at night.

5.2 Future work

There are a number of ways the work presented in this thesis could be improved upon and where further understanding is still required. As already mentioned the quantifi-

cation of OA remains a significant challenge to the aerosol community going forwards due to the lack of authentic standards. Whilst the methodology developed in Chapter 2 showed reasonable quantification accuracy in the BBOA samples it remains unknown in other OA applications and future work should test the methodology for OA samples from different sources. For example, in the York archive there are filters collected from different megacities (e.g Delhi, Beijing, Singapore, Manchester) and from chamber experiments of OA from cooking or vehicular emissions. Furthermore, to examine the complete chemical composition it is required to analyse the positive mode ESI mass spectra and future work must develop a similar semi-quantification method. This is however hampered by the lack of standards available, and as there is a greater quantity of chemical functionality that can be analysed in positive mode ESI an increased quantity of standards is needed. The lack of commercially available standards can be somewhat overcome through the synthesis of SOA markers but is significantly more time consuming. Furthermore, it would greatly benefit the advancement of analytical aerosol science to share any synthetic or commercial standards between research groups so that open source quantification methods such as in Chapter 2 can be more readily developed and then shared amongst the community. Future work should also investigate matrix effects which, by obtaining more authentic standards, may allow a better understanding of their occurrence and accounting for them. The phenomenon of ionisation efficiency is not isolated to UHPLC-HRMS analysis and the procurement of analytical standards for SOA markers may also enable the development of methods to account for instrument sensitivity in online measurements such as Iodide Chemical Ionisation Mass Spectrometry (I-CIMS) [167]. Quantification of the I-CIMS measurements of guaiacol oxidation products would enable an improved assessment of the model prediction accuracy compared to measured concentrations. Furthermore, the main disadvantage to I-CIMS measurements is the lack of isomeric separation which affected the comparison of the modelled products to measurement in Chapter 4 when guaiacol oxidation products had the same m/z and molecular formula. The community would greatly benefit from advancements in measurement technology coupling I-CIMS with separation methods, such as gas chromatography, which would enable the separation of these isomeric products and improve the model evaluation presented in Chapter 4.

In addition to improving measurement capability, the work from this thesis would benefit from repeating the experiments with some adaptions to the presented protocol. Firstly, in the University of Manchester chamber experiments described in Chapter 3 the fresh samples were taken on a different day to the aged samples and whilst the composition between different days is reasonably repeatable, an improved comparison would analyse fresh emissions once injected inside the chamber before aging. The main barrier to this is the need for high mass loading for offline UHPLC-HRMS analysis and future work would need to redesign the experiments to use a much greater initial particle concentration. Secondly, the guaiacol mechanism was validated against a single experiment, therefore, further repeats across a wider range of conditions are required. For example, across different VOC:NO_x ratios for high to low NO_x environments to determine the sensitivity of certain mechanistic pathways and to better constrain the OH abstraction versus addition pathways from the initial precursor as well as probing for RO_2 autoxidation in the early stages of the experiment to produce OH. It would also be beneficial to conduct experiments at different RH for determination of SOA yields or in the presence of seed. As I-CIMS measurements can be impacted by humidity, conducting experiments over a wide range of RH could help determine to what extent the results presented in Chapter 4 may have been impacted by the experimental design. Furthermore, high concentrations ($\approx$ 500 ppb) of guaiacol were used in these experiments and future work may benefit from using more atmospherically relevant concentrations of the VOC precursor.

Overall, a wealth of data was collected in the preparation of this thesis and there are many possible future directions of research. For example, applying the semi-quantitative methodology in Chapter 2 to OA collected in the Manchester burn experiments from different fuel types to probe differences in chemical composition and in the development of SOA markers. During the EUPHORE campaign in Chapter 4, data was also collected for furanic compounds across a similar set of experiments. The atmospheric chemistry of these compounds is also relatively unknown and closing this gap would help constrain the impact of biomass burning on air quality and climate in models. Future mechanism development would certainly benefit from an improvement to the SAR protocol through experimental evaluation of kinetic rate coefficients belonging to oxygenated aromatics. With the range of experiments conducted

throughout this thesis SOA markers could be developed that are source-specific or distinct to fresh and aged emissions. For example, the EUPHORE experiments could be used to develop unique SOA tracers to each biomass burning VOC. Finally, as the guaiacol mechanism developed in Chapter 4 still has missing OH reactivity compared to observations and this is most likely from missing chemistry of the oxidation products, it would be of value to conduct experiments starting with the oxidation product rather than the precursor VOC.

5.3 Final remarks

It is hoped that the work in this thesis addresses some fundamental challenges in the analytical study of organic aerosols and contributes to the chemical understanding of biomass burning emissions in the atmosphere. However, the complexity of the atmosphere will likely continue to present challenges for analytical scientists and atmospheric chemists in the future study of biomass burning emissions in the years to come.

Appendix A

Supporting Information for Chapter 4

6.99D-11*0.16 : GUAIACOL + OH = OMC6H4O ;

6.99D-11*0.06 : GUAIACOL + OH = CATECHOL ;

6.99D-11*0.119 : GUAIACOL + OH = GUAIAO2 ;

6.99D-11*0.179 : GUAIACOL + OH = GUAIAOXMUC + HO2 ;

6.99D-11*0.482 : GUAIACOL + OH = OMCATECHOL + HO2 ;

2.10D-17: GUAIACOL + NO3 = NO3GUAIACOLPROD ;

2.08D-12 : OMC6H4O + NO2 = NGUAIACOL ;

2.60D-10 : NGUAIACOL + OH = NGUAIA1O ;

2.08D-12 : NGUAIA1O + NO2 = DNGUAIACOL ;

KRO2NO : GUAIAO2 + NO = GUAIACO + NO2 ;

KRO2NO3 : GUAIAO2 + NO3 = GUAIACO + NO2 ;

4.378D-12*0.8*RO2 : GUAIAO2 = GUAIACO ;

4.378D-12*0.2*RO2 : GUAIAO2 = GUAIACOH ;

KRO2HO2 : GUAIAO2 + HO2 = GUAIACOOH ;

J<41> : GUAIACOOH = GUAIACO + OH ;

2.56D-10 : GUAIACOH + OH = GUAIACO ;

KDEC*0.3 : GUAIACO = OMC5CO14OH + GLYOX + HO2 ;

KDEC*0.7 : GUAIACO = OMPBZQONE + HO2;

J<31> : GLYOX = CO + CO + H2 ;

J<32> : GLYOX = CO + HCHO ;

J<33> : GLYOX = CO + CO + HO2 + HO2 ;

3.1D-12*EXP(340/TEMP) : GLYOX + OH = HCOCO ;

KNO3AL : GLYOX + NO3 = HCOCO + HNO3 ;

KAPNO : HCOCO3 + NO = CO + HO2 + NO2 ;

KFPAN : HCOCO3 + NO2 = CO + HO2 + NO3 ;

KRO2NO3*1.74 : HCOCO3 + NO3 = CO + HO2 + NO2 ;

KAPHO2*0.41 : HCOCO3 + HO2 = HCOCO3H ;

KAPHO2*0.15 : HCOCO3 + HO2 = HCOCO2H + O3 ;

1.00D-11*0.7*RO2 : HCOCO3 = CO + HO2 ;

1.00D-11*0.3*RO2 : HCOCO3 = HCOCO2H ;

1.58D-11 : HCOCO3H + OH = HCOCO3 ;

J<41> : HCOCO3H = CO + HO2 + OH ;

J<15> : HCOCO3H = CO + HO2 + OH ;

1.23D-11 : HCOCO2H + OH = CO + HO2 ;

5.4D-12*EXP(135/TEMP) : HCHO + OH = CO + HO2 ;

J<11> : HCHO = CO + HO2 + HO2 ;

J<12> : HCHO = CO + H2 ;

5.5D-16 : HCHO + NO3 = CO + HNO3 + HO2 ;

J<34> : HCOCO2H = CO + HO2 + HO2 ;

KAPHO2*0.44 : HCOCO3 + HO2 = CO + HO2 + OH ;

7.00D11*EXP(-3160/TEMP) : HCOCO = CO + CO + HO2 ;

5.00D-12*O2 : HCOCO = CO + CO + HO2 ;

5.00D-12*O2*3.2*EXP(-550/TEMP) : HCOCO = HCOCO3 ;

5.00D-12*O2*3.2*(1-EXP(-550/TEMP)) : HCOCO = CO + OH ;

1.73D-10*0.03 : OMCATECHOL + OH = OMCATEC1O ;

1.73D-10*0.618 : OMCATECHOL + OH = OMCATECO2 ;

1.73D-10*0.265 : OMCATECHOL + OH = OMCATOXMUC + HO2;

1.73D-10*0.087 : OMCATECHOL + OH = OMBENZ135OH + HO2 ;

2.08D-12 : OMCATEC1O + NO2 = NOMCATECHOL ;

KRO2NO : OMCATECO2 + NO = OMCATECO + NO2 ;

KRO2NO3 : OMCATECO2 + NO3 = OMCATECO + NO2 ;

KRO2HO2 : OMCATECO2 + HO2 = OMCATECOOH ;

1.25D-13*0.2*RO2 : OMCATECO2 = OMCATECOH ;

1.25D-13*0.8*RO2 : OMCATECO2 = OMCATECO ;

J<41> : OMCATECOOH = OMCATECO ;

2.72D-10 : OMCATECOH + OH = OMCATECO + OH ;

KDEC*0.3 : OMCATECO = OMCATPBZQONE + HO2 ;

KDEC *0.7 : OMCATECO = OMC4CO142OH + HCOCO2H + HO2 ;

J<4>*0.5 : OMC4CO142OH = OM2OHFUONE ;

J<4>*0.5 : OMC4CO142OH = OMC42OHCO14O2 + HO2 ;

5.59D-11 : OMC4CO142OH + OH = OMC42OHCO14O2 + HO2 ;

KAPNO : OMC42OHCO14O2 + NO = OMC42OHCO14O + NO2;

KRO2NO3 : OMC42OHCO14O2 + NO3 = OMC42OHCO14O + NO2 ;

KAPHO2*0.5 : OMC42OHCO14O2 + HO2 = OMC42OHCO14O + OH ;

KAPHO2*0.37 : OMC4C2OHCO14O2 + HO2 = OMC42OHCO14OOH ;

KAPHO2*0.13 : OMC4C2OHCO14O2 + HO2 = COOMEC2OHCO2H + O3;

1.00D-11*RO2*0.2 : OMC4C2OHCO14O2 = COOMEC2OHCO2H;

1.00D-11*RO2*0.8 : OMC4C2OHCO14O2 = OMC42OHCO14O ;

KFPAN : OMC42OHCO14O2 + NO2 = OMC42OHCO14PAN ;

KBPAN : OMC42OHCO14PAN = NO2 + OMC42OHCO14O2 ;

J<24> : COOMEC2OHCO2H = HCOCO2H + COOMECOHO2 ;

J<23> : COOMEC2OHCO2H = HCOCO2H + COOMECOHO2 ;

4.89D-11 : COOMEC2OHCO2H + OH = OMC42OHCO14O ;

KDEC*0.8 : OMC42OHCO14O = MALANHYOH + CH3O3 ;

KDEC*0.2 : OMC42OHCO14O = OMCOCO2H + HO2 + CO ;

1.73D-9*0.13: OMBENZ135OH + OH = OMBENZ1345OH + HO2 ;

1.73D-9*0.26: OMBENZ135OH + OH = OMBENZ135EPOX + HO2 ;

1.73D-9*0.61: OMBENZ135OH + OH = OMBENZ135O2 ;

7.95D-11 : OMPBZQONE + OH = OMPBZQO2 ;

KRO2NO : OMPBZQO2 + NO = OMPBZQO + NO2 ;

KRO2NO3 : OMPBZQO2 + NO3 = OMPZQO + NO2 ;

2.00D-14*0.6*RO2 : OMPBZQO2 = OMPBZQO ;

2.00D-14*0.2*RO2 : OMPBZQO2 = OMPBZQCO ;

2.00D-14*0.2*RO2 : OMPBZQO2 = OMPBZQOH ;

KRO2HO2 : OMPBZQO2 + HO2 = OMPBZQOOH ;

J<41> : OMPBZQOOH = OMPBZQO + OH ;

1.43D-10 : OMPBZQOOH + OH = OMPBZQCO + OH ;

7.45D-11 : OMPBZQOH + OH = OMPBZQCO + HO2 ;

5.32D-11 : OMPBZQCO + OH = C613CO2OH4OMCO3 ;

KDEC : OMPBZQO = C613CO2OH4OMCO3 ;

2.62D-11 : OMC5CO14OH + OH = OMC5CO14CO2 ;

J<24> : OMC5CO14OH = HCOCO2H + HO2 + CO + OMCO3 ;

J<23> : OMC5CO14OH = HCOCO2H + HO2 + CO + OMCO3 ;

KFPAN : OMCO3 + NO2 = OMPAN ;

KBPAN : OMPAN = OMCO3 + NO2 ;

KDEC*0.01 : OMC5CO14CO2 = OMGLYOX + HO2+ CO ;

KDEC*0.99 : OMC5CO14CO2 = MALANHY + CH3O3 ;

1.4D-12 : MALANHY + OH = MALANHYO2 ;

KRO2NO : MALANHYO2 + NO = MALANHYO + NO2 ;

KDEC : MALANHYO = HCOCOHCO3 ;

KAPNO : HCOCOHCO3 + NO = GLYOX + HO2 + NO2 ;

KFPAN : HCOCOHCO3 + NO2 = HCOCOHPAN ;

KBPAN : HCOCOHPAN = HCOCOHCO3 + NO2 ;

KRO2NO3*1.74 : HCOCOHCO3 + NO3 = GLYOX + HO2 + NO2 ;

KAPHO2*0.56 : HCOCOHCO3 + HO2 = HCOCOHCO3H ;

1.00D-11*RO2 : HCOCOHCO3 = GLYOX + HO2 ;

6.97D-11 : HCOCOHPAN + OH = CO + GLYOX + NO2 ;

J<41> : HCOCOHCO3H = GLYOX + HO2 + OH ;

7.33D-11 : HCOCOHCO3H + OH = HCOCOHCO3 ;

KRO2NO3 : MALANHYO2 + NO3 = MALANHYO + NO2 ;

KRO2HO2*0.625 : HO2 + MALANHYO2 = MALANHYOOH ;

8.80D-13*0.6*RO2 : MALANHYO2 = MALANHYO ;

8.80D-13*0.2*RO2 : MALANHYO2 = MALANHY2OH ;

8.80D-13*0.2*RO2 : MALANHYO2 = MALNHYOHCO ;

J<41> : MALANHYOOH = MALANHYO + OH ;

4.66D-11 : MALANHYOOH + OH = MALNHYOHCO + OH ;

2.55D-11 : MALANHY2OH + OH = HO2 + MALNHYOHCO ;

5.68D-12 : MALNHYOHCO + OH = CO + CO + CO + HO2 ;

KAPHO2*0.44 : HCOCOHCO3 + HO2 = GLYOX + HO2 + OH ;

KAPNO : C613CO2OH4OMCO3 + NO = C5134CO2OH4OM + HO2 + CO + NO2 ;

KRO2NO3 : C613CO2OH4OMCO3 + NO3 = C5134CO2OH4OM + HO2 + CO + NO2;

KAPHO2*0.42 : C613CO2OH4OMCO3 + HO2 = C5134CO2OH4OM + HO2 + CO + OH ;

1.00D-11*RO2 : C613CO2OH4OMCO3 = C5134CO2OH4OM + HO2 + CO ;

KFPAN : C613CO2OH4OMCO3 + NO2 = C6135CO2OH4OMPAN ;

KBPAN : C6135CO2OH4OMPAN = C613CO2OH4OMCO3 + NO2 ;

KAPHO2*0.58 : C613CO2OH4OMCO3 + HO2 = C613CO2OH4OMCOOH ;

5.74D-11 : C6135CO2OH4OMCOOH + OH = C613CO2OH4OMCO3 ;

J<34> : C5134CO2OH4OM = OMCO23CHO + HO2 + CO ;

J<15> : C5134CO2OH4OM = OMCO23CHO + HO2 + CO ;

1.11D-11 : C5134CO2OH4OM + OH = OMC44CO + HO2 ;

J<41> : C613CO2OH4OMCOOH + OH = C5134CO2OH4OM + HO2 +CO + OH ;

1.65D-12 : DNGUAIACOL + OH = DNGUAIAO2 ;

KRO2NO : DNGUAIAO2 + NO = DNGUAIAO + NO2 ;

KRO2NO3 : DNGUAIAO2 + NO3 = DNGUAIAO + NO ;

4.39D-12*0.8*RO2 : DNGUAIAO2 = DNGUAIAO ;

4.39D-12*0.2*RO2 : DNGUAIAO2 = DNGUAIAOH ;

KRO2HO2 : DNGUAIAO2 = DNGUAIAOOH ;

J<41> : DNGUAIAOOH = DNGUAIACO ;

KDEC : DNGUAIAO = NC4DOMCO2H + HCOCO2H + NO2 ;

7.91D-11 : GUAIAOXMUC + OH = EPOXPRODUCTS ;

J<4>*0.1*0.5 : GUAIAOXMUC = EPXC4DIAL + HO2 + CO ;

J<4>*0.1*0.5 : GUAIAOXMUC = OMC4CO14OH2CO3 + HO2 + CO ;

J<15>*2 : C32OH13CO = CO + GLYOX + HO2 + HO2 ;

1.36D-10 : C32OH13CO + OH = HCOCOHCO3 ;

KRO2NO : C3DIALO2 + NO = C3DIALO + NO2 ;

KDEC : C3DIALO = CO + GLYOX + HO2 ;

KRO2NO3 : C3DIALO2 + NO3 = C3DIALO + NO2 ;

KRO2HO2*0.520 : C3DIALO2 + HO2 = C3DIALOOH ;

8.80D-13*RO2*0.6 : C3DIALO2 = C3DIALO ;

8.80D-13*RO2*0.2 : C3DIALO2 = C32OH13CO ;

8.80D-13*RO2*0.2 : C3DIALO2 = C33CO ;

J<41> : C3DIALOOH = C3DIALO + OH ;

J<15>*2 : C3DIALOOH = CO + GLYOX + HO2 + OH ;

1.44D-10 : C3DIALOOH + OH = C33CO + OH ;

J<15>*2 : C33CO = CO + CO + CO + HO2 + HO2 ;

5.77D-11 : C33CO + OH = CO + CO + CO + HO2 ;

J<17>*2 : EPXC4DIAL = C3DIALO2 + CO + HO2 ;

4.32D-11 : EPXC4DIAL + OH = EPXDLCO3 ;

2*KNO3AL*4.0 : EPXC4DIAL + NO3 = EPXDLCO3 + HNO3 ;

KAPNO : EPXDLCO3 + NO = C3DIALO2 + NO2 ;

KFPAN : EPXDLCO3 + NO2 = EPXDLPAN ;

KBPAN : EPXDLPAN = EPXDLCO3 + NO2 ;

KRO2NO3*1.74 : EPXDLCO3 + NO3 = C3DIALO2 + NO2 ;

KAPHO2*0.41 : EPXDLCO3 + HO2 = EPXDLCO3H ;

KAPHO2*0.15 : EPXDLCO3 + HO2 = EPXDLCO2H + O3 ;

1.00D-11*RO2*0.7 : EPXDLCO3 = C3DIALO2 ;

1.00D-11*RO2*0.3 : EPXDLCO3 = EPXDLCO2H ;

2.29D-11 : EPXDLPAN + OH = C33CO + CO + NO2 ; J<41> : EPXDLCO3H = C3DIALO2 + OH ;

J<17> : EPXDLCO3H = C3DIALO2 + OH ;

2.62D-11 : EPXDLCO3H + OH = EPXDLCO3 ;

J<17> : EPXDLCO2H = C3DIALO2 + HO2 ;

2.31D-11 : EPXDLCO2H + OH = C3DIALO2 ;

KAPHO2*0.44 : EPXDLCO3 + HO2 = C3DIALO2 + OH ;

2.93D-11*0.82 : NOMCATECHOL + OH = NOMCATECO2;

2.93D-11*0.18 : NOMCATECHOL + OH = NOMCATEC1O ;

KRO2NO : NOMCATECO2 + NO = NOMCATECO + NO2 ;

KRO2NO3 : NOMCATECO2 + NO3 = NOMCATECO + NO2 ;

KRO2HO2 : NOMCATECO2 + HO2 = NOMCATECOOH ;

8.00D-13*RO2 : NOMCATECO2 = NOMCATECO ;

1.90D-12*EXP(190/TEMP) : NOMCATECOOH + OH = NOMCATECO2 ;

J<41> : NOMCATECOOH = NOMCATECO ;

KDEC : NOMCATECO = NC4DOMCO2H + HCOCO2H + HO2 ;

1.90D-12*EXP(190/TEMP) : NC4DOMCO2H + OH = NC4DOMCO2 ;

KDEC : NC4DOMCO2 = OMMALANHY + NO2 ;

2.08D-12 : NOMCATEC1O + NO2 = DNOMCATECHOL ;

1.0D-10 : CATECHOL + OH = CATEC1O ;

9.9D-11 : CATECHOL + NO3 = CATEC1O + HNO3 ;

9.2D-18 : CATECHOL + O3 = CATECOOA ;

KDEC : CATECOOA = HCOCO2H + HO2 + MALDALCO2H + OH ;

2.08D-12 : CATEC1O + NO2 = NCATECHOL ;

2.86D-13 : CATEC1O + O3 = CATEC1O2 ;

KRO2NO : CATEC1O2 + NO = CATEC1O + NO2 ;

KRO2NO3 : CATEC1O2 + NO3 = CATEC1O + NO2 ;

KRO2HO2*0.770 : CATEC1O2 + HO2 = CATEC1OOH ;

8.80D-13*RO2 : CATEC1O2 = CATEC1O ;

J<41> : CATEC1OOH = CATEC1O + OH ;

1.90D-12*EXP(190/TEMP) : CATEC1OOH + OH = CATEC1O2 ;

3.47D-12 : NCATECHOL + OH = NCATECO2 ;

2.60D-12 : NCATECHOL + NO3 = NNCATECO2 ;

KRO2NO : NCATECO2 + NO = NCATECO + NO2 ;

KRO2NO3 : NCATECO2 + NO3 = NCATECO + NO2 ;

KDEC : NCATECO = HCOCO2H + HO2 + NC4DCO2H ;

KRO2HO2*0.770 : HO2 + NCATECO2 = NCATECOOH ;

8.00D-13*RO2 : NCATECO2 = NCATECO ;

J<41> : NCATECOOH = NCATECO + OH ;

1.90D-12*EXP(190/TEMP) : NCATECOOH + OH = NCATECO2 ;

KRO2NO : NNCATECO2 + NO = NNCATECO + NO2 ;

KRO2NO3 : NNCATECO2 + NO3 = NNCATECO + NO2 ;

KDEC : NNCATECO = HCOCO2H + NC4DCO2H + NO2 ;

KRO2HO2*0.770 : HO2 + NNCATECO2 = NNCATECOOH ;

8.00D-13*RO2 : NNCATECO2 = NNCATECO ;

J<41> : NNCATECOOH = NNCATECO + OH ;

1.90D-12*EXP(190/TEMP) : NNCATECOOH + OH = NNCATECO2 ;

1.90D-12*EXP(190/TEMP) : NC4DCO2H + OH = NC4DCO2 ;

KDEC : NC4DCO2 = MALANHY + NO2 ;

J<18> : MALDALCO2H = CO + CO + HCOCO2H + HO2 + HO2 ;

J<19> : MALDALCO2H = CO + CO + HCOCO2H + HO2 + HO2 ;

3.70D-11 : MALDALCO2H + OH = MALDIALCO2 ;

KDEC*0.40 : MALDIALCO2 = CO + GLYOX + HO2 ;

KDEC*0.60 : MALDIALCO2 = HO2 + MALANHY ;

Bibliography

[1] World Health Organisation. *Ambient (outdoor) air pollution*. 2024. URL: https://www.who.int/news-room/fact-sheets/detail/ambient-(outdoor)-air-quality-and-health.

[2] Cohen, A. J., Brauer, M., Burnett, R., Anderson, H. R., Frostad, J., Estep, K., Balakrishnan, K., Brunekreef, B., Dandona, L., Dandona, R., Feigin, V., Freedman, G., Hubbell, B., Jobling, A., Kan, H., Knibbs, L., Liu, Y., Martin, R., Morawska, L., Pope, C. A., Shin, H., Straif, K., Shaddick, G., Thomas, M., Dingenen, R. van, Donkelaar, A. van, Vos, T., Murray, C. J., and Forouzanfar, M. H. Estimates and 25-year trends of the global burden of disease attributable to ambient air pollution: an analysis of data from the Global Burden of Diseases Study 2015. *The Lancet* 389 (10082 2017), pp. 1907–1918. DOI: 10.1016/S0140-6736(17)30505-6.

[3] Okello, G., Devereux, G., and Semple, S. Women and girls in resource poor countries experience much greater exposure to household air pollutants than men: Results from Uganda and Ethiopia. *Environment International* 119 (2018), pp. 429–437. DOI: 10.1016/J.ENVINT.2018.07.002.

[4] Clougherty, J. E. A growing role for gender analysis in air pollution epidemiology. *Environmental Health Perspectives* 118 (2 2010), pp. 167–176. DOI: 10.1289/EHP.0900994.

[5] Lelieveld, J., Evans, J. S., Fnais, M., Giannadaki, D., and Pozzer, A. The contribution of outdoor air pollution sources to premature mortality on a global scale. *Nature 2015 525:7569* 525 (7569 2015), pp. 367–371. DOI: 10.1038/nature15371.

[6] Juginović, A., Vuković, M., Aranza, I., and Biloš, V. Health impacts of air pollution exposure from 1990 to 2019 in 43 European countries. *Scientific Reports 2021 11:1* 11 (1 2021), pp. 1–15. DOI: 10.1038/s41598-021-01802-5.

[7] GBD 2021 Risk Factor Collaborators. Global burden and strength of evidence for 88 risk factors in 204 countries and 811 subnational locations, 1990–2021: a systematic

analysis for the Global Burden of Disease Study 2021. *The Lancet* 403 (10440 2024), pp. 2162–2203. DOI: 10.1016/S0140-6736(24)00933-4.

[8] Rinnan, R., Iversen, L. L., Tang, J., Vedel-Petersen, I., Schollert, M., and Schurgers, G. Separating direct and indirect effects of rising temperatures on biogenic volatile emissions in the Arctic. *Proceedings of the National Academy of Sciences of the United States of America* 117 (51 2020), pp. 32476–32483. DOI: 10.1073/PNAS.2008901117.

[9] Qin, M., She, Y., Wang, M., Wang, H., Chang, Y., Tan, Z., An, J., Huang, J., Yuan, Z., Lu, J., Wang, Q., Liu, C., Liu, Z., Xie, X., Li, J., Liao, H., Pye, H. O., Huang, C., Guo, S., Hu, M., Zhang, Y., Jacob, D. J., and Hu, J. Increased urban ozone in heatwaves due to temperature-induced emissions of anthropogenic volatile organic compounds. *Nature Geoscience 2025 18:1* 18 (1 2025), pp. 50–56. DOI: 10.1038/s41561-024-01608-w.

[10] Air Quality Expert Group. *Non-methane Volatile Organic Compounds in the UK*. 2020. URL: https://uk-air.defra.gov.uk/assets/documents/reports/cat09/2006240803_Non_Methane_Volatile_Organic_Compounds_in_the_UK.pdf.

[11] United Kingdom Government. *Clean Air Act*. 1956. URL: https://www.legislation.gov.uk/ukpga/Eliz2/4-5/52/enacted.

[12] Lewis, A. C., Hopkins, J. R., Carslaw, D. C., Hamilton, J. F., Nelson, B. S., Stewart, G., Dernie, J., Passant, N., and Murrells, T. An increasing role for solvent emissions and implications for future measurements of volatile organic compounds. *Philosophical Transactions of the Royal Society A* 378 (2183 2020). DOI: 10.1098/RSTA.2019.0328.

[13] Department for Environment, Food Rural Affairs. *Emissions of air pollutants in the UK – Non-methane volatile organic compounds (NMVOCs)*. 2024. URL: https://www.gov.uk/government/statistics/emissions-of-air-pollutants/emissions-of-air-pollutants-in-the-uk-non-methane-volatile-organic-compounds-nmvocs.

[14] Department for Environment Food & Rural Affairs (DEFRA). *Burning in UK Homes and Gardens Research Report*. 2020. URL: https://uk-air.defra.gov.uk/library/reports?report_id=1014.

[15] McDuffie, E. E., Martin, R. V., Spadaro, J. V., Burnett, R., Smith, S. J., O'Rourke, P., Hammer, M. S., Donkelaar, A. van, Bindle, L., Shah, V., Jaeglé, L., Luo, G., Yu, F., Adeniran, J. A., Lin, J., and Brauer, M. Source sector and fuel contributions to ambient PM2.5 and attributable mortality across multiple spatial scales. *Nat. Commun.* 12 (1 2021), pp. 1–12. DOI: 10.1038/s41467-021-23853-y.

[16] Valdez, R. B., Tabatabai, M., Al-Hamdan, M. Z., Wilus, D., Hood, D. B., Im, W., Nori-Sarma, A., Ramesh, A., Donneyong, M. M., Langston, M. A., Mouton, C. P., and Juárez, P. D. Association of diabetes and exposure to fine particulate matter (PM2.5) in the Southeastern United States. *Hygiene and Environmental Health Advances* 4 (2022), p. 100024. DOI: 10.1016/J.HEHA.2022.100024.

[17] GBD 2019 Diabetes and Air Pollution Collaborators. Estimates, trends, and drivers of the global burden of type 2 diabetes attributable to PM2·5 air pollution, 1990–2019: an analysis of data from the Global Burden of Disease Study 2019. *The Lancet Planetary Health* 6 (7 2022), e586–e600. DOI: 10.1016/S2542-5196(22)00122-X.

[18] Landrigan, P. J., Fuller, R., Acosta, N. J., Adeyi, O., Arnold, R., Basu, N. (, Baldé, A. B., Bertollini, R., Bose-O'Reilly, S., Boufford, J. I., Breysse, P. N., Chiles, T., Mahidol, C., Coll-Seck, A. M., Cropper, M. L., Fobil, J., Fuster, V., Greenstone, M., Haines, A., Hanrahan, D., Hunter, D., Khare, M., Krupnick, A., Lanphear, B., Lohani, B., Martin, K., Mathiasen, K. V., McTeer, M. A., Murray, C. J., Ndahimananjara, J. D., Perera, F., Potočnik, J., Preker, A. S., Ramesh, J., Rockström, J., Salinas, C., Samson, L. D., Sandilya, K., Sly, P. D., Smith, K. R., Steiner, A., Stewart, R. B., Suk, W. A., Schayck, O. C. van, Yadama, G. N., Yumkella, K., and Zhong, M. The Lancet Commission on pollution and health. *The Lancet* 391 (10119 2018), pp. 462–512. DOI: 10.1016/S0140-6736(17)32345-0.

[19] Apte, J. S., Brauer, M., Cohen, A. J., Ezzati, M., and Pope, C. A. Ambient PM2.5 Reduces Global and Regional Life Expectancy. *Environmental Science and Technology Letters* 5 (9 2018), pp. 546–551. DOI: 10.1021/acs.estlett.8b00360.

[20] Department for Environment, Food Rural Affairs. *Particulate matter (PM10/PM2.5) - GOV.UK*. 2024. URL: https://www.gov.uk/government/statistics/air-quality-statistics/concentrations-of-particulate-matter-pm10-and-pm25.

[21] Air Quality Expert Group. *Ultrafine Particle (UFP) in the UK*. 2018. URL: https://uk-air.defra.gov.uk/assets/documents/reports/cat09/1807261113_180703_UFP_Report_FINAL_for_publication.pdf.

[22] Bond, T. C., Doherty, S. J., Fahey, D. W., Forster, P. M., Berntsen, T., Deangelo, B. J., Flanner, M. G., Ghan, S., Kärcher, B., Koch, D., Kinne, S., Kondo, Y., Quinn, P. K., Sarofim, M. C., Schultz, M. G., Schulz, M., Venkataraman, C., Zhang, H., Zhang, S., Bellouin, N., Guttikunda, S. K., Hopke, P. K., Jacobson, M. Z., Kaiser, J. W., Klimont, Z., Lohmann, U., Schwarz, J. P., Shindell, D., Storelvmo, T., Warren, S. G., and Zender, C. S. Bounding the

role of black carbon in the climate system: A scientific assessment. *Journal of Geophysical Research: Atmospheres* 118 (11 2013), pp. 5380–5552. DOI: 10.1002/JGRD.50171.

[23] Kiehl, J. T. and Briegleb, B. P. The Relative Roles of Sulfate Aerosols and Greenhouse Gases in Climate Forcing. *Science* 260 (5106 1993), pp. 311–314. DOI: 10.1126/SCIENCE.260.5106.311.

[24] Laskin, A., Laskin, J., and Nizkorodov, S. A. Chemistry of Atmospheric Brown Carbon. *Chemical Reviews* 115 (10 2015), pp. 4335–4382. DOI: 10.1021/CR5006167.

[25] Bellouin, N., Quaas, J., Gryspeerdt, E., Kinne, S., Stier, P., Watson-Parris, D., Boucher, O., Carslaw, K. S., Christensen, M., Daniau, A. L., Dufresne, J. L., Feingold, G., Fiedler, S., Forster, P., Gettelman, A., Haywood, J. M., Lohmann, U., Malavelle, F., Mauritsen, T., McCoy, D. T., Myhre, G., Mülmenstädt, J., Neubauer, D., Possner, A., Rugenstein, M., Sato, Y., Schulz, M., Schwartz, S. E., Sourdeval, O., Storelvmo, T., Toll, V., Winker, D., and Stevens, B. Bounding Global Aerosol Radiative Forcing of Climate Change. *Reviews of Geophysics* 58 (1 2020), e2019RG000660. DOI: 10.1029/2019RG000660.

[26] Forster, P., Storelvmo, T., Armour, K., Collins, W., Dufresne, J. L., Frame, D., Lunt, D., Mauritsen, T., Palmer, M., Watanabe, M., Wild, M., and Zhang, H. The Earth's Energy Budget, Climate Feedbacks, and Climate Sensitivity. *Climate Change 2021: The Physical Science Basis. Contribution of Working Group I to the Sixth Assessment Report of the Intergovernmental Panel on Climate Change*. Cambridge University Press, 2021.

[27] Fuzzi, S., Baltensperger, U., Carslaw, K., Decesari, S., Gon, H. D. van der, Facchini, M. C., Fowler, D., Koren, I., Langford, B., Lohmann, U., Nemitz, E., Pandis, S., Riipinen, I., Rudich, Y., Schaap, M., Slowik, J. G., Spracklen, D. V., Vignati, E., Wild, M., Williams, M., and Gilardoni, S. Particulate matter, air quality and climate: lessons learned and future needs. *Atmospheric Chemistry and Physics* 15 (14 2015), pp. 8217–8299. DOI: 10.5194/acp-15-8217-2015.

[28] Jimenez, J. L., Canagaratna, M. R., Donahue, N. M., Prevot, A. S., Zhang, Q., Kroll, J. H., DeCarlo, P. F., Allan, J. D., Coe, H., Ng, N. L., Aiken, A. C., Docherty, K. S., Ulbrich, I. M., Grieshop, A. P., Robinson, A. L., Duplissy, J., Smith, J. D., Wilson, K. R., Lanz, V. A., Hueglin, C., Sun, Y. L., Tian, J., Laaksonen, A., Raatikainen, T., Rautiainen, J., Vaattovaara, P., Ehn, M., Kulmala, M., Tomlinson, J. M., Collins, D. R., Cubison, M. J., Dunlea, E. J., Huffman, J. A., Onasch, T. B., Alfarra, M. R., Williams, P. I., Bower, K., Kondo, Y., Schneider, J., Drewnick, F., Borrmann, S., Weimer, S., Demerjian, K., Salcedo, D., Cottrell, L., Griffin, R., Takami, A., Miyoshi, T., Hatakeyama, S., Shimono, A.,

Sun, J. Y., Zhang, Y. M., Dzepina, K., Kimmel, J. R., Sueper, D., Jayne, J. T., Herndon, S. C., Trimborn, A. M., Williams, L. R., Wood, E. C., Middlebrook, A. M., Kolb, C. E., Baltensperger, U., and Worsnop, D. R. Evolution of organic aerosols in the atmosphere. *Science* 326 (5959 2009), pp. 1525–1529. DOI: 10.1126/SCIENCE.1180353.

[29] Zhang, Q., Alfarra, M. R., Worsnop, D. R., Allan, J. D., Coe, H., Canagaratna, M. R., and Jimenez, J. L. Deconvolution and quantification of hydrocarbon-like and oxygenated organic aerosols based on aerosol mass spectrometry. *Environmental Science and Technology* 39 (13 2005), pp. 4938–4952. DOI: 10.1021/ES048568L/.

[30] Chen, G., Canonaco, F., Tobler, A., Aas, W., Alastuey, A., Allan, J., Atabakhsh, S., Aurela, M., Baltensperger, U., Bougiatioti, A., Brito, J. F. D., Ceburnis, D., Chazeau, B., Chebaicheb, H., Daellenbach, K. R., Ehn, M., Haddad, I. E., Eleftheriadis, K., Favez, O., Flentje, H., Font, A., Fossum, K., Freney, E., Gini, M., Green, D. C., Heikkinen, L., Herrmann, H., Kalogridis, A. C., Keernik, H., Lhotka, R., Lin, C., Lunder, C., Maasikmets, M., Manousakas, M. I., Marchand, N., Marin, C., Marmureanu, L., Mihalopoulos, N., Močnik, G., Nęcki, J., O'Dowd, C., Ovadnevaite, J., Peter, T., Petit, J. E., Pikridas, M., Platt, S. M., Pokorná, P., Poulain, L., Priestman, M., Riffault, V., Rinaldi, M., Różański, K., Schwarz, J., Sciare, J., Simon, L., Skiba, A., Slowik, J. G., Sosedova, Y., Stavroulas, I., Styszko, K., Teinemaa, E., Timonen, H., Tremper, A., Vasilescu, J., Via, M., Vodička, P., Wiedensohler, A., Zografou, O., Minguillón, M. C., and Prévôt, A. S. European aerosol phenomenology 8: Harmonised source apportionment of organic aerosol using 22 Year-long ACSM/AMS datasets. *Environment International* 166 (2022), p. 107325. DOI: 10.1016/J.ENVINT.2022.107325.

[31] Hallquist, M., Wenger, J. C., Baltensperger, U., Rudich, Y., Simpson, D., Claeys, M., Dommen, J., Donahue, N. M., George, C., Goldstein, A. H., Hamilton, J. F., Herrmann, H., Hoffmann, T., Iinuma, Y., Jang, M., Jenkin, M. E., Jimenez, J. L., Kiendler-Scharr, A., Maenhaut, W., Mcfiggans, G., Mentel, T. F., Monod, A., Prévôt, A. S. H., Seinfeld, J. H., Surratt, J. D., Szmigielski, R., and Wildt, J. The formation, properties and impact of secondary organic aerosol: current and emerging issues. *Atmos. Chem. Phys* 9 (2009), pp. 5155–5236. DOI: 10.5194/acp-9-5155-2009.

[32] Tsigaridis, K., Daskalakis, N., Kanakidou, M., Adams, P. J., Artaxo, P., Bahadur, R., Balkanski, Y., Bauer, S. E., Bellouin, N., Benedetti, A., Bergman, T., Berntsen, T. K., Beukes, J. P., Bian, H., Carslaw, K. S., Chin, M., Curci, G., Diehl, T., Easter, R. C., Ghan, S. J., Gong, S. L., Hodzic, A., Hoyle, C. R., Iversen, T., Jathar, S., Jimenez, J. L., Kaiser, J. W., Kirkevåg, A., Koch, D., Kokkola, H., Lee, Y. H., Lin, G., Liu, X., Luo, G., Ma, X.,

Mann, G. W., Mihalopoulos, N., Morcrette, J.-J., Müller, J.-F., Myhre, G., Myriokefalitakis, S., Ng, N. L., O'Donnell, D., Penner, J. E., Pozzoli, L., Pringle, K. J., Russell, L. M., Schulz, M., Sciare, J., Seland, Ø., Shindell, D. T., Sillman, S., Skeie, R. B., Spracklen, D., Stavrakou, T., Steenrod, S. D., Takemura, T., Tiitta, P., Tilmes, S., Tost, H., Noije, T. van, Zyl, P. G. van, Salzen, K. von, Yu, F., Wang, Z., Wang, Z., Zaveri, R. A., Zhang, H., Zhang, K., Zhang, Q., and Zhang, X. The AeroCom evaluation and intercomparison of organic aerosol in global models. *Atmospheric Chemistry and Physics* 14 (19 2014), pp. 10845–10895. DOI: 10.5194/acp-14-10845-2014.

[33] Goldstein, A. H. and Galbally, I. E. Known and unexplored organic constituents in the earth's atmosphere. *Environmental Science and Technology* 41 (5 2007), pp. 1514–1521. DOI: 10.1021/ES072476P.

[34] Hodzic, A., Kasibhatla, P. S., Jo, D. S., Cappa, C. D., Jimenez, J. L., Madronich, S., and Park, R. J. Rethinking the global secondary organic aerosol (SOA) budget: stronger production, faster removal, shorter lifetime. *Atmospheric Chemistry and Physics* 16 (12 2016), pp. 7917–7941. DOI: 10.5194/acp-16-7917-2016.

[35] Heald, C. L., Ridley, D. A., Kreidenweis, S. M., and Drury, E. E. Satellite observations cap the atmospheric organic aerosol budget. *Geophysical Research Letters* 37 (24 2010). DOI: 10.1029/2010GL045095.

[36] Lin, G., Penner, J. E., and Zhou, C. How will SOA change in the future? *Geophysical Research Letters* 43 (4 2016), pp. 1718–1726. DOI: 10.1002/2015GL067137.

[37] Kelly, J. M., Doherty, R. M., O'Connor, F. M., and Mann, G. W. The impact of biogenic, anthropogenic, and biomass burning volatile organic compound emissions on regional and seasonal variations in secondary organic aerosol. *Atmospheric Chemistry and Physics* 18 (10 2018), pp. 7393–7422. DOI: 10.5194/ACP-18-7393-2018.

[38] Kroll, J. H. and Seinfeld, J. H. Chemistry of secondary organic aerosol: Formation and evolution of low-volatility organics in the atmosphere. *Atmospheric Environment* 42 (16 2008), pp. 3593–3624. DOI: 10.1016/J.ATMOSENV.2008.01.003.

[39] Heard, D. E. and Pilling, M. J. Measurement of OH and HO2 in the Troposphere. *Chemical Reviews* 103 (12 2003), pp. 5163–5198. DOI: 10.1021/CR020522S.

[40] Monks, P. S. Gas-phase radical chemistry in the troposphere. *Chemical Society Reviews* 34 (5 2005), pp. 376–395. DOI: 10.1039/B307982C.

[41] Brown, S. S. and Stutz, J. Nighttime radical observations and chemistry. *Chemical Society Reviews* 41 (19 2012), pp. 6405–6447. DOI: 10.1039/C2CS35181A.

[42] Seinfeld, J. H. Urban Air Pollution: State of the Science. *Science* 243 (4892 1989), pp. 745–752. DOI: 10.1126/science.243.4892.745.

[43] Ren, X., Brune, W. H., Mao, J., Mitchell, M. J., Lesher, R. L., Simpas, J. B., Metcalf, A. R., Schwab, J. J., Cai, C., Li, Y., Demerjian, K. L., Felton, H. D., Boynton, G., Adams, A., Perry, J., He, Y., Zhou, X., and Hou, J. Behavior of OH and HO2 in the winter atmosphere in New York City. *Atmospheric Environment* 40 (SUPPL. 2 2006), pp. 252–263. DOI: 10.1016/J.ATMOSENV.2005.11.073.

[44] Heard, D. E., Carpenter, L. J., Creasey, D. J., Hopkins, J. R., Lee, J. D., Lewis, A. C., Pilling, M. J., Seakins, P. W., Carslaw, N., and Emmerson, K. M. High levels of the hydroxyl radical in the winter urban troposphere. *Geophysical Research Letters* 31 (18 2004), p. 18112. DOI: 10.1029/2004GL020544.

[45] Zheng, J., Shi, X., Ma, Y., Ren, X., Jabbour, H., Diao, Y., Wang, W., Ge, Y., Zhang, Y., and Zhu, W. Contribution of nitrous acid to the atmospheric oxidation capacity in an industrial zone in the Yangtze River Delta region of China. *Atmospheric Chemistry and Physics* 20 (9 2020), pp. 5457–5475. DOI: 10.5194/acp-20-5457-2020.

[46] Lee, J. D., Whalley, L. K., Heard, D. E., Stone, D., Dunmore, R. E., Hamilton, J. F., Young, D. E., Allan, J. D., Laufs, S., and Kleffmann, J. Detailed budget analysis of HONO in central London reveals a missing daytime source. *Atmospheric Chemistry and Physics* 16 (5 2016), pp. 2747–2764. DOI: 10.5194/acp-16-2747-2016.

[47] Brown, S. S., Dubé, W. P., Fuchs, H., Ryerson, T. B., Wollny, A. G., Brock, C. A., Bahreini, R., Middlebrook, A. M., Neuman, T. A., Atlas, E., Roberts, J. M., Osthoff, H. D., Trainer, M., Fehsenfeld, F. C., and Ravishankara, A. R. Reactive uptake coefficients for N2O5 determined from aircraft measurements during the Second Texas Air Quality Study: Comparison to current model parameterizations. *Journal of Geophysical Research: Atmospheres* 114 (D7 2009). DOI: 10.1029/2008JD011679.

[48] Galib, M. and Limmer, D. T. Reactive uptake of N2O5 by atmospheric aerosol is dominated by interfacial processes. *Science* 371 (6532 2021), pp. 921–925. DOI: 10.1126/SCIENCE.ABD7716.

[49] Newland, M. J., Mouchel-Vallon, C., Valorso, R., Aumont, B., Vereecken, L., Jenkin, M. E., and Rickard, A. R. Estimation of mechanistic parameters in the gas-phase reactions of ozone with alkenes for use in automated mechanism construction. *Atmospheric Chemistry and Physics* 22 (9 2022), pp. 6167–6195. DOI: 10.5194/acp-22-6167-2022.

[50] Atkinson, R. and Arey, J. Atmospheric Degradation of Volatile Organic Compounds. *Chemical Reviews* 103 (12 2003), pp. 4605–4638. DOI: 10.1021/CR0206420.

[51] Jokinen, T., Berndt, T., Makkonen, R., Kerminen, V. M., Junninen, H., Paasonen, P., Stratmann, F., Herrmann, H., Guenther, A. B., Worsnop, D. R., Kulmala, M., Ehn, M., and Sipilä, M. Production of extremely low volatile organic compounds from biogenic emissions: Measured yields and atmospheric implications. *Proceedings of the National Academy of Sciences of the United States of America* 112 (23 2015), pp. 7123–7128. DOI: 10.1073/PNAS.1423977112.

[52] Ehn, M., Thornton, J. A., Kleist, E., Sipilä, M., Junninen, H., Pullinen, I., Springer, M., Rubach, F., Tillmann, R., Lee, B., Lopez-Hilfiker, F., Andres, S., Acir, I. H., Rissanen, M., Jokinen, T., Schobesberger, S., Kangasluoma, J., Kontkanen, J., Nieminen, T., Kurtén, T., Nielsen, L. B., Jørgensen, S., Kjaergaard, H. G., Canagaratna, M., Maso, M. D., Berndt, T., Petäjä, T., Wahner, A., Kerminen, V. M., Kulmala, M., Worsnop, D. R., Wildt, J., and Mentel, T. F. A large source of low-volatility secondary organic aerosol. *Nature 2014 506:7489* 506 (7489 2014), pp. 476–479. DOI: 10.1038/nature13032.

[53] Jenkin, M. E., Valorso, R., Aumont, B., and Rickard, A. R. Estimation of rate coefficients and branching ratios for reactions of organic peroxy radicals for use in automated mechanism construction. *Atmospheric Chemistry and Physics* 19 (11 2019), pp. 7691–7717. DOI: 10.5194/acp-19-7691-2019.

[54] Singh, H. B. and Field, M. Reactive nitrogen in the troposphere. *Environmental Science and Technology* 21 (4 1987), pp. 320–327. DOI: 10.1021/ES00158A001.

[55] Newland, M. J., Bryant, D. J., Dunmore, R. E., Bannan, T. J., Acton, W. J. F., Langford, B., Hopkins, J. R., Squires, F. A., Dixon, W., Drysdale, W. S., Ivatt, P. D., Evans, M. J., Edwards, P. M., Whalley, L. K., Heard, D. E., Slater, E. J., Woodward-Massey, R., Ye, C., Mehra, A., Worrall, S. D., Bacak, A., Coe, H., Percival, C. J., Hewitt, C. N., Lee, J. D., Cui, T., Surratt, J. D., Wang, X., Lewis, A. C., Rickard, A. R., and Hamilton, J. F. Low-NO atmospheric oxidation pathways in a polluted megacity. *Atmospheric Chemistry and Physics* 21 (3 2021), pp. 1613–1625. DOI: 10.5194/acp-21-1613-2021.

[56] Berndt, T., Mentler, B., Scholz, W., Fischer, L., Herrmann, H., Kulmala, M., and Hansel, A. Accretion Product Formation from Ozonolysis and OH Radical Reaction of -Pinene: Mechanistic Insight and the Influence of Isoprene and Ethylene. *Environmental Science and Technology* 52 (19 2018), pp. 11069–11077. DOI: 10.1021/ACS.EST.8B02210.

[57] Berndt, T., Scholz, W., Mentler, B., Fischer, L., Herrmann, H., Kulmala, M., and Hansel, A. Accretion Product Formation from Self- and Cross-Reactions of RO2 Radicals in the Atmosphere. *Angewandte Chemie International Edition* 57 (14 2018), pp. 3820–3824. DOI: 10.1002/ANIE.201710989.

[58] Zhao, D., Pullinen, I., Fuchs, H., Schrade, S., Wu, R., Acir, I.-H., Tillmann, R., Rohrer, F., Wildt, J., Guo, Y., Kiendler-Scharr, A., Wahner, A., Kang, S., Vereecken, L., and Mentel, T. F. Highly oxygenated organic molecule (HOM) formation in the isoprene oxidation by NO_3 radical. *Atmospheric Chemistry and Physics* 21 (12 2021), pp. 9681–9704. DOI: 10.5194/acp-21-9681-2021.

[59] Shi, X., Tang, R., Dong, Z., Liu, H., Xu, F., Zhang, Q., Zong, W., and Cheng, J. A neglected pathway for the accretion products formation in the atmosphere. *Science of The Total Environment* 848 (2022), p. 157494. DOI: 10.1016/J.SCITOTENV.2022.157494.

[60] Fleming, L. T., Lin, P., Roberts, J. M., Selimovic, V., Yokelson, R., Laskin, J., Laskin, A., and Nizkorodov, S. A. Molecular composition and photochemical lifetimes of brown carbon chromophores in biomass burning organic aerosol. *Atmos. Chem. Phys.* 20 (2020), pp. 1105–1129. DOI: 10.5194/acp-20-1105-2020.

[61] Pankow, J. F. An absorption model of the gas/aerosol partitioning involved in the formation of secondary organic aerosol. *Atmospheric Environment* 28 (2 1994), pp. 189–193. DOI: 10.1016/1352-2310(94)90094-9.

[62] Pankow, J. F., Seinfeld, J. H., Asher, W. E., and Erdakos, G. B. Modeling the formation of secondary organic aerosol. 1. Application of theoretical principles to measurements obtained in the -pinene/, -pinene/, sabinene/, 3-carene/, and cyclohexene/ozone systems. *Environmental Science and Technology* 35 (6 2001), pp. 1164–1172. DOI: 10.1021/ES001321D.

[63] Donahue, N. M., Robinson, A. L., Stanier, C. O., and Pandis, S. N. Coupled partitioning, dilution, and chemical aging of semivolatile organics. *Environmental Science and Technology* 40 (8 2006), pp. 2635–2643. DOI: 10.1021/ES052297C.

[64] Kulmala, M., Vehkamäki, H., Petäjä, T., Maso, M. D., Lauri, A., Kerminen, V. M., Birmili, W., and McMurry, P. H. Formation and growth rates of ultrafine atmospheric particles: a review of observations. *Journal of Aerosol Science* 35 (2 2004), pp. 143–176. DOI: 10.1016/J.JAEROSCI.2003.10.003.

[65] Wang, Z. B., Hu, M., Yue, D. L., Zheng, J., Zhang, R. Y., Wiedensohler, A., Wu, Z. J., Nieminen, T., and Boy, M. Evaluation on the role of sulfuric acid in the mechanisms of new particle formation for Beijing case. *Atmospheric Chemistry and Physics* 11 (24 2011), pp. 12663–12671. DOI: 10.5194/ACP-11-12663-2011.

[66] Paasonen, P., Nieminen, T., Asmi, E., Manninen, H. E., Petäjä, T., Plass-Dülmer, C., Flentje, H., Birmili, W., Wiedensohler, A., Hõrrak, U., Metzger, A., Hamed, A., Laaksonen, A., Facchini, M. C., Kerminen, V. M., and Kulmala, M. On the roles of sulphuric acid and low-volatility organic vapours in the initial steps of atmospheric new particle formation. *Atmospheric Chemistry and Physics* 10 (22 2010), pp. 11223–11242. DOI: 10.5194/ACP-10-11223-2010.

[67] Kulmala, M. and Kerminen, V. M. On the formation and growth of atmospheric nanoparticles. *Atmospheric Research* 90 (2-4 2008), pp. 132–150. DOI: 10.1016/J.ATMOSRES.2008.01.005.

[68] Benson, D. R., Yu, J. H., Markovich, A., and Lee, S.-H. Ternary homogeneous nucleation of H_2SO_4, NH_3, and H_2O under conditions relevant to the lower troposphere. *Atmospheric Chemistry and Physics* 11 (10 2011), pp. 4755–4766. DOI: 10.5194/acp-11-4755-2011.

[69] Zhang, R., Suh, I., Zhao, J., Zhang, D., Fortner, E. C., Tie, X., Molina, L. T., and Molina, M. J. Atmospheric new particle formation enhanced by organic acids. *Science* 304 (5676 2004), pp. 1487–1490. DOI: 10.1126/SCIENCE.1095139.

[70] Kirkby, J., Amorim, A., Baltensperger, U., Carslaw, K. S., Christoudias, T., Curtius, J., Donahue, N. M., Haddad, I. E., Flagan, R. C., Gordon, H., Hansel, A., Harder, H., Junninen, H., Kulmala, M., Kürten, A., Laaksonen, A., Lehtipalo, K., Lelieveld, J., Möhler, O., Riipinen, I., Stratmann, F., Tomé, A., Virtanen, A., Volkamer, R., Winkler, P. M., and Worsnop, D. R. Atmospheric new particle formation from the CERN CLOUD experiment. *Nature Geoscience 2023 16:11* 16 (11 2023), pp. 948–957. DOI: 10.1038/s41561-023-01305-0.

[71] Jiang, B. and Xia, D. Role identification of NH3 in atmospheric secondary new particle formation in haze occurrence of China. *Atmospheric Environment* 163 (2017), pp. 107–117. DOI: 10.1016/J.ATMOSENV.2017.05.035.

[72] Nair, A. A., Yu, F., and Luo, G. The importance of ammonia for springtime atmospheric new particle formation and aerosol number abundance over the United States. *Science*

of The Total Environment 863 (2023), p. 160756. DOI: 10.1016/J.SCITOTENV.2022.160756.

[73] Cai, J., Sulo, J., Gu, Y., Holm, S., Cai, R., Thomas, S., Neuberger, A., Mattsson, F., Paglione, M., Decesari, S., Rinaldi, M., Yin, R., Aliaga, D., Huang, W., Li, Y., Gramlich, Y., Ciarelli, G., Quéléver, L., Sarnela, N., Lehtipalo, K., Zannoni, N., Wu, C., Nie, W., Kangasluoma, J., Mohr, C., Kulmala, M., Zha, Q., Stolzenburg, D., and Bianchi, F. Elucidating the mechanisms of atmospheric new particle formation in the highly polluted Po Valley, Italy. *Atmospheric Chemistry and Physics* 24 (4 2024), pp. 2423–2441. DOI: 10.5194/acp-24-2423-2024.

[74] Kirkby, J., Duplissy, J., Sengupta, K., Frege, C., Gordon, H., Williamson, C., Heinritzi, M., Simon, M., Yan, C., Almeida, J., Trostl, J., Nieminen, T., Ortega, I. K., Wagner, R., Adamov, A., Amorim, A., Bernhammer, A. K., Bianchi, F., Breitenlechner, M., Brilke, S., Chen, X., Craven, J., Dias, A., Ehrhart, S., Flagan, R. C., Franchin, A., Fuchs, C., Guida, R., Hakala, J., Hoyle, C. R., Jokinen, T., Junninen, H., Kangasluoma, J., Kim, J., Krapf, M., Kurten, A., Laaksonen, A., Lehtipalo, K., Makhmutov, V., Mathot, S., Molteni, U., Onnela, A., Perakyla, O., Piel, F., Petaja, T., Praplan, A. P., Pringle, K., Rap, A., Richards, N. A., Riipinen, I., Rissanen, M. P., Rondo, L., Sarnela, N., Schobesberger, S., Scott, C. E., Seinfeld, J. H., Sipila, M., Steiner, G., Stozhkov, Y., Stratmann, F., Tomé, A., Virtanen, A., Vogel, A. L., Wagner, A. C., Wagner, P. E., Weingartner, E., Wimmer, D., Winkler, P. M., Ye, P., Zhang, X., Hansel, A., Dommen, J., Donahue, N. M., Worsnop, D. R., Baltensperger, U., Kulmala, M., Carslaw, K. S., and Curtius, J. Ion-induced nucleation of pure biogenic particles. *Nature 2016 533:7604* 533 (7604 2016), pp. 521–526. DOI: 10.1038/nature17953.

[75] Bianchi, F., Kurtén, T., Riva, M., Mohr, C., Rissanen, M. P., Roldin, P., Berndt, T., Crounse, J. D., Wennberg, P. O., Mentel, T. F., Wildt, J., Junninen, H., Jokinen, T., Kulmala, M., Worsnop, D. R., Thornton, J. A., Donahue, N., Kjaergaard, H. G., and Ehn, M. Highly Oxygenated Organic Molecules (HOM) from Gas-Phase Autoxidation Involving Peroxy Radicals: A Key Contributor to Atmospheric Aerosol. *Chemical Reviews* 119 (6 2019), pp. 3472–3509. DOI: 10.1021/ACS.CHEMREV.8B00395.

[76] Junninen, H., Ahonen, L., Bianchi, F., Quéléver, L., Schallhart, S., Dada, L., Manninen, H. E., Leino, K., Lampilahti, J., Mazon, S. B., Rantala, P., Räty, M., Kontkanen, J., Negri, S., Aliaga, D., Garmash, O., Alekseychik, P., Lipp, H., Tamme, K., Levula, J., Sipilä, M., Ehn, M., Worsnop, D., Zilitinkevich, S., Mammarella, I., Rinne, J., Vesala, T., Petäjä, T., Kerminen, V. M., and Kulmala, M. Terpene emissions from boreal wetlands can initiate

stronger atmospheric new particle formation than boreal forests. *Communications Earth Environment 2022 3:1* 3 (1 2022), pp. 1–9. DOI: 10.1038/s43247-022-00406-9.

[77] Huang, W., Junninen, H., Garmash, O., Lehtipalo, K., Stolzenburg, D., Lampilahti, J. L., Ezhova, E., Schallhart, S., Rantala, P., Aliaga, D., Ahonen, L., Sulo, J., Quéléver, L. L., Cai, R., Alekseychik, P., Mazon, S. B., Yao, L., Blichner, S. M., Zha, Q., Mammarella, I., Kirkby, J., Kerminen, V. M., Worsnop, D. R., Kulmala, M., and Bianchi, F. Potential pre-industrial–like new particle formation induced by pure biogenic organic vapors in Finnish peatland. *Science Advances* 10 (14 2024). DOI: 10.1126/SCIADV.ADM9191.

[78] Andreae, M. O., Andreae, T. W., Ditas, F., and Pöhlker, C. Frequent new particle formation at remote sites in the subboreal forest of North America. *Atmospheric Chemistry and Physics* 22 (4 2022), pp. 2487–2505. DOI: 10.5194/acp-22-2487-2022.

[79] Molteni, U., Bianchi, F., Klein, F., Haddad, I. E., Frege, C., Rossi, M. J., Dommen, J., and Baltensperger, U. Formation of highly oxygenated organic molecules from aromatic compounds. *Atmospheric Chemistry and Physics* 18 (3 2018), pp. 1909–1921. DOI: 10.5194/acp-18-1909-2018.

[80] Crounse, J. D., Nielsen, L. B., Jørgensen, S., Kjaergaard, H. G., and Wennberg, P. O. Autoxidation of organic compounds in the atmosphere. *Journal of Physical Chemistry Letters* 4 (20 2013), pp. 3513–3520. DOI: 10.1021/JZ4019207.

[81] Zhang, Y., Chen, Y., Lambe, A. T., Olson, N. E., Lei, Z., Craig, R. L., Zhang, Z., Gold, A., Onasch, T. B., Jayne, J. T., Worsnop, D. R., Gaston, C. J., Thornton, J. A., Vizuete, W., Ault, A. P., and Surratt, J. D. Effect of the Aerosol-Phase State on Secondary Organic Aerosol Formation from the Reactive Uptake of Isoprene-Derived Epoxydiols (IEPOX). *Environmental Science and Technology Letters* 5 (3 2018), pp. 167–174. DOI: 10.1021/ACS.ESTLETT.8B00044.

[82] Mettke, P., Brüggemann, M., Mutzel, A., Gräfe, R., and Herrmann, H. Secondary Organic Aerosol (SOA) through Uptake of Isoprene Hydroxy Hydroperoxides (ISOPOOH) and its Oxidation Products. *ACS Earth and Space Chemistry* 7 (5 2023), pp. 1025–1037. DOI: 10.1021/ACSEARTHSPACECHEM.2C00385.

[83] Fu, T. M., Jacob, D. J., and Heald, C. L. Aqueous-phase reactive uptake of dicarbonyls as a source of organic aerosol over eastern North America. *Atmospheric Environment* 43 (10 2009), pp. 1814–1822. DOI: 10.1016/J.ATMOSENV.2008.12.029.

[84] Zhang, Q., Jimenez, J. L., Canagaratna, M. R., Allan, J. D., Coe, H., Ulbrich, I., Alfarra, M. R., Takami, A., Middlebrook, A. M., Sun, Y. L., Dzepina, K., Dunlea, E., Docherty, K., DeCarlo, P. F., Salcedo, D., Onasch, T., Jayne, J. T., Miyoshi, T., Shimono, A., Hatakeyama, S., Takegawa, N., Kondo, Y., Schneider, J., Drewnick, F., Borrmann, S., Weimer, S., Demerjian, K., Williams, P., Bower, K., Bahreini, R., Cottrell, L., Griffin, R. J., Rautiainen, J., Sun, J. Y., Zhang, Y. M., and Worsnop, D. R. Ubiquity and dominance of oxygenated species in organic aerosols in anthropogenically-influenced Northern Hemisphere midlatitudes. *Geophysical Research Letters* 34 (13 2007). DOI: 10.1029/2007GL029979.

[85] Zhang, Q., Worsnop, D. R., Canagaratna, M. R., and Jimenez, J. L. Hydrocarbon-like and oxygenated organic aerosols in Pittsburgh: insights into sources and processes of organic aerosols. *Atmospheric Chemistry and Physics* 5.12 (2005), pp. 3289–3311. DOI: 10.5194/acp-5-3289-2005.

[86] Guenther, A. B., Jiang, X., Heald, C. L., Sakulyanontvittaya, T., Duhl, T., Emmons, L. K., and Wang, X. The Model of Emissions of Gases and Aerosols from Nature version 2.1 (MEGAN2.1): an extended and updated framework for modeling biogenic emissions. *Geoscientific Model Development* 5 (6 2012), pp. 1471–1492. DOI: 10.5194/gmd-5-1471-2012.

[87] Zhang, H., Yee, L. D., Lee, B. H., Curtis, M. P., Worton, D. R., Isaacman-VanWertz, G., Offenberg, J. H., Lewandowski, M., Kleindienst, T. E., Beaver, M. R., Holder, A. L., Lonneman, W. A., Docherty, K. S., Jaoui, M., Pye, H. O., Hu, W., Day, D. A., Campuzano-Jost, P., Jimenez, J. L., Guo, H., Weber, R. J., Gouw, J. D., Koss, A. R., Edgerton, E. S., Brune, W., Mohr, C., Lopez-Hilfiker, F. D., Lutz, A., Kreisberg, N. M., Spielman, S. R., Hering, S. V., Wilson, K. R., Thornton, J. A., and Goldstein, A. H. Monoterpenes are the largest source of summertime organic aerosol in the southeastern United States. *Proceedings of the National Academy of Sciences of the United States of America* 115 (9 2018), pp. 2038–2043. DOI: 10.1073/PNAS.1717513115.

[88] Bryant, D. J., Dixon, W. J., Hopkins, J. R., Dunmore, R. E., Pereira, K. L., Shaw, M., Squires, F. A., Bannan, T. J., Mehra, A., Worrall, S. D., Bacak, A., Coe, H., Percival, C. J., Whalley, L. K., Heard, D. E., Slater, E. J., Ouyang, B., Cui, T., Surratt, J. D., Liu, D., Shi, Z., Harrison, R., Sun, Y., Xu, W., Lewis, A. C., Lee, J. D., Rickard, A. R., and Hamilton, J. F. Strong anthropogenic control of secondary organic aerosol formation from isoprene in Beijing. *Atmos. Chem. Phys.* 20 (2020), pp. 7531–7552. DOI: 10.5194/acp-20-7531-2020.

[89] Hamilton, J. F., Bryant, D. J., Edwards, P. M., Ouyang, B., Bannan, T. J., Mehra, A., Mayhew, A. W., Hopkins, J. R., Dunmore, R. E., Squires, F. A., Lee, J. D., Newland, M. J., Worrall, S. D., Bacak, A., Coe, H., Whalley, L. K., Heard, D. E., Slater, E. J., Jones, R. L., Cui, T., Surratt, J. D., Reeves, C. E., Mills, G. P., Grimmond, S., Sun, Y., Xu, W., Shi, Z., and Rickard, A. R. Key Role of NO3 Radicals in the Production of Isoprene Nitrates and Nitrooxyorganosulfates in Beijing. *Environmental Science and Technology* 55 (2 2021), pp. 842–853. DOI: 10.1021/ACS.EST.0C05689.

[90] Brüggemann, M., Xu, R., Tilgner, A., Kwong, K. C., Mutzel, A., Poon, H. Y., Otto, T., Schaefer, T., Poulain, L., Chan, M. N., and Herrmann, H. Organosulfates in Ambient Aerosol: State of Knowledge and Future Research Directions on Formation, Abundance, Fate, and Importance. *Environmental Science and Technology* 54 (7 2020), pp. 3767–3782. DOI: 10.1021/ACS.EST.9B06751.

[91] Koss, A. R., Sekimoto, K., Gilman, J. B., Selimovic, V., Coggon, M. M., Zarzana, K. J., Yuan, B., Lerner, B. M., Brown, S. S., Jimenez, J. L., Krechmer, J., Roberts, J. M., Warneke, C., Yokelson, R. J., and Gouw, J. de. Non-methane organic gas emissions from biomass burning: identification, quantification, and emission factors from PTR-ToF during the FIREX 2016 laboratory experiment. *Atmos. Chem. Phys.* 18 (5 2018), pp. 3299–3319. DOI: 10.5194/acp-18-3299-2018.

[92] Stockwell, C. E., Veres, P. R., Williams, J., and Yokelson, R. J. Characterization of biomass burning emissions from cooking fires, peat, crop residue, and other fuels with high-resolution proton-transfer-reaction time-of-flight mass spectrometry. *Atmospheric Chemistry and Physics* 15 (2 2015), pp. 845–865. DOI: 10.5194/acp-15-845-2015.

[93] Coggon, M. M., Lim, C. Y., Koss, A. R., Sekimoto, K., Yuan, B., Gilman, J. B., Hagan, D. H., Selimovic, V., Zarzana, K. J., Brown, S. S., Roberts, J. M., Müller, M., Yokelson, R., Wisthaler, A., Krechmer, J. E., Jimenez, J. L., Cappa, C., Kroll, J. H., Gouw, J. D., and Warneke, C. OH chemistry of non-methane organic gases (NMOGs) emitted from laboratory and ambient biomass burning smoke: Evaluating the influence of furans and oxygenated aromatics on ozone and secondary NMOG formation. *Atmospheric Chemistry and Physics* 19 (23 2019), pp. 14875–14899. DOI: 10.5194/acp-19-14875-2019.

[94] Lauraguais, A., Coeur-Tourneur, C., Cassez, A., Deboudt, K., Fourmentin, M., and Choël, M. Atmospheric reactivity of hydroxyl radicals with guaiacol (2-methoxyphenol), a biomass burning emitted compound: Secondary organic aerosol formation and gas-

phase oxidation products. *Atmospheric Environment* 86 (2014), pp. 155–163. DOI: 10.1016/J.ATMOSENV.2013.11.074.

[95] Meng, L., Coeur, C., Fayad, L., Houzel, N., Genevray, P., Bouzidi, H., Tomas, A., and Chen, W. Secondary organic aerosol formation from the gas-phase reaction of guaiacol (2-methoxyphenol) with NO3 radicals. *Atmospheric Environment* 240 (2020). DOI: 10.1016/j.atmosenv.2020.117740.

[96] Fang, Z., Lai, A., Cai, D., Li, C., Carmieli, R., Chen, J., Wang, X., and Rudich, Y. Secondary Organic Aerosol Generated from Biomass Burning Emitted Phenolic Compounds: Oxidative Potential, Reactive Oxygen Species, and Cytotoxicity. *Environmental Science Technology* 58.19 (2024), pp. 8194–8206. DOI: 10.1021/acs.est.3c09903.

[97] Joo, T., Rivera-Rios, J. C., Takeuchi, M., Alvarado, M. J., and Ng, N. L. Secondary Organic Aerosol Formation from Reaction of 3-Methylfuran with Nitrate Radicals. *ACS Earth and Space Chemistry* 3 (6 2019), pp. 922–934. DOI: 10.1021/acsearthspacechem.9b00068.

[98] Jiang, X., Tsona, N. T., Jia, L., Liu, S., Zhang, H., Xu, Y., and Du, L. Secondary organic aerosol formation from photooxidation of furan: Effects of NOx and humidity. *Atmospheric Chemistry and Physics* 19 (21 2019), pp. 13591–13609. DOI: 10.5194/acp-19-13591-2019.

[99] Fredrickson, C. D., Palm, B. B., Lee, B. H., Zhang, X., Orlando, J. J., Tyndall, G. S., Garofalo, L. A., Pothier, M. A., Farmer, D. K., Decker, Z. C., Robinson, M. A., Brown, S. S., Murphy, S. M., Shen, Y., Sullivan, A. P., Schobesberger, S., and Thornton, J. A. Formation and Evolution of Catechol-Derived SOA Mass, Composition, Volatility, and Light Absorption. *ACS Earth and Space Chemistry* 6 (4 2022), pp. 1067–1079. DOI: 10.1021/ACSEARTHSPACECHEM.2C00007.

[100] Srivastava, D., Vu, T. V., Tong, S., Shi, Z., and Harrison, R. M. Formation of secondary organic aerosols from anthropogenic precursors in laboratory studies. *npj Climate and Atmospheric Science 2022 5:1* 5 (1 2022), pp. 1–30. DOI: 10.1038/s41612-022-00238-6.

[101] Hui, L., Liu, X., Tan, Q., Feng, M., An, J., Qu, Y., Zhang, Y., and Cheng, N. VOC characteristics, sources and contributions to SOA formation during haze events in Wuhan, Central China. *Science of The Total Environment* 650 (2019), pp. 2624–2639. DOI: 10.1016/J.SCITOTENV.2018.10.029.

[102] Gentner, D. R., Isaacman, G., Worton, D. R., Chan, A. W., Dallmann, T. R., Davis, L., Liu, S., Day, D. A., Russell, L. M., Wilson, K. R., Weber, R., Guha, A., Harley, R. A., and Goldstein, A. H. Elucidating secondary organic aerosol from diesel and gasoline vehicles through detailed characterization of organic carbon emissions. *Proceedings of the National Academy of Sciences of the United States of America* 109 (45 2012), pp. 18318–18323. DOI: 10.1073/PNAS.1212272109.

[103] Morino, Y., Li, Y., Fujitani, Y., Sato, K., Inomata, S., Tanabe, K., Jathar, S. H., Kondo, Y., Nakayama, T., Fushimi, A., Takami, A., and Kobayashi, S. Secondary organic aerosol formation from gasoline and diesel vehicle exhaust under light and dark conditions. *Environmental Science: Atmospheres* 2 (1 2022), pp. 46–64. DOI: 10.1039/D1EA00045D.

[104] Andreae, M. O. Emission of trace gases and aerosols from biomass burning – an updated assessment. *Atmos. Chem. Phys.* 19 (13 2019), pp. 8523–8546. DOI: 10.5194/acp-19-8523-2019.

[105] Lan, R., Eastham, S. D., Liu, T., Norford, L. K., and Barrett, S. R. Air quality impacts of crop residue burning in India and mitigation alternatives. *Nature Communications 2022 13:1* 13 (1 2022), pp. 1–13. DOI: 10.1038/s41467-022-34093-z.

[106] Leppälahti, J. and Koljonen, T. Nitrogen evolution from coal, peat and wood during gasification: Literature review. *Fuel Processing Technology* 43 (1 1995), pp. 1–45. DOI: 10.1016/0378-3820(94)00123-B.

[107] Akherati, A., He, Y., Coggon, M. M., Koss, A. R., Hodshire, A. L., Sekimoto, K., Warneke, C., Gouw, J. D., Yee, L., Seinfeld, J. H., Onasch, T. B., Herndon, S. C., Knighton, W. B., Cappa, C. D., Kleeman, M. J., Lim, C. Y., Kroll, J. H., Pierce, J. R., and Jathar, S. H. Oxygenated Aromatic Compounds are Important Precursors of Secondary Organic Aerosol in Biomass-Burning Emissions. *Environ. Sci. Technol.* 54 (14 2020), pp. 8568–8579. DOI: 10.1021/acs.est.0c01345.

[108] Burling, I. R., Yokelson, R. J., Griffith, D. W. T., Johnson, T. J., Veres, P., Roberts, J. M., Warneke, C., Urbanski, S. P., Reardon, J., Weise, D. R., Hao, W. M., and Gouw, J. de. Laboratory measurements of trace gas emissions from biomass burning of fuel types from the southeastern and southwestern United States. *Atmospheric Chemistry and Physics* 10 (22 2010), pp. 11115–11130. DOI: 10.5194/acp-10-11115-2010.

[109] Zhu, B., Huang, X. F., Xia, S. Y., Lin, L. L., Cheng, Y., and He, L. Y. Biomass-burning emissions could significantly enhance the atmospheric oxidizing capacity in continen-

tal air pollution. *Environmental Pollution* 285 (2021), p. 117523. DOI: 10.1016/J.ENVPOL.2021.117523.

[110] Bourgeois, I., Peischl, J., Neuman, J. A., Brown, S. S., Thompson, C. R., Aikin, K. C., Allen, H. M., Angot, H., Apel, E. C., Baublitz, C. B., Brewer, J. F., Campuzano-Jost, P., Commane, R., Crounse, J. D., Daube, B. C., DiGangi, J. P., Diskin, G. S., Emmons, L. K., Fiore, A. M., Gkatzelis, G. I., Hills, A., Hornbrook, R. S., Huey, L. G., Jimenez, J. L., Kim, M., Lacey, F., McKain, K., Murray, L. T., Nault, B. A., Parrish, D. D., Ray, E., Sweeney, C., Tanner, D., Wofsy, S. C., and Ryerson, T. B. Large contribution of biomass burning emissions to ozone throughout the global remote troposphere. *Proceedings of the National Academy of Sciences of the United States of America* 118 (52 2021), e2109628118. DOI: 10.1073/PNAS.2109628118.

[111] Xu, L., Crounse, J. D., Vasquez, K. T., Allen, H., Wennberg, P. O., Bourgeois, I., Brown, S. S., Campuzano-Jost, P., Coggon, M. M., Crawford, J. H., DiGangi, J. P., Diskin, G. S., Fried, A., Gargulinski, E. M., Gilman, J. B., Gkatzelis, G. I., Guo, H., Hair, J. W., Hall, S. R., Halliday, H. A., Hanisco, T. F., Hannun, R. A., Holmes, C. D., Huey, L. G., Jimenez, J. L., Lamplugh, A., Lee, Y. R., Liao, J., Lindaas, J., Neuman, J. A., Nowak, J. B., Peischl, J., Peterson, D. A., Piel, F., Richter, D., Rickly, P. S., Robinson, M. A., Rollins, A. W., Ryerson, T. B., Sekimoto, K., Selimovic, V., Shingler, T., Soja, A. J., Clair, J. M., Tanner, D. J., Ullmann, K., Veres, P. R., Walega, J., Warneke, C., Washenfelder, R. A., Weibring, P., Wisthaler, A., Wolfe, G. M., Womack, C. C., and Yokelson, R. J. Ozone chemistry in western U.S. wildfire plumes. *Science Advances* 7 (50 2021), p. 3648. DOI: 10.1126/SCIADV.ABL3648.

[112] Liao, J., Wolfe, G. M., Hannun, R. A., Clair, J. M. S., Hanisco, T. F., Gilman, J. B., Lamplugh, A., Selimovic, V., Diskin, G. S., Nowak, J. B., Halliday, H. S., DiGangi, J. P., Hall, S. R., Ullmann, K., Holmes, C. D., Fite, C. H., Agastra, A., Ryerson, T. B., Peischl, J., Bourgeois, I., Warneke, C., Coggon, M. M., Gkatzelis, G. I., Sekimoto, K., Fried, A., Richter, D., Weibring, P., Apel, E. C., Hornbrook, R. S., Brown, S. S., Womack, C. C., Robinson, M. A., Washenfelder, R. A., Veres, P. R., and Neuman, J. A. Formaldehyde evolution in US wildfire plumes during the Fire Influence on Regional to Global Environments and Air Quality experiment (FIREX-AQ). *Atmospheric Chemistry and Physics* 21 (24 2021), pp. 18319–18331. DOI: 10.5194/acp-21-18319-2021.

[113] Decker, Z. C. J., Robinson, M. A., Barsanti, K. C., Bourgeois, I., Coggon, M. M., DiGangi, J. P., Diskin, G. S., Flocke, F. M., Franchin, A., Fredrickson, C. D., Gkatzelis, G. I., Hall, S. R., Halliday, H., Holmes, C. D., Huey, L. G., Lee, Y. R., Lindaas, J., Middlebrook, A. M.,

Montzka, D. D., Moore, R., Neuman, J. A., Nowak, J. B., Palm, B. B., Peischl, J., Piel, F., Rickly, P. S., Rollins, A. W., Ryerson, T. B., Schwantes, R. H., Sekimoto, K., Thornhill, L., Thornton, J. A., Tyndall, G. S., Ullmann, K., Rooy, P. V., Veres, P. R., Warneke, C., Washenfelder, R. A., Weinheimer, A. J., Wiggins, E., Winstead, E., Wisthaler, A., Womack, C., and Brown, S. S. Nighttime and daytime dark oxidation chemistry in wildfire plumes: an observation and model analysis of FIREX-AQ aircraft data. *Atmospheric Chemistry and Physics* 21 (21 2021), pp. 16293–16317. DOI: 10.5194/acp-21-16293-2021.

[114] Decker, Z. C., Zarzana, K. J., Coggon, M., Min, K. E., Pollack, I., Ryerson, T. B., Peischl, J., Edwards, P., Dubé, W. P., Markovic, M. Z., Roberts, J. M., Veres, P. R., Graus, M., Warneke, C., Gouw, J. D., Hatch, L. E., Barsanti, K. C., and Brown, S. S. Nighttime Chemical Transformation in Biomass Burning Plumes: A Box Model Analysis Initialized with Aircraft Observations. *Environmental Science and Technology* 53 (5 2019), pp. 2529–2538. DOI: 10.1021/ACS.EST.8B05359.

[115] Tsimpidi, A. P., Karydis, V. A., Pandis, S. N., and Lelieveld, J. Global combustion sources of organic aerosols: model comparison with 84 AMS factor-analysis data sets. *Atmospheric Chemistry and Physics* 16 (14 2016), pp. 8939–8962. DOI: 10.5194/acp-16-8939-2016.

[116] Kourtchev, I., Godoi, R. H. M., Connors, S., Levine, J. G., Archibald, A. T., Godoi, A. F. L., Paralovo, S. L., Barbosa, C. G. G., Souza, R. A. F., Manzi, A. O., Seco, R., Sjostedt, S., Park, J.-H., Guenther, A., Kim, S., Smith, J., Martin, S. T., and Kalberer, M. Molecular composition of organic aerosols in central Amazonia: an ultra-high-resolution mass spectrometry study. *Atmos. Chem. Phys.* 16 (18 2016), pp. 11899–11913. DOI: 10.5194/acp-16-11899-2016.

[117] Iinuma, Y., Böge, O., and Herrmann, H. Methyl-nitrocatechols: Atmospheric tracer compounds for biomass burning secondary organic aerosols. *Environ. Sci. Technol.* 44 (2010), pp. 8453–8459. DOI: 10.1021/es102938a.

[118] Piot, C., Jaffrezo, J.-L., Cozic, J., Pissot, N., Haddad, I. E., Marchand, N., and Besombes, J.-L. Quantification of levoglucosan and its isomers by High Performance Liquid Chromatography – Electrospray Ionization tandem Mass Spectrometry and its applications to atmospheric and soil samples. *Atmos. Meas. Tech.* (1 2012), pp. 141–148. DOI: 10.5194/amt-5-141-2012.

[119] Kitanovski, Z., Grgić, I., Yasmeen, F., Claeys, M., and Čusak, A. Development of a liquid chromatographic method based on ultraviolet–visible and electrospray ionization mass spectrometric detection for the identification of nitrocatechols and related tracers in biomass burning atmospheric organic aerosol. *Rapid Commun. Mass Spectrom.* 26 (7 2012), pp. 793–804. DOI: 10.1002/RCM.6170.

[120] Connolly, R., Marlier, M. E., Garcia-Gonzales, D. A., Wilkins, J., Su, J., Bekker, C., Jung, J., Bonilla, E., Burnett, R. T., Zhu, Y., and Jerrett, M. Mortality attributable to PM2.5 from wildland fires in California from 2008 to 2018. *Science Advances* 10 (23 2024), p. 1252. DOI: 10.1126/SCIADV.ADL1252.

[121] International Energy Agency. *World Energy Outlook 2022*. 2022. URL: https://www.iea.org/reports/world-energy-outlook-2022.

[122] Srivastava, D., Saksakulkrai, S., Acton, W. J. F., Rooney, D. J., Hall, J., Hou, S., Wolstencroft, M., Bartington, S., Harrison, R. M., Shi, Z., and Bloss, W. J. Comparative receptor modelling for the sources of fine particulate matter (PM2.5) at urban sites in the UK. *Atmospheric Environment* 343 (2025), p. 120963. DOI: 10.1016/J.ATMOSENV.2024.120963.

[123] International Energy Agency. *Tracking SDG 7: The Energy Progress Report 2024*. International Renewable Energy Agency, International Energy Agency, the United Nations Statistics Division (UNSD), World Bank and the World Health Organization, 2024. URL: https://www.irena.org/Publications/2024/Jun/Tracking-SDG-7-The-Energy-Progress-Report-2024.

[124] World Health Organisation (WHO). *Household air pollution*. 2022. URL: https://www.who.int/news-room/fact-sheets/detail/household-air-pollution-and-health.

[125] Andreae, M. O. and Merlet, P. Emission of trace gases and aerosols from biomass burning. *Glob. Biogeochem. Cycles* 15 (4 2001), pp. 955–966. DOI: 10.1029/2000GB001382.

[126] Gilman, J. B., Lerner, B. M., Kuster, W. C., Goldan, P. D., Warneke, C., Veres, P. R., Roberts, J. M., Gouw, J. A. de, Burling, I. R., and Yokelson, R. J. Biomass burning emissions and potential air quality impacts of volatile organic compounds and other trace gases from fuels common in the US. *Atmos. Chem. Phys.* 15 (24 2015), pp. 13915–13938. DOI: 10.5194/acp-15-13915-2015.

[127] Sekimoto, K., Koss, A. R., Gilman, J. B., Selimovic, V., Coggon, M. M., Zarzana, K. J., Yuan, B., Lerner, B. M., Brown, S. S., Warneke, C., Yokelson, R. J., Roberts, J. M., and Gouw, J. de. High- and low-temperature pyrolysis profiles describe volatile organic

compound emissions from western US wildfire fuels. *Atmos. Chem. Phys.* 18 (13 2018), pp. 9263–9281. DOI: 10.5194/acp-18-9263-2018.

[128] Shen, G., Xue, M., Wei, S., Chen, Y., Zhao, Q., Li, B., Wu, H., and Tao, S. Influence of fuel moisture, charge size, feeding rate and air ventilation conditions on the emissions of PM, OC, EC, parent PAHs, and their derivatives from residential wood combustion. *Journal of Environmental Sciences* 25 (9 2013), pp. 1808–1816. DOI: 10.1016/S1001-0742(12)60258-7.

[129] Weimer, S., Alfarra, M. R., Schreiber, D., Mohr, M., Prévôt, A. S., and Baltensperger, U. Organic aerosol mass spectral signatures from wood-burning emissions: Influence of burning conditions and wood type. *J. Geophys. Res.* 113 (D10 2008), p. 10304. DOI: 10.1029/2007JD009309.

[130] Pavagadhi, S., Betha, R., Venkatesan, S., Balasubramanian, R., and Hande, M. P. Physicochemical and toxicological characteristics of urban aerosols during a recent Indonesian biomass burning episode. *Environ. Sci. Pollut. Res.* 20 (4 2013), pp. 2569–2578. DOI: 10.1007/S11356-012-1157-9.

[131] Verma, P. K., Sah, D., Dubey, J., Kumari, K. M., and Lakhani, A. Mutagenic and Cancer Risk Estimation of Particulate Bound Polycyclic Aromatic Hydrocarbons from the Emission of Different Biomass Fuels. *Chemical Research in Toxicology* 34 (3 2021), pp. 743–753. DOI: 10.1021/ACS.CHEMRESTOX.0C00378.

[132] Akagi, S. K., Yokelson, R. J., Wiedinmyer, C., Alvarado, M. J., Reid, J. S., Karl, T., Crounse, J. D., and Wennberg, P. O. Emission factors for open and domestic biomass burning for use in atmospheric models. *Atmospheric Chemistry and Physics* 11 (9 2011), pp. 4039–4072. DOI: 10.5194/acp-11-4039-2011.

[133] Zhang, X., Lin, Y. H., Surratt, J. D., and Weber, R. J. Sources, composition and absorption Ångström exponent of light-absorbing organic components in aerosol extracts from the los angeles basin. *Environ. Sci. Technol.* 47 (8 2013), pp. 3685–3693. DOI: 10.1021/ES305047B.

[134] Hatch, L. E., Yokelson, R. J., Stockwell, C. E., Veres, P. R., Simpson, I. J., Blake, D. R., Orlando, J. J., and Barsanti, K. C. Multi-instrument comparison and compilation of non-methane organic gas emissions from biomass burning and implications for smoke-derived secondary organic aerosol precursors. *Atmospheric Chemistry and Physics* 17 (2 2017), pp. 1471–1489. DOI: 10.5194/acp-17-1471-2017.

[135] Stefenelli, G., Jiang, J., Bertrand, A., Bruns, E. A., Pieber, S. M., Baltensperger, U., Marchand, N., Aksoyoglu, S., Prévôt, A. S. H., Slowik, J. G., and Haddad, I. E. Secondary organic aerosol formation from smoldering and flaming combustion of biomass: a box model parametrization based on volatility basis set. *Atmos. Chem. Phys.* 19 (17 2019), pp. 11461–11484. DOI: 10.5194/acp-19-11461-2019.

[136] Nozière, B., Kalberer, M., Claeys, M., Allan, J., Decesari, S., Finessi, E., Glasius, M., Grgic, I., Hamilton, J. F., Hoffmann, T., Iinuma, Y., Jaoui, M., Kahnt, A., Kampf, C. J., Kourtchev, I., Maenhaut, W., Marsden, N., Saarikoski, S., Schnelle-Kreis, J., Surratt, J. D., Szidat, S., Szmigielski, R., and Wisthaler, A. The Molecular Identification of Organic Compounds in the Atmosphere: State of the Art and Challenges. *Chem. Rev.* 110 (2015), pp. 3919–3983. DOI: 10.1021/cr5003485.

[137] Leppla, D., Zannoni, N., Kremper, L., Williams, J., Pöhlker, C., Sá, M., Solci, M. C., and Hoffmann, T. Varying chiral ratio of pinic acid enantiomers above the Amazon rainforest. *Atmospheric Chemistry and Physics* 23 (2 2023), pp. 809–820. DOI: 10.5194/acp-23-809-2023.

[138] Hamilton, J. F., Webb, P. J., Lewis, A. C., Hopkins, J. R., Smith, S., and Davy, P. Partially oxidised organic components in urban aerosol using GCXGC-TOF/MS. *Atmospheric Chemistry and Physics* 4 (5 2004), pp. 1279–1290. DOI: 10.5194/acp-4-1279-2004.

[139] Wang, K., Zhang, Y., Huang, R. J., Cao, J., and Hoffmann, T. UHPLC-Orbitrap mass spectrometric characterization of organic aerosol from a central European city (Mainz, Germany) and a Chinese megacity (Beijing). *Atmospheric Environment* 189 (2018), pp. 22–29. DOI: 10.1016/J.ATMOSENV.2018.06.036.

[140] Lewis, A. C., Carslaw, N., Marriott, P. J., Kinghorn, R. M., Morrison, P., Lee, A. L., Bartie, K. D., and Pilling, M. J. A larger pool of ozone-forming carbon compounds in urban atmospheres. *Nature 2000 405:6788* 405 (6788 2000), pp. 778–781. DOI: 10.1038/35015540.

[141] Stewart, G. J., Acton, W. J. F., Nelson, B. S., Vaughan, A. R., Hopkins, J. R., Arya, R., Mondal, A., Jangirh, R., Ahlawat, S., Yadav, L., Sharma, S. K., Dunmore, R. E., Yunus, S. S., Hewitt, C. N., Nemitz, E., Mullinger, N., Gadi, R., Sahu, L. K., Tripathi, N., Rickard, A. R., Lee, J. D., Mandal, T. K., and Hamilton, J. F. Emissions of non-methane volatile organic compounds from combustion of domestic fuels in Delhi, India. *Atmos. Chem. Phys.* 21 (4 2021), pp. 2383–2406. DOI: 10.5194/acp-21-2383-2021.

[142] Budisulistiorini, S. H., Riva, M., Williams, M., Chen, J., Itoh, M., Surratt, J. D., and Kuwata, M. Light-Absorbing Brown Carbon Aerosol Constituents from Combustion of Indonesian Peat and Biomass. *Environ. Sci. Technol.* 51 (8 2017), pp. 4415–4423. DOI: 10.1021/acs.est.7b00397.

[143] Daellenbach, K. R., Kourtchev, I., Vogel, A. L., Bruns, E. A., Jiang, J., Petäjä, T., Jaffrezo, J.-L., Aksoyoglu, S., Kalberer, M., Baltensperger, U., Haddad, I. E., and Prévôt, A. S. H. Impact of anthropogenic and biogenic sources on the seasonal variation in the molecular composition of urban organic aerosols: a field and laboratory study using ultra-high-resolution mass spectrometry. *Atmos. Chem. Phys.* 19 (9 2019), pp. 5973–5991. DOI: 10.5194/acp-19-5973-2019.

[144] Bryant, D. J., Nelson, B. S., Swift, S. J., Budisulistiorini, S. H., Drysdale, W. S., Vaughan, A. R., Newland, M. J., Hopkins, J. R., Cash, J. M., Langford, B., Nemitz, E., Acton, W. J. F., Hewitt, C. N., Mandal, T., Gurjar, B. R., Gadi, R., Lee, J. D., Rickard, A. R., and Hamilton, J. F. Biogenic and anthropogenic sources of isoprene and monoterpenes and their secondary organic aerosol in Delhi, India. *Atmos. Chem. Phys.* 23 (2023), pp. 61–83. DOI: 10.5194/acp-23-61-2023.

[145] Surratt, J. D., Kroll, J. H., Kleindienst, T. E., Edney, E. O., Claeys, M., Sorooshian, A., Ng, N. L., Offenberg, J. H., Lewandowski, M., Jaoui, M., Flagan, R. C., and Seinfeld, J. H. Evidence for organosulfates in secondary organic aerosol. *Environmental Science and Technology* 41 (2 2007), pp. 517–527. DOI: 10.1021/ES062081Q.

[146] Wang, Z., Ge, Y., Bi, S., Liang, Y., and Shi, Q. Molecular characterization of organic aerosol in winter from Beijing using UHPLC-Orbitrap MS. *Sci. Tot. Environ.* 812 (2022), p. 151507. DOI: 10.1016/j.scitotenv.2021.151507.

[147] Zubarev, R. A. and Makarov, A. Orbitrap mass spectrometry. *Analytical Chemistry* 85 (11 2013), pp. 5288–5296. DOI: 10.1021/AC4001223.

[148] Oss, M., Kruve, A., Herodes, K., and Leito, I. Electrospray Ionization Efficiency Scale of Organic Compounds. *Anal. Chem.* 82 (2010), pp. 2865–2872. DOI: 10.1021/ac902856t.

[149] Liigand, P., Liigand, J., Kaupmees, K., and Kruve, A. 30 Years of research on ESI/MS response: Trends, contradictions and applications. *Anal. Chim. Acta.* 1152 (2021), p. 238117. DOI: 10.1016/J.ACA.2020.11.049.

[150] Kenseth, C. M., Hafeman, N. J., Huang, Y., Dalleska, N. F., Stoltz, B. M., and Seinfeld, J. H. Synthesis of Carboxylic Acid and Dimer Ester Surrogates to Constrain the Abundance and Distribution of Molecular Products in -Pinene and -Pinene Secondary Organic Aerosol. *Cite This: Environ. Sci. Technol* 54 (2020), pp. 12829–12839. DOI: 10.1021/acs.est.0c01566.

[151] Matuszewski, B. K., Constanzer, M. L., and Chavez-Eng, C. M. Strategies for the Assessment of Matrix Effect in Quantitative Bioanalytical Methods Based on HPLC-MS/MS. *Anal.Chem.* 75 (13 2003), pp. 3019–3030. DOI: 10.1021/ac020361s.

[152] Trufelli, H., Palma, P., Famiglini, G., and Cappiello, A. An overview of matrix effects in liquid chromatography–mass spectrometry. *Mass Spec. Rev.* 30 (3 2011), pp. 491–509. DOI: 10.1002/MAS.20298.

[153] Chambers, E., Wagrowski-Diehl, D. M., Lu, Z., and Mazzeo, J. R. Systematic and comprehensive strategy for reducing matrix effects in LC/MS/MS analyses. *Journal of Chromatography B* 852 (1-2 2007), pp. 22–34. DOI: 10.1016/J.JCHROMB.2006.12.030.

[154] Jimenez, J. L., Jayne, J. T., Shi, Q., Kolb, C. E., Worsnop, D. R., Yourshaw, I., Seinfeld, J. H., Flagan, R. C., Zhang, X., Smith, K. A., Morris, J. W., and Davidovits, P. Ambient aerosol sampling using the Aerodyne Aerosol Mass Spectrometer. *Journal of Geophysical Research: Atmospheres* 108 (D7 2003). DOI: 10.1029/2001JD001213.

[155] Ng, N. L., Canagaratna, M. R., Zhang, Q., Jimenez, J. L., Tian, J., Ulbrich, I. M., Kroll, J. H., Docherty, K. S., Chhabra, P. S., Bahreini, R., Murphy, S. M., Seinfeld, J. H., Hildebrandt, L., Donahue, N. M., DeCarlo, P. F., Lanz, V. A., Prévôt, A. S. H., Dinar, E., Rudich, Y., and Worsnop, D. R. Organic aerosol components observed in Northern Hemispheric datasets from Aerosol Mass Spectrometry. *Atmospheric Chemistry and Physics* 10 (10 2010), pp. 4625–4641. DOI: 10.5194/acp-10-4625-2010.

[156] Cubison, M. J., Ortega, A. M., Hayes, P. L., Farmer, D. K., Day, D., Lechner, M. J., Brune, W. H., Apel, E., Diskin, G. S., Fisher, J. A., Fuelberg, H. E., Hecobian, A., Knapp, D. J., Mikoviny, T., Riemer, D., Sachse, G. W., Sessions, W., Weber, R. J., Weinheimer, A. J., Wisthaler, A., and Jimenez, J. L. Effects of aging on organic aerosol from open biomass burning smoke in aircraft and laboratory studies. *Atmos. Chem. Phys* 11 (2011), pp. 12049–12064. DOI: 10.5194/acp-11-12049-2011.

[157] Ulbrich, I. M., Canagaratna, M. R., Zhang, Q., Worsnop, D. R., and Jimenez, J. L. Interpretation of organic components from Positive Matrix Factorization of aerosol mass

spectrometric data. *Atmospheric Chemistry and Physics* 9 (9 2009), pp. 2891–2918. DOI: 10.5194/acp-9-2891-2009.

[158] Lopez-Hilfiker, F. D., Mohr, C., Ehn, M., Rubach, F., Kleist, E., Wildt, J., Mentel, T. F., Lutz, A., Hallquist, M., Worsnop, D., and Thornton, J. A. A novel method for online analysis of gas and particle composition: description and evaluation of a Filter Inlet for Gases and AEROsols (FIGAERO). *Atmospheric Measurement Techniques* 7 (4 2014), pp. 983–1001. DOI: 10.5194/amt-7-983-2014.

[159] Eichler, P., Müller, M., D'Anna, B., and Wisthaler, A. A novel inlet system for online chemical analysis of semi-volatile submicron particulate matter. *Atmospheric Measurement Techniques* 8 (3 2015), pp. 1353–1360. DOI: 10.5194/amt-8-1353-2015.

[160] Barreira, L. M. F., Ylisirniö, A., Pullinen, I., Buchholz, A., Li, Z., Lipp, H., Junninen, H., Hõrrak, U., Noe, S. M., Krasnova, A., Krasnov, D., Kask, K., Talts, E., Niinemets, Ü., Ruiz-Jimenez, J., and Schobesberger, S. The importance of sesquiterpene oxidation products for secondary organic aerosol formation in a springtime hemiboreal forest. *Atmospheric Chemistry and Physics* 21 (15 2021), pp. 11781–11800. DOI: 10.5194/acp-21-11781-2021.

[161] Ye, C., Yuan, B., Lin, Y., Wang, Z., Hu, W., Li, T., Chen, W., Wu, C., Wang, C., Huang, S., Qi, J., Wang, B., Wang, C., Song, W., Wang, X., Zheng, E., Krechmer, J. E., Ye, P., Zhang, Z., Wang, X., Worsnop, D. R., and Shao, M. Chemical characterization of oxygenated organic compounds in the gas phase and particle phase using iodide CIMS with FIGAERO in urban air. *Atmospheric Chemistry and Physics* 21 (11 2021), pp. 8455–8478. DOI: 10.5194/acp-21-8455-2021.

[162] Müller, M., Eichler, P., D'Anna, B., Tan, W., and Wisthaler, A. Direct Sampling and Analysis of Atmospheric Particulate Organic Matter by Proton-Transfer-Reaction Mass Spectrometry. *Analytical Chemistry* 89 (20 2017), pp. 10889–10897. DOI: 10.1021/ACS.ANALCHEM.7B02582.

[163] Lopez-Hilfiker, F. D., Pospisilova, V., Huang, W., Kalberer, M., Mohr, C., Stefenelli, G., Thornton, J. A., Baltensperger, U., Prevot, A. S. H., and Slowik, J. G. An extractive electrospray ionization time-of-flight mass spectrometer (EESI-TOF) for online measurement of atmospheric aerosol particles. *Atmospheric Measurement Techniques* 12 (9 2019), pp. 4867–4886. DOI: 10.5194/amt-12-4867-2019.

[164] Lee, C. P., Riva, M., Wang, D., Tomaz, S., Li, D., Perrier, S., Slowik, J. G., Bourgain, F., Schmale, J., Prevot, A. S., Baltensperger, U., George, C., and Haddad, I. E. Online Aerosol Chemical Characterization by Extractive Electrospray Ionization-Ultrahigh-Resolution Mass Spectrometry (EESI-Orbitrap). *Environmental Science and Technology* 54 (7 2020), pp. 3871–3880. DOI: 10.1021/acs.est.9b07090.

[165] Reinecke, T., Leiminger, M., Jordan, A., Wisthaler, A., and Müller, M. Ultrahigh Sensitivity PTR-MS Instrument with a Well-Defined Ion Chemistry. *Analytical Chemistry* 95 (32 2023), pp. 11879–11884. DOI: 10.1021/ACS.ANALCHEM.3C02669.

[166] Lee, B. H., Lopez-Hilfiker, F. D., Mohr, C., Kurtén, T., Worsnop, D. R., and Thornton, J. A. An iodide-adduct high-resolution time-of-flight chemical-ionization mass spectrometer: Application to atmospheric inorganic and organic compounds. *Environmental Science and Technology* 48 (11 2014), pp. 6309–6317. DOI: 10.1021/ES500362A.

[167] Iyer, S., Lopez-Hilfiker, F., Lee, B. H., Thornton, J. A., and Kurtén, T. Modeling the Detection of Organic and Inorganic Compounds Using Iodide-Based Chemical Ionization. *Journal of Physical Chemistry A* 120 (4 2016), pp. 576–587. DOI: 10.1021/ACS.JPCA.5B09837.

[168] Bi, C., Krechmer, J. E., Frazier, G. O., Xu, W., Lambe, A. T., Claflin, M. S., Lerner, B. M., Jayne, J. T., Worsnop, D. R., Canagaratna, M. R., and Isaacman-VanWertz, G. Quantification of isomer-resolved iodide chemical ionization mass spectrometry sensitivity and uncertainty using a voltage-scanning approach. *Atmospheric Measurement Techniques* 14 (10 2021), pp. 6835–6850. DOI: 10.5194/amt-14-6835-2021.

[169] Pereira, K. L., Ward, M. W., Wilkinson, J. L., Sallach, J. B., Bryant, D. J., Dixon, W. J., Hamilton, J. F., and Lewis, A. C. An Automated Methodology for Non-targeted Compositional Analysis of Small Molecules in High Complexity Environmental Matrices Using Coupled Ultra Performance Liquid Chromatography Orbitrap Mass Spectrometry. *Environ. Sci. Technol.* 55 (2021), pp. 7365–7375. DOI: 10.1021/acs.est.0c08208.

[170] Ma, J., Ungeheuer, F., Zheng, F., Du, W., Wang, Y., Cai, J., Zhou, Y., Yan, C., Liu, Y., Kulmala, M., Daellenbach, K. R., and Vogel, A. L. Nontarget Screening Exhibits a Seasonal Cycle of PM2.5Organic Aerosol Composition in Beijing. *Environ. Sci. Technol.* 56 (2022), pp. 7017–7028. DOI: 10.1021/ACS.EST.1C06905.

[171] Wan, Y., Xing, C., Wang, X., Yang, Z., Huang, X., Ge, X., Du, L., Wang, Q., and Yu, H. Nontarget Tandem High-Resolution Mass Spectrometry Analysis of Functionalized

Organic Compounds in Atmospherically Relevant Samples. *Environ. Sci. Technol. Lett.* 9 (2022), pp. 1022–1029. DOI: 10.1021/ACS.ESTLETT.2C00788.

[172] Wang, X., Hayeck, N., Brüggemann, M., Abis, L., Riva, M., Lu, Y., Wang, B., Chen, J., George, C., and Wang, L. Chemical Characteristics and Brown Carbon Chromophores of Atmospheric Organic Aerosols Over the Yangtze River Channel: A Cruise Campaign. *J. Geophys. Res.: Atmos.* 125 (2020), e2020JD032497. DOI: 10.1029/2020JD032497.

[173] Wang, Z., Zhang, J., Zhang, L., Liang, Y., and Shi, Q. Characterization of nitroaromatic compounds in atmospheric particulate matter from Beijing. *Atmos. Environ.* 246 (2021), p. 118046. DOI: 10.1016/J.ATMOSENV.2020.118046.

[174] Brüggemann, M., Pinxteren, D. V., Wang, Y., Yu, J. Z., and Herrmann, H. Quantification of known and unknown terpenoid organosulfates in PM10 using untargeted LC–HRMS/MS: contrasting summertime rural Germany and the North China Plain. *Environmental Chemistry* 16 (5 2019), pp. 333–346. DOI: 10.1071/EN19089.

[175] Song, K., Guo, S., Gong, Y., Lv, D., Wan, Z., Zhang, Y., Fu, Z., Hu, K., and Lu, S. Non-target scanning of organics from cooking emissions using comprehensive two-dimensional gas chromatography-mass spectrometer (GC×GC-MS). *Applied Geochemistry* 151 (2023), p. 105601. DOI: 10.1016/J.APGEOCHEM.2023.105601.

[176] Kim, S., Kramer, R. W., and Hatcher, P. G. Graphical Method for Analysis of Ultrahigh-Resolution Broadband Mass Spectra of Natural Organic Matter, the Van Krevelen Diagram. *Analytical Chemistry* 75 (20 2003), pp. 5336–5344. DOI: 10.1021/AC034415P.

[177] Nguyen, T. B., Bateman, A. P., Bones, D. L., Nizkorodov, S. A., Laskin, J., and Laskin, A. High-resolution mass spectrometry analysis of secondary organic aerosol generated by ozonolysis of isoprene. *Atmospheric Environment* 44 (8 2010), pp. 1032–1042. DOI: 10.1016/J.ATMOSENV.2009.12.019.

[178] Dzepina, K., Mazzoleni, C., Fialho, P., China, S., Zhang, B., Owen, R. C., Helmig, D., Hueber, J., Kumar, S., Perlinger, J. A., Kramer, L. J., Dziobak, M. P., Ampadu, M. T., Olsen, S., Wuebbles, D. J., and Mazzoleni, L. R. Molecular characterization of free tropospheric aerosol collected at the Pico Mountain Observatory: A case study with a long-range transported biomass burning plume. *Atmos. Chem. Phys.* 15 (2015), pp. 5047–5068. DOI: 10.5194/acp-15-5047-2015.

[179] Brege, M., Paglione, M., Gilardoni, S., Decesari, S., Facchini, M. C., and Mazzoleni, L. R. Molecular insights on aging and aqueous-phase processing from ambient biomass burning emissions-influenced Po Valley fog and aerosol. *Atmos. Chem. Phys.* 18 (2018), pp. 13197–13214. DOI: 10.5194/acp-18-13197-2018.

[180] Brege, M. A., China, S., Schum, S., Zelenyuk, A., and Mazzoleni, L. R. Extreme Molecular Complexity Resulting in a Continuum of Carbonaceous Species in Biomass Burning Tar Balls from Wildfire Smoke. *ACS Earth Space Chem.* 5 (2021), pp. 2729–2739. DOI: 10.1021/ACSEARTHSPACECHEM.1C00141.

[181] Liigand, J., Wang, T., Kellogg, J., Smedsgaard, J., Cech, N., and Kruve, A. Quantification for non-targeted LC/MS screening without standard substances. *Sci. Rep.* 10 (2020), p. 5808. DOI: 10.1038/s41598-020-62573-z.

[182] Mayhew, A. W., Topping, D. O., and Hamilton, J. F. New Approach Combining Molecular Fingerprints and Machine Learning to Estimate Relative Ionization Efficiency in Electrospray Ionization. *ACS Omega* 5 (2020), pp. 9510–9516. DOI: 10.1021/ACSOMEGA.0C00732.

[183] Pieke, E. N., Granby, K., Trier, X., and Smedsgaard, J. A framework to estimate concentrations of potentially unknown substances by semi-quantification in liquid chromatography electrospray ionization mass spectrometry. *Anal. Chim. Acta.* 975 (2017), pp. 30–41. DOI: 10.1016/J.ACA.2017.03.054.

[184] Kruve, A., Kiefer, K., and Hollender, J. Benchmarking of the quantification approaches for the non-targeted screening of micropollutants and their transformation products in groundwater. *Anal. Bioanal. Chem.* 413 (2021), pp. 1549–1559. DOI: 10.1007/S00216-020-03109-2.

[185] Bryant, D. J., Mayhew, A. W., Pereira, K. L., Budisulistiorini, S. H., Prior, C., Unsworth, W., Topping, D. O., Rickard, A. R., and Hamilton, J. F. Overcoming the lack of authentic standards for the quantification of biogenic secondary organic aerosol markers. *Environ. Sci.: Atmos.* 3 (2023), pp. 221–229. DOI: 10.1039/D2EA00074A.

[186] Herrera-Lopez, S., Hernando, M. D., García-Calvo, E., Fernández-Alba, A. R., and Ulaszewska, M. M. Simultaneous screening of targeted and nontargeted contaminants using an LC-QTOF-MS system and automated MS/MS library searching. *J. Mass Spectrom.* 49 (2014), pp. 878–893. DOI: 10.1002/JMS.3428.

[187] Ibáñez, M., Sancho, J. V., Hernández, F., McMillan, D., and Rao, R. Rapid non-target screening of organic pollutants in water by ultraperformance liquid chromatography coupled to time-of-light mass spectrometry. *TrAC, Trends Anal. Chem.* 27 (2008), pp. 481–489. DOI: 10.1016/J.TRAC.2008.03.007.

[188] Fu, Y., Zhao, C., Lu, X., and Xu, G. Nontargeted screening of chemical contaminants and illegal additives in food based on liquid chromatography–high resolution mass spectrometry. *TrAC, Trends Anal. Chem.* 96 (2017), pp. 89–98. DOI: 10.1016/J.TRAC.2017.07.014.

[189] Smith, J. S., Laskin, A., and Laskin, J. Molecular characterization of biomass burning aerosols using high-resolution mass spectrometry. *Anal. Chem.* 81 (2009), pp. 1512–1521. DOI: 10.1021/AC8020664.

[190] Kruve, A. Influence of mobile phase, source parameters and source type on electrospray ionization efficiency in negative ion mode. *J. Mass Spectrom.* 51 (2016), pp. 596–601. DOI: 10.1002/JMS.3790.

[191] Henriksen, T., Juhler, R. K., Svensmark, B., and Cech, N. B. The relative influences of acidity and polarity on responsiveness of small organic molecules to analysis with negative ion electrospray ionization mass spectrometry (ESI-MS). *J. Am. Soc. Mass Spectrom.* 16 (2005), pp. 446–455. DOI: 10.1016/J.JASMS.2004.11.021.

[192] Liigand, J., Kruve, A., Leito, I., Girod, M., and Antoine, R. Effect of mobile phase on electrospray ionization efficiency. *J. Am. Soc. Mass Spectrom.* 25 (11 2014), pp. 1853–1861. DOI: 10.1007/s13361-014-0969-x.

[193] Huffman, B. A., Poltash, M. L., and Hughey, C. A. Effect of polar protic and polar aprotic solvents on negative-ion electrospray ionization and chromatographic separation of small acidic molecules. *Anal. Chem.* 84 (22 2012), pp. 9942–9950. DOI: 10.1021/ac302397b.

[194] Kruve, A., Kaupmees, K., Liigand, J., and Leito, I. Negative Electrospray Ionization via Deprotonation: Predicting the Ionization Efficiency. *Anal. Chem* 86 (2014), p. 4830. DOI: 10.1021/ac404066v.

[195] Liigand, P., Liigand, J., Cuyckens, F., Vreeken, R. J., and Kruve, A. Ionisation efficiencies can be predicted in complicated biological matrices: A proof of concept. *Anal. Chim. Acta.* 1032 (2018), pp. 68–74. DOI: 10.1016/J.ACA.2018.05.072.

[196] Aalizadeh, R., Panara, A., and Thomaidis, N. S. Development and Application of a Novel Semi-quantification Approach in LC-QToF-MS Analysis of Natural Products. *J. Am. Soc. Mass Spectrom.* 32 (2021), pp. 1412–1423. DOI: 10.1021/JASMS.1C00032.

[197] Sepman, H., Malm, L., Peets, P., Macleod, M., Martin, J., Breitholtz, M., and Kruve, A. Bypassing the Identification: MS2Quant for Concentration Estimations of Chemicals Detected with Nontarget LC-HRMS from MS 2 Data. *Anal. Chem* 95 (2023), pp. 12329–12338. DOI: 10.1021/acs.analchem.3c01744.

[198] Yang, Y., Yang, L., Zheng, M., Cao, D., and Liu, G. Data acquisition methods for non-targeted screening in environmental analysis. *TrAC, Trends Anal. Chem.* 160 (2023), p. 116966. DOI: 10.1016/J.TRAC.2023.116966.

[199] Guo, J. and Huan, T. Comparison of Full-Scan, Data-Dependent, and Data-Independent Acquisition Modes in Liquid Chromatography-Mass Spectrometry Based Untargeted Metabolomics. *Anal. Chem.* 92 (2020), pp. 8072–8080. DOI: 10.1021/ACS.ANALCHEM.9B05135.

[200] Bonner, R. and Hopfgartner, G. SWATH data independent acquisition mass spectrometry for metabolomics. *TrAC, Trends Anal. Chem.* 120 (2019), p. 115278. DOI: 10.1016/J.TRAC.2018.10.014.

[201] McCord, J., Newton, S., and Strynar, M. Validation of quantitative measurements and semi-quantitative estimates of emerging perfluoroethercarboxylic acids (PFECAs) and hexfluoroprolyene oxide acids (HFPOAs). *J. Chromatogr. A* 1551 (2018), pp. 52–58. DOI: 10.1016/J.CHROMA.2018.03.047.

[202] Li, W., Cao, M., Ge, P., Fu, X., Tang, J., and Chen, M. Identification and semi-quantification of nitrooxy organosulfates in aerosol particles by HPLC-MS/MS. *Anal. Methods* 14 (2022), pp. 2531–2540. DOI: 10.1039/D2AY00460G.

[203] Wang, Y., Liang, S., Breton, M. L., Wang, Q. Q., Liu, Q., Ho, C. H., Kuang, B. Y., Wu, C., Hallquist, M., Tong, R., and Yu, J. Z. Field observations of C2 and C3 organosulfates and insights into their formation mechanisms at a suburban site in Hong Kong. *Sci. Total Environ.* 904 (2023), p. 166851. DOI: 10.1016/J.SCITOTENV.2023.166851.

[204] Wang, Y., Ma, Y., Kuang, B., Lin, P., Liang, Y., Huang, C., and Yu, J. Z. Abundance of organosulfates derived from biogenic volatile organic compounds: Seasonal and spatial contrasts at four sites in China. *Sci. Total Environ.* 806 (2022), p. 151275. DOI: 10.1016/J.SCITOTENV.2021.151275.

[205] Rattanavaraha, W., Chu, K., Budisulistiorini, S. H., Riva, M., Lin, Y.-H., Edgerton, E. S., Baumann, K., Shaw, S. L., Guo, H., King, L., Weber, R. J., Neff, M. E., Stone, E. A., Offenberg, J. H., Zhang, Z., Gold, A., and Surratt, J. D. Assessing the impact of anthropogenic pollution on isoprene-derived secondary organic aerosol formation in PM 2.5 collected from the Birmingham, Alabama, ground site during the 2013 Southern Oxidant and Aerosol Study. *Atmos. Chem. Phys* 16 (2016), pp. 4897–4914. DOI: 10.5194/acp-16-4897-2016.

[206] Priyadarshani, A., Hettiyadura, S., Al-Naiema, I. M., Hughes, D. D., Fang, T., and Stone, E. A. Organosulfates in Atlanta, Georgia: anthropogenic influences on biogenic secondary organic aerosol formation. *Atmos. Chem. Phys* 19 (2019), pp. 3191–3206. DOI: 10.5194/acp-19-3191-2019.

[207] Chen, Y., Dombek, T., Hand, J., Zhang, Z., Gold, A., Ault, A. P., Levine, K. E., and Surratt, J. D. Seasonal Contribution of Isoprene-Derived Organosulfates to Total Water-Soluble Fine Particulate Organic Sulfur in the United States. *ACS Earth Space Chem.* 5 (2021), pp. 2419–2432. DOI: 10.1021/acsearthspacechem.1c00102.

[208] Martinsson, J., Monteil, G., Sporre, M. K., Maria, A., Hansen, K., Kristensson, A., Stenström, K. E., Swietlicki, E., and Glasius, M. Exploring sources of biogenic secondary organic aerosol compounds using chemical analysis and the FLEXPART model. *Atmos. Chem. Phys* 17 (2017), pp. 11025–11040. DOI: 10.5194/acp-17-11025-2017.

[209] Kanellopoulos, P. G., Kotsaki, S. P., Chrysochou, E., Koukoulakis, K., Zacharopoulos, N., Philippopoulos, A., and Bakeas, E. PM 2.5-bound organosulfates in two Eastern Mediterranean cities: The dominance of isoprene organosulfates. *Chemosphere* 297 (2022), p. 134103. DOI: 10.1016/j.chemosphere.2022.134103.

[210] McCord, J. P., Groff, L. C., and Sobus, J. R. Quantitative non-targeted analysis: Bridging the gap between contaminant discovery and risk characterization. *Environ. Int.* 158 (2022), p. 107011. DOI: 10.1016/J.ENVINT.2021.107011.

[211] Hettiyadura, A. P. S., Jayarathne, T., Baumann, K., Goldstein, A. H., Gouw, J. A. D., Koss, A., Keutsch, F. N., Skog, K., and Stone, E. A. Qualitative and quantitative analysis of atmospheric organosulfates in Centreville, Alabama. *Atmos. Chem. Phys* 17 (2017), pp. 1343–1359. DOI: 10.5194/acp-17-1343-2017.

[212] Cech, N. B., Krone, J. R., and Enke, C. G. Predicting Electrospray Response from Chromatographic Retention Time. *Int. J. Mass Spectrom. Ion Processes* 10 (1999), pp. 208–213. DOI: 10.1021/ac0006019.

[213] Kim, Y., Pike, K. A., Gray, R., Sprankle, J. W., Faust, J. A., and Edmiston, P. L. Non-targeted identification and semi-quantitation of emerging per- and polyfluoroalkyl substances (PFAS) in US rainwater. *Environ. Sci.: Processes Impacts* 25 (2023), pp. 1771–1787. DOI: 10.1039/D2EM00349J.

[214] Shao, Y., Wang, Y., Du, M., Voliotis, A., Alfarra, M. R., O'Meara, S. P., Turner, S. F., and McFiggans, G. Characterisation of the Manchester Aerosol Chamber facility. *Atmos. Meas. Tech.* 15 (2022), pp. 539–559. DOI: 10.5194/amt-15-539-2022.

[215] Yang, X. J., Qu, Y., Yuan, Q., Wan, P., Du, Z., Chen, D., and Wong, C. Effect of ammonium on liquid- and gas-phase protonation and deprotonation in electrospray ionization mass spectrometry. *Analyst* 138 (2 2012), pp. 659–665. DOI: 10.1039/C2AN36022E.

[216] Rauha, J. P., Vuorela, H., and Kostiainen, R. Effect of eluent on the ionization efficiency of flavonoids by ion spray, atmospheric pressure chemical ionization, and atmospheric pressure photoionization mass spectrometry. *J. Mass Spectrom.* 36 (12 2001), pp. 1269–1280. DOI: 10.1002/JMS.231.

[217] Kostiainen, R. and Kauppila, T. J. Effect of eluent on the ionization process in liquid chromatography–mass spectrometry. *J. Chromatogr. A* 1216 (4 2009), pp. 685–699. DOI: 10.1016/J.CHROMA.2008.08.095.

[218] Pluskal, T., Castillo, S., Villar-Briones, A., and Orešič, M. MZmine 2: Modular framework for processing, visualizing, and analyzing mass spectrometry-based molecular profile data. *BMC Bioinformatics* 11 (1 2010), pp. 1–11. DOI: 10.1186/1471-2105-11-395.

[219] Schmid, R., Heuckeroth, S., Korf, A., Smirnov, A., Myers, O., Dyrlund, T. S., Bushuiev, R., Murray, K. J., Hoffmann, N., Lu, M., Sarvepalli, A., Zhang, Z., Fleischauer, M., Dührkop, K., Wesner, M., Hoogstra, S. J., Rudt, E., Mokshyna, O., Brungs, C., Ponomarov, K., Mutabdžija, L., Damiani, T., Pudney, C. J., Earll, M., Helmer, P. O., Fallon, T. R., Schulze, T., Rivas-Ubach, A., Bilbao, A., Richter, H., Nothias, L. F., Wang, M., Orešič, M., Weng, J. K., Böcker, S., Jeibmann, A., Hayen, H., Karst, U., Dorrestein, P. C., Petras, D., Du, X., and Pluskal, T. Integrative analysis of multimodal mass spectrometry data in MZmine 3. *Nature Biotechnology 2023 41:4* 41 (4 2023), pp. 447–449. DOI: 10.1038/s41587-023-01690-2.

[220] Pluskal, T., Uehara, T., and Yanagida, M. Highly accurate chemical formula prediction tool utilizing high-resolution mass spectra, MS/MS fragmentation, heuristic rules, and

isotope pattern matching. *Anal. Chem.* 84 (2012), pp. 4396–4403. DOI: 10.1021/AC3000418.

[221] Schymanski, E. L., Singer, H. P., Slobodnik, J., Ipolyi, I. M., Oswald, P., Krauss, M., Schulze, T., Haglund, P., Letzel, T., Grosse, S., Thomaidis, N. S., Bletsou, A., Zwiener, C., Ibáñez, M., Portolés, T., Boer, R. D., Reid, M. J., Onghena, M., Kunkel, U., Schulz, W., Guillon, A., Noyon, N., Leroy, G., Bados, P., Bogialli, S., Stipaničev, D., Rostkowski, P., and Hollender, J. Non-target screening with high-resolution mass spectrometry: Critical review using a collaborative trial on water analysis. *Anal. Bioanal. Chem.* 407 (2015), pp. 6237–6255. DOI: 10.1007/S00216-015-8681-7.

[222] Schulze, B., Jeon, Y., Kaserzon, S., Heffernan, A. L., Dewapriya, P., O'Brien, J., Ramos, M. J. G., Gorji, S. G., Mueller, J. F., Thomas, K. V., and Samanipour, S. An assessment of quality assurance/quality control efforts in high resolution mass spectrometry non-target workflows for analysis of environmental samples. *TrAC, Trends Anal. Chem.* 133 (2020), p. 116063. DOI: 10.1016/J.TRAC.2020.116063.

[223] Williams, M. L., Olomukoro, A. A., Emmons, R. V., Godage, N. H., and Gionfriddo, E. Matrix effects demystified: Strategies for resolving challenges in analytical separations of complex samples. *J. Sep. Sci.* 46 (23 2023), p. 2300571. DOI: 10.1002/JSSC.202300571.

[224] Pihlström, T., Fernández-Alba, A. R., Amate, C. F., Poulsen, M. E., Lippold, R., Cabrera, L. C., Pelosi, P., Valverde, A., Mol, H., Jezussek, M., Malato, O., and Štěpán, R. Analytical Quality Control and Method Validation Procedures for Pesticide Residues Analysis in Food and Feed SANTE 11312/2021 (2021).

[225] Li, Y., Wang, L., Zheng, M., Lin, Y., Xu, H., Liu, A., Hua, Y., Jiang, Y., Ning, K., and Hu, S. Thin-layer chromatography coupled with HPLC-DAD/UHPLC-HRMS for target and non-target determination of emerging halogenated organic contaminants in animal-derived foods. *Food Chem.* 404 (2023), p. 134678. DOI: 10.1016/J.FOODCHEM.2022.134678.

[226] Rutkowska, E., Łozowicka, B., and Kaczyński, P. Three approaches to minimize matrix effects in residue analysis of multiclass pesticides in dried complex matrices using gas chromatography tandem mass spectrometry. *Food Chem.* 279 (2019), pp. 20–29. DOI: 10.1016/J.FOODCHEM.2018.11.130.

[227] Economou, A., Botitsi, H., Antoniou, S., and Tsipi, D. Determination of multi-class pesticides in wines by solid-phase extraction and liquid chromatography-tandem mass spectrometry. *J. Chromatogr. A* 1216 (31 2009), pp. 5856–5867. DOI: 10.1016/J.CHROMA.2009.06.031.

[228] Amarandei, C., Olariu, R. I., and Arsene, C. Implications of Matrix Effects in Quantitative HPLC/ESI-ToF-MS Analyses of Atmospheric Organic Aerosols. *Proceedings* 55 (1 2020), p. 6. DOI: 10.3390/PROCEEDINGS2020055006.

[229] Parshintsev, J., Hyötyläinen, T., Parshintsev, R. J. Z., and Hyötyläinen, T. Methods for characterization of organic compounds in atmospheric aerosol particles. *Anal. Bioanal. Chem.* 407 (2014), pp. 5877–5897. DOI: 10.1007/S00216-014-8394-3.

[230] Marín, J. M., Gracia-Lor, E., Sancho, J. V., López, F. J., and Hernández, F. Application of ultra-high-pressure liquid chromatography–tandem mass spectrometry to the determination of multi-class pesticides in environmental and wastewater samples: Study of matrix effects. *J.Chromatogr. A* 1216 (9 2009), pp. 1410–1420. DOI: 10.1016/J.CHROMA.2008.12.094.

[231] Evans, R., Bryant, D., Voliotis, A., Hu, D., Wu, H., Syafira, S., Oghama, O., McFiggans, G., Hamilton, J., and Rickard, A. A Semi-Quantitative Approach to Nontarget Compositional Analysis of Complex Samples. *Anal. Chem.* 96 (2024), pp. 18349–18358. DOI: 10.1021/acs.analchem.4c00819.

[232] Abrahamsson, D. P., Park, J. S., Singh, R. R., Sirota, M., and Woodruff, T. J. Applications of Machine Learning to in Silico Quantification of Chemicals without Analytical Standards. *J. Chem. Inf. Model.* 60 (2020), pp. 2718–2727. DOI: 10.1021/ACS.JCIM.9B01096.

[233] Dong, J., Cao, D. S., Miao, H. Y., Liu, S., Deng, B. C., Yun, Y. H., Wang, N. N., Lu, A. P., Zeng, W. B., and Chen, A. F. ChemDes: An integrated web-based platform for molecular descriptor and fingerprint computation. *J. Cheminf.* 7 (2015), pp. 1–10. DOI: 10.1186/S13321-015-0109-Z.

[234] Malm, L., Liigand, J., Aalizadeh, R., Alygizakis, N., Ng, K., Frokjær, E. E., Nanusha, M. Y., Hansen, M., Plassmann, M., Bieber, S., Letzel, T., Balest, L., Abis, P. P., Mazzetti, M., Kasprzyk-Hordern, B., Ceolotto, N., Kumari, S., Hann, S., Kochmann, S., Steininger-Mairinger, T., Soulier, C., Mascolo, G., Murgolo, S., Garcia-Vara, M., Alda, M. L. de, Hollender, J., Arturi, K., Coppola, G., Peruzzo, M., Joerss, H., Neut-Marchand, C. van der, Pieke, E. N., Gago-Ferrero, P., Gil-Solsona, R., Licul-Kucera, V., Roscioli, C., Valsecchi, S., Luckute, A., Christensen, J. H., Tisler, S., Vughs, D., Meekel, N., Andújar, T., Aurich,

D., Schymanski, E. L., Frigerio, G., Macherius, A., Kunkel, U., Bader, T., Rostkowski, P., Gundersen, H., Valdecanas, B., Davis, W. C., Schulze, B., Kaserzon, S., Pijnappels, M., Esperanza, M., Fildier, A., Vulliet, E., Wiest, L., Covaci, A., Schönleben, A. M., Belova, L., Celma, A., Bijlsma, L., Caupos, E., Mebold, E., Roux, J. L., Troia, E., Rijke, E. de, Helmus, R., Leroy, G., Haelewyck, N., Chrastina, D., Verwoert, M., Thomaidis, N. S., and Kruve, A. Quantification Approaches in Non-Target LC/ESI/HRMS Analysis: An Interlaboratory Comparison. *Anal. Chem.* 96 (2024), pp. 16215–16226. DOI: 10.1021/acs.analchem.4c02902.

[235] Li, S., Liu, D., Hu, D., Kong, S., Wu, Y., Ding, S., Cheng, Y., Qiu, H., Zheng, S., Yan, Q., Zheng, H., Hu, K., Zhang, J., Zhao, D., Liu, Q., Sheng, J., Ye, J., He, H., and Ding, D. Evolution of Organic Aerosol From Wood Smoke Influenced by Burning Phase and Solar Radiation. *J. Geophys. Res.* 126 (8 2021). DOI: 10.1029/2021JD034534.

[236] Lin, P., Bluvshtein, N., Rudich, Y., Nizkorodov, S. A., Laskin, J., and Laskin, A. Molecular Chemistry of Atmospheric Brown Carbon Inferred from a Nationwide Biomass Burning Event. *Environ. Sci. Technol.* 51 (20 2017), pp. 11561–11570. DOI: 10.1021/acs.est.7b02276.

[237] Casey, J., Mittal, L., Buchanan, L., Fuller, G., and Mead, I. *London wood burning project: air quality data collection*. Environmental Research Group, Imperial College London, 2023.

[238] Allan, J. D., Williams, P. I., Morgan, W. T., Martin, C. L., Flynn, M. J., Lee, J., Nemitz, E., Phillips, G. J., Gallagher, M. W., and Coe, H. Contributions from transport, solid fuel burning and cooking to primary organic aerosols in two UK cities. *Atmos. Chem. Phys* 10 (2010), pp. 647–668. DOI: 10.5194/acp-10-647-2010.

[239] Andrew Price-Allison Jenny Jones, A. W. *Future Fuels Report*. Department for Environment Food Rural Affairs, 2022. URL: https://uk-air.defra.gov.uk/library/reports?report_id=1134.

[240] Czech, H., Sippula, O., Kortelainen, M., Tissari, J., Radischat, C., Passig, J., Streibel, T., Jokiniemi, J., and Zimmermann, R. On-line analysis of organic emissions from residential wood combustion with single-photon ionisation time-of-flight mass spectrometry (SPI-TOFMS). *Fuel* 177 (2016), pp. 334–342. DOI: 10.1016/J.FUEL.2016.03.036.

[241] Liu, W. J., Li, W. W., Jiang, H., and Yu, H. Q. Fates of Chemical Elements in Biomass during Its Pyrolysis. *Chem. Rev.* 117 (9 2017), pp. 6367–6398. DOI: 10.1021/acs.chemrev.6b00647.

[242] Claeys, M., Vermeylen, R., Yasmeen, F., Gómez-González, Y., Chi, X., Maenhaut, W., Mészáros, T., and Salma, I. Chemical characterisation of humic-like substances from urban, rural and tropical biomass burning environments using liquid chromatography with UV/vis photodiode array detection and electrospray ionisation mass spectrometry. *Environ. Chem.* 9 (3 2012), p. 273. DOI: 10.1071/EN11163.

[243] Iinuma, Y., Brüggemann, E., Gnauk, T., Müller, K., Andreae, M. O., Helas, G., Parmar, R., and Herrmann, H. Source characterization of biomass burning particles: The combustion of selected European conifers, African hardwood, savanna grass, and German and Indonesian peat. *J. Geophys. Res. Atmos.* 112 (8 2007). DOI: 10.1029/2006JD007120.

[244] Capes, G., Johnson, B., McFiggans, G., Williams, P. I., Haywood, J., and Coe, H. Aging of biomass burning aerosols over West Africa: Aircraft measurements of chemical composition, microphysical properties, and emission ratios. *J. Geophys. Res. Atmos.* 113 (23 2008). DOI: 10.1029/2008JD009845.

[245] Wang, Y., Hu, M., Lin, P., Guo, Q., Wu, Z., Li, M., Zeng, L., Song, Y., Zeng, L., Wu, Y., Guo, S., Huang, X., and He, L. Molecular Characterization of Nitrogen-Containing Organic Compounds in Humic-like Substances Emitted from Straw Residue Burning. *Environ. Sci. Technol.* 51 (11 2017), pp. 5951–5961. DOI: 10.1021/acs.est.7b00248.

[246] Smith, D. M., Cui, T., Fiddler, M. N., Pokhrel, R. P., Surratt, J. D., and Bililign, S. Laboratory studies of fresh and aged biomass burning aerosol emitted from east African biomass fuels-Part 2: Chemical properties and characterization. *Atmos. Chem. Phys.* 20 (17 2020), pp. 10169–10191. DOI: 10.5194/acp-20-10169-2020.

[247] Zangrando, R., Barbaro, E., Zennaro, P., Rossi, S., Kehrwald, N. M., Gabrieli, J., Barbante, C., and Gambaro, A. Molecular Markers of Biomass Burning in Arctic Aerosols. *Environ. Sci. Technol.* 47 (2013), pp. 8565–8574. DOI: 10.1021/es400125r.

[248] Li, Z., Wen, Q., and Zhang, R. Sources, health effects and control strategies of indoor fine particulate matter (PM2.5): A review. *Sci. Tot. Environ.* 586 (2017), pp. 610–622. DOI: 10.1016/J.SCITOTENV.2017.02.029.

[249] Simoneit, B. R. T., Rogge, W. F., Mazurek, M. A., Standley, L. J., Hlldemann, L. M., and Cass, G. R. Lignin Pyrolysis Products, Lignans, and Resin Acids as Specific Tracers of Plant Classes in Emissions from Biomass Combustion. *Environ. Sci. Technol.* 27 (1993), pp. 2533–2541. DOI: 10.1021/es00048a034.

[250] Jiang, H., Li, J., Chen, D., Tang, J., Cheng, Z., Mo, Y., Su, T., Tian, C., Jiang, B., Liao, Y., and Zhang, G. Biomass burning organic aerosols significantly influence the light absorption properties of polarity-dependent organic compounds in the Pearl River Delta Region, China. *Environ. Int.* 144 (2020), p. 106079. DOI: 10.1016/J.ENVINT.2020.106079.

[251] Cai, D., Wang, X., George, C., Cheng, T., Herrmann, H., Li, X., and Chen, J. Formation of Secondary Nitroaromatic Compounds in Polluted Urban Environments. *J. Geophys. Res.: Atmos.* 127 (10 2022), e2021JD036167. DOI: 10.1029/2021JD036167.

[252] Zhou, Y., West, C. P., Hettiyadura, A. P., Pu, W., Shi, T., Niu, X., Wen, H., Cui, J., Wang, X., and Laskin, A. Molecular Characterization of Water-Soluble Brown Carbon Chromophores in Snowpack from Northern Xinjiang, China. *Environ. Sci. Technol.* 56 (7 2022), pp. 4173–4186. DOI: 10.1021/acs.est.1C07972.

[253] Lin, P., Aiona, P. K., Li, Y., Shiraiwa, M., Laskin, J., Nizkorodov, S. A., and Laskin, A. Molecular Characterization of Brown Carbon in Biomass Burning Aerosol Particles. *Environ. Sci. Technol.* 50 (21 2016), pp. 11815–11824. DOI: 10.1021/acs.est.6b03024.

[254] Gilardoni, S., Massoli, P., Paglione, M., Giulianelli, L., Carbone, C., Rinaldi, M., Decesari, S., Sandrini, S., Costabile, F., Gobbi, G. P., Pietrogrande, M. C., Visentin, M., Scotto, F., Fuzzi, S., and Facchini, M. C. Direct observation of aqueous secondary organic aerosol from biomass-burning emissions. *Proc. Natl. Acad. Sci. USA* 113 (36 2016), pp. 10013–10018. DOI: 10.1073/PNAS.1602212113.

[255] Simoneit, B. R. Biomass burning — a review of organic tracers for smoke from incomplete combustion. *Appl. Geochem.* 17 (3 2002), pp. 129–162. DOI: 10.1016/S0883-2927(01)00061-0.

[256] Voliotis, A., Wang, Y., Shao, Y., Du, M., Bannan, T. J., Percival, C. J., Pandis, S. N., Alfarra, M. R., and Mcfiggans, G. Exploring the composition and volatility of secondary organic aerosols in mixed anthropogenic and biogenic precursor systems. *Atmos. Chem. Phys* 21 (2021), pp. 14251–14273. DOI: 10.5194/acp-21-14251-2021.

[257] Voliotis, A., Du, M., Wang, Y., Shao, Y., Alfarra, M. R., Bannan, T. J., Hu, D., Pereira, K. L., Hamilton, J. F., Hallquist, M., Mentel, T. F., and Mcfiggans, G. Chamber investigation of the formation and transformation of secondary organic aerosol in mixtures of biogenic and anthropogenic volatile organic compounds. *Atmos. Chem. Phys* 22 (2022), pp. 14147–14175. DOI: 10.5194/acp-22-14147-2022.

[258] Voliotis, A., Du, M., Wang, Y., Shao, Y., Bannan, T. J., Flynn, M., Pandis, S. N., Percival, C. J., Alfarra, M. R., and McFiggans, G. The influence of the addition of isoprene on the volatility of particles formed from the photo-oxidation of anthropogenic–biogenic mixtures. *Atmos.Chem. Phys.* 22 (20 2022), pp. 13677–13693. DOI: 10.5194/acp-22-13677-2022.

[259] Leskinen, J., Tissari, J., Uski, O., Virén, A., Torvela, T., Kaivosoja, T., Lamberg, H., Nuutinen, I., Kettunen, T., Joutsensaari, J., Jalava, P. I., Sippula, O., Hirvonen, M. R., and Jokiniemi, J. Fine particle emissions in three different combustion conditions of a wood chip-fired appliance – Particulate physico-chemical properties and induced cell death. *Atmos. Environ.* 86 (2014), pp. 129–139. DOI: 10.1016/J.ATMOSENV.2013.12.012.

[260] Kalogridis, A. C., Popovicheva, O. B., Engling, G., Diapouli, E., Kawamura, K., Tachibana, E., Ono, K., Kozlov, V. S., and Eleftheriadis, K. Smoke aerosol chemistry and aging of Siberian biomass burning emissions in a large aerosol chamber. *Atmos. Environ.* 185 (2018), pp. 15–28. DOI: 10.1016/j.atmosenv.2018.04.033.

[261] Young, D. E., Allan, J. D., Williams, P. I., Green, D. C., Harrison, R. M., Yin, J., Flynn, M. J., Gallagher, M. W., and Coe, H. Investigating a two-component model of solid fuel organic aerosol in London: processes, PM 1 contributions, and seasonality. *Atmos. Chem. Phys* 15 (2015), pp. 2429–2443. DOI: 10.5194/acp-15-2429-2015.

[262] Lee, T., Sullivan, A. P., MacK, L., Jimenez, J. L., Kreidenweis, S. M., Onasch, T. B., Worsnop, D. R., Malm, W., Wold, C. E., Hao, W. M., and Collett, J. L. Chemical smoke marker emissions during flaming and smoldering phases of laboratory open burning of wildland fuels. *Aerosol Sci. Technol.* 44 (9 2010). DOI: 10.1080/02786826.2010.499884.

[263] Shafizadeh, F. Introduction to pyrolysis of biomass. *J. Anal. Appl. Pyrolysis* 3 (4 1982), pp. 283–305. DOI: 10.1016/0165-2370(82)80017-X.

[264] Jolleys, M. D., Coe, H., Mcfiggans, G., Taylor, J. W., O'shea, S. J., Breton, M. L., Bauguitte, J.-B., Moller, S., Carlo, P. D., Aruffo, E., Palmer, P. I., Lee, J. D., Percival, C. J., and Gallagher, M. W. Properties and evolution of biomass burning organic aerosol from Canadian boreal forest fires. *Atmos. Chem. Phys* 15 (2015), pp. 3077–3095. DOI: 10.5194/acp-15-3077-2015.

[265] Adler, G., Flores, J. M., Riziq, A. A., Borrmann, S., and Rudich, Y. Chemical, physical, and optical evolution of biomass burning aerosols: a case study. *Atmos. Chem. Phys* 11 (2011), pp. 1491–1503. DOI: 10.5194/acp-11-1491-2011.

[266] Budisulistiorini, S. H., Chen, J., Itoh, M., and Kuwata, M. Can Online Aerosol Mass Spectrometry Analysis Classify Secondary Organic Aerosol (SOA) and Oxidized Primary Organic Aerosol (OPOA)? A Case Study of Laboratory and Field Studies of Indonesian Biomass Burning. *ACS Earth and Space Chemistry* 5 (12 2021), pp. 3511–3522. DOI: 10.1021/acsearthspacechem.1c00319.

[267] Roberts, J. M., Stockwell, C. E., Yokelson, R. J., Gouw, J. D., Liu, Y., Selimovic, V., Koss, A. R., Sekimoto, K., Coggon, M. M., Yuan, B., Zarzana, K. J., Brown, S. S., Santin, C., Doerr, S. H., and Warneke, C. The nitrogen budget of laboratory-simulated western US wildfires during the FIREX 2016 Fire Lab study. *Atmos. Chem. Phys* 20 (2020), pp. 8807–8826. DOI: 10.5194/acp-20-8807-2020.

[268] Lobert, J. M. and Warnatz, J. Emissions from the combustion process in vegetation. *Fire in the Environment: The Ecological, Atmospheric, and Climatic Importance of Vegetation Fires*. John Wiley & Sons Ltd, 1993, pp. 15–37.

[269] Jenkins, B. M., Turn, S. Q., Williams, R. B., Chang, D. P. Y., Raabe, O. G., Paskind, J., and Teague, S. Quantitative Assessment of Gaseous and Condensed Phase Emissions from Open Burning of Biomass in a Combustion Wind Tunnel. *Global Biomass Burning: Atmospheric, Climatic, and Biospheric Implications*. MIT Press, 1991, pp. 305–317.

[270] Oppenheimer, C., Tsanev, V. I., Allen, A. G., McGonigle, A. J., Cardoso, A. A., Wiatr, A., Paterlini, W., and Dias, C. D. M. NO2 emissions from agricultural burning in São Paulo, Brazil. *Environ. Sci. Technol.* 38 (17 2004), pp. 4557–4561. DOI: 10.1021/ES0496219.

[271] Delmas, R., Lacaux, J. P., Menaut, J. C., Abbadie, L., Roux, X. L., Helas, G., and Lobert, J. Nitrogen compound emission from biomass burning in tropical African savanna FOS/DECAFE 1991 experiment (Lamto, Ivory Coast). *J. Atmos. Chem.* 22 (1-2 1995), pp. 175–193. DOI: 10.1007/BF00708188.

[272] Koch, B. P. and Dittmar, T. From mass to structure: An aromaticity index for high-resolution mass data of natural organic matter. *Rapid Commun. Mass Spectrom.* 20 (5 2006), pp. 926–932. DOI: 10.1002/rcm.2386.

[273] Bertrand, A., Stefenelli, G., Jen, C. N., Pieber, S. M., Bruns, E. A., Ni, H., Temime-Roussel, B., Slowik, J. G., Goldstein, A. H., Haddad, I. E., Baltensperger, U., Prévôt, A. S., Wortham, H., and Marchand, N. Evolution of the chemical fingerprint of biomass burning organic aerosol during aging. *Atmos. Chem. Phys.* 18 (10 2018), pp. 7607–7624. DOI: 10.5194/acp-18-7607-2018.

[274] Liang, Y., Stamatis, C., Fortner, E. C., Wernis, R. A., Rooy, P. V., Majluf, F., Yacovitch, T. I., Daube, C., Herndon, S. C., Kreisberg, N. M., Barsanti, K. C., and Goldstein, A. H. Emissions of organic compounds from western US wildfires and their near-fire transformations. *Atmos. Chem. Phys* 22 (2022), pp. 9877–9893. DOI: 10.5194/acp-22-9877-2022.

[275] Wang, X., Hayeck, N., Brüggemann, M., Yao, L., Chen, H., Zhang, C., Emmelin, C., Chen, J., George, C., and Wang, L. Chemical Characteristics of Organic Aerosols in Shanghai: A Study by Ultrahigh-Performance Liquid Chromatography Coupled With Orbitrap Mass Spectrometry. *J. Geophys. Res.: Atmos.* 122 (21 2017), pp. 11, 703–11, 722. DOI: 10.1002/2017JD026930.

[276] Qi, L., Chen, M., Stefenelli, G., Pospisilova, V., Tong, Y., Bertrand, A., Hueglin, C., Ge, X., Baltensperger, U., Prévôt, A. S. H., and Slowik, J. G. Organic aerosol source apportionment in Zurich using an extractive electrospray ionization time-of-flight mass spectrometer (EESI-TOF-MS) – Part 2: Biomass burning influences in winter. *Atmos. Chem. Phys.* 19 (12 2019), pp. 8037–8062. DOI: 10.5194/acp-19-8037-2019.

[277] Bruns, E. A., Krapf, M., Orasche, J., Huang, Y., Zimmermann, R., Drinovec, L., Močnik, G., El-Haddad, I., Slowik, J. G., Dommen, J., Baltensperger, U., and Prévôt, A. S. H. Characterization of primary and secondary wood combustion products generated under different burner loads. *Atmos. Chem. Phys* 15 (2015), pp. 2825–2841. DOI: 10.5194/acp-15-2825-2015.

[278] Fitzpatrick, E. M., Jones, J. M., Pourkashanian, M., Ross, A. B., Williams, A., and Bartle, K. D. Mechanistic aspects of soot formation from the combustion of pine wood. *Energy Fuels* 22 (6 2008), pp. 3771–3778. DOI: 10.1021/EF800456K.

[279] Orasche, J., Schnelle-Kreis, J., Schön, C., Hartmann, H., Ruppert, H., Arteaga-Salas, J. M., and Zimmermann, R. Comparison of emissions from wood combustion. Part 2: Impact of combustion conditions on emission factors and characteristics of particle-bound organic species and polycyclic aromatic hydrocarbon (PAH)-related toxicological potential. *Energy Fuels* 27 (3 2013), pp. 1482–1491. DOI: 10.1021/EF301506H.

[280] Kjällstrand, J. and Olsson, M. Chimney emissions from small-scale burning of pellets and fuelwood—examples referring to different combustion appliances. *Biomass Bioenergy* 27 (6 2004), pp. 557–561. DOI: 10.1016/J.BIOMBIOE.2003.08.014.

[281] Fang, Z., Li, C., He, Q., Czech, H., Gröger, T., Zeng, J., Fang, H., Xiao, S., Pardo, M., Hartner, E., Meidan, D., Wang, X., Zimmermann, R., Laskin, A., and Rudich, Y. Secondary organic aerosols produced from photochemical oxidation of secondarily evaporated biomass burning organic gases: Chemical composition, toxicity, optical properties, and climate effect. *Environ. Int.* 157 (2021). DOI: 10.1016/j.envint.2021.106801.

[282] Kundu, S., Kawamura, K., Andreae, T. W., Hoffer, A., and Andreae, M. O. Molecular distributions of dicarboxylic acids, ketocarboxylic acids and -dicarbonyls in biomass burning aerosols: implications for photochemical production and degradation in smoke layers. *Atmos. Chem. Phys* 10 (2010), pp. 2209–2225. DOI: 10.5194/acp-10-2209-2010.

[283] Liang, Y., Jen, C. N., Weber, R. J., Misztal, P. K., and Goldstein, A. H. Chemical composition of PM 2.5 in October 2017 Northern California wildfire plumes. *Atmos. Chem. Phys* 21 (2021), pp. 5719–5737. DOI: 10.5194/acp-21-5719-2021.

[284] Li, J., Li, J., Wang, G., Zhang, T., Dai, W., Ho, K. F., Wang, Q., Shao, Y., Wu, C., and Li, L. Molecular characteristics of organic compositions in fresh and aged biomass burning aerosols. *Sci. Tot. Environ.* 741 (2020). DOI: 10.1016/j.scitotenv.2020.140247.

[285] Kim, Y. H., Sinha, A., George, I. J., DeMarini, D. M., Grieshop, A. P., and Gilmour, M. I. Toxicity of fresh and aged anthropogenic smoke particles emitted from different burning conditions. *Sci. Tot. Environ.* 892 (2023), p. 164778. DOI: 10.1016/J.SCITOTENV.2023.164778.

[286] Desyaterik, Y., Sun, Y., Shen, X., Lee, T., Wang, X., Wang, T., and Collett, J. L. Speciation of "brown" carbon in cloud water impacted by agricultural biomass burning in eastern China. *J. Geophys. Res.: Atmos.* 118 (13 2013), pp. 7389–7399. DOI: 10.1002/JGRD.50561.

[287] Bertrand, A., Stefenelli, G., Bruns, E. A., Pieber, S. M., Temime-Roussel, B., Slowik, J. G., Prévôt, A. S., Wortham, H., Haddad, I. E., and Marchand, N. Primary emissions and secondary aerosol production potential from woodstoves for residential heating: Influence of the stove technology and combustion efficiency. *Atmos. Environ.* 169 (2017), pp. 65–79. DOI: 10.1016/J.ATMOSENV.2017.09.005.

[288] Grieshop, A. P., Logue, J. M., Donahue, N. M., and Robinson, A. L. Laboratory investigation of photochemical oxidation of organic aerosol from wood fires 1: measurement and simulation of organic aerosol evolution. *Atmos. Chem. Phys.* 9 (4 2009), pp. 1263–1277. DOI: 10.5194/acp-9-1263-2009.

[289] Tasoglou, A., Saliba, G., Subramanian, R., and Pandis, S. N. Absorption of chemically aged biomass burning carbonaceous aerosol. *J. Aerosol Sci.* 113 (2017), pp. 141–152. DOI: 10.1016/J.JAEROSCI.2017.07.011.

[290] Chen, L., Bao, Z., Wu, X., Li, K., Han, L., Zhao, X., Zhang, X., Wang, Z., Azzi, M., and Cen, K. The effects of humidity and ammonia on the chemical composition of secondary aerosols from toluene/NOx photo-oxidation. *Sci. Tot. Environ.* 728 (2020), p. 138671. DOI: 10.1016/J.SCITOTENV.2020.138671.

[291] Loza, C. L., Chhabra, P. S., Yee, L. D., Craven, J. S., Flagan, R. C., and Seinfeld, J. H. Chemical aging of m-xylene secondary organic aerosol: laboratory chamber study. *Atmos. Chem. Phys.* 12 (1 2012), pp. 151–167. DOI: 10.5194/acp-12-151-2012.

[292] Chhabra, P. S., Flagan, R. C., and Seinfeld, J. H. Elemental analysis of chamber organic aerosol using an aerodyne high-resolution aerosol mass spectrometer. *Atmos. Chem. Phys.* 10 (9 2010), pp. 4111–4131. DOI: 10.5194/acp-10-4111-2010.

[293] Ofner, J., Krüger, H.-U., Grothe, H., Schmitt-Kopplin, P., Whitmore, K., and Zetzsch, C. Physico-chemical characterization of SOA derived from catechol and guaiacol – a model substance for the aromatic fraction of atmospheric HULIS. *Atmos. Chem. Phys.* 11 (1 2011), pp. 1–15. DOI: 10.5194/acp-11-1-2011.

[294] An, Y., Xu, J., Feng, L., Zhang, X., Liu, Y., Kang, S., Jiang, B., and Liao, Y. Molecular characterization of organic aerosol in the Himalayas: insight from ultra-high-resolution mass spectrometry. *Atmos. Chem. Phys.* 19 (2 2019), pp. 1115–1128. DOI: 10.5194/acp-19-1115-2019.

[295] Bloss, C., Wagner, V., Bonzanini, A., Jenkin, M. E., Wirtz, K., Martin-Reviejo, M., and Pilling, M. J. Evaluation of detailed aromatic mechanisms (MCMv3 and MCMv3.1) against environmental chamber data. *Atmos. Chem. Phys* 5 (2005), pp. 623–639. DOI: 10.5194/acp-5-623-2005.

[296] Zhang, J., Liu, D., Kong, S., Wu, Y., Li, S., Hu, D., Hu, K., Ding, S., Qiu, H., Li, W., and Liu, Q. Contrasting resistance of polycyclic aromatic hydrocarbons to atmospheric oxidation influenced by burning conditions. *Environ. Res.* 211 (2022), p. 113107. DOI: 10.1016/J.ENVRES.2022.113107.

[297] Jen, C. N., Hatch, L. E., Selimovic, V., Yokelson, R. J., Weber, R., Fernandez, A. E., Kreisberg, N. M., Barsanti, K. C., and Goldstein, A. H. Speciated and total emission factors of particulate organics from burning western US wildland fuels and their dependence on

combustion efficiency. *Atmos. Chem. Phys* 19 (2019), pp. 1013–1026. DOI: 10.5194/acp-19-1013-2019.

[298] Li, Y., Pöschl, U., and Shiraiwa, M. Molecular corridors and parameterizations of volatility in the chemical evolution of organic aerosols. *Atmos. Chem. Phys.* 16 (5 2016), pp. 3327–3344. DOI: 10.5194/ACP-16-3327-2016.

[299] Ward, T. J., Semmens, E. O., Weiler, E., Harrar, S., and Noonan, C. W. Efficacy of interventions targeting household air pollution from residential wood stoves. *J. Expo. Sci Environ. Epidemiol.* 27 (1 2015), pp. 64–71. DOI: 10.1038/jes.2015.73.

[300] Yokelson, R. J., Christian, T. J., Karl, T. G., and Guenther, A. The tropical forest and fire emissions experiment: laboratory fire measurements and synthesis of campaign data. *Atmospheric Chemistry and Physics* 8 (13 2008), pp. 3509–3527. DOI: 10.5194/acp-8-3509-2008.

[301] Crutzen, P. J. and Andreae, M. O. Biomass Burning in the Tropics: Impact on Atmospheric Chemistry and Biogeochemical Cycles. *Science* 250 (4988 1990), pp. 1669–1678. DOI: 10.1126/SCIENCE.250.4988.1669.

[302] Yue, X. and Unger, N. Fire air pollution reduces global terrestrial productivity. *Nature Communications 2018 9:1* 9 (1 2018), pp. 1–9. DOI: 10.1038/s41467-018-07921-4.

[303] Crippa, P., Castruccio, S., Archer-Nicholls, S., Lebron, G. B., Kuwata, M., Thota, A., Sumin, S., Butt, E., Wiedinmyer, C., and Spracklen, D. V. Population exposure to hazardous air quality due to the 2015 fires in Equatorial Asia. *Scientific Reports 2016 6:1* 6 (1 2016), pp. 1–9. DOI: 10.1038/srep37074.

[304] Venkataraman, C., Habib, G., Eiguren-Fernandez, A., Miguel, A. H., and Friedlander, S. K. Residential biofuels in South Asia: Carbonaceous aerosol emissions and climate impacts. *Science* 307 (5714 2005), pp. 1454–1456. DOI: 10.1126/SCIENCE.1104359.

[305] Reddington, C. L., Yoshioka, M., Balasubramanian, R., Ridley, D., Toh, Y. Y., Arnold, S. R., and Spracklen, D. V. Contribution of vegetation and peat fires to particulate air pollution in Southeast Asia. *Environmental Research Letters* 9 (9 2014), p. 094006. DOI: 10.1088/1748-9326/9/9/094006.

[306] Yokelson, R. J., Crounse, J. D., DeCarlo, P. F., Karl, T., Urbanski, S., Atlas, E., Campos, T., Shinozuka, Y., Kapustin, V., Clarke, A. D., Weinheimer, A., Knapp, D. J., Montzka, D. D., Holloway, J., Weibring, P., Flocke, F., Zheng, W., Toohey, D., Wennberg, P. O., Wiedinmyer, C., Mauldin, L., Fried, A., Richter, D., Walega, J., Jimenez, J. L., Adachi, K.,

Buseck, P. R., Hall, S. R., and Shetter, R. Emissions from biomass burning in the Yucatan. *Atmospheric Chemistry and Physics* 9 (15 2009), pp. 5785–5812. DOI: 10.5194/acp-9-5785-2009.

[307] Hartikainen, A., Yli-Pirilä, P., Tiitta, P., Leskinen, A., Kortelainen, M., Orasche, J. R., Schnelle-Kreis, J. R., Lehtinen, K. E. J., Zimmermann, R., Jokiniemi, J., and Sippula, O. Volatile Organic Compounds from Logwood Combustion: Emissions and Transformation under Dark and Photochemical Aging Conditions in a Smog Chamber. *Environ. Sci. Technol.* 52 (2018), pp. 4979–4988. DOI: 10.1021/acs.est.7b06269.

[308] Müller, M., Anderson, B. E., Beyersdorf, A. J., Crawford, J. H., Diskin, G. S., Eichler, P., Fried, A., Keutsch, F. N., Mikoviny, T., Thornhill, K. L., Walega, J. G., Weinheimer, A. J., Yang, M., Yokelson, R. J., and Wisthaler, A. In situ measurements and modeling of reactive trace gases in a small biomass burning plume. *Atmospheric Chemistry and Physics* 16 (6 2016), pp. 3813–3824. DOI: 10.5194/acp-16-3813-2016.

[309] Yee, L. D., Kautzman, K. E., Loza, C. L., Schilling, K. A., Coggon, M. M., Chhabra, P. S., Chan, M. N., Chan, A. W., Hersey, S. P., Crounse, J. D., Wennberg, P. O., Flagan, R. C., and Seinfeld, J. H. Secondary organic aerosol formation from biomass burning intermediates: Phenol and methoxyphenols. *Atmospheric Chemistry and Physics* 13 (16 2013), pp. 8019–8043. DOI: 10.5194/acp-13-8019-2013.

[310] Zhang, H., Yang, B., Wang, Y., Shu, J., Zhang, P., Ma, P., and Li, Z. Gas-Phase Reactions of Methoxyphenols with NO3 Radicals: Kinetics, Products, and Mechanisms. *Journal of Physical Chemistry A* 120 (8 2016), pp. 1213–1221. DOI: 10.1021/ACS.JPCA.5B10406.

[311] Jiang, J., Carter, W. P., Cocker, D. R., and Barsanti, K. C. Development and Evaluation of a Detailed Mechanism for Gas-Phase Atmospheric Reactions of Furans. *ACS Earth and Space Chemistry* 4 (8 2020), pp. 1254–1268. DOI: 10.1021/acsearthspacechem.0c00058.

[312] Wei, B., Sun, J., Mei, Q., and He, M. Mechanism and kinetic of nitrate radical-initiated atmospheric reactions of guaiacol (2-methoxyphenol). *Computational and Theoretical Chemistry* 1129 (2018), pp. 1–8. DOI: 10.1016/J.COMPTC.2018.02.014.

[313] Yang, B., Zhang, H., Wang, Y., Zhang, P., Shu, J., Sun, W., and Ma, P. Experimental and theoretical studies on gas-phase reactions of NO3 radicals with three methoxyphenols: Guaiacol, creosol, and syringol. *Atmospheric Environment* 125 (2016), pp. 243–251. DOI: 10.1016/J.ATMOSENV.2015.11.028.

[314] Mcdonald, J. D., Zielinska, B., Fujita, E. M., Sagebiel, J. C., Chow, J. C., and Watson, J. G. Fine particle and gaseous emission rates from residential wood combustion. *Environmental Science and Technology* 34 (11 2000), pp. 2080–2091. DOI: 10.1021/es9909632.

[315] Liu, C., Chen, D., and Chen, X. Atmospheric Reactivity of Methoxyphenols: A Review. *Environmental Science and Technology* 56 (5 2022), pp. 2897–2916. DOI: 10.1021/ACS.EST.1C06535.

[316] Liu, C. and Zeng, C. Heterogeneous kinetics of methoxyphenols in the OH-initiated reactions under different experimental conditions. *Chemosphere* 209 (2018), pp. 560–567. DOI: 10.1016/J.CHEMOSPHERE.2018.06.131.

[317] Bari, M. A., Baumbach, G., Kuch, B., and Scheffknecht, G. Wood smoke as a source of particle-phase organic compounds in residential areas. *Atmospheric Environment* 43 (31 2009), pp. 4722–4732. DOI: 10.1016/J.ATMOSENV.2008.09.006.

[318] Schauer, J. J., Kleeman, M. J., Cass, G. R., and Simoneit, B. R. Measurement of emissions from air pollution sources. 3. C1-C29 organic compounds from fireplace combustion of wood. *Environ. Sci. Technol.* 35 (9 2001), pp. 1716–1728. DOI: 10.1021/es001331e.

[319] Coeur-Tourneur, C., Cassez, A., and Wenger, J. C. Rate coefficients for the gas-phase reaction of hydroxyl radicals with 2-methoxyphenol (guaiacol) and related compounds. *Journal of Physical Chemistry A* 114 (43 2010), pp. 11645–11650. DOI: 10.1021/JP1071023.

[320] Liu, C., Liu, J., Liu, Y., Chen, T., and He, H. Secondary organic aerosol formation from the OH-initiated oxidation of guaiacol under different experimental conditions. *Atmospheric Environment* 207 (2019), pp. 30–37. DOI: 10.1016/J.ATMOSENV.2019.03.021.

[321] Priya, A. M. and Lakshmipathi, S. DFT study on abstraction reaction mechanism of oh radical with 2-methoxyphenol. *Journal of Physical Organic Chemistry* 30 (12 2017), e3713. DOI: 10.1002/POC.3713.

[322] He, L., Schaefer, T., Otto, T., Kroflič, A., and Herrmann, H. Kinetic and Theoretical Study of the Atmospheric Aqueous-Phase Reactions of OH Radicals with Methoxyphenolic Compounds. *Journal of Physical Chemistry A* 123 (36 2019), pp. 7828–7838. DOI: 10.1021/ACS.JPCA.9B05696.

[323] An, Z., Sun, J., Han, D., Mei, Q., Wei, B., Wang, X., and He, M. Theoretical study on the mechanisms, kinetics and ecotoxicity assessment of OH-initiated reactions of guaiacol in atmosphere and wastewater. *Science of The Total Environment* 685 (2019), pp. 729–740. DOI: 10.1016/J.SCITOTENV.2019.06.229.

[324] Sun, Y., Xu, F., Li, X., Zhang, Q., and Gu, Y. Mechanisms and kinetic studies of OH-initiated atmospheric oxidation of methoxyphenols in the presence of O2 and NOx. *Physical Chemistry Chemical Physics* 21 (39 2019), pp. 21856–21866. DOI: 10.1039/C9CP03246K.

[325] Finewax, Z., Gouw, J. A. D., and Ziemann, P. J. Identification and Quantification of 4-Nitrocatechol Formed from OH and NO3 Radical-Initiated Reactions of Catechol in Air in the Presence of NOx: Implications for Secondary Organic Aerosol Formation from Biomass Burning. *Environmental Science and Technology* 52 (4 2018), pp. 1981–1989. DOI: 10.1021/acs.est.7b05864.

[326] Kroflič, A., Anders, J., Ivana Drventić, D., Mettke, P., Böge, O., Mutzel, A., Kleffmann, J., and Herrmann, H. Guaiacol Nitration in a Simulated Atmospheric Aerosol with an Emphasis on Atmospheric Nitrophenol Formation Mechanisms. *ACS Earth and Space Chemistry* 5 (2021), pp. 1083–1093. DOI: 10.1021/ACSEARTHSPACECHEM.1C00014.

[327] Bloss, C., Wagner, V., Jenkin, M. E., Volkamer, R., Bloss, W. J., Lee, J. D., Heard, D. E., Wirtz, K., Martin-Reviejo, M., Rea, G., Wenger, J. C., and Pilling, M. J. Development of a detailed chemical mechanism (MCMv3.1) for the atmospheric oxidation of aromatic hydrocarbons. *Atmospheric Chemistry and Physics* 5 (3 2005), pp. 641–664. DOI: 10.5194/acp-5-641-2005.

[328] Pereira, K. L., Hamilton, J. F., Rickard, A. R., Bloss, W. J., Alam, M. S., Camredon, M., Ward, M. W., Wyche, K. P., Muñoz, A., Vera, T., Vázquez, M., Borrás, E., and Ródenas, M. Insights into the Formation and Evolution of Individual Compounds in the Particulate Phase during Aromatic Photo-Oxidation. *Environmental Science and Technology* 49 (22 2015), pp. 13168–13178. DOI: 10.1021/ACS.EST.5B03377.

[329] Bali, K., Kumar, A., and Chourasiya, S. Emission estimates of trace gases (VOCs and NOx) and their reactivity during biomass burning period (2003–2017) over Northeast India. *Journal of Atmospheric Chemistry* 78 (1 2021), pp. 17–34. DOI: 10.1007/S10874-020-09413-6/FIGURES/7.

[330] Kumar, A., Bali, K., Singh, S., Naja, M., and Mishra, A. K. Estimates of reactive trace gases (NMVOCs, CO and NOx) and their ozone forming potentials during forest fire over Southern Himalayan region. *Atmospheric Research* 227 (2019), pp. 41–51. DOI: 10.1016/J.ATMOSRES.2019.04.028.

[331] Sommariva, R., Cox, S., Martin, C., Borońska, K., Young, J., Jimack, P. K., Pilling, M. J., Matthaios, V. N., Nelson, B. S., Newland, M. J., Panagi, M., Bloss, W. J., Monks, P. S., and Rickard, A. R. AtChem (version 1), an open-source box model for the Master Chemical Mechanism. *Geoscientific Model Development* 13 (1 2020), pp. 169–183. DOI: 10.5194/gmd-13-169-2020.

[332] Saunders, S. M., Jenkin, M. E., Derwent, R. G., and Pilling, M. J. Protocol for the development of the Master Chemical Mechanism, MCM v3 (Part A): tropospheric degradation of non-aromatic volatile organic compounds. *Atmospheric Chemistry and Physics* 3 (1 2003), pp. 161–180. DOI: 10.5194/acp-3-161-2003.

[333] Alfarra, R., Camredon, M., Cazaunau, M., Doussin, J.-F., Fuchs, H., Jorga, S., McFiggans, G., Newland, M. J., Pandis, S., Rickard, A. R., and Saathoff, H. Physical and Chemical Characterization of the Chamber. *A Practical Guide to Atmospheric Simualtion Chambers*. Springer, 2023.

[334] Zádor, J., Turányi, T., Wirtz, K., and Pilling, M. J. Measurement and investigation of chamber radical sources in the European Photoreactor (EUPHORE). *Journal of Atmospheric Chemistry* 55 (2 2006), pp. 147–166. DOI: 10.1007/S10874-006-9033-Y.

[335] Jenkin, M. E., Saunders, S. M., and Pilling, M. J. The tropospheric degradation of volatile organic compounds: A protocol for mechanism development. *Atmospheric Environment* 31 (1 1997), pp. 81–104. DOI: 10.1016/S1352-2310(96)00105-7.

[336] Jenkin, M. E., Saunders, S. M., Wagner, V., and Pilling, M. J. Protocol for the development of the Master Chemical Mechanism, MCM v3 (Part B): tropospheric degradation of aromatic volatile organic compounds. *Atmospheric Chemistry and Physics* 3 (1 2003), pp. 181–193. DOI: 10.5194/acp-3-181-2003.

[337] Atkinson, R. and Carter, W. P. Kinetics and Mechanisms of the Gas-Phase Reactions of Ozone with Organic Compounds under Atmospheric Conditions. *Chemical Reviews* 84 (5 1984), pp. 437–470. DOI: 10.1021/CR00063A002.

[338] Atkinson, R., Baulch, D. L., Cox, R. A., Crowley, J. N., Hampson, R. F., Hynes, R. G., Jenkin, M. E., Rossi, M. J., and Troe, J. Evaluated kinetic and photochemical data for atmospheric chemistry: Volume II – gas phase reactions of organic species. *Atmospheric Chemistry and Physics* 6 (11 2006), pp. 3625–4055. DOI: 10.5194/acp-6-3625-2006.

[339] Jenkin, M. E., Valorso, R., Aumont, B., Rickard, A. R., and Wallington, T. J. Estimation of rate coefficients and branching ratios for gas-phase reactions of OH with aromatic organic compounds for use in automated mechanism construction. *Atmospheric Chemistry and Physics* 18 (13 2018), pp. 9329–9349. DOI: 10.5194/ACP-18-9329-2018.

[340] Coeur-Tourneur, C., Henry, F., Janquin, M. A., and Brutier, L. Gas-phase reaction of hydroxyl radicals with m-, o- and p-cresol. *International Journal of Chemical Kinetics* 38 (9 2006), pp. 553–562. DOI: 10.1002/KIN.20186.

[341] Aumont, B., Szopa, S., and Madronich, S. Modelling the evolution of organic carbon during its gas-phase tropospheric oxidation: development of an explicit model based on a self generating approach. *Atmospheric Chemistry and Physics* 5 (9 2005), pp. 2497–2517. DOI: 10.5194/acp-5-2497-2005.

[342] Hudman, R. C., Jacob, D. J., Cooper, O. R., Evans, M. J., Heald, C. L., Park, R. J., Fehsenfeld, F., Flocke, F., Holloway, J., Hübler, G., Kita, K., Koike, M., Kondo, Y., Neuman, A., Nowak, J., Oltmans, S., Parrish, D., Roberts, J. M., and Ryerson, T. Ozone production in transpacific Asian pollution plumes and implications for ozone air quality in California. *Journal of Geophysical Research: Atmospheres* 109 (D23 2004), pp. 1–14. DOI: 10.1029/2004JD004974.

[343] Wang, W. C., Liang, X. Z., Dudek, M. P., Pollard, D., and Thompson, S. L. Atmospheric ozone as a climate gas. *Atmospheric Research* 37 (1-3 1995), pp. 247–256. DOI: 10.1016/0169-8095(94)00080-W.

[344] Wang, W. C. Tropospheric ozone and climate change. *Air and Waste* 43 (10 1993), pp. 1332–1334. DOI: 10.1080/1073161X.1993.10467207.

[345] Orlando, J. J., Tyndall, G. S., and Wallington, T. J. The Atmospheric Chemistry of Alkoxy Radicals. *Chemical Reviews* 103 (12 2003), pp. 4657–4689. DOI: 10.1021/CR020527P.

[346] Valiev, R. R., Hasan, G., Salo, V. T., Kubečka, J., and Kurten, T. Intersystem Crossings Drive Atmospheric Gas-Phase Dimer Formation. *Journal of Physical Chemistry A* 123 (30 2019), pp. 6596–6604. DOI: 10.1021/ACS.JPCA.9B02559.

[347] Takegawa, N., Kondo, Y., Koike, M., Ko, M., Kita, K., Blake, D. R., Nishi, N., Hu, W., Liley, J. B., Kawakami, S., Shirai, T., Miyazaki, Y., Ikeda, H., Russell-Smith, J., and Ogawa, T. Removal of NOx and NOy in biomass burning plumes in the boundary layer over northern Australia. *Journal of Geophysical Research: Atmospheres* 108 (D10 2003). DOI: 10.1029/2002JD002505.

[348] Jalava, P. I., Wang, Q., Kuuspalo, K., Ruusunen, J., Hao, L., Fang, D., Väisänen, O., Ruuskanen, A., Sippula, O., Happo, M. S., Uski, O., Kasurinen, S., Torvela, T., Koponen, H., Lehtinen, K. E., Komppula, M., Gu, C., Jokiniemi, J., and Hirvonen, M. R. Day and night variation in chemical composition and toxicological responses of size segregated urban air PM samples in a high air pollution situation. *Atmospheric Environment* 120 (2015), pp. 427–437. DOI: 10.1016/J.ATMOSENV.2015.08.089.

[349] Mohan, V., Soni, V. K., and Mishra, R. K. Analysing the impact of day-night road traffic variation on ultrafine particle number size distribution and concentration at an urban site in the megacity Delhi. *Atmospheric Pollution Research* 15 (4 2024), p. 102065. DOI: 10.1016/J.APR.2024.102065.

[350] Zhang, Q., Xu, Y., and Jia, L. Secondary organic aerosol formation from OH-initiated oxidation of m-xylene: effects of relative humidity on yield and chemical composition. *Atmospheric Chemistry and Physics* 19 (23 2019), pp. 15007–15021. DOI: 10.5194/acp-19-15007-2019.

[351] Chhabra, P. S., Ng, N. L., Canagaratna, M. R., Corrigan, A. L., Russell, L. M., Worsnop, D. R., Flagan, R. C., and Seinfeld, J. H. Elemental composition and oxidation of chamber organic aerosol. *Atmospheric Chemistry and Physics* 11 (17 2011), pp. 8827–8845. DOI: 10.5194/acp-11-8827-2011.

[352] Nakao, S., Clark, C., Tang, P., Sato, K., and III, D. C. Secondary organic aerosol formation from phenolic compounds in the absence of NO_x. *Atmospheric Chemistry and Physics* 11 (20 2011), pp. 10649–10660. DOI: 10.5194/acp-11-10649-2011.

[353] Bejan, I., Aal, Y. A. E., Barnes, I., Benter, T., Bohn, B., Wiesen, P., and Kleffmann, J. The photolysis of ortho-nitrophenols: a new gas phase source of HONO. *Physical Chemistry Chemical Physics* 8 (17 2006), pp. 2028–2035. DOI: 10.1039/B516590C.

[354] Sumlin, B., Fortner, E., Lambe, A., Shetty, N. J., Daube, C., Liu, P., Majluf, F., Herndon, S., and Chakrabarty, R. K. Diel cycle impacts on the chemical and light absorption properties of organic carbon aerosol from wildfires in the western United States. *Atmospheric Chemistry and Physics* 21 (15 2021), pp. 11843–11856. DOI: 10.5194/acp-21-11843-2021.

[355] Zhao, R., Lee, A. K. Y., Huang, L., Li, X., Yang, F., and Abbatt, J. P. D. Photochemical processing of aqueous atmospheric brown carbon. *Atmospheric Chemistry and Physics* 15 (11 2015), pp. 6087–6100. DOI: 10.5194/acp-15-6087-2015. URL: https://acp.copernicus.org/articles/15/6087/2015/.

[356] Buchholz, A., Ylisirniö, A., Huang, W., Mohr, C., Canagaratna, M., Worsnop, D. R., Schobesberger, S., and Virtanen, A. Deconvolution of FIGAERO–CIMS thermal desorption profiles using positive matrix factorisation to identify chemical and physical processes during particle evaporation. *Atmospheric Chemistry and Physics* 20 (13 2020), pp. 7693–7716. DOI: 10.5194/acp-20-7693-2020.

[357] Wang, J., Zhang, X., Guo, J., Wang, Z., and Zhang, M. Observation of nitrous acid (HONO) in Beijing, China: Seasonal variation, nocturnal formation and daytime budget. *Science of The Total Environment* 587-588 (2017), pp. 350–359. DOI: 10.1016/J.SCITOTENV.2017.02.159.

[358] Shaw, D. R., Carter, T. J., Davies, H. L., Harding-Smith, E., Crocker, E. C., Beel, G., Wang, Z., and Carslaw, N. INCHEM-Py v1.2: a community box model for indoor air chemistry. *Geoscientific Model Development* 16 (24 2023), pp. 7411–7431. DOI: 10.5194/gmd-16-7411-2023.